Effects of Vertical Acceleration on Prestressed Concrete Bridges

by

Daniel Scott Broekhuizen, B.S.E.

Thesis

Presented to the Faculty of the Graduate School
of The University of Texas at Austin
in Partial Fulfillment
of the Requirements
for the degree of

Master of Science in Engineering

The University of Texas at Austin
August 1996

ABSTRACT

Effects of Vertical Acceleration on Prestressed Concrete Bridges

by

Daniel Scott Broekhuizen, M.S.E

The University of Texas at Austin, 1996

SUPERVISOR: John E. Breen

This thesis evaluates the potential effects of vertical ground accelerations, when combined with the horizontal components of motion, on the seismic response of highway bridges. The thesis pays particular attention to prestressed concrete bridge spans. The effects examined are the stresses in the piers and the girders, the potentially harmful effects of vertical accelerations that may offset the girder dead load balanced by the tendon uplift forces, the maximum ductility requirement if there is inelastic action, and the potential slippage and permanent displacements at the seats of the girders.

A series of parametric studies is done on simple models of highway bridges. After this, detailed studies are conducted on the north and south connectors and the separation and overhead of the I5/SR14 interchange damaged in the 1994 Northridge earthquake. Elastic are used to evaluate the bridge's behavior. Recommendations for possible design code changes are suggested at the end.

ACKNOWLEDGEMENTS

I would like to thank the many people who helped me during my research project and the writing of this thesis. First of all, I wish to wholeheartedly thank my Lord Jesus Christ, whose care and guiding hand watched over me during this work. I also want to thank my wife, Helen, whose encouragement kept me going many times.

Dr. Breen deserves my special thanks for his insight into this project and his wonderful help at each stage of the research. Thanks to Dr. Roesset for his work on the computer modelling aspect of the project. I wish to especially thank Chih-Peng for all of his patience with me, for the many analyses he did on the computer, and for his help with Chapters 3 and 4. Without him I could not have finished the project. I also wish to thank my parents, friends from First Evangelical Free Church, and other family members who were there for me when I needed anything.

I also wish to thank the National Science foundation and the Texas Structural Steel Institute for their financial support while I was working on this project. It was greatly appreciated.

Table of Contents

List of Tables viii

List of Figures x

Chapter 1 - Background 1

1.1 Introduction 1

1.2 Interaction of Vertical Accelerations with Prestressed Concrete Bridges 2

1.3 Objectives 4

1.4 Previous Research 6

1.5 Organization of Thesis 11

Chapter 2 - Bridge Descriptions and Earthquake Records 13

2.1 Northridge Earthquake Overview 13

2.2 Damage During 1971 San Fernando Earthquake 15

2.3 Damage During 1994 Northridge Earthquake 17

2.4 Bridge Descriptions 22

2.5 Tendon Layouts 46

2.6 Northridge Earthquake Records 49

Chapter 3 - Computer Program and Model 51

3.1 Description of Computer Program BRIDGEQUAKE 51

3.2 Modeling of Structure 54

3.3 Seismic Excitation 55

Table of Contents (con't)

Chapter 4 - Analysis of Superstructure 57

4.1 Characteristics of Earthquake Motion 57

4.2 Analysis of Simple Frames 62

4.3 Study of Multi-Span Frames 72

4.4 Summary of Parametric Studies 84

4.5 Analysis of Draped Tendons 86

Chapter 5 - Analysis of Substructure 100

5.1 Introduction 100

5.2 Column Interaction Diagrams 101

5.3 Sylmar Hospital Earthquake Results 102

5.4 Artificial Earthquake Results 114

5.5 UBC/AASHTO Analysis 134

5.6 Two Components of Acceleration vs. Three Components of Acceleration 152

5.7 Comparison to Observed Damage After Northridge Earthquake . . . 156

Chapter 6 - Analysis of Hinges

6.1 Hinge Restrainer Stiffness 165

6.2 Stiffnesses for Structures Studied 167

6.3 Joint Displacement Results 168

Chapter 7 - Conclusions 173

Table of Contents (con't)

7.1 Summary of Findings 174

7.2 Conclusions 176

7.3 Design Recommendations 178

7.4 Possible Future Research 178

Appendix A - CALTRANS Bridge Plans 180

Appendix B - NCEER-Lamont-Doherty Observatory Artificial Earthquake Records 212

Appendix C - Calculation of Moment Capacity 225

Appendix D - Calculation of Prestress Moments and Stresses 227

Appendix E - Column Interaction Diagram Calculation 233

Bibliography 242

Vita 245

List of Tables

Table

2.1 Pier heights (above ground) for North Connector 28

2.2 Dimensions of box girder cross section for North Connector 31

2.3 Number of #18 longitudinal bars per pier 32

2.4 Pier heights (above ground) for Separation and Overhead 34

2.5 Pile depth (below grade) for Separation and Overhead 34

2.6 Pier data for the Separation and Overhead 39

2.7 Pier heights (above ground) for South Connector 41

2.8 Pile depth (below grade) for South Connector 41

2.9 Pier data for the South Connector 46

2.10 Cable eccentricities 48

2.11 Distance between eccentricity points 48

4.1 Accelerations for single span frames with varying span length 65

4.2 Accelerations for single span frames with varying column height 69

4.3 Cross-section properties for North Connector 88

4.4 Cross-section properties for Separation and Overhead 89

4.5 Cross-section properties for South Connector 89

4.6 Maximum allowable tensile stresses 96

5.1 In-plane moment results for North Connector 102

List of Tables (con't)

Table

5.2 Out-of-plane moment results for North Connector 107

5.3 In-plane moment results for North Connector 114

5.4 In-plane moment results for North Connector 140

5.5 Out-of-plane moments for Separation and Overhead 147

5.6 Results of adding vertical acceleration for Ramp L 153

5.7 Results of adding vertical acceleration for Ramp M 154

5.8 Results of adding vertical acceleration for Ramp C 155

6.1 Restrainer units for each bridge 167

6.2 Cable restrainer unit stiffnesses 168

List of Figures

Figure

1.1 Load-balancing forces due to prestressing tendons 4

  1.1(a) Linearly draped tendon 4
  1.1(b) Parabolic tendon 4
  1.1(c) Continuous spans with parabolic tendons 4

1.2 Time history of applied shear vs. shear capacity 8

1.3 Time history of abutment vertical force 8

1.4 Displacement ductility 10

1.5 Column interaction diagram 11

2.1 SR14/I5 overview 15

2.2 North Connector after 1971 San Fernando earthquake 16

2.3 Separation and Overhead after 1971 San Fernando earthquake 18

2.4 South Connector after 1971 San Fernando earthquake 19

2.5 Proposed failure of North Connector during 1994 Northridge earthquake 20

  2.5 (a) Bridge before earthquake 20
  2.5 (b) Pier #2 fails in shear 20
  2.5 (c) Drop-in span #1 falls off of supports 21
  2.5 (d) Cantilevering span #2 fails due to negative moment at pier #3 21

2.6 Proposed failure of Separation and Overhead during 1994 Northridge earthquake 23

  2.6 (a) Pier #2 fails in shear 23
  2.6 (b) Hinge forms in positive moment region at pier #2 23
  2.6 (c) Span #1 collapses and falls off of abutment seat 24

List of Figures (con't)

Figure

2.6 (d) Span #2 collapses due to negative moment failure and tendon rupture . . . 24
2.6 (e) Span #3 collapses due to negative moment failure at pier #3 . . . 25

2.7 North Connector elevation view . . . 26

2.8 North Connector plan view . . . 27

2.9 North Connector 2-box girder detail . . . 29

2.10 North Connector 3-box girder detail . . . 30

2.11 North Connector pier detail . . . 33

2.12 Separation and Overhead elevation view . . . 35

2.13 Separation and Overhead plan view . . . 36

2.14 Separation and Overhead box girder detail . . . 38

2.15 Separation and Overhead pier detail . . . 40

2.16 South Connector elevation view . . . 43

2.17 South Connector plan view . . . 44

2.18 South Connector box girder detail . . . 45

2.19 South Connector pier detail . . . 47

2.20 Cable eccentricity diagram . . . 49

2.21 Cable eccentricity diagram . . . 49

3.1 1994 UBC horizontal motion response spectrum . . . 55

4.1 Sylmar Hospital E-W records during Northridge earthquake . . . 59

List of Figures (con't)

Figure

4.1(a) Corrected accelerogram in E-W direction 59
4.1(b) FFT amplitude spectrum in E-W direction 59
4.1(c) Absolute acceleration spectrum in E-W direction 59

4.2 Sylmar Hospital N-S records during Northridge earthquake 60

4.2(a) Corrected accelerogram in N-S direction 60
4.2(b) FFT amplitude spectrum in N-S direction 60
4.2(c) Absolute acceleration spectrum in N-S direction 60

4.3 Sylmar Hospital vertical records during Northridge earthquake 61

4.3(a) Corrected accelerogram in vertical direction 61
4.3(b) FFT amplitude spectrum in vertical direction 61
4.3(c) Absolute acceleration spectrum in vertical direction 61

4.4 Single span frames 62

4.5 Transfer functions at mid-span for single span case 64

4.6 Transfer functions of single span frames with a span length of 100 feet . . . 67

4.7 Transfer functions of single span frames with a span length of 200 feet . . . 68

4.8 Vibration shapes and deformed amplitudes for a single span frame (pier height = 200 feet, span length = 200 feet) 71

4.8(a) Transfer function at mid-span of monolithic frame 71
4.8(b)-4.8(d) Deformed shapes and amplitudes due to unit excitation at supports 71

4.9 Multi-span configurations 73

4.10 Effect of span length on maximum acceleration (2-span case) 74

4.10(a) At 1/10th span (station - 1) 74

List of Figures (con't)

Figure

4.10(b) At mid-span (station - 2) 74
4.10(c) At interior joint (station - 3) 74

4.11 Effect of span length on maximum acceleration (3-span case) 75

4.11(a) At 1/10th span (station - 1) 75
4.11(b) At mid-span of exterior beam (station - 2) 75
4.11(c) At interior column top (station - 3) 75
4.11(d) At mid-span of interior beam (station - 4) 75

4.12 Effect of column height on maximum accelerations at three different positions of the 2-span frames (span lengths = 100 feet and 200 feet) 77

4.12(a) At 1/10th span (station - 1) 77
4.12(b) At mid-span (station - 2) 77
4.12(c) At interior beam-column connection (station - 3) 77

4.13 Effect of column height on maximum accelerations at four different positions of the 3-span frames (span lengths = 100 feet and 200 feet) 78

4.13(a) At 1/10th span (station - 1) 78
4.13(b) At mid-span of exterior beam (station - 2) 78
4.13(c) At interior column top (station - 3) 78
4.13(d) At mid-span of interior beam (station - 4) 78

4.14 Transfer functions for 2-span frames (column height = 20') 80

4.15 Transfer functions for 3-span frames (column height = 20') 81

4.16 Vibration shapes and deformed amplitudes for a 2-span frame (column height = 20 feet, span length = 200 feet) 82

4.16(a) First mode 82
4.16(b) Second mode 82

List of Figures (con't)

Figure

4.17 Vibration shapes and deformed amplitudes for a 3-span frame (column height = 20 feet, span length = 200 feet) 83

- 4.17(a) First mode 83
- 4.17(b) Second mode 83
- 4.17(c) Third mode of hinged frame 83
- 4.17(d) Third mode of monolithic frame 83

4.18 Top fiber stress under "weightless" conditions 93

4.19 Bottom fiber stress under "weightless" conditions 93

4.20 Top fiber stress under "weightless" conditions 94

4.21 Bottom fiber stress under "weightless" conditions 94

4.22 Top fiber stress under "weightless" conditions 95

4.23 Bottom fiber stress under "weightless" conditions 95

4.24 Percent of dead load moment balanced 98

4.25 Percent of dead load moment balanced 98

4.26 Percent of dead load moment balanced 98

5.1 Moment Interaction Diagram 100

5.2 In-plane bending column interaction curves for pier top of North Connector piers using Sylmar Hospital earthquake record 103

5.3 In-plane bending column interaction curves for pier bottom of North Connector piers using Sylmar Hospital earthquake record 104

5.4 Out-of-plane bending column interaction curves for pier top of North Connector piers using Sylmar Hospital earthquake record 105

List of Figures (con't)

Figure

5.5 Out-of-plane bending column interaction curves for pier bottom of North Connector piers using Sylmar Hospital earthquake record 106

5.6 In-plane bending column interaction curves for pier top of Separation and Overhead piers using Sylmar Hospital earthquake record 108

5.7 In-plane bending column interaction curves for flare bottom of Separation and Overhead piers using Sylmar Hospital earthquake record . . . 109

5.8 In-plane bending column interaction curves for pier bottom of Separation and Overhead piers using Sylmar Hospital earthquake record . . . 110

5.9 Out-of-plane bending column interaction curves for pier top of Separation and Overhead piers using Sylmar Hospital earthquake record . . . 111

5.10 Out-of-plane bending column interaction curves for flare bottom of Separation and Overhead piers using Sylmar Hospital earthquake record 112

5.11 Out-of-plane bending column interaction curves for pier bottom of Separation and Overhead piers using Sylmar Hospital earthquake record 113

5.12 In-plane bending column interaction curves for pier top of South Connector piers using Sylmar Hospital earthquake record 115

5.13 In-plane bending column interaction curves for pier bottom of South Connector piers using Sylmar Hospital earthquake record 116

5.14 Out-of-plane bending column interaction curves for pier top of South Connector piers using Sylmar Hospital earthquake record 117

5.15 Out-of-plane bending column interaction curves for pier bottom of South Connector piers using Sylmar Hospital earthquake record 118

List of Figures (con't)

Figure

5.16 In-plane bending column interaction curves for pier top of North Connector piers using NCEER artificial earthquake record 119

5.17 In-plane bending column interaction curves for pier bottom of North Connector piers using NCEER artificial earthquake record 120

5.18 Out-of-plane bending column interaction curves for pier top of North Connector piers using NCEER artificial earthquake record 121

5.19 Out-of-plane bending column interaction curves for pier bottom of North Connector piers using NCEER artificial earthquake record 122

5.20 In-plane bending column interaction curves for pier top of Separation and Overhead piers using NCEER artificial earthquake record 124

5.21 In-plane bending column interaction curves for flare bottom of Separation and Overhead piers using NCEER artificial earthquake record . . 125

5.22 In-plane bending column interaction curves for pier bottom of Separation and Overhead piers using NCEER artificial earthquake record . . 126

5.23 Out-of-plane bending column interaction curves for pier top of Separation and Overhead piers using NCEER artificial earthquake record . . 127

5.24 Out-of-plane bending column interaction curves for flare bottom of Separation and Overhead piers using NCEER artificial earthquake record 128

5.25 Out-of-plane bending column interaction curves for pier bottom of Separation and Overhead piers using NCEER artificial earthquake record 129

5.26 In-plane bending column interaction curves for pier top of South Connector piers using NCEER artificial earthquake record 130

List of Figures (con't)

Figure

5.27 In-plane bending column interaction curves for pier bottom of South Connector piers using NCEER artificial earthquake record 131

5.28 Out-of-plane bending column interaction curves for pier top of South Connector piers using NCEER artificial earthquake record 132

5.29 Out-of-plane bending column interaction curves for pier bottom of South Connector piers using NCEER artificial earthquake record 133

5.30 UBC/AASHTO design spectrum 134

5.31 Simulated earthquake time history 135

5.32 In-plane bending column interaction curves for pier top of North Connector piers using UBC/AASHTO earthquake record 136

5.33 In-plane bending column interaction curves for pier bottom of North Connector piers using UBC/AASHTO earthquake record 137

5.34 Out-of-plane bending column interaction curves for pier top of North Connector piers using UBC/AASHTO earthquake record 138

5.35 Out-of-plane bending column interaction curves for pier bottom of North Connector piers using UBC/AASHTO earthquake record 139

5.36 In-plane bending column interaction curves for pier top of Separation and Overhead piers using UBC/AASHTO earthquake record 141

5.37 In-plane bending column interaction curves for flare bottom of Separation and Overhead piers using UBC/AASHTO earthquake record . . . 142

5.38 In-plane bending column interaction curves for pier bottom of Separation and Overhead piers using UBC/AASHTO earthquake record . . . 143

5.39 Out-of-plane bending column interaction curves for pier top of Separation and Overhead piers using UBC/AASHTO earthquake record . . . 144

List of Figures (con't)

Figure

5.40 Out-of-plane bending column interaction curves for flare bottom of Separation and Overhead piers using UBC/AASHTO earthquake record 145

5.41 Out-of-plane bending column interaction curves for pier bottom of Separation and Overhead piers using UBC/AASHTO earthquake record 146

5.42 In-plane bending column interaction curves for pier top of South Connector piers using UBC/AASHTO earthquake record 148

5.43 In-plane bending column interaction curves for pier bottom of South Connector piers using UBC/AASHTO earthquake record 149

5.44 Out-of-plane bending column interaction curves for pier top of South Connector piers using UBC/AASHTO earthquake record 150

5.45 Out-of-plane bending column interaction curves for pier bottom of South Connector piers using UBC/AASHTO earthquake record 151

6.1 Movement-equalizer bolt 158

6.2 Hinge restrainer detail (using bars) 159

6.2(a) Overview of bar assembly 159
6.2(b) Detail of bar assembly 160

6.3 Hinge restrainer detail (using cables) 161

6.3(a) Overview of cable assembly 161
6.3(b) Detail of cable assembly 162

6.4 Schematic showing failure of hinge restrainer assembly 163

6.4(a) Hinge restrainer before earthquake 163
6.4(b) Hinge restrainer stretches but keeps bridge together at hinge . . . 163

List of Figures (con't)

Figure

6.4(c) If deflection is too big, the steel pipe could crack and the restrainers could rupture, resulting in the girder unseating 164

6.5 Example of gap in hinge seat 166

6.6 Joint displacements for North Connector 169

6.7 Joint displacements for Separation and Overhead 170

6.8 Joint displacements for South Connector 171

A.1 North Connector general plan 181

A.2 North Connector typical section No. 1 182

A.3 North Connector typical section No. 2 183

A.4 North Connector girder layout No. 1 184

A.5 North Connector girder layout No. 2 185

A.6 North Connector span 1 prestressing details 186

A.7 North Connector spans 4 & 5 prestressing details 187

A.8 North Connector pier details 188

A.9 North Connector hinge restrainer 189

A.10 North Connector grid grades 190

A.11 Separation and Overhead general plan 191

A.12 Separation and Overhead typical section 192

A.13 Separation and Overhead girder layout 1 193

List of Figures (con't)

Figure

A.14 Separation and Overhead girder layout 3 194

A.15 Separation and Overhead girder layout 5 195

A.16 Separation and Overhead prestressing details 196

A.17 Separation and Overhead pier details 197

A.18 Separation and Overhead prestressed box girder hinge detail - elastomeric 198

A.19 Separation and Overhead hinge restrainer (Type 1) 199

A.20 Separation and Overhead restrainer unit (Type 2) 200

A.21 Separation and Overhead grid grades 201

A.22 South Connector general plan 202

A.23 South Connector typical section 203

A.24 South Connector girder layout 2 204

A.25 South Connector girder layout 4 205

A.26 South Connector prestressing details 206

A.27 South Connector pier details 1 207

A.28 South Connector pier details 2 208

A.29 South Connector prestressed box girder hinge detail - elastomeric 209

A.30 South Connector hinge restrainer 210

A.31 South Connector grid grades 211

List of Figures (con't)

Figure

B.1 Artificial earthquake accelerations in E-W direction 213

B.2 Artificial earthquake accelerations in N-S direction 214

B.3 Artificial earthquake accelerations in vertical direction 215

B.4 Artificial earthquake velocities in E-W direction 216

B.5 Artificial earthquake velocities in N-S direction 217

B.6 Artificial earthquake velocities in vertical direction 218

B.7 Artificial earthquake displacements in E-W direction 219

B.8 Artificial earthquake displacements in N-S direction 220

B.9 Artificial earthquake displacements in vertical direction 221

B.10 Artificial earthquake response spectrum accelerations in E-W direction . 222

B.11 Artificial earthquake response spectrum accelerations in N-S direction . . 223

B.12 Artificial earthquake response spectrum accelerations in vertical direction 224

D.1 Areas used for calculation of secondary moment 232

E.1 Moment interaction diagram for the longitudinal moments in piers #3,4,6,7, and 10 of the North Connector 240

E.2 Force diagram used to calculate moment interaction diagram 241

CHAPTER 1

BACKGROUND

Bridges are vital structures in the United States transportation network. A bridge's function is basically threefold. First, the bridge has to durably span waterways, railroads, valleys, and other obstacles. The bridge also must provide smooth passageways for the movement of people and vehicles over these obstacles. Finally, the bridge must also resist the lateral thrust of wind, earth, and water with minimal or no damage. When bridges experience a loss of function during a natural disaster, it can result in snarled traffic, significant cost to both government and people, inefficiency in the movement of emergency vehicles so vital in the aftermath of a natural disaster, and possibly even death.

1.1 Introduction

Beginning with the San Fernando earthquake of 1971, there has been an increase in the awareness of the potentially damaging effects that earthquakes can have on bridges. That magnitude 6.6 earthquake caused approximately $15 million in damage to bridges in the area.[20] The 1989 Loma Prieta magnitude 7.1 earthquake caused widespread damage ($1.8 billion)[17] to bridges in the San Francisco Bay area. Many people still vividly remember the images of the collapsed upper deck of the I880 Cypress Viaduct and the collapsed span of the San Francisco-Oakland Bay Bridge.

On Monday, January 17, 1994, a magnitude 6.8 earthquake occurred in Northridge, California, approximately 20 miles northwest of downtown Los Angeles. Like the previous earthquakes, it again caused substantial damage ($100 million) to bridges. In addition to the substantial horizontal accelerations, high vertical accelerations were recorded in many different locations during the earthquake. A vertical acceleration of 1.18g was recorded at Tarzana, and vertical accelerations of approximately 0.6g were recorded at many different locations.[20] This has caused structural engineers to look into the effects of vertical acceleration on the response of bridges. Generally, vertical accelerations are not considered in the current codes.

1.2 Interaction of Vertical Accelerations with Prestressed Concrete Bridges

The seismic design of buildings and bridges is usually carried out considering one component of horizontal acceleration at a time. The interaction of two horizontal components are considered in a few rare cases, but vertical accelerations have previously been virtually neglected. It is commonly felt that vertical motions are less important than horizontal motions, and that they can be ignored without compromising the safety of the structure. This is because vertical accelerations decrease rapidly with distance from the fault and are generally smaller than horizontal accelerations (often less than two-thirds). In addition, buildings are generally very stiff in the vertical direction. Vertical live loads and gravity loads can change in a building by a large amount without significantly altering the performance of the structure. However, bridges are not the same as buildings. They are not as stiff in the vertical direction. If the vertical component of acceleration has a significant amount of energy in the same frequency range as the natural frequency of the bridge, the effect of vertical acceleration may be significant.

Vertical accelerations can have three important effects on bridges that are worth consideration:

(1) The accelerations may directly affect the vertical inertia forces, which would in turn affect the values of the vertical forces in the piers and girders.

(2) The vertical ground motion may thus change the values of the vertical reactions at the ends of the girders, which would change the horizontal friction force on the elastomeric bearing pads or other supports.

(3) The vertical accelerations may also negatively affect prestressed concrete girders which have been designed using the load balancing technique. In this technique, upward internal forces, consisting of the vertical component of the prestressing force, are applied in the construction phase in order to "balance" or counteract the dead load shear and moments. If significant upward accelerations occur, which counteract the effects of gravity acting on the bridge mass to produce the dead load, then the opposing forces resulting from the upward component of the prestressing forces might actually produce reversed moments which could crack those girders which no longer have sufficient dead load moment to counter the prestressing moment. Figure 1.1 shows the basic concepts of load balancing for various tendon

patterns.

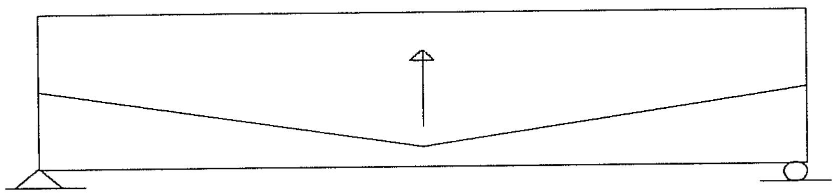

(a) - Linearly draped tendon

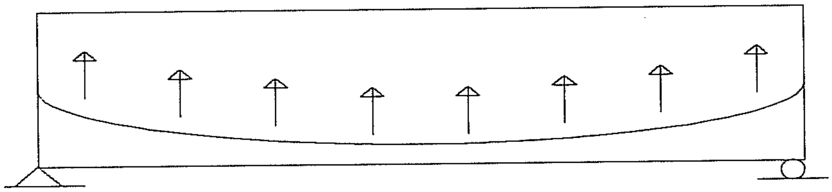

(b) - Parabolic tendon

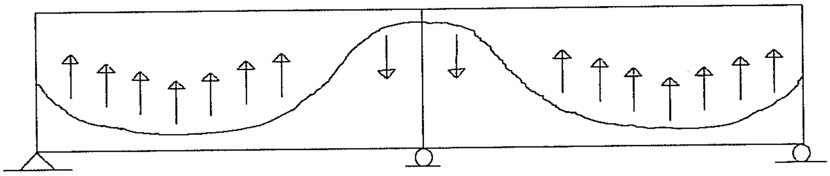

(c) - Continuous spans with parabolic tendons

Figure 1.1 - Load balancing effects

1.3 Objectives

The goal of this study is to systematically evaluate the potentially harmful effects of seismic induced vertical accelerations on prestressed concrete bridges.

More specifically, the objectives are as follows:

- to analytically investigate the effects that vertical ground accelerations can have on the seismic response and performance of bridge structures (or highway overpasses), when combined with the two corresponding horizontal components of acceleration.
- to correlate the effects predicted by computer models to actual damage observed during the Northridge earthquake.
- to examine the range of typical designs of post-tensioned bridges usually used in high seismic regions to determine the levels of "load balancing" used by designers and to investigate the potential effects of vertical accelerations on these bridge structures.
- to assess the adequacy of present bridge design provisions, which generally ignore vertical accelerations, and to determine the need to modify these requirements on the basis of the observed damage and the results of this study.

The effects of the vertical accelerations to be considered are:

- actions and resulting stresses in the piers and girders in the elastic range.
- ductility demands where there is any inelastic action.
- sliding of the girders over the bearing seats with estimates of maximum and permanent motions.
- the possibility of cracking of the deck due to negative moments at midspans

in prestressed girders designed using the "load balancing" techniques and then subjected to vertical accelerations.

- the likelihood and magnitude of positive moments at the supports of continuous spans due to vertical accelerations.

The computer model further described in Chapter 3 and traditional analytical tools will be used to study these effects.

1.4 Previous Research

There has not been much research found on the topic of the effect of vertical accelerations on prestressed concrete bridges. However, the research that has been noted in this area provides a useful basis for this study.

1.4.1 Computer Modelling

One of the first seismic related bridge computer modelling studies was carried out by Imbsen et al. in June of 1978.[9] This study was done following the extensive damage of the 1971 San Fernando earthquake. The Imbsen et al. study compared the parametric results of performing a linear analysis, a response spectrum analysis, and a nonlinear analysis on three curved bridges. They concluded that redistribution of forces and location and magnitude of maximum ductility demands cannot be accurately predicted by an elastic model. Nonlinear techniques need to be used to study local yielding, hinge and foundation behavior, and energy absorption. Another key conclusion they reached is that excitation from accelerations in both horizontal directions should be considered. No specific mention was made of vertical accelerations, but they recommended doing further studies with all three components of excitation included to account for possible coupling effects.

One of the major studies that has examined the effect of vertical accelerations on bridges was reported by Saadeghvaziri and Foutch in 1988 and 1990.[15,16] They used 3-dimensional finite element modelling to investigate the effects of vertical motion in reinforced concrete bridges. They modelled some columns under both horizontal and vertical motion and some under horizontal motion only. There were a couple of important ramifications that resulted from this study. Results showed that vertical acceleration caused fluctuating axial forces and moments in the columns. This caused instability in the hysteresis loops for the columns and increased the ductility demands. The addition of vertical motion also caused a fluctuation in the shear capacity of the column. The effect of vertical axial loads can be seen from ACI Equation (11-4),[5] where

$$V_c = 2\left(1 + \frac{N_u}{2000\,A_g}\right)\sqrt{f_c'}\,b_w\,d \qquad (1.1)$$

as N_u, the axial load, decreases, the amount of shear that can be carried by the concrete, V_c, also decreases. This could lead to a shear failure if the column has inadequate reinforcement in the transverse direction. Figure 1.2, taken from the Saadeghvaziri and Foutch report,[16] gives an example of this phenomenon. Finally, Saadeghvaziri and Foutch also found that including vertical accelerations in the analysis sometimes caused three times the dead load force to be applied to the abutments. This is not accounted for in current design codes. Figure 1.3, also taken from their report,[16] shows the fluctuation in the computed abutment vertical force.

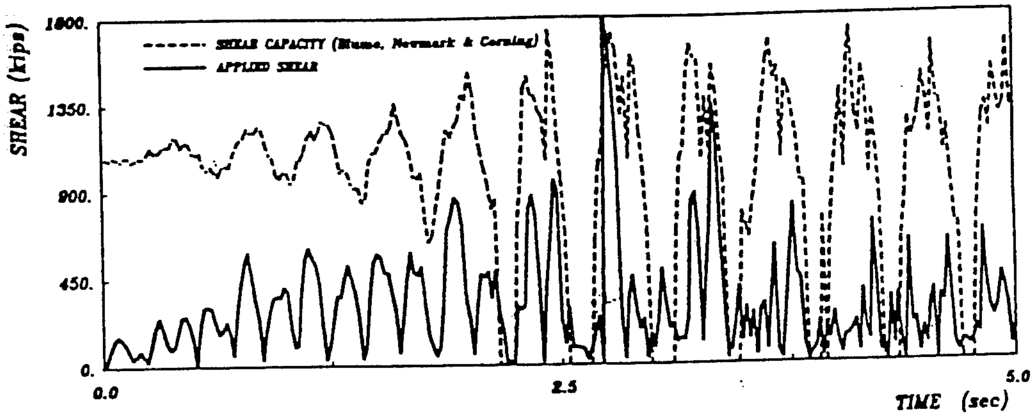

Figure 1.2 - Time history of applied shear vs. shear capacity[16]

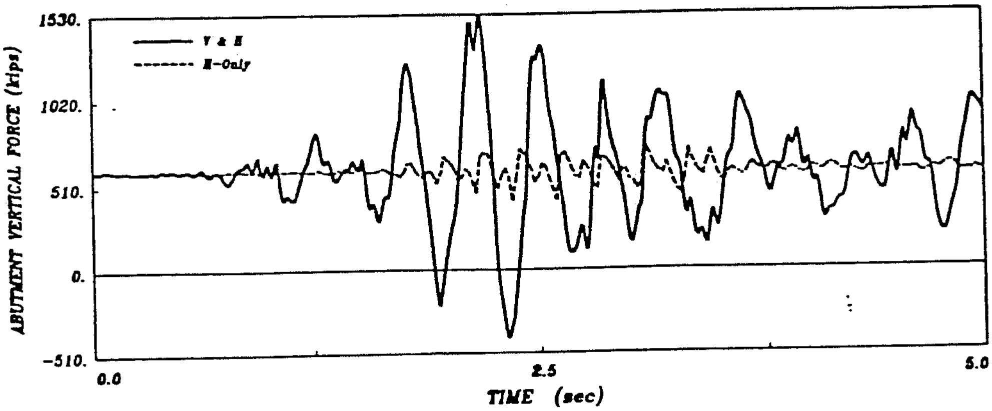

Figure 1.3 - Time histories of abutment vertical force[16]

Another study which included the effects of vertical acceleration was carried out by Fenves and Desroches in 1994.[8] This study compared the strong motion records from the Interstate 10/Interstate 215 Northwest connector in the Landers and Big Bear earthquakes of 1992 to a computer model of the same bridge. While the effects of vertical accelerations were never explicitly studied, the report emphasized the effects of nonlinear hinge behavior. The study showed that in special cases hinge pounding can cause increased forces and ductility demand in the columns. Other than this exception, Fenves and Desroches found that standard linear finite element modeling techniques (with nonlinear hinge models), can adequately model the response of curved bridges. However, the maximum accelerations in the Landers and Big Bear earthquakes (~ 0.1g horizontal and ~ 0.06g vertical) were much lower than those in the Northridge earthquake.

1.4.2 Experimental Studies

Not many experimental studies have been conducted that have evaluated the effect of vertical accelerations on bridges. However, some studies have been performed on the inelastic behavior of bridge columns. Stone and Choek[6,18] tested columns designed in accordance with 1983 California Department of Transportation (CALTRANS) specifications. Using the definition of displacement ductility, μ, shown in Figure 1.4, they found that higher displacement ductilities were achieved for columns with higher axial loads. This implies lower displacement ductilities for columns with reduced axial loads. This could prove to be very important for this present study since vertical accelerations can reduce or increase the axial load on the column by a significant amount.

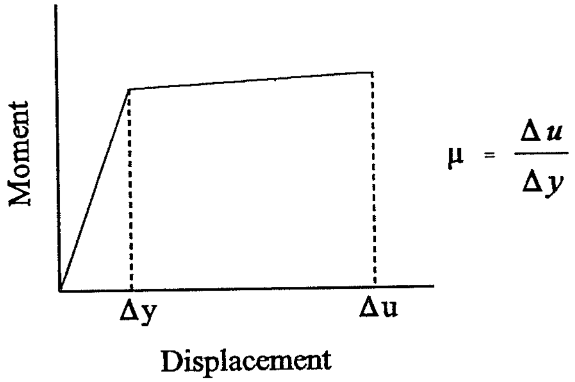

$$\mu = \frac{\Delta u}{\Delta y}$$

Figure 1.4 - Displacement ductility

The models also showed that as the axial load P increased, the ultimate moment M also increased. This is expected, as seen in Figure 1.5, for those cases which start out well below the balance point on the P-M interaction diagram and which do not substantially exceed the balance point after load changes. Displacement ductility values of 6 were achieved for columns with an aspect ratio (length / diameter) of 6 and ductility values of 10 were achieved for columns with an aspect ratio of 3.

The only report found on the dynamic testing of a bridge model was that performed by Williams and Godden.[23] They conducted shake table tests , with horizontal accelerations only, on the Interstate 5/Interstate 14 South Connector Overcrossing. In order to obtain good comparison between analytical results and

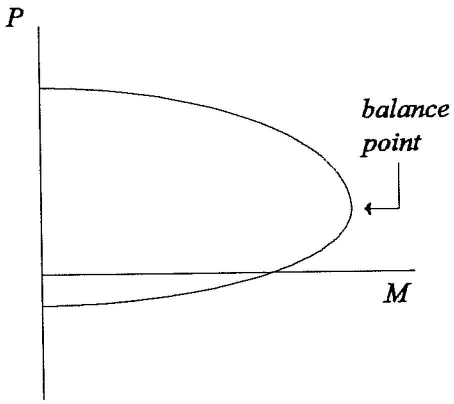

Figure 1.5 - Moment interaction diagram

experimental results, they had to empirically estimate the stiffness of the abutments and the friction at the hinges. Damage in these tests was concentrated at the hinges. This showed that hinges are very important to the performance of the bridge. The damage was reduced by increasing the torsional stiffness at the hinge.

Other studies have also been carried out in order to match strong motion records from instrumented bridges to computer models,[22] but these are not directly pertinent to this particular study.

1.5 Organization of Thesis

Chapter 2 of this thesis includes the description of the damaged bridges considered in this study as well as earthquake records from instruments near the bridges. Chapter 3 contains the description of the computer program and the modelling assumptions made. The results of the analysis of the box girder and prestressing forces are presented in Chapter 4. Chapter 5 gives the analysis of the columns and their ductility, while Chapter 6 discusses the effects of vertical accelerations on the hinges. Chapter 7 concludes the thesis with a summation of the results and recommendations for design codes and future research.

CHAPTER 2

BRIDGE DESCRIPTIONS AND EARTHQUAKE RECORDS

2.1 Northridge Earthquake Overview

The Northridge earthquake of January 17, 1994, was not as large in Richter magnitude as the 1989 Loma Prieta earthquake, but it occurred in a more heavily populated area. As a result, the significant damage was much more widespread. The earthquake caused extensive damage to parking garages, houses, steel moment-resisting frames, and reinforced concrete buildings. As in previous earthquakes, some of the most dramatic damage occurred in highway bridges. Six major highway bridges collapsed and 157 other bridges suffered some damage.[20] The bridges that collapsed were Interstate 5 at the Gavin Canyon Undercrossing, 2 bridges at the State Route 14 Interchange with Interstate 5, State Route 118 at San Fernando Mission Boulevard and Gothic Avenue, Interstate 10 at the La Cienega Boulevard - Venice Boulevard Separation, and the Fairfax Avenue - Washington Boulevard Undercrossing.[13,20]

Many strong motion instruments were triggered by the event. These instruments are operated by several different agencies, including the California Division of Mines and Geology (CDMG) Strong Motion Instrumentation Program (CSMIP), the United States Geological Survey (USGS), and the California Institute of Technology.[12] Accelerations in both the horizontal and vertical directions were recorded, including some horizontal and vertical accelerations of over 1g near the epicenter. In some locations, the single-degree-of-freedom response resulting from various recorded horizontal ground accelerations exceeded the design response spectrum in the *Uniform Building Code*,[21] sometimes by a factor as high as 2.5.[20] The 1994 *Uniform Building Code*,[21] recommends that the horizontal acceleration spectrum scaled by a value of two-thirds be used for the vertical acceleration response spectrum.

There were three main criteria considered when selecting the bridge(s) to be examined in this present study. The first was that they had to have some spans consisting of prestressed box girder sections. The second criterion was that the bridge had to have experienced some damage during the Northridge earthquake. The third consideration was that there had to be strong motion records taken on or fairly near (within three miles) the bridge. Based on these criteria, the Interstate 5/State Route 14 bridge was chosen. The bridge is located north of Northridge. During the earthquake, spans on two sections of the interchange, the north connector (Ramp M) and the separation and overhead (Ramp C), collapsed. There was also evidence of pounding between spans at several hinge locations.[13] An overview of the bridge can be seen in Figure 2.1.

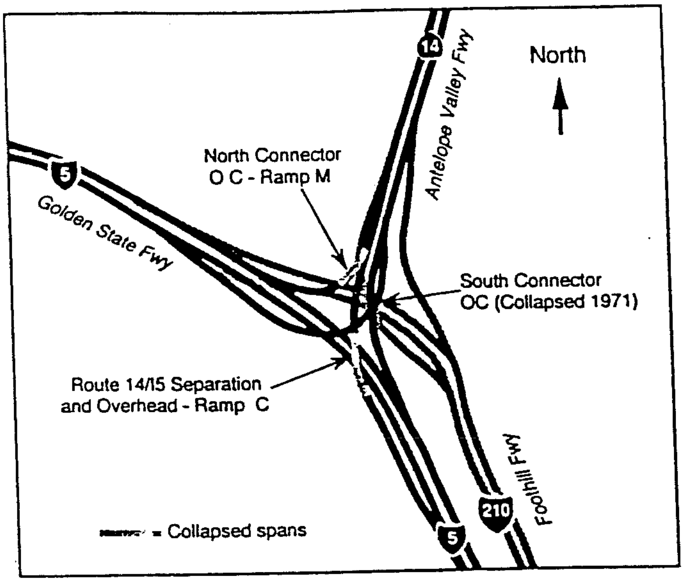
14
Antelope Valley Fwy
North
5
Golden State Fwy
North Connector
O C - Ramp M
South Connector
OC (Collapsed 1971)
Route 14/I5 Separation
and Overhead - Ramp C
= Collapsed spans
Foothill Fwy
5
210

Figure 2.1 - SR14/I5 overview[20]

2.2 Damage During 1971 San Fernando Earthquake

The bridge was designed in 1968 and was under construction when the 1971 San Fernando earthquake struck.

2.2.1 North Connector (Ramp M)

Most of this bridge had been constructed when the San Fernando earthquake struck. Figure 2.2 shows the state of construction at the time of the earthquake in 1971. The portion from pier 8 to abutment 11 was yet to be constructed. Only minor damage was reported in this bridge, the most serious of which was permanent offsets at the hinges near piers 4 and 6.[20]

2.2.2 Separation and Overhead (Ramp C)

At the time of the San Fernando earthquake, this bridge had Piers 2 and 3

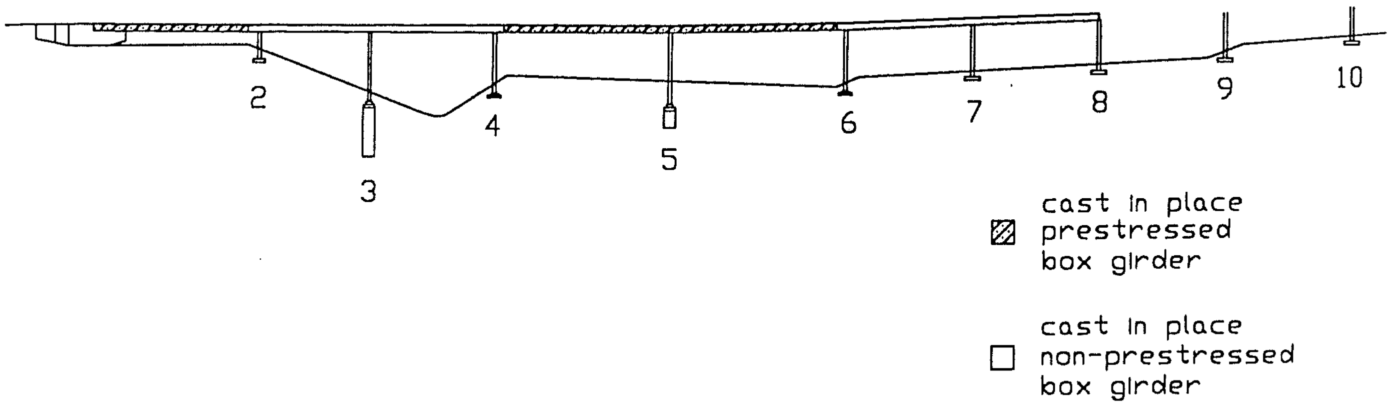

2
3
4
5
6
7
8
9
10
▨ cast in place prestressed box girder
☐ cast in place non-prestressed box girder

Figure 2.2 - North Connector after 1971 San Fernando earthquake

complete (shown in Figure 2.3). The bottom soffit and webs of the cast-in-place box girder were also complete and resting on falsework. Settlement of this falsework caused damage in the pier caps, and cracks in the soffit slabs and webs. It is not exactly known when or how this damage was repaired.[20]

2.2.3 South Connector (Ramp L)

This ramp was complete at the time of the San Fernando earthquake and it collapsed between piers 5 and 7. This damage is shown in Figure 2.4. The ramp was rebuilt with improved pier reinforcement.[20]

2.2.4 Retrofit Procedures

After the San Fernando earthquake in 1971, the bridges were retrofitted with cable restrainer units. The initial hinge restrainers that existed in these bridges were not adequate.[14]

2.3 Damage During 1994 Northridge Earthquake

2.3.1 North Connector (Ramp M)

During the Northridge earthquake, spans 1 and 2 of this bridge collapsed. The failure is believed to have been started by the failure of pier 2. Due to this failure, the simply supported span 1 fell off of the abutment seat and the cantilevering action caused a negative moment failure at pier 3. Pier 2 is the shortest in the bridge, so it is probable that it attracted a large percentage of the lateral force and failed in shear.[13] This suggested sequence of failure can be seen in Figure 2.5.

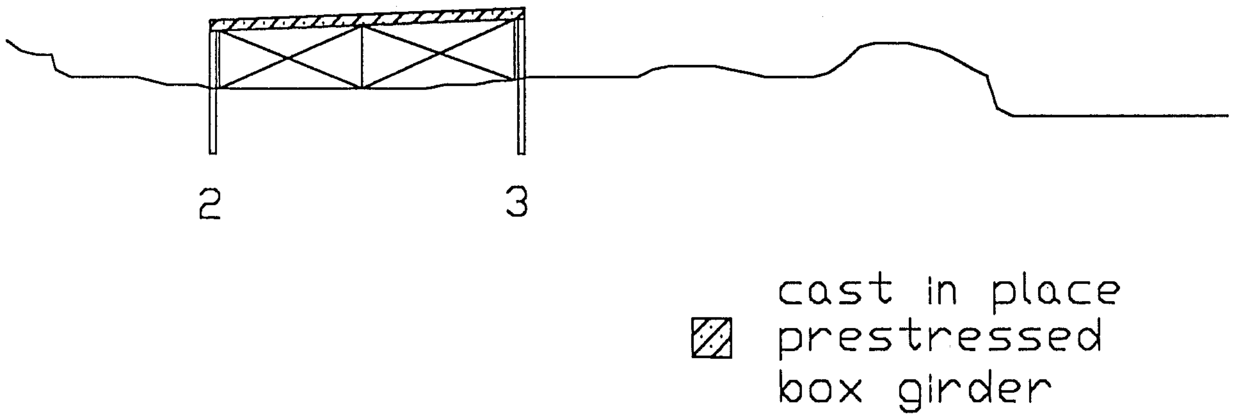
2
3
▨ cast in place prestressed box girder

Figure 2.3 - Separation and Overhead after 1971 San Fernando earthquake

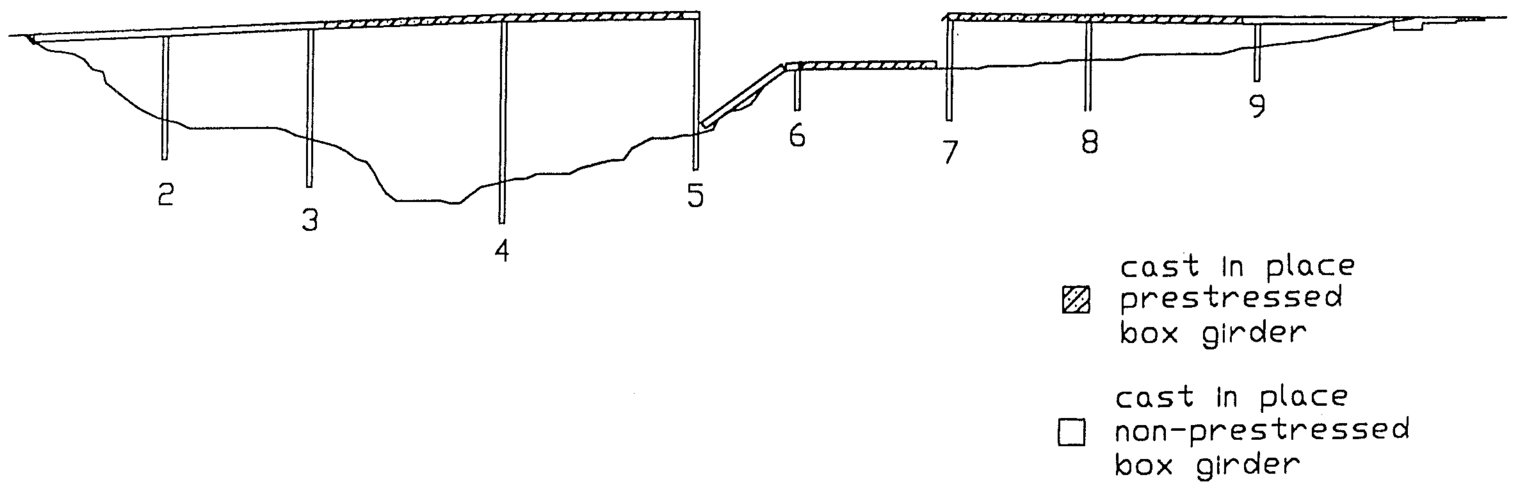
2
3
4
5
6
7
8
9
▨ cast in place prestressed box girder
☐ cast in place non-prestressed box girder

Figure 2.4 - South Connector after 1971 San Fernando earthquake

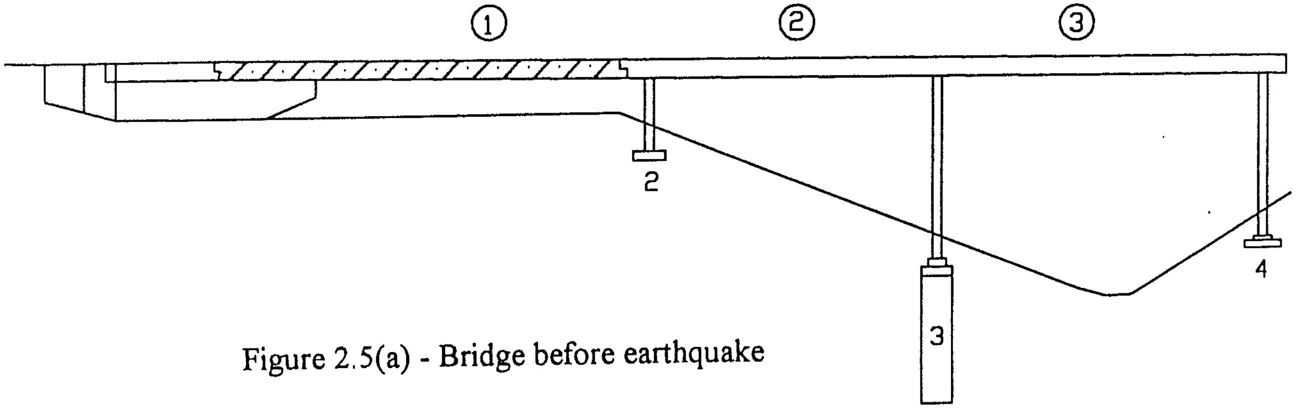

Figure 2.5(a) - Bridge before earthquake

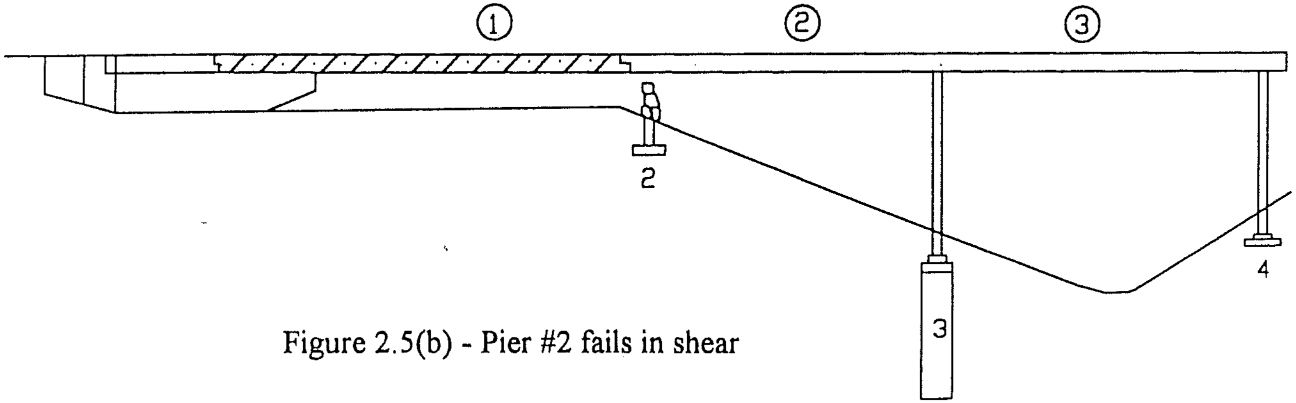

Figure 2.5(b) - Pier #2 fails in shear

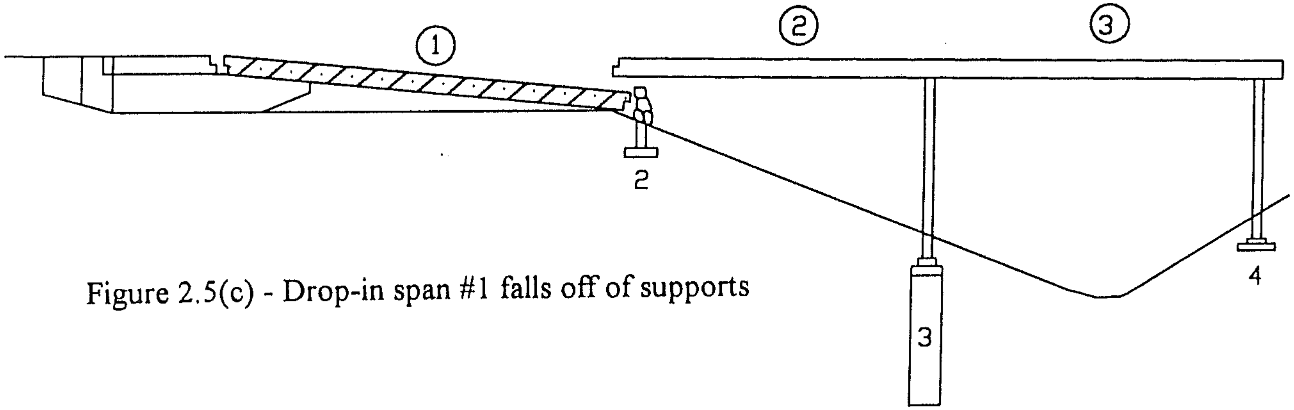

Figure 2.5(c) - Drop-in span #1 falls off of supports

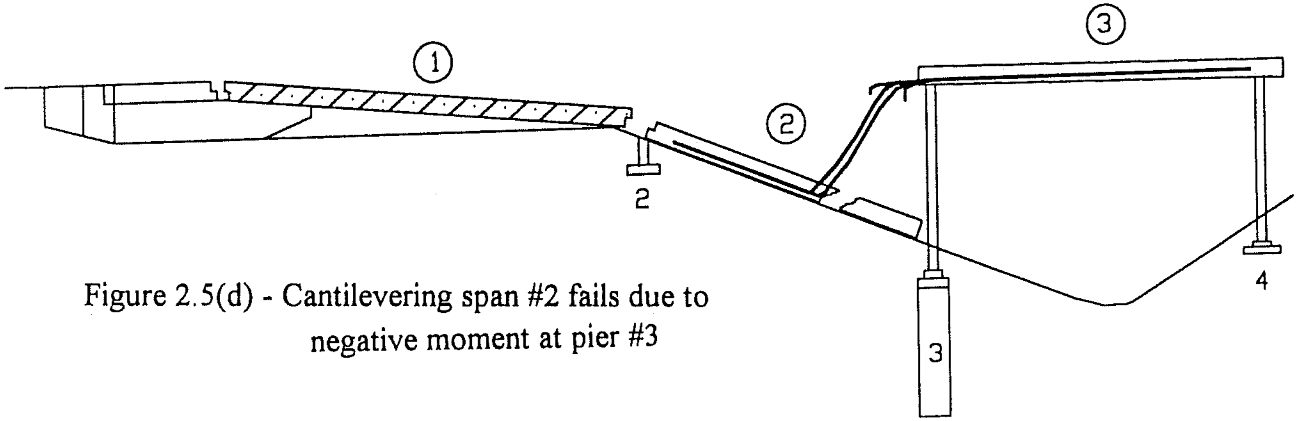

Figure 2.5(d) - Cantilevering span #2 fails due to negative moment at pier #3

Figure 2.5 - Proposed failure of North Connector during 1994 Northridge earthquake

2.3.2 Separation and Overhead (Ramp C)

It is assumed that this bridge most likely collapsed because pier 2 failed in shear, and therefore lost its axial load capacity. The bridge could not span from the abutment to pier 3, and a positive moment hinge then formed at the collapsed pier 2. Pier 3 could not carry the span between piers 2 and 3 by cantilever action and therefore another hinge formed at pier 3. The prestressing tendons fractured at pier 3 and the negative moment capacity was lost. This caused the collapse of the span between the pier 3 and the hinge.[13] This failure sequence can be seen in the schematic drawings of Figure 2.6.

2.3.3 South Connector (Ramp L)

No significant damage was done to this bridge in the Northridge earthquake. Analyses will still be run for this bridge however, to see if the results differ in any way from the first two bridges.

2.4 Bridge Descriptions

The descriptions of these bridges were taken off of the "as-built" plans (Shown in Appendix A) obtained from CALTRANS, except where reconnaissance reports gave more accurate descriptions.

2.4.1 North Overcrossing (Ramp M)

The north connector overcrossing is a 10 span bridge with a total length of 1532' as seen in Figures 2.7 and 2.8. All 9 piers are single column bents, which range in height according to Table 2.1.

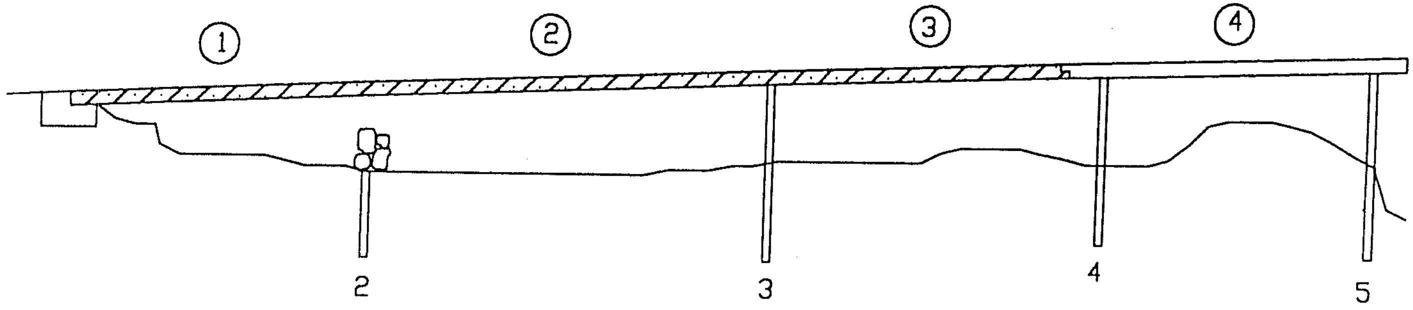

Figure 2.6(a) - Pier #2 fails in shear

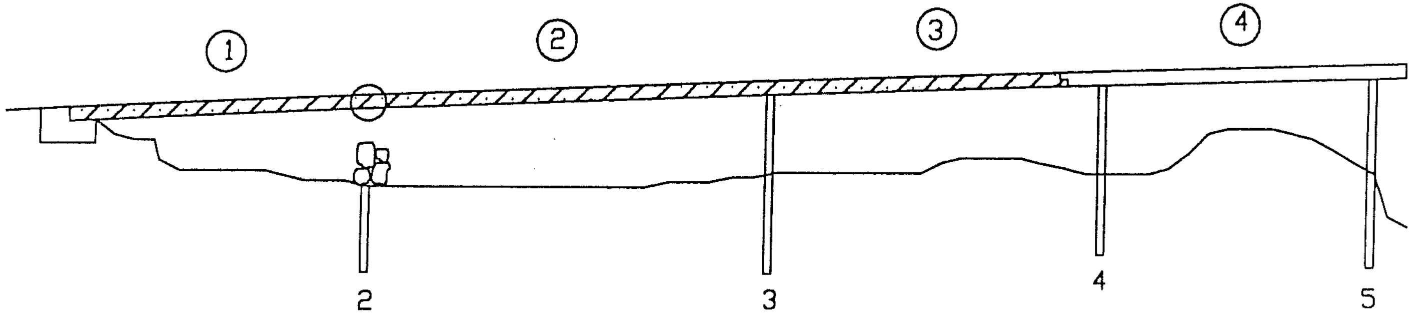

Figure 2.6(b) - Hinge forms in positive moment region at pier #2

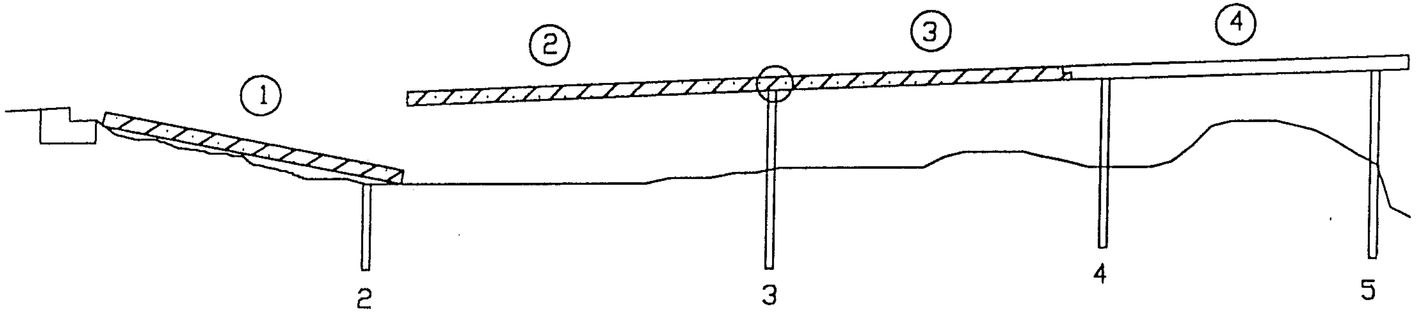

Figure 2.6(c) - Span #1 collapses and falls off of abutment seat

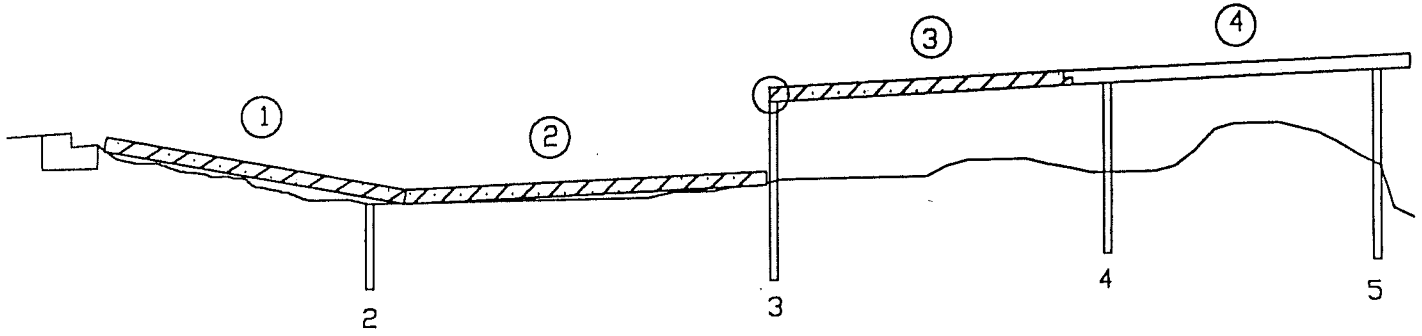

Figure 2.6(d) - Span #2 collapses due to negative moment failure and tendon rupture

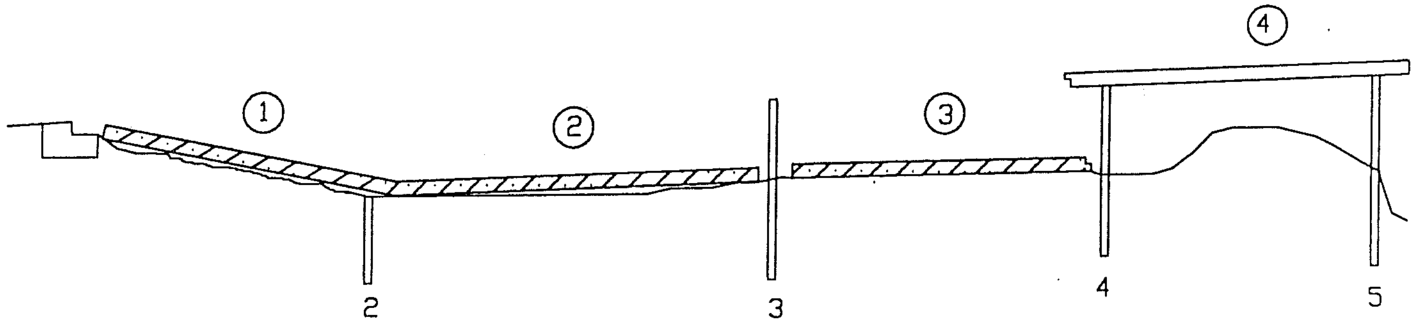

Figure 2.6(e) - Span #3 collapses due to negative moment failure at pier #3

Figure 2.6 - Proposed failure of Separation and Overhead during 1994 Northridge earthquake

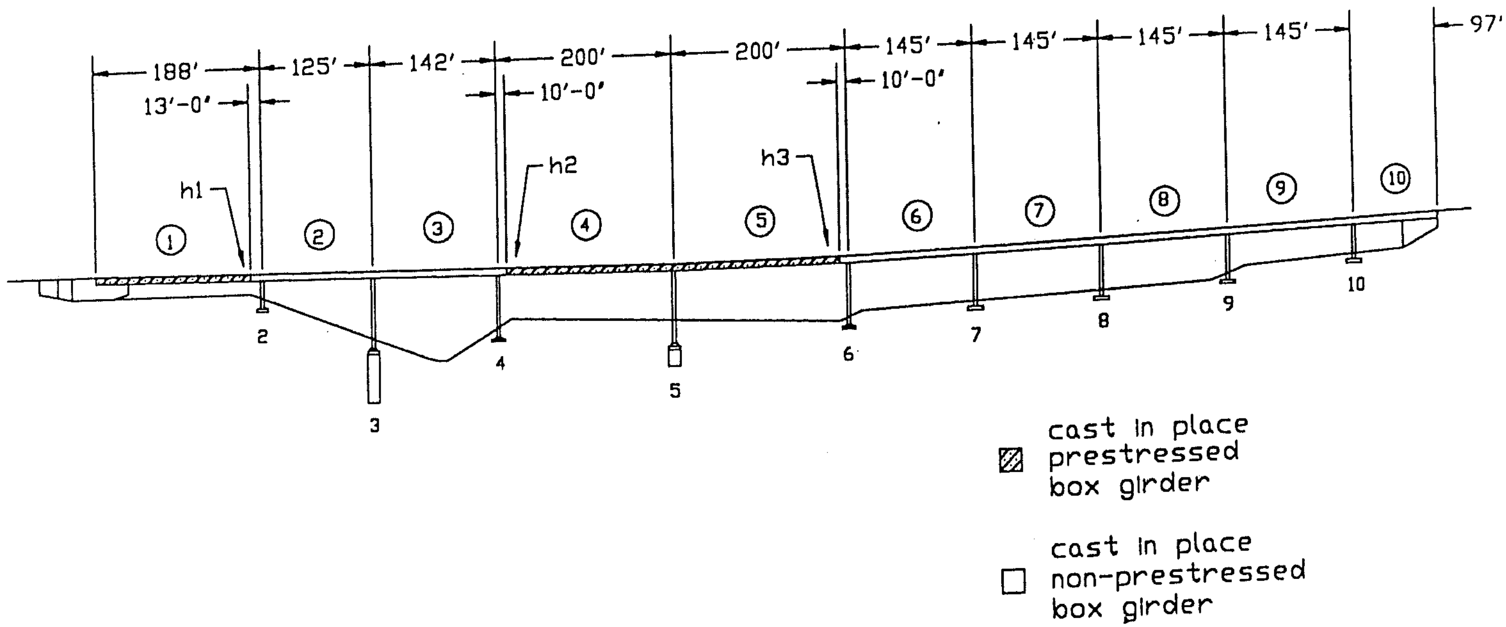
188'
13'-0"
125'
142'
200'
10'-0"
200'
145'
10'-0"
145'
145'
145'
97'
h1
h2
h3
①
②
③
④
⑤
⑥
⑦
⑧
⑨
⑩
2
3
4
5
6
7
8
9
10
▨ cast in place prestressed box girder
☐ cast in place non-prestressed box girder

Figure 2.7 - North Connector elevation view

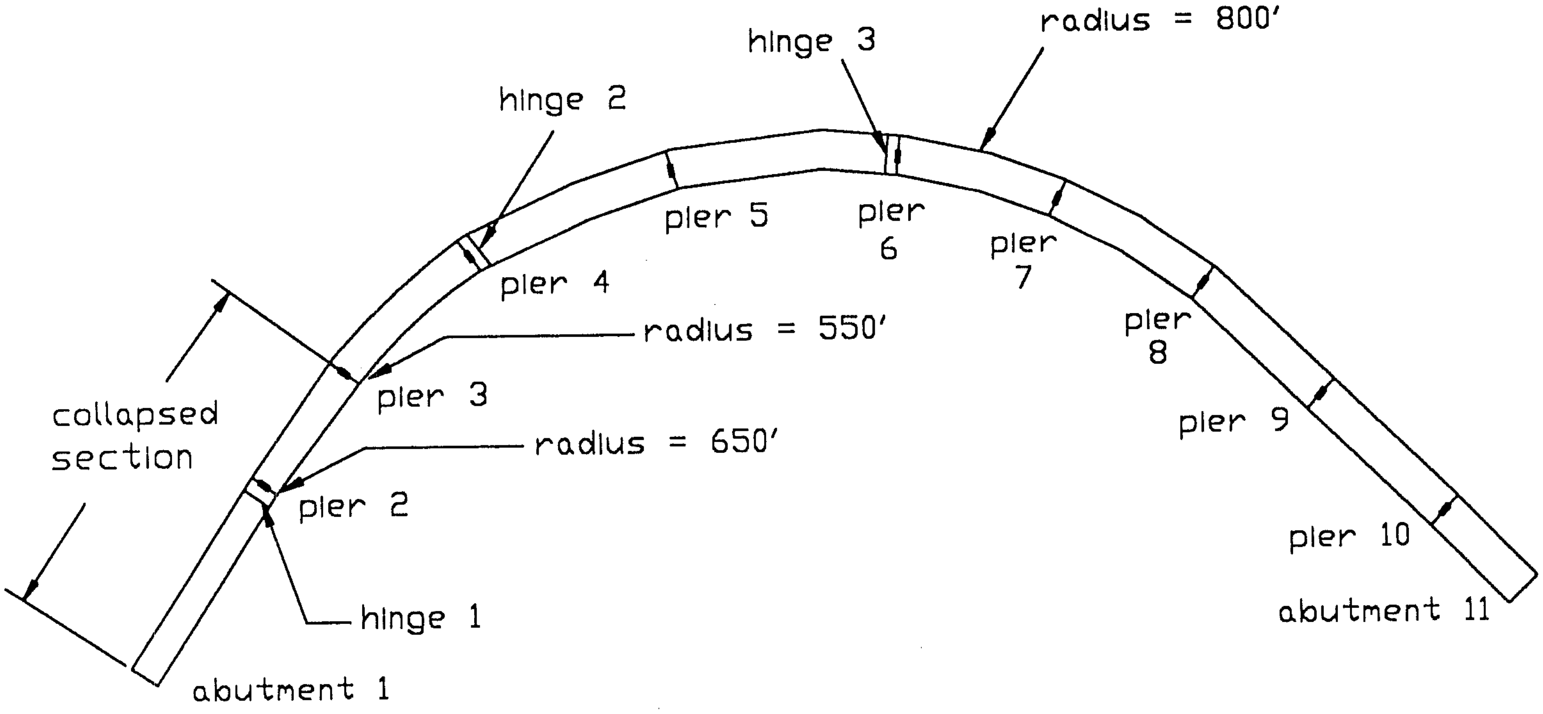
radius = 800'
hinge 3
hinge 2
pier 5
pier 6
pier 7
pier 4
radius = 550'
pier 8
collapsed section
pier 3
radius = 650'
pier 9
pier 2
pier 10
hinge 1
abutment 11
abutment 1

Figure 2.8 - North Connector plan view

Table 2.1 - Pier Heights (above ground) for North Overcrossing

pier number	2	3	4	5	6	7	8	9	10
height (ft)	16.5	67	58	55	57	46	46	39	28

Between piers 2 and 3 the radius of curvature varies from 800' to 650'. Between piers 3 and 8, the radius of curvature is 550'. The other spans of the bridge are straight. The width of the bridge is 26' in span 1, varies from 26' at the start of span 2 to 34' at the end of span 2, and is 34' from the start of span 3 to the end of the bridge. Spans 1, 4, and 5 are post-tensioned concrete, while the others spans are conventionally reinforced with Grade 60 steel, except for transverse deck reinforcement and stirrups, which are Grade 40 steel. Expansion joints are provided at the abutments and near piers 2, 4, 6, and 8.

The superstructure consists of a varying box girder cross section. From abutment 1 to pier 3, the cross section is a two-cell box girder. At pier 3, the cross section becomes a three-cell box girder and continues as such for the rest of the bridge. The box girder is 7'-9" deep with a deck slab thickness that varies from 6.25" to 8.5" and a soffit thickness that varies from 5.5" to 8.5". The specific dimensions can be seen in Table 2.2 and the basic cross sections can be seen in Figures 2.9 and 2.10.

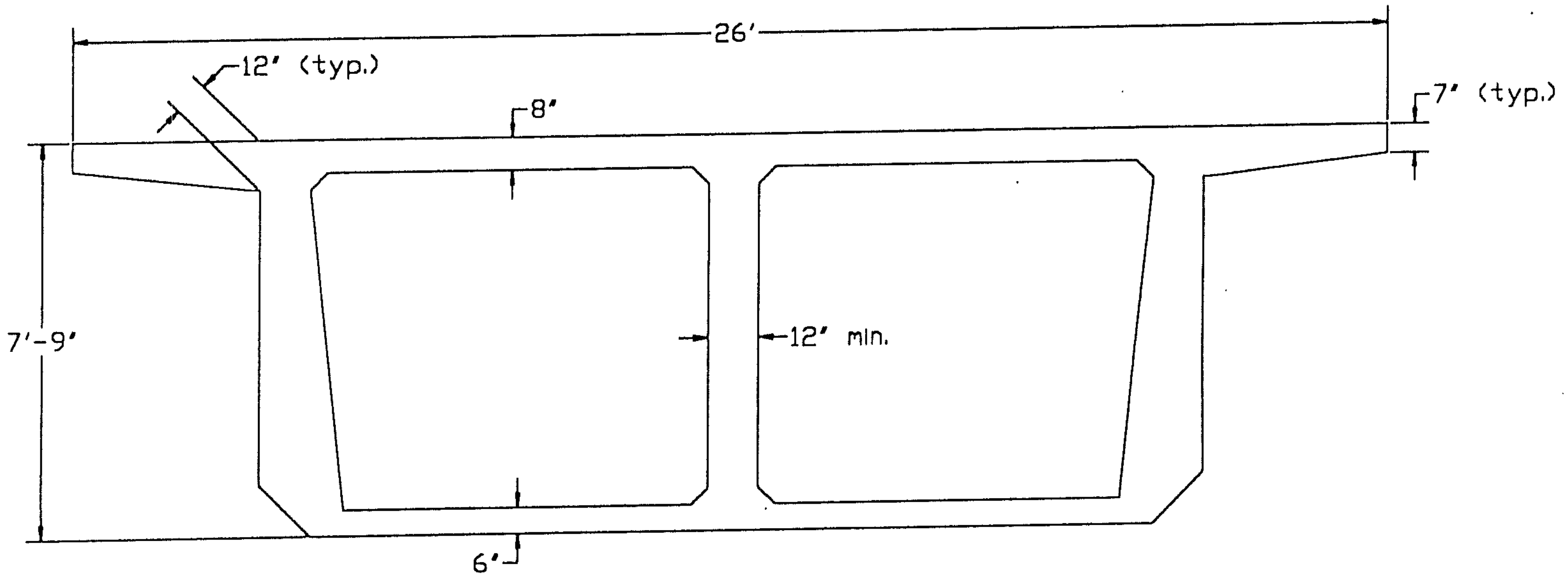
26'
12' (typ.)
8'
7' (typ.)
7'-9'
12' min.
6'

Figure 2.9 - North Connector 2-box girder detail

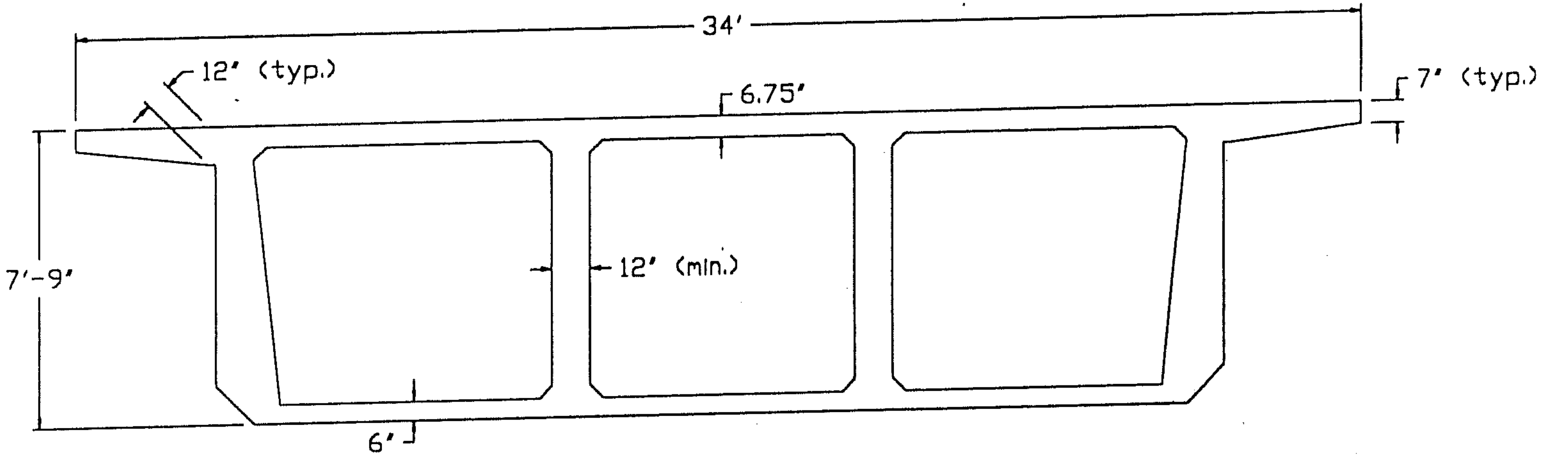
34'
12' (typ.)
6.75'
7' (typ.)
7'-9'
12' (min.)
6'

Figure 2.10 - North Connector 3-box girder detail

Table 2.2 - Dimensions of Box Girder Cross Section for North Connector

location	girder width	deck slab thickness	soffit thickness	web thickness
abutment 1 → hinge 1	26'	8"	6"	12" min.
hinge 1 → pier 2	26'	6.25"	5.5"	23"
pier 2 → pier 3	varies	8.5"	8.5"	8" min.
pier 3 → hinge 2	varies	7"	6"	8" min.
hinge 2 → hinge 3	34'	6.75"	6"	12" min.
hinge 3 → abutment 11	34'	7"	6"	8" min.

The prestressed box girder in span 1 contains 26 tendons, each consisting of 12 - 0.5" diameter strands. The prestressed box girder in spans 4 and 5 contains an additional 4 tendons, each consisting of 11 - 0.5" diameter strands. Spans 2, 3, 4, 6, and 9 (of which only span 4 is prestressed concrete) were strengthened for live load early in 1993 by adding 7 and 12 - 0.5" diameter strands in the bottom soffit.

All of the piers have a 8' by 4' rectangular cross section with a 14" chamfer in each corner. As seen in Table 2.3, the vertical reinforcement varies between 34 and 52 #18 bars placed in one elliptical ring.

Table 2.3 - Number of #18 Longitudinal Bars per Pier

Piers	Number of bars
2,7,8	42
3,4,6,9,10	34
5	52

Figure 2.11 shows the pier geometry and reinforcing details. Transverse reinforcement consists of #4 bars placed 12" on center, except for pier 10, which was constructed after 1971. Pier 10 has #4 double spiral ties on a 3.5" spacing. In the longitudinal direction of piers 1-9, three #4 cross-ties are provided as shown in Figure 2.11.

Footings for this bridge are approximately 3 to 4 feet deep in the soil. They are spread footings, except for piers 3 and 5, which are further supported by piles. According to Priestly,[13] the footings have lengths in the longitudinal direction of the bridge of 13.5' and lengths in the transverse direction of the bridge of 24' or 27.5'. This varies slightly from what is shown in the plans. The footings have a bottom layer of reinforcement of either #11, #14, or #18 bars.

Finally, the expansion joints are detailed with 3 restrainer units at each hinge. Each restrainer unit consists of seven 0.75" bars in an 8" extra strong galvanized steel pipe bearing against a 12" by 12" by 2.5" anchor plate (Figure 6.1). Cable restrainers were later added in 1972 after the San Fernando earthquake (Figure 6.2)[2].

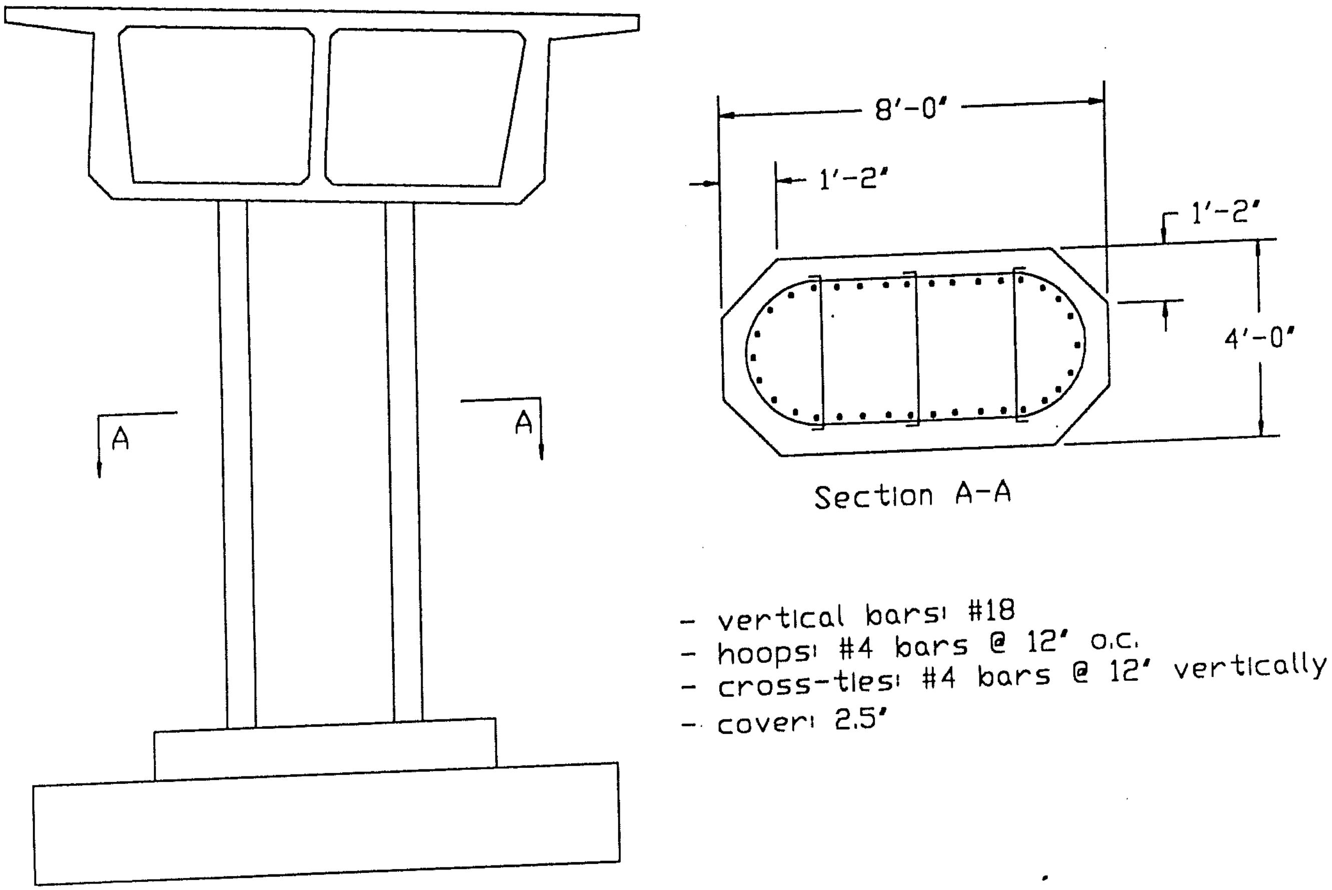
A
A
8'-0"
1'-2"
1'-2"
4'-0"
Section A-A

- vertical bars: #18
- hoops: #4 bars @ 12" o.c.
- cross-ties: #4 bars @ 12" vertically
- cover: 2.5"

Figure 2.11 - North Connector pier detail

Seat widths are generally 14" to 16".

2.4.2 Separation and Overhead (Ramp C)

The separation and overhead ramp is a 10 span bridge with a total length of 1582'. All 9 piers are single column bents. Information on the column heights is found in Tables 2.4 and 2.5. The bridge crosses a relatively deep valley, which results in the tall columns being in the middle of the bridge.

Table 2.4 - Pier Heights (above ground) for Separation and Overhead[2]

pier number	2	3	4	5	6	7	8	9	10
height (ft)	23.5	29.5	48.5	47	83.75	103.25	89	95	45.5

Table 2.5 - Pile Depth (below grade) for Separation and Overhead[2]

pier number	2	3	4	5	6	7	8	9	10
height (ft)	48	55	35	46	48	60	35	35	52

The bridge has a constant radius of curvature of 2200', thus only mild curvature. The width of the deck is 53' for the entire bridge, about 1.5 times the width of the other two bridges in this study. Spans 1, 2, 3, 5, 6, 9, and 10 are post-tensioned concrete, while the others spans are conventionally reinforced with Grade 40 steel. Expansion joints are provided at the abutments and near columns 4, 5, 7, and 9. Overviews of the separation and overhead structure are given in Figures 2.12 and 2.13.

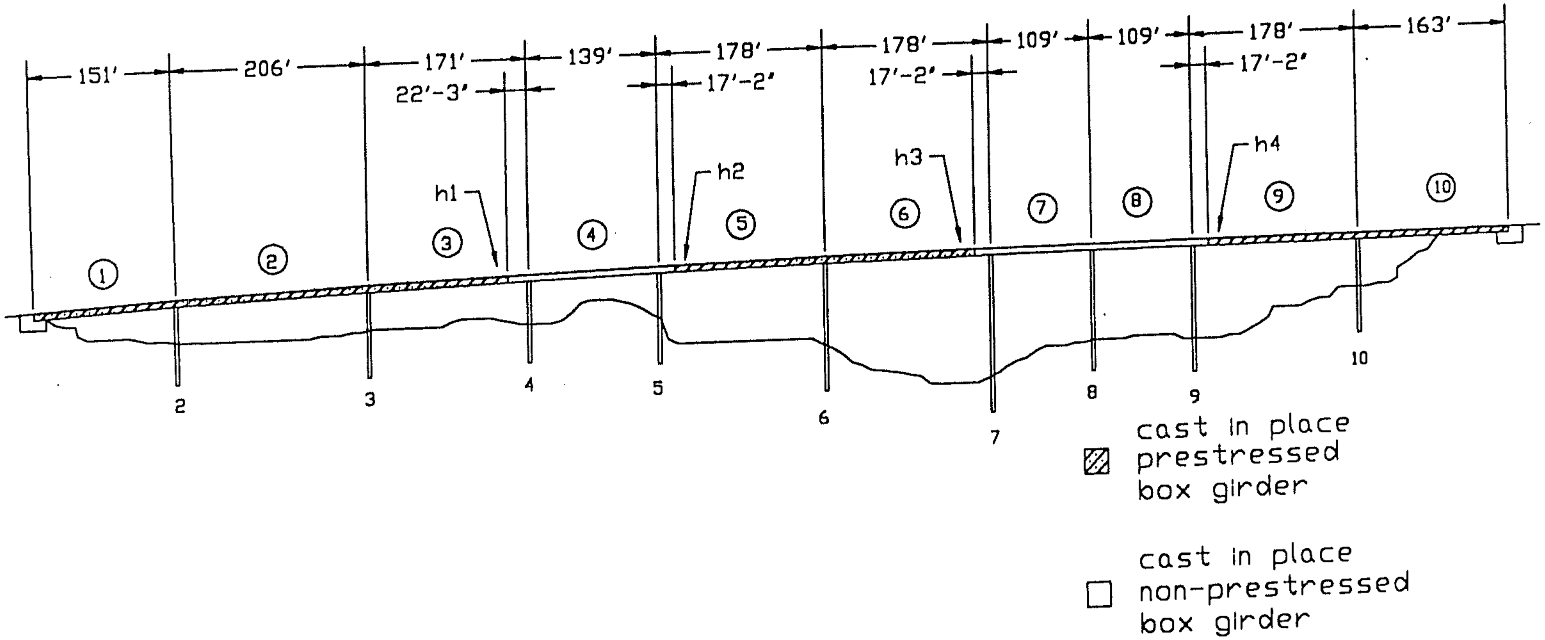
151'
206'
171'
139'
178'
178'
109'
109'
178'
163'
22'-3'
17'-2'
17'-2'
17'-2'
h1
h2
h3
h4
①
②
③
④
⑤
⑥
⑦
⑧
⑨
⑩
2
3
4
5
6
7
8
9
10
▨ cast in place prestressed box girder
☐ cast in place non-prestressed box girder

Figure 2.12 - Separation and Overhead elevation view

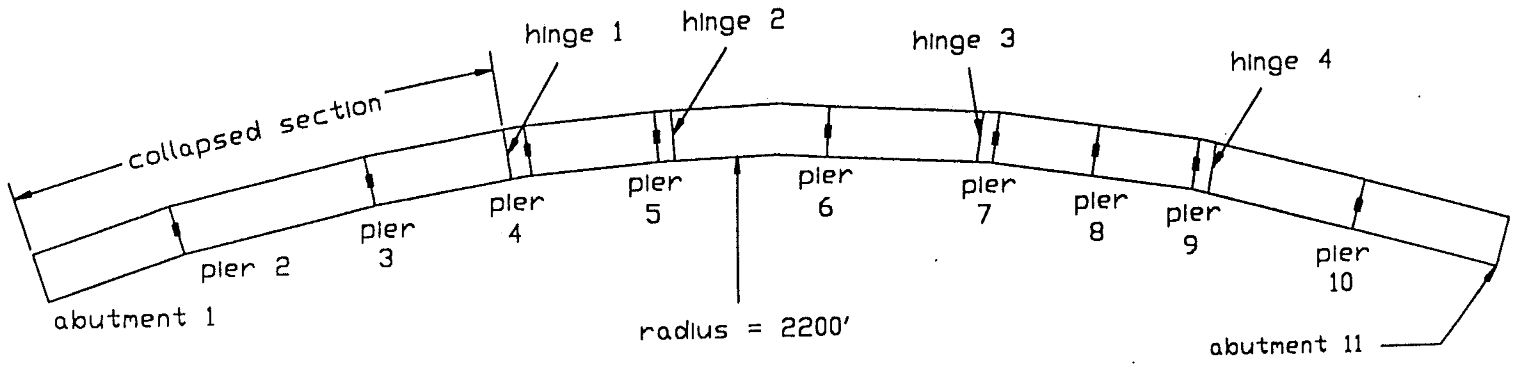

collapsed section
hinge 1
hinge 2
hinge 3
hinge 4
pier 2
pier 3
pier 4
pier 5
pier 6
pier 7
pier 8
pier 9
pier 10
abutment 1
radius = 2200'
abutment 11

Figure 2.13 - Separation and Overhead plan view

The superstructure consists of a box girder cross section. The prestressed concrete box girder has a height of 7'. The deck slab is 7" thick and the soffit is 6" thick. The conventionally reinforced box girder also has a height of 7', but the deck slab thickness and soffit thickness are 7.25" and 6.25" respectively. The prestressed box girder in all the spans contain 36 tendons, each containing of 10 - 0.5" diameter strands. Upon observation after the Northridge earthquake, it was found that the steel ducts were ungrouted. Reasons for this are unknown.[13] A basic cross section can be seen in Figure 2.14.

All of the single column bents are 12' long in the transverse direction and are either 4', 5', or 6' wide in the longitudinal direction. The piers flare in the transverse direction to a width of 26' at the top of the pier. The 12' by 4' piers have a 14" chamfer in each corner, the 12' by 5' piers have a 17.5" chamfer, and the 12' by 6' piers have a 21" chamfer. The vertical reinforcement varies between 28 and 40 Grade 60 #18 bars placed in one elliptical ring. Some piers also include some additional #5 bars in the flare which provide additional moment capacity and help tie the pier to the superstructure. Table 2.6 gives the column dimensions and other important data for the individual columns.

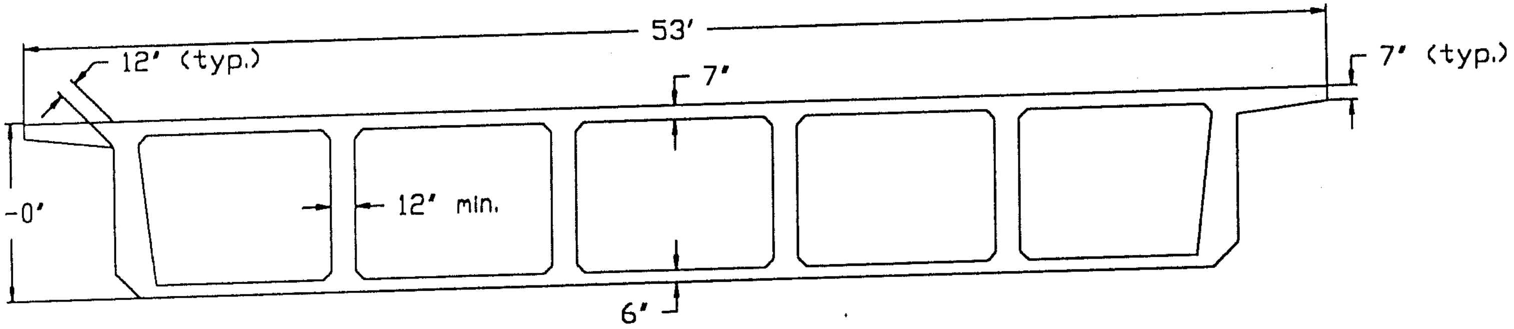
53'
12' (typ.)
7'
7' (typ.)
7'-0'
12' min.
6'

Figure 2.14 - Separation and Overhead box girder detail

Table 2.6 - Pier Data for the Separation and Overhead

Pier	width (ft)	number of #18 bars	number of #5 bars
2	4	40	----
3	4	40	----
4	4	32	16
5	4	32	16
6	5	40	----
7	6	32	24
8	6	32	20
9	6	32	20
10	4	32	20

In addition, pier #6 has a 30" by 78" void in the center and piers #6-#8 each have a 42" by 78" void down the center. Figure 2.15 shows the geometric and reinforcing details for a typical column. Transverse reinforcement consists of #4 bars placed 12" on center. In the longitudinal direction of all the piers, near the base and middle of the pier, three additional #4 cross-ties are provided. Five additional #4 cross-ties are located in the flare. According to observations made in the field, the piers are supported on 12' diameter circular pile shafts.[13]

Finally, the expansion joints for this bridge have cable restrainers and "equalizing" bolts. The equalizing bolt detail can be seen in Figure 6.3. There are five 4-bar restrainers per expansion joint, which were added after the San Fernando

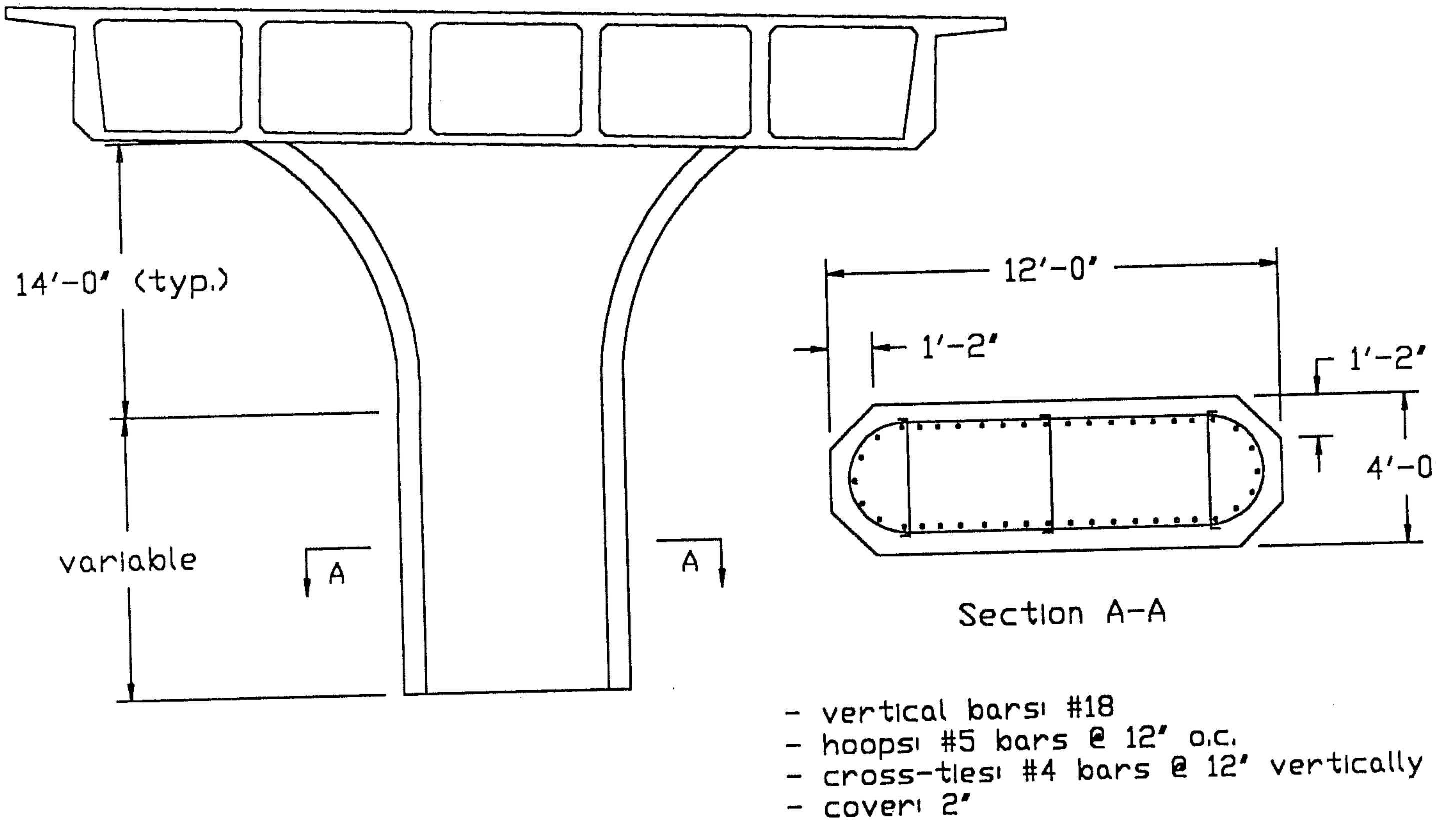
14'-0" (typ.)
variable
A
A
12'-0"
1'-2"
1'-2"
4'-0"
Section A-A
- vertical bars: #18
- hoops: #5 bars @ 12" o.c.
- cross-ties: #4 bars @ 12" vertically
- cover: 2"

Figure 2.15 - Separation and Overhead pier detail

earthquake. Each restrainer consists of 1.0" diameter high strength bolts swaged to 0.75" diameter cable. The restrainer assemblies are 48" long. The cable are tightened to 45 foot-pounds of torque and then released 1.25". This allows for some movement before force is developed in the cables. There are also three "equalizing" bolts per hinge, each 1.0" in diameter. As in the north connector, the seat widths are generally 14" to 16". Each web was also supported on a 10" by 40" by 2" thick elastomeric bearing pad.

2.4.3 South Overcrossing (Ramp L)

The south connector overcrossing is a 9 span bridge with a total length of 1349'. All 8 piers are single column bents and have a large range of heights as listed in Table 2.7.

Table 2.7 - Pier Heights (above ground) for South Connector

pier number	2	3	4	5	6	7	8	9
height (ft)	78	110	142	103	41	41	27	14

Table 2.8 - Pile Depth (below grade) for South Connector

pier number	2	3	4	5	6	7	8	9
height (ft)	34	36	45	36	41	40	53	36

The bridge has a constant radius of curvature of 550'. The width of the bridge is a uniform 34'. Spans 3, 4, 6, 7, and 8 are post-tensioned concrete, while the others spans are conventionally reinforced with Grade 60 steel, except for transverse deck reinforcement and stirrups, which are Grade 40 steel. Expansion joints were provided at the abutments and near piers 3, 5, 6, and 9. Overviews of the south connector can be seen in Figures 2.16 and 2.17.

The superstructure consists of a box girder cross section. The prestressed concrete box girder has a height of 7'. The deck slab is 7" thick and the soffit is 6" thick. The conventionally reinforced box girder also has a height of 7', but the deck slab thickness and soffit thickness are 7.25" and 6.25" respectively. The prestressed box girder in all the spans contain 14 tendons, each containing of 28 - 0.5" diameter strands. A basic cross section can be seen in Figure 2.18.

All of the single column bents are 10' long in the transverse direction. The piers are again either 4', 5', or 6' wide in the longitudinal direction. The 10' by 4' piers have a 14" chamfer in each corner, the 10' by 5' piers have a 17.5" chamfer, and the 10' by 6' piers have a 21" chamfer. The vertical reinforcement varies and consists of between 40 and 52 Grade 60 #18 bars placed in one elliptical ring. Table 2.9 gives the vital pier information.

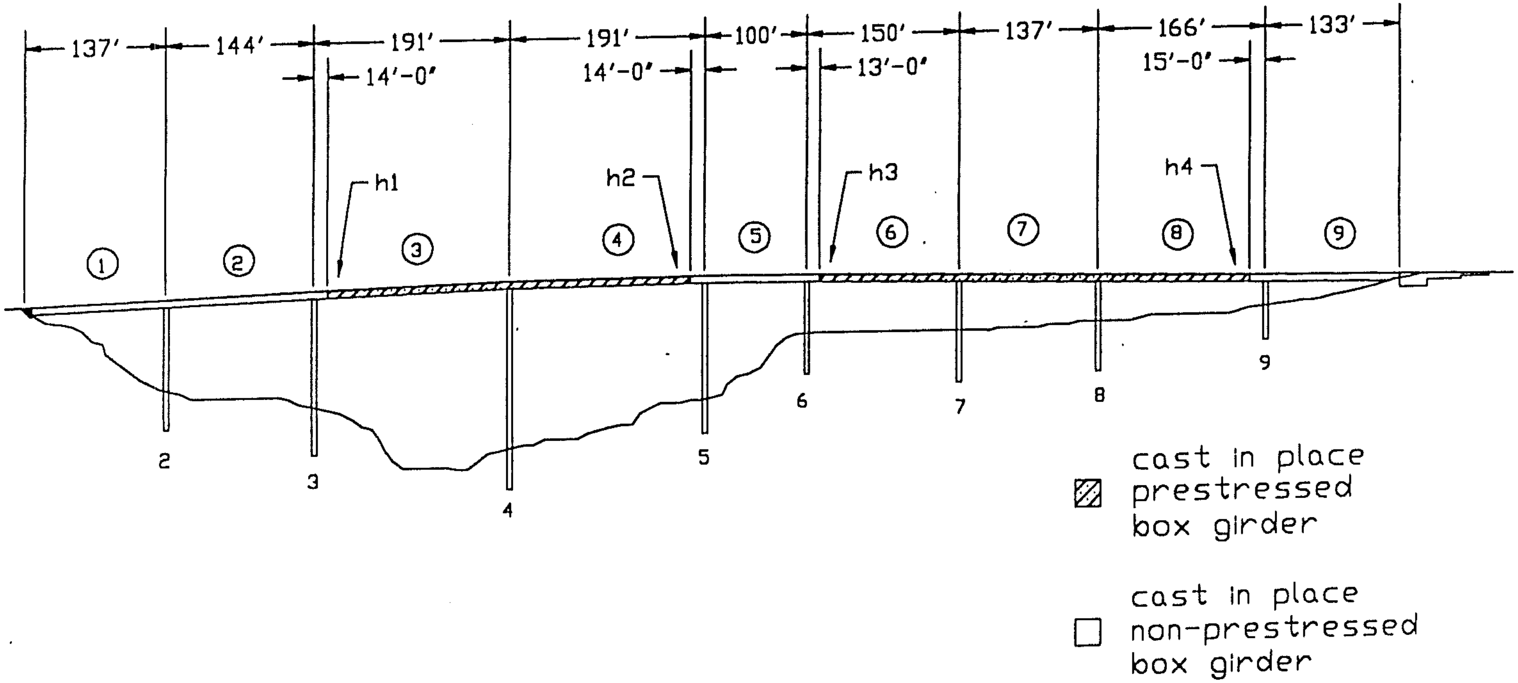
137'
144'
191'
191'
100'
150'
137'
166'
133'
14'-0"
14'-0"
13'-0"
15'-0"
h1
h2
h3
h4
①
②
③
④
⑤
⑥
⑦
⑧
⑨
2
3
4
5
6
7
8
9
▨ cast in place prestressed box girder
☐ cast in place non-prestressed box girder

Figure 2.16 - South Connector elevation view

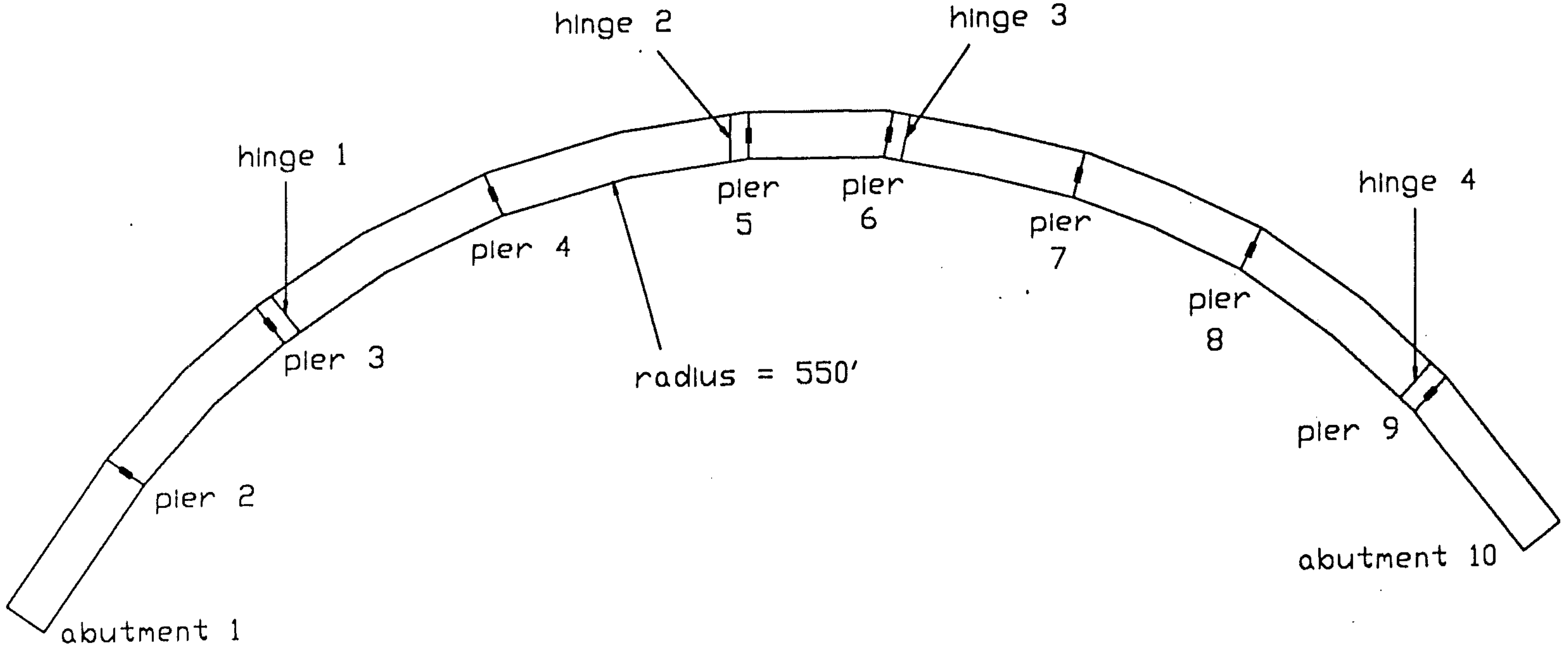
hinge 2
hinge 3
hinge 1
hinge 4
pier 5
pier 6
pier 4
pier 7
pier 3
pier 8
radius = 550′
pier 9
pier 2
abutment 10
abutment 1

Figure 2.17 - South Connector plan view

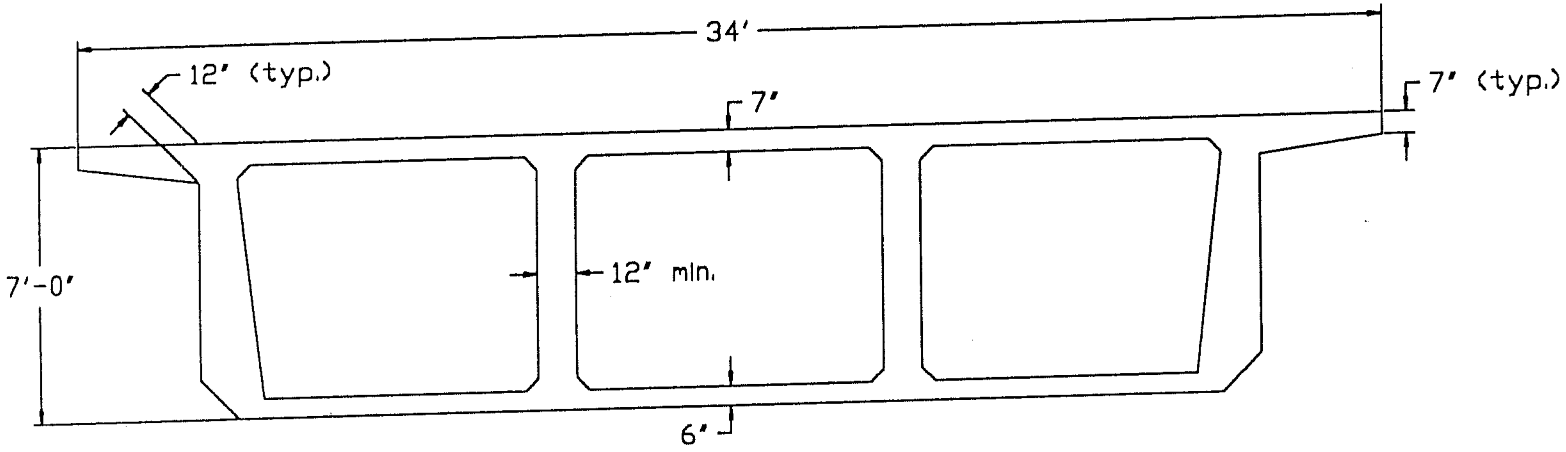
34'
12' (typ.)
7' (typ.)
7'
12' min.
7'-0'
6'

Figure 2.18 - South Connector box girder detail

Table 2.9 - Pier Data for the South Connector

Pier	width (ft)	number of #18 bars
2	5	40
3	6	40
4	6	52
5	6	40
6	4	40
7	4	48
8	4	48
9	4	48

Figure 2.19 shows the pier geometry and reinforcing details. Transverse reinforcement consists of #4 bars placed 12" on center. In the longitudinal direction of all the piers, three additional #4 cross-ties are provided. From the "as-built" plans, it appears that the piers are supported on multiple 16" diameter concrete piles.

As with the separation and overhead structure, there are 3 "movement-equalizing" bolts at each hinge. Cable restrainers, also 5 4-bar restrainer assemblies as in the separation and overhead structure, were later added after the San Fernando earthquake. Seat widths are generally 14" to 16". Each web is also supported on a 10" by 40" by 2" thick elastomeric bearing pad.

2.5 Tendon Layouts

An important part of evaluating the effect of vertical acceleration on the

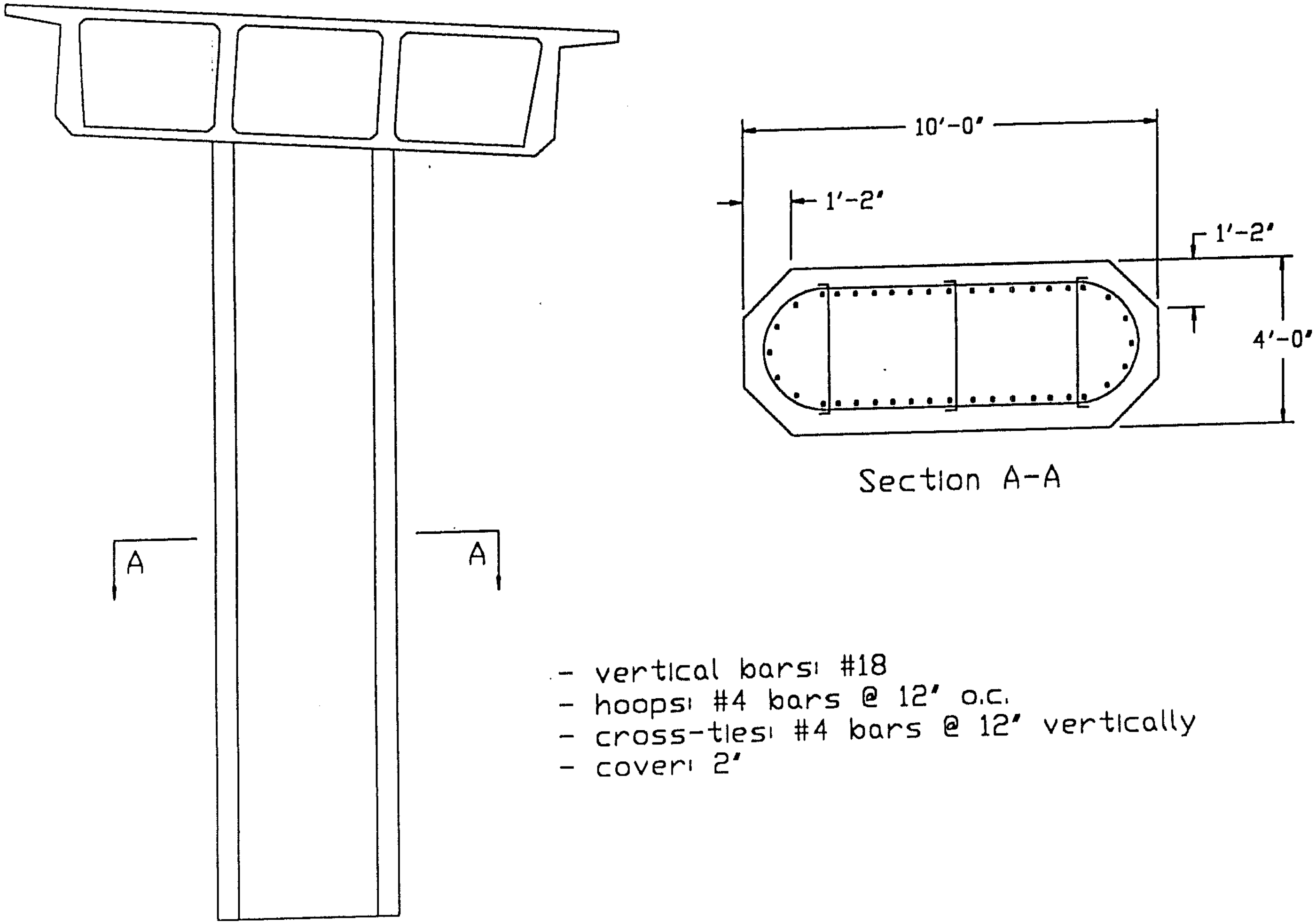
A
A
10'-0"
1'-2"
1'-2"
4'-0"
Section A-A

- vertical bars: #18
- hoops: #4 bars @ 12" o.c.
- cross-ties: #4 bars @ 12" vertically
- cover: 2"

Figure 2.19 - South Connector pier detail

superstructure of the bridges as it pertains to the loss of dead load is knowledge of the tendon layouts. The necessary information is given in Tables 2.10 and 2.11 as well as Figures 2.20 and 2.21. It is assumed that the tendons are parabolic between the points listed and symmetric about the center line of the prestressed spans.

Table 2.10 - Cable Eccentricities

bridge	spans	A	B	C	D	E	F
ramp M	1	4'-4"	12"	---	---	---	---
ramp M	4-5	4'-¼"	10"	5'-⅛"	1'-2"	---	---
ramp C	1-3	3'-9⅜"	1'-11"	4'-3"	10"	5'-1"	9"
ramp C	5-6	3'-9⅜"	10"	4'-10"	10"	---	---
ramp C	9-10	3'-9⅜"	9"	5'-1"	10"	---	---
ramp L	3-4	3'-10"	11"	5'-1"	1'-1"	---	---
ramp L	6-8	3'-10¼"	11"	4'-4¼"	11"	5'-1¾"	1'-4¼"

Table 2.11 - Distance Between Eccentricity Points

bridge	spans	W	X	Y	Z
ramp M	1	.5L	---	---	---
ramp M	4-5	.45L	.4L	---	---
ramp C	1-3	.45L	.3L	.1L	.4L
ramp C	5-6	.45L	.4L	---	---
ramp C	9-10	.5L	.4L	---	---
ramp L	3-4	.4L	.5L	---	---
ramp L	6-8	.4L	.4L	.1L	.4L

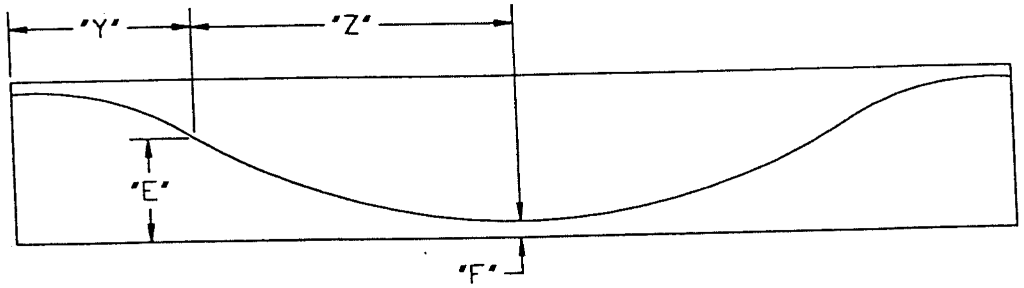

Figure 2.20 - Cable eccentricity diagram

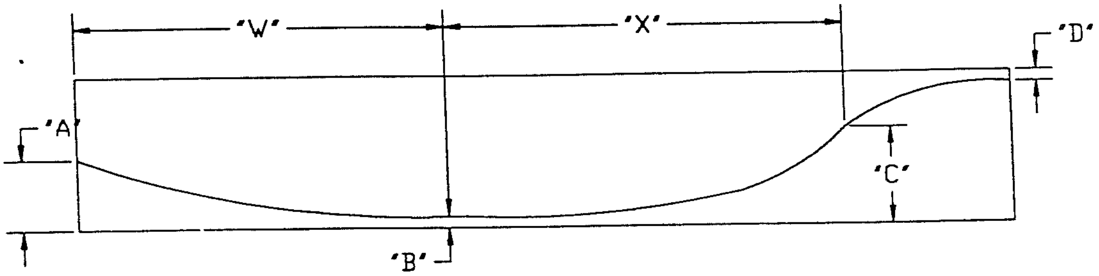

Figure 2.21 - Cable eccentricity diagram

2.6 Northridge Earthquake Records

One set of strong motion records (CSMIP) was obtained at Sylmar Hospital. Sylmar Hospital is located approximately 15 km NNE of the epicenter and approximately 4 km east of the bridge. The maximum free-field ground accelerations at Sylmar Hospital were 0.91g and 0.6g in the horizontal and vertical directions, respectively.[7] The USGS recorded a horizontal acceleration of 0.98g and a vertical acceleration of 0.52g about 4 km south of the bridge site at the base of the

Jenson Filtration Plant.[20] This agrees well with the Sylmar records.

2.6.1 Sylmar Hospital Accelograph

The free-field acceleration earthquake records from the Sylmar Hospital site are given in Figures 4.1 through 4.3 of Chapter 4. The plots are of baseline corrected accelerations, Fourier amplitude spectra, and response spectra for 0%, 2%, 5%, 10%, and 20% damping.[7] The accelerations were modified using a baseline correction method so that when the acceleration graph was integrated permanent velocities did not occur. As mentioned previously, the maximum acceleration in the horizontal direction is 0.91g and maximum acceleration in the vertical direction is 0.6g.

2.6.2 Synthetic Earthquake Data

In addition to the records from Sylmar Hospital, the Lamont-Doherty Earth Observatory at Columbia University in New York developed synthetic earthquake records for this particular bridge site for the National Center for Earthquake Engineering Research.[19] They are given in Appendix B. The synthetic data only exist for Ramp C. The highest horizontal acceleration is approximately 0.55g and the maximum vertical acceleration is approximately 0.17g. These are significantly lower than the records from Sylmar hospital, but the frequency of these accelerations is closer to the natural frequency of the bridge. Therefore, computer runs will also be performed with these accelerograms.

CHAPTER 3

COMPUTER PROGRAM AND MODEL

In order to perform the analysis of the three bridges described in the previous chapter, a computer program was developed by Yu[24] to study the effects of seismic loading. The program and the structural dynamics principles on which the program is based are briefly described in the following sections.

3.1 Description of Computer Program BRIDGEQUAKE

Computer program BRIDGEQUAKE was developed for this study by Yu as a part of the overall NSF project on the effect of vertical accelerations on prestressed concrete bridges. It carries out linear elastic analyses assuming a three-dimensional frame. Although the elastic analysis puts a constraint on the results, this type of analysis was used for the ease of programming, the fact that basic behavior could be studied, and because CALTRANS makes allowance for it in their analysis methods for columns (see Chapter 5). Three degrees correspond to translation along the three axes and the other three to rotations around those same axes. The equations of motion for a linear member are:

For axial motion,

$$\bar{m}\frac{\partial^2 u}{\partial t^2} - \frac{\partial}{\partial x}\left(EA\frac{\partial u}{\partial x}\right) = 0 \qquad (3.1)$$

For torsional motion,
$$GJ \frac{\partial^2 \theta}{\partial x^2} - \bar{m} r^2 \frac{\partial^2 \theta}{\partial t^2} = 0 \tag{3.2}$$

For the flexural motion of each member, the "Timoshenko" beam was used instead of the more traditional "Bernoulli" beam. The "Timoshenko" beam includes values for rotary inertia (third term) and shear deformations (fourth term).

$$\begin{aligned} EI \frac{\partial^4 u}{\partial x^4} + \bar{m} \frac{\partial^2 u}{\partial t^2} - \bar{m} r^2 \frac{\partial^4 u}{\partial x^2 \partial t^2} \\ + \frac{\bar{m}}{\kappa A G} (\bar{m} r^2 \frac{\partial^4 u}{\partial t^4} - EI \frac{\partial^4 u}{\partial x^2 \partial t^2}) = 0 \end{aligned} \tag{3.3}$$

In the above equations, the following notation has been used:

$\bar{m}$ = mass per unit length

E = Young's modulus

A = area

G = shear modulus

J = St. Venant's torsion constant

r = radius of gyration

I = moment of inertia

κ = shear coefficient

u = deformation

x = axis direction

θ = rotation

t = time

The value for the shear modulus, G, was calculated using the formula:

$$G = \frac{E}{2(1 + \nu)} \tag{3.4}$$

in which ν is Poisson's ratio.

The computer program solves the dynamic equations of motion in the frequency domain. This method has the advantage that it can easily incorporate the effect of distributed masses and mass moments of inertia along each member. In the frequency domain, the basic dynamic equation can be written in the form:

$$[-\omega^2 \boldsymbol{M} + \boldsymbol{K}]\boldsymbol{U}(\omega) = \boldsymbol{P}(\omega) \tag{3.5}$$

or

$$\boldsymbol{S}\,\boldsymbol{U}(\omega) = \boldsymbol{P}(\omega) \tag{3.6}$$

When damping of a linear hysteretic nature is included, the stiffness matrix **K** is replaced by:

$$\boldsymbol{K}_D = (1 + 2i\xi)\boldsymbol{K} \tag{3.7}$$

ξ, which is the damping coefficient, was taken as 5% for this study.

3.2 Modeling of the Structure

The bridge decks and columns were modeled as space frame members. The computer program does not handle curved members, so the curved portion of the superstructure was modeled with short straight members. This way the overall bridge could still be modeled as curved. Properties of the bridge cross section and piers were taken from the as-built drawings as described in Chapter 2. The modeling of the hinge restrainers will be specifically discussed in Chapter 6.

In order to solve the equations of motion, it was necessary to model the piles and spread footings that were supporting the bridge. First, the dynamic stiffness of the footings or the piles (at their head) were obtained in the frequency domain. These stiffnesses were then added to the corresponding stiffness terms of the structure.

The structure dynamic stiffness matrix could then be rearranged into the format shown in Equation 3.8 below.

$$\begin{bmatrix} S_{ff} & S_{fs} \\ S_{sf} & S_{ss} + S_p^* \end{bmatrix} \begin{bmatrix} \ddot{U}_f \\ \ddot{U}_s \end{bmatrix} = \begin{bmatrix} 0 \\ S_p^* \ddot{U}_{sg} \end{bmatrix} \tag{3.8}$$

In this equation , the subscript "f" refers to the free degrees of freedom and the subscript "s" to the supported degrees of freedom. $\ddot{U}_f$ and $\ddot{U}_s$ are the accelerations in terms of frequency of the free and supported degrees of freedom, respectively. The term $S_p^* \ddot{U}_{sg}$ is the pile head stiffness (or footing stiffness) multiplied by the ground motion accelerations. Equation 3.8 is solved for the accelerations. These accelerations are then converted to velocities and displacements. The displacements are used to calculate member forces.

3.3 Seismic Excitation

The ground motion used in Equation 3.8 was the motion that would occur at the surface of the soil. This implies that kinematic interaction effects were neglected. Ground motions were applied in the two horizontal directions as well as the vertical direction. The longitudinal ground motion was applied in a direction parallel to a straight line in between the two abutments. The time histories used were described in Section 2.6. One case was also run using the 1994 UBC response spectrum from Figure 3.1.

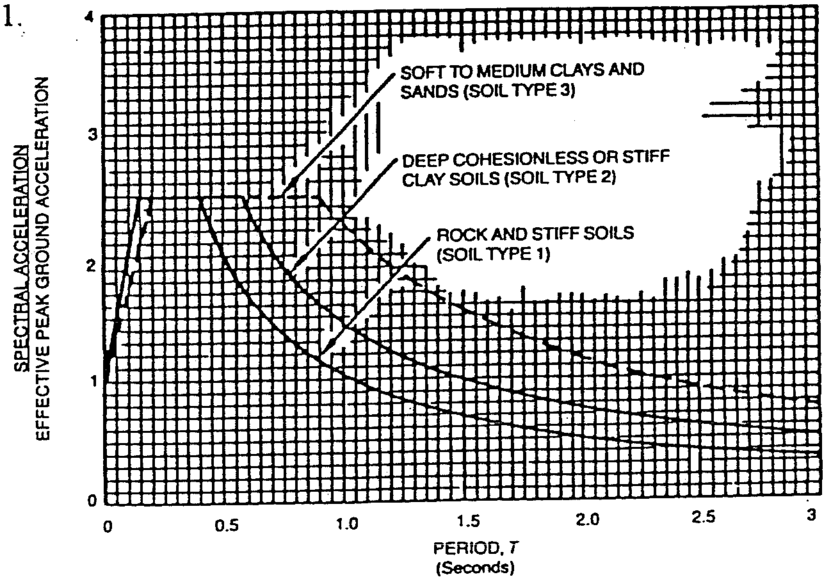

Figure 3.1 - 1994 UBC horizontal motion response spectrum[21]

The vertical acceleration response spectrum was taken as two-thirds of the horizontal acceleration response spectrum. A final case was also run using the simulated earthquake data for the NCEER study given in Appendix B. The results of all these simulations are presented in Chapters 5 and 6 as they relate to axial forces and moments in the columns as well as displacements at the hinges.

CHAPTER 4

ANALYSIS OF SUPERSTRUCTURE

4.1 Characteristics of Earthquake Motion

Earthquake energy emitted from the hypocenter is carried by waves with different frequency components. As these waves propagate through different geological profiles in different directions, components with frequencies close to the natural frequency of a specific soil deposit will be amplified. The measured ground motion generally has predominantly long periods for a soft soil basin and predominantly high frequencies for a hard rock site. The predominant frequency is also determined by the direction of ground motion. In general, vertical earthquake motion has predominantly higher frequency components than the horizontal motions.

The characteristics of an earthquake can be assessed by examining the time history of acceleration, the frequency amplitude spectrum of the accelerograms, and/or the response spectra. The frequency amplitude spectrum shows the frequency decomposition of the earthquake motion. The response spectra provide information about the effects of earthquakes on structures with specific natural frequencies. In this thesis, the absolute acceleration spectrum, which is the linear response acceleration of a single degree of freedom system to earthquake motion as a function of its natural frequency and damping, is presented as the response spectrum of the given earthquake motion. Figures 4.1 through 4.3 illustrate the accelerograms and spectra in the three directions of ground motion recorded at the Sylmar Hospital parking lot during the Northridge earthquake. Figures (a) are the time histories of the earthquake motions, figures (b) show the corresponding frequency amplitude spectra calculated with the Fast Fairer Transform (FFT). NP is the number of points used to perform the FFT and the vertical scale represents the "acceleration" in the frequency domain), and figures (c) are the corresponding absolute acceleration response spectra. The accelerograms shown in these figures are modified records of the corrected accelerograms provided by CSMIP.[7] An additional baseline correction procedure was applied by Yu[24] so that the direct integrated velocities would be zero at the end of the time history.

Figure 4.1 shows the characteristics of the ground motion in the E-W direction, which has a maximum baseline corrected acceleration of 0.6g. Two different peaks can be observed in Figure 4.1(c). One is between 1.5 Hz and 3 Hz and the other is near 9 Hz. Figure 4.2 shows the spectra for the N-S component, which has a maximum baseline corrected acceleration of 0.84g. The predominant frequency is approximately 3 Hz and two other minor peaks occur at 7 Hz and 11 Hz. Figure 4.3 shows the characteristics of the ground motion in the vertical direction, which has a maximum baseline corrected acceleration of 0.54g. The amplitude spectrum indicates a wide range of frequencies with significant amplitudes with the predominant frequencies in this direction ranging from 6 Hz to 12 Hz.

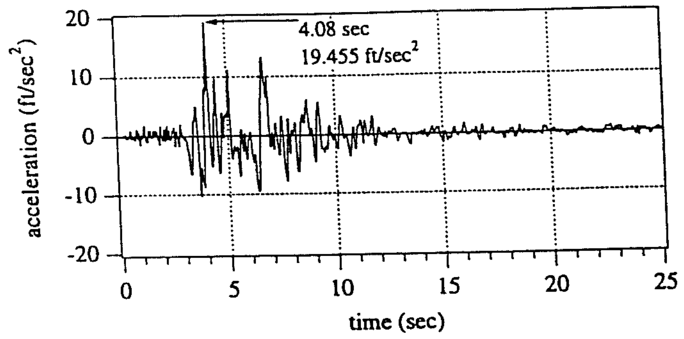

(a) - Corrected accelerogram in E-W direction

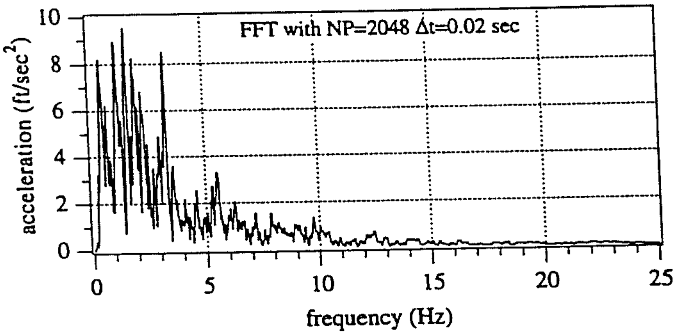

(b) - FFT amplitude spectrum in E-W direction

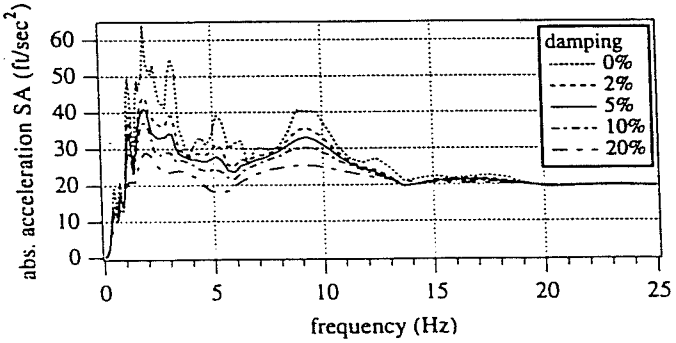

(c) - Absolute acceleration spectrum in E-W direction

Figure 4.1 - Sylmar Hospital E-W records during Northridge earthquake

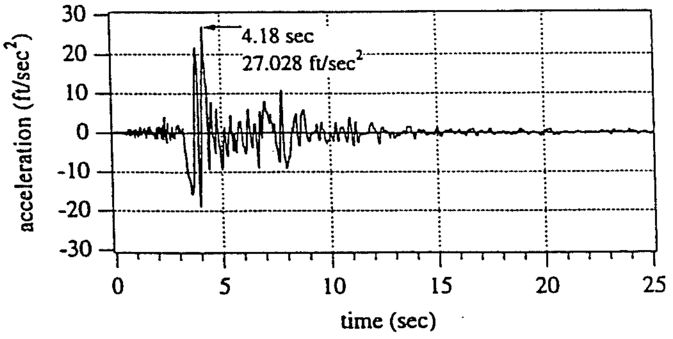

(a) - Corrected accelerogram in N-S direction

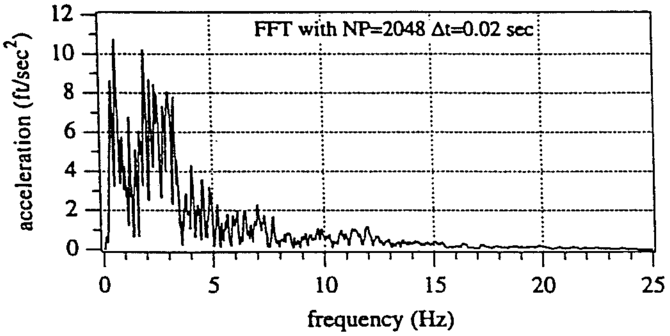

(b) - FFT amplitude spectrum in N-S direction

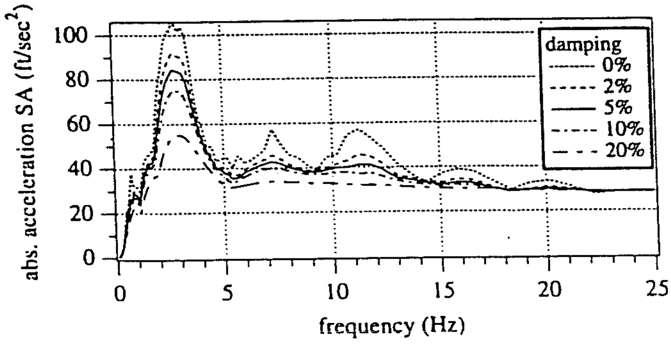

(c) - Absolute acceleration spectrum in N-S direction

Figure 4.2 - Sylmar Hospital N-S records during Northridge earthquake

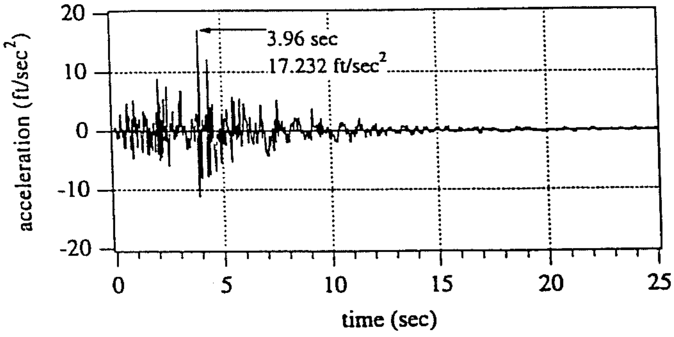

(a) - Corrected accelerogram in vertical direction

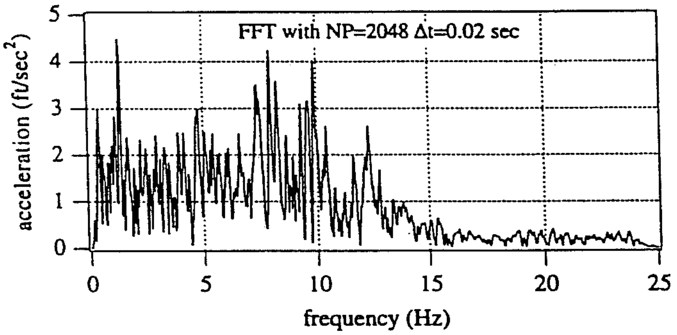

(b) - FFT amplitude spectrum in vertical direction

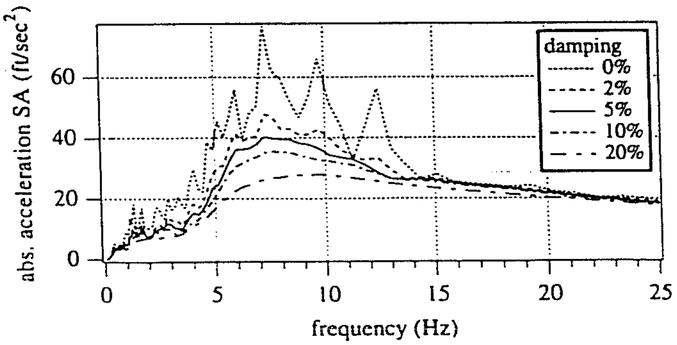

(c) - Absolute acceleration spectrum in vertical direction

Figure 4.3 - Sylmar Hospital vertical records during Northridge earthquake

4.2 Analysis of Simple Frames

When frames are subjected to vertical ground motions, two independent vertical vibration types can be identified -- the flexural (vertical or transverse) vibration of the horizontal member (beam or deck) and the vertical or axial vibration of the vertical member (column). The predominant mode of these vibrations will depend on the span length and the column height. The effects of span length and column height on the natural frequency of vertical structural vibrations were studied using symmetric single span frames with columns fixed at the bases as shown in Figure 4.4.

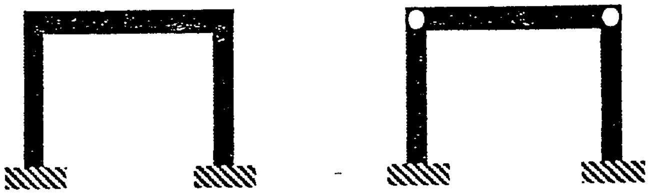

Figure 4.4 - Single span frames

The beam-column connections were modelled as the two extremes, one being fully monolithic while the other was modelled as completely hinged (no rotational stiffness). The hinged model ignored the small vertical effects of the longitudinal hinge restrainers, as this parametric study was used only to compare the two extremes.

The ground acceleration used was the vertical component of the Sylmar Hospital parking lot records shown in Figure 4.3(a). Columns and beams were modeled using the cross-sectional properties of pier 2 and the deck of the south connector overcrossing (Ramp L) shown in Figures 2.14 and 2.15. Material damping coefficient of 5% was assumed in all cases.

4.2.1 Effect of Span Length

Figure 4.5 shows the variation of the natural frequency of these frames with span length. A column height of 20' was used, which causes the natural frequency associated with column vibration to be very high and thus to be essentially uncoupled from the girder vibration shown in these plots. According to Figure 4.3 (c), the dominant frequency of the vertical earthquake motion ranges from 6 Hz to 12 Hz for 5% damping. Frequencies smaller than 5 Hz contribute relatively little and modes with frequencies greater than 12 Hz would not be substantially amplified. As the span length increases from 50' to 250', the fundamental frequency decreases from 22 Hz to 1 Hz. The second mode becomes apparent for spans of 150' and greater. The second mode is around 16-18 Hz for 150' span lengths and this frequency decreases as the span length increases. The third mode appears in spans of 200' and greater. Table 4.1 shows the maximum accelerations at the midspan of the beam and the time at which they occurred.

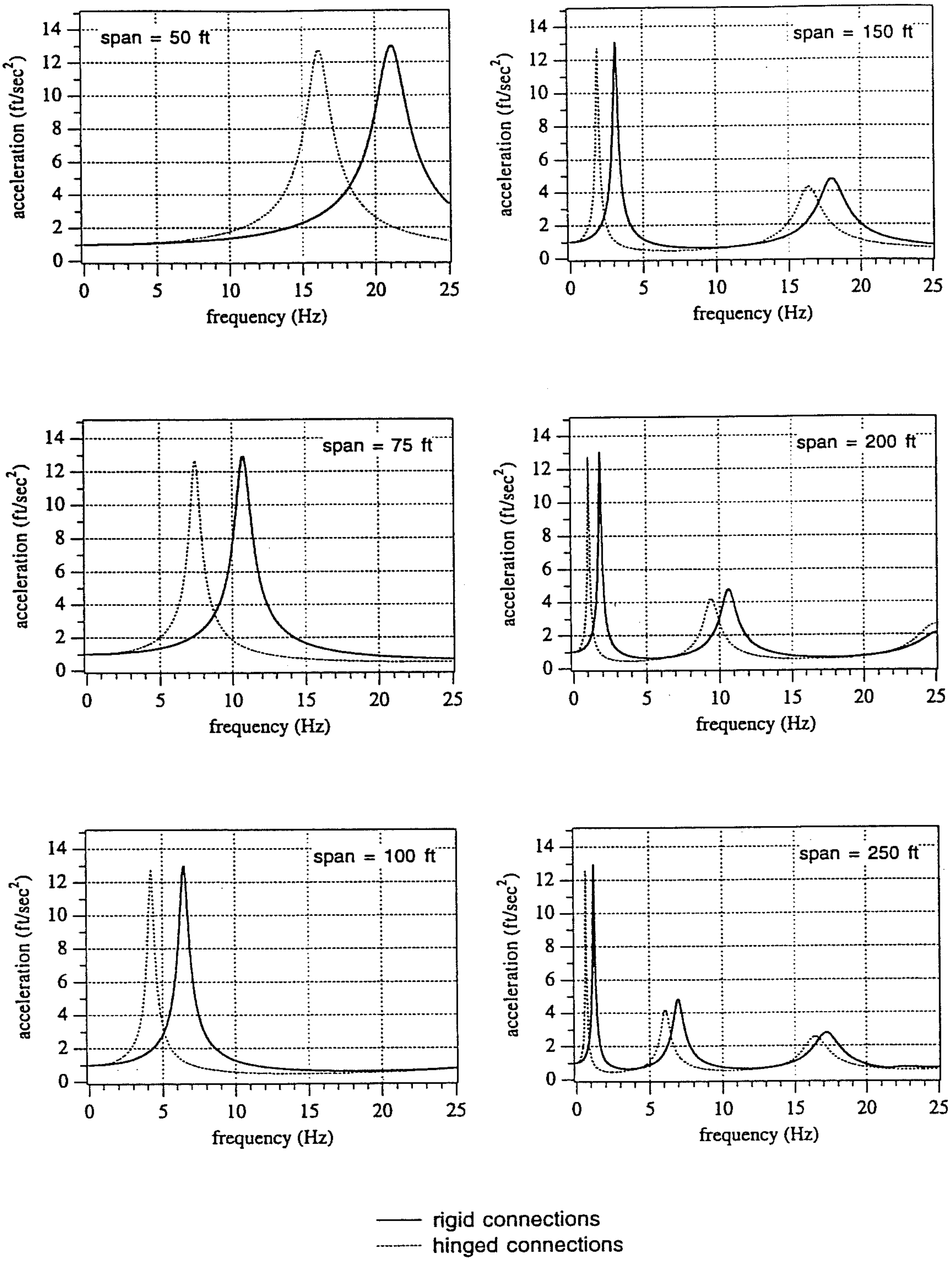

Figure 4.5 - Transfer functions at mid-span for single span case

Table 4.1 - Accelerations for single-span frames with varying span length

	monolithic connection (M)			hinged connection (H)		
span length (feet)	max. accel. (ft/sec^2)	amplification ratio	time (sec)	max. accel. (ft/sec^2)	amplification ratio	time (sec)
50	28.86	1.67	3.96	29.96	1.74	3.96
75	47.56	2.76	3.98	65.28	3.79	4.46
100	52.23	3.03	4.08	24.09	1.40	3.96
150	20.58	1.19	3.96	15.84	0.92	3.96
200	24.69	1.43	3.98	21.97	1.27	4.04
250	28.70	1.67	4.42	22.22	1.29	4.00

End restraints affect the frequencies of vibration. The beam-column joint hinges reduce the flexural stiffness of the beam. Thus, the natural frequency of hinged frames are slightly lower than those of monolithic frames. High maximum acceleration can be expected if the fundamental frequency of the structure lies in the dominant region of earthquake motion. The reason that the maximum acceleration increases from the 150' to 250' span lengths is that while their first mode frequencies are very low, the second mode frequency occurs in the dominant region of the earthquake spectrum. According to Figure 4.3 (a), the maximum vertical acceleration occurred at 3.96 seconds. When the amplification of the vertical acceleration is substantial, the maximum acceleration occurs at a later time, such as cases M-75, M-100, M-250, and H-75 in Table 4.1. As seen in Figure 4.5, these cases all have frequency peaks between 6 Hz and 12 Hz, the dominant region of the earthquake spectrum.

Therefore, as far as the vertical component of motion for the Sylmar Hospital parking lot is concerned, horizontal members with a fundamental frequency between 6 Hz and 12 Hz undergo a significant vertical acceleration amplification. Horizontal members that are very stiff ($F_n > 15$ Hz) undergo maximum accelerations close to the maximum ground acceleration.

4.2.2 Effect of Column Height

It is obvious that the natural frequency associated with column vibration should decrease as column height increases since the axial stiffness of the column would be reduced with increasing length. Also, longer columns provide less end restraint to the beam, and thus the column height also slightly affects the natural frequencies of beam vibration. In this sub-section, the column height is changed from 20' to 250' to show its effect on frequency and the maximum accelerations associated with column vibration. Figures 4.6 and 4.7 show the transfer function for cases with varying column heights and span lengths equal to 100' and 200' respectively. The frames with 100' spans all have a fundamental frequency near 4 to 5 Hz, while the frames with 200' spans all have their first two modes located near 2 Hz and 10 Hz. Table 4.2 lists the maximum accelerations at the midspan of the beam for the various combinations corresponding to Figures 4.6 and 4.7. The amplification factors are listed underneath the corresponding accelerations.

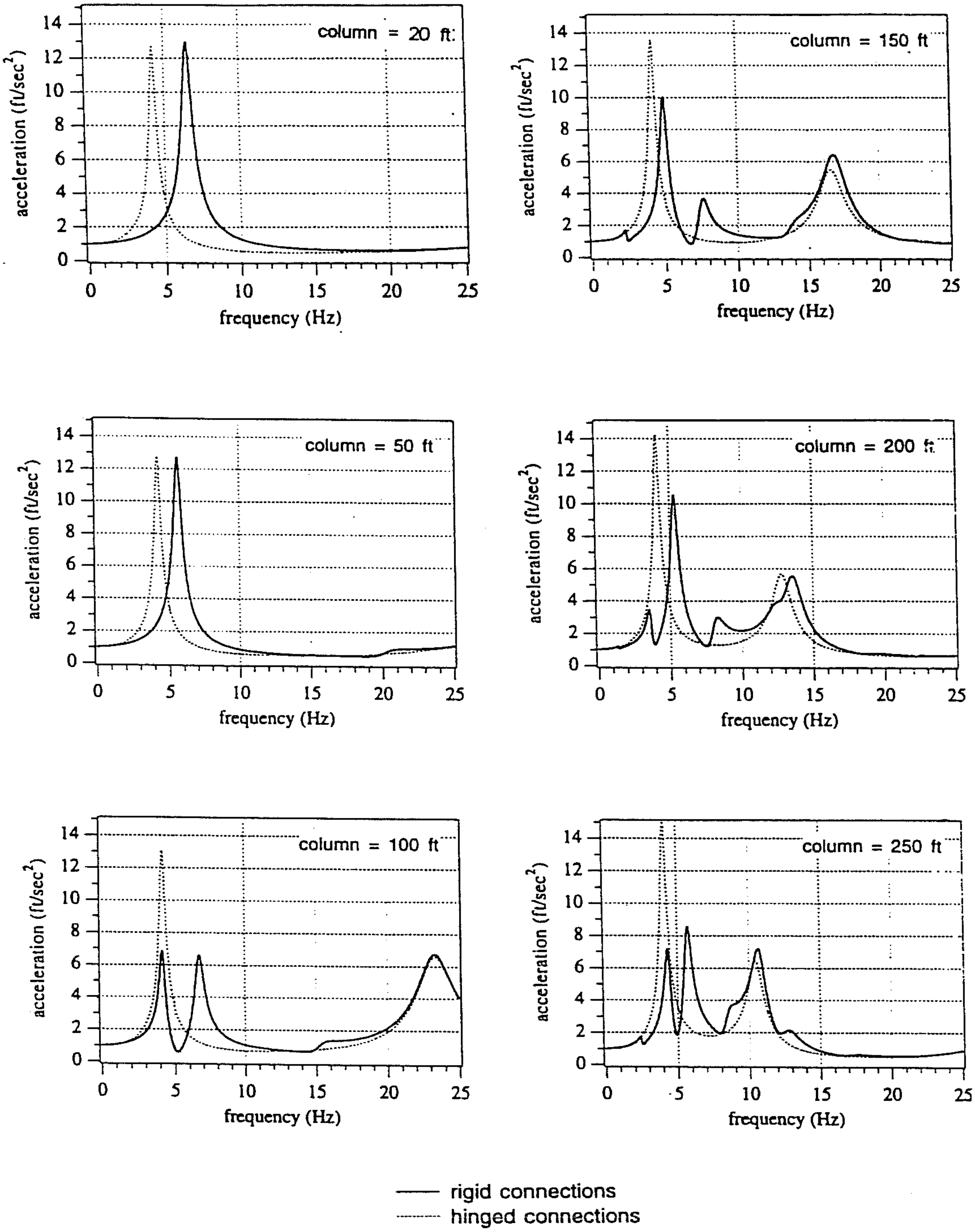

Figure 4.6 - Transfer functions of single span frames with a span length of 100 feet

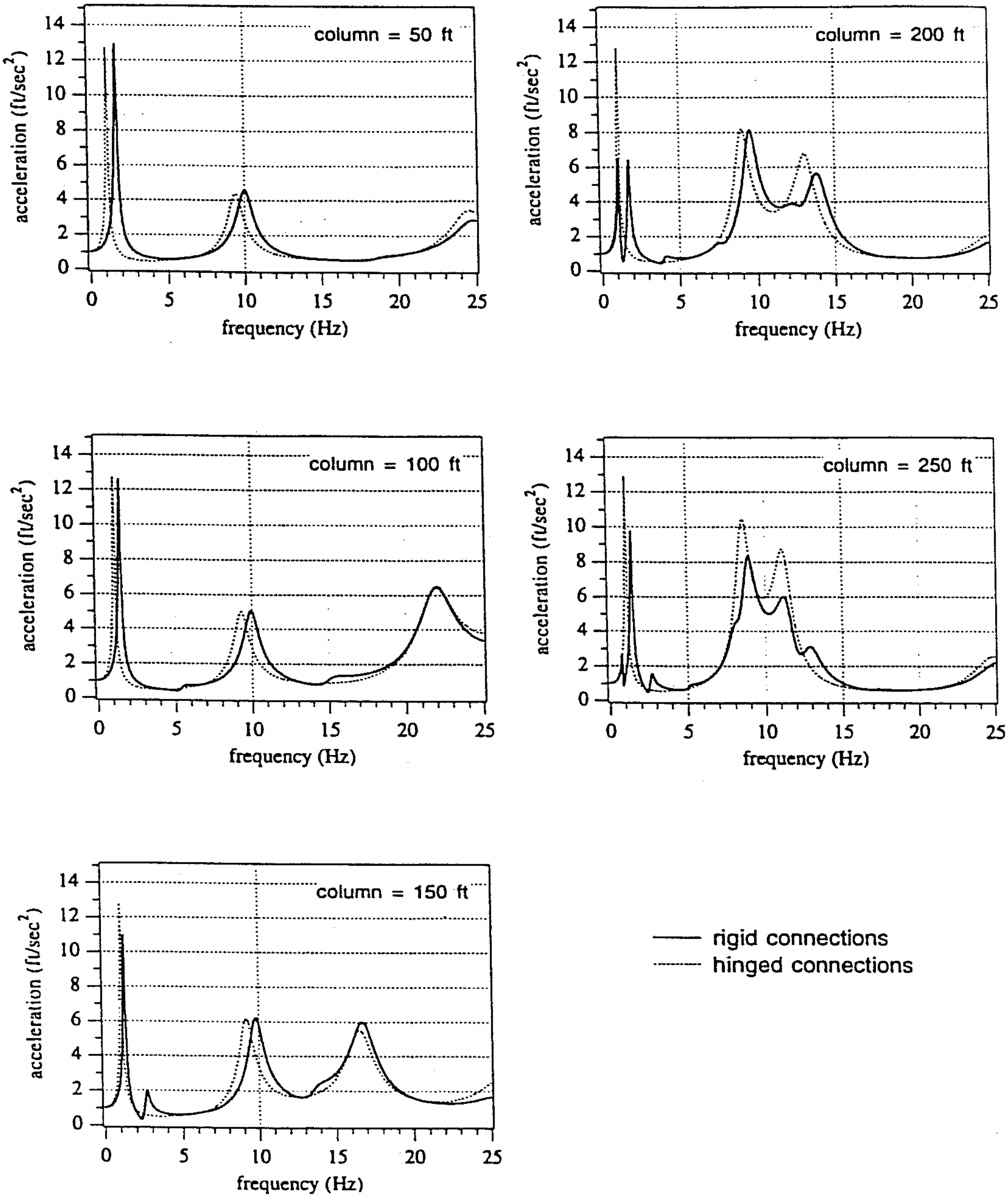

Figure 4.7 - Transfer functions of single span frames with a span length of 200 feet

In the cases with a span length of 100', the hinged frame has lower maximum accelerations and slightly smaller fundamental frequencies than the monolithic frame. In the frames with a 200' span, the hinge does not cause the vibration frequencies to move into or out of the dominant frequency region. Therefore, there is only a small difference between the maximum accelerations for the two different types of frames, except for a column height of 250', where the difference is more substantial.

Table 4.2 - Accelerations for single-span frames with varying column height

	span length = 100'		span length = 200'	
	accelerations (ft/sec^2) (amplification factor)		accelerations (ft/sec^2) (amplification factor)	
column height (ft)	monolithic	hinged	monolithic	hinged
20	52.2 (3.03)	24.1 (1.40)	24.7 (1.43)	22.0 (1.28)
50	46.2 (2.68)	24.5 (1.42)	28.8 (1.67)	22.7 (1.32)
100	34.4 (2.00)	28.1 (1.63)	25.8 (1.50)	22.4 (1.30)
150	38.5 (2.23)	30.0 (1.74)	31.2 (1.81)	31.3 (1.82)
200	46.7 (2.71)	30.5 (1.77)	39.3 (2.28)	40.1 (2.33)
250	63.7 (3.70)	38.8 (2.25)	43.0 (2.50)	56.6 (3.28)

For column heights above 100', longer columns lead to higher maximum accelerations due to the decrease in the natural frequency. As more modes of the column vibration move from the high frequency area toward the dominant frequency region, their contribution to the vertical acceleration of the beam is increased. In the given examples, the column vibration significantly affects the vertical acceleration of the beam at column heights of 200' or greater. Amplification factors for columns that were 200' tall or greater had amplification factors ranging from 1.77 to as high as 3.70.

4.2.3 Deformed Shapes of Vibration

According to the transfer functions calculated in the previous sections, the natural frequencies of a member vary somewhat with different end constraints. In the hinged cases, the dominant frequencies are due to the column axial vibration and beam flexural vibration. In the monolithic cases, more than two frequency peaks could be observed in most cases, including the cases with taller columns where twin peaks occur near the fundamental frequency (see Figure 4.7 -- 200' span case).

Figure 4.8 illustrates the deformed shapes and amplitudes for the first few natural frequencies of a single span frame, when both the column height and the span length are 200'. Figure 4.8 (a) is the transfer function showing four peaks that correspond to the first four modes of vibration. For the frequencies dominated by beam vibrations, shown in Figure 4.8 (b), the amplitude at midspan is higher than that at the end by a factor of approximately 5. As seen in Figure 4.8 (b), vibrations

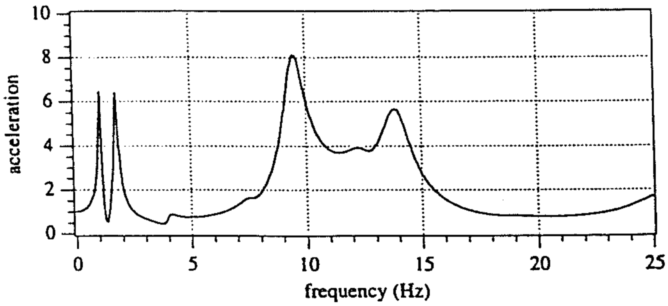

(a) - Transfer function at mid-span of monolithic frame

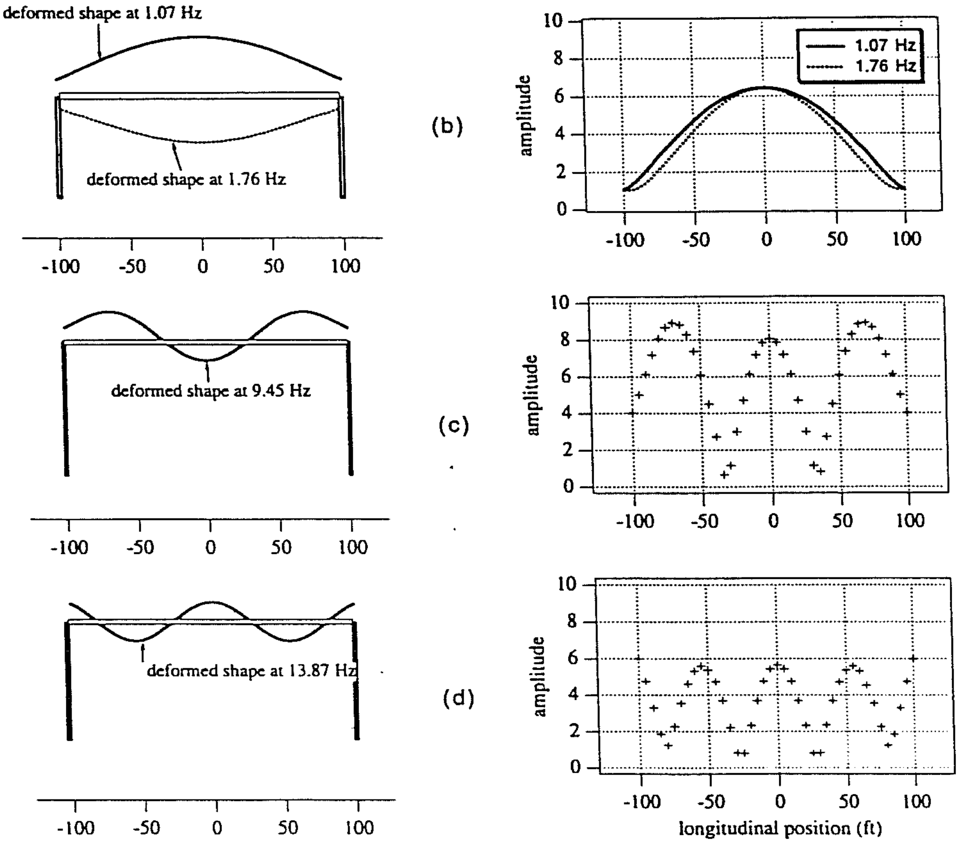

(b) - (d) - Deformed shapes and amplitudes due to unit excitation at supports

Figure 4.8 - Vibration shapes and deformed amplitudes for a single span frame (pier height = 200 feet, span length = 200 feet)

associated with the twin peaks have somewhat similar deformed shapes. One shape (1.05 Hz) is close to the vibration mode of a hinged beam where there is no rotational constraint, while the other (1.73 Hz) is similar to modes of beams with fixed end restraints. In Figure 4.8 (c) and (d), the deformed shape indicates that both column and beam vibration contribute to deformation. It is clear from the amplitude plots that the amplitude at the ends of the spans are more than three times higher than in Figure 4.8 (a), which means the columns contribute more to the vibration shapes at higher frequencies.

4.3 Study of Multi-Span Frames

Parametric studies similar to those described in Section 4.2 were conducted for symmetric 2-span and symmetric 3-span frames. As expected, the magnitude of the maximum deck acceleration depends on whether or not the natural frequencies of the structural system and the forcing frequencies of the significant ground motion are close to each other. Figure 4.9 shows the configurations of the multi-span frames studied. The hinge at the 1/10th point of each span is an idealized simulation of the location and function of the expansion joints found in many CALTRANS bridges. Since retrofitting, these hinges connect each deck with cable restrainers. The deck acceleration was studied at several locations along the span length, which are marked in the figure. Results for multi-span frames are presented in the form of maximum deck acceleration versus both span length and column height. Deformed shapes of vibrations are also illustrated at certain frequencies.

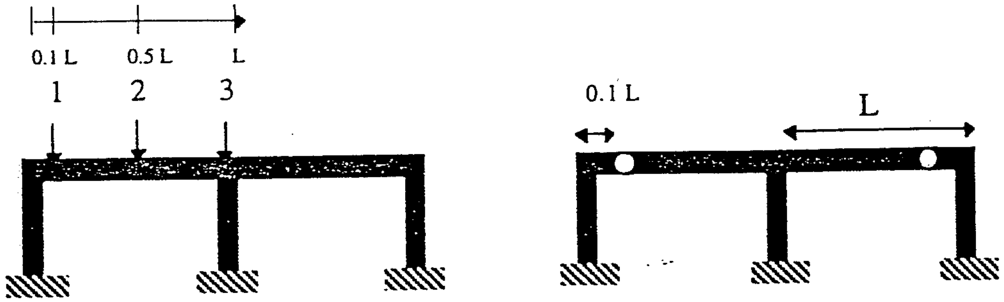

(a)-2-span monolithic.

(b)-2-span hinged at 1/10th span.

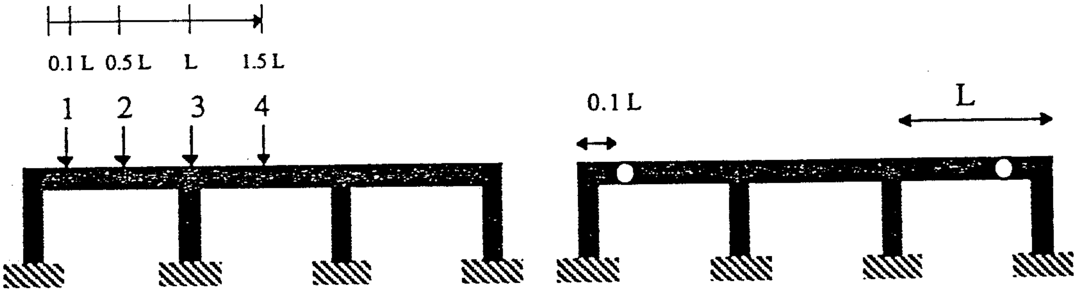

(c)-3-span monolithic.

(d)-3-span hinged at 1/10th span.

location
1 : 1/10th span from left column
2 : mid-span of left span.
3 : top of interior column.
4 : mid-span of interior span.

Figure 4.9 - Multi-span configurations

4.3.1 Effect of Span Length

Figures 4.10 and 4.11 show the variation of maximum acceleration with different span lengths. The column was again assumed to be 20' high so that the amplification associated with column axial vibration could be minimized. The span length was again varied from 50' to 250'. As shown in Figures 4.10 (a) and 4.11 (a), the maximum acceleration at Station 1, the hinge location in the hinged frame, becomes significant as the span length increases above 150'. The increase is

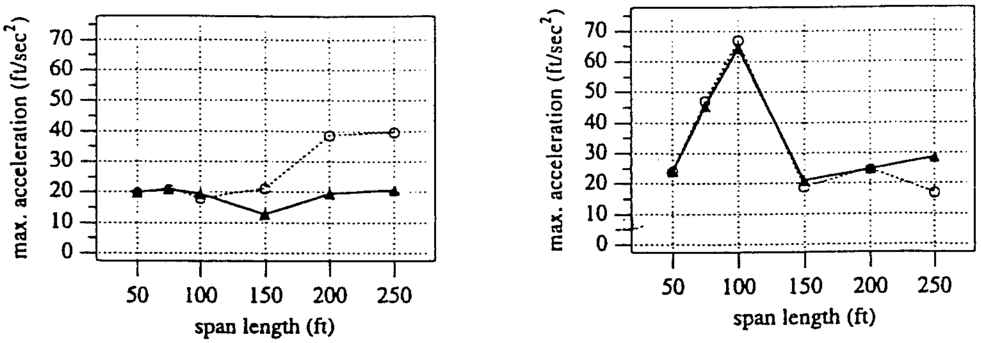

(a) - At 1/10th span (station - 1)

(b) - At mid-span (station - 2)

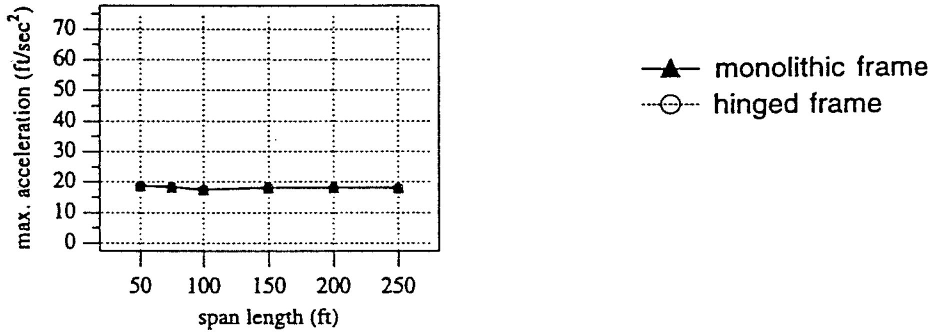

(c) - At interior joint (station - 3)

Figure 4.10 - Effect of span length on maximum acceleration (2-span case)

primarily caused by the second mode of flexural vibration. At the midspan positions, maximum accelerations reach their peak values with a span length of 100', which has a fundamental frequency of approximately 7.5 Hz. As expected, Figures 4.10 (c) and 4.11(c) show hardly any effect of span length on the vertical acceleration at the top of the interior column since the column is very short.

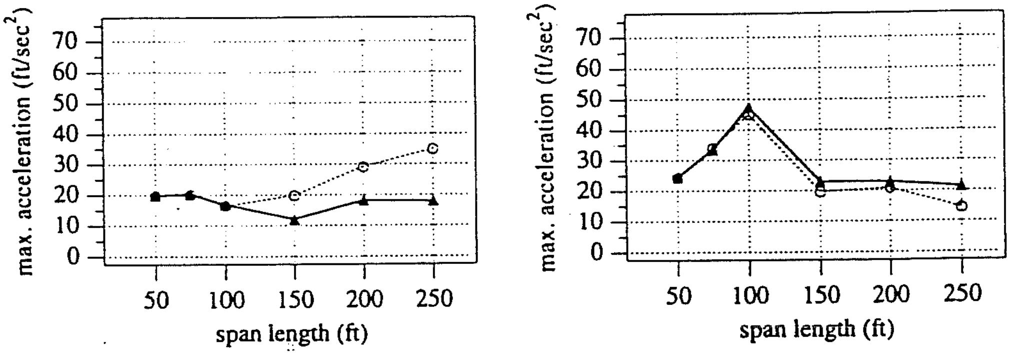

(a) - At 1/10th span (station - 1)

(b) - At mid-span of exterior beam (station - 2)

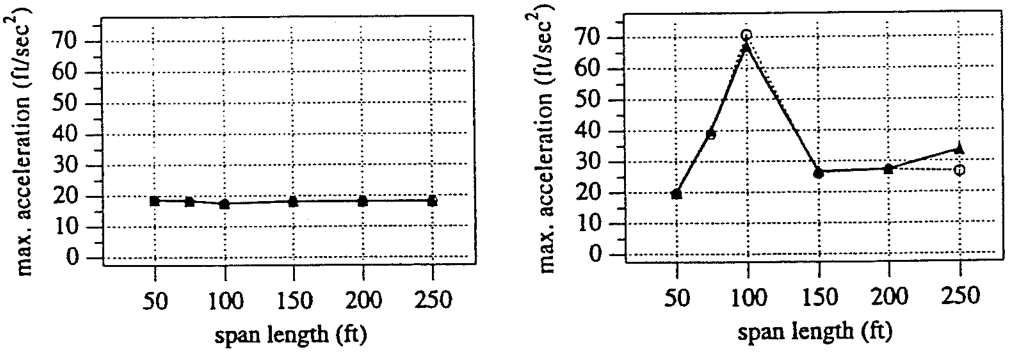

(c) - At interior column top (station - 3)

(d) - At mid-span of interior beam (station - 4)

—▲— monolithic   —○— hinged

Figure 4.11 - Effect of span length on maximum acceleration (3-span case)

4.3.2 Effect of Column Height

Figures 4.12 and 4.13 show the variation of maximum vertical acceleration with column height for 100' and 200' span lengths. The axial vibration of the columns generally has higher natural frequencies than the flexural vibration of the beams and the significant components of the measured Sylmar Hospital ground motion. Therefore, changing column height within certain ranges should not affect the vertical acceleration to a large extent.

The graphs show the general trend that increasing the column height increases the maximum vertical accelerations. The increase is much more dramatic for the 200' span case. At Stations 1 and 3 (Figures 4.12 (a) , 4.12 (c), 4.13 (a), and 4.13(c)), there is approximately a 100% increase in the maximum acceleration from the 20' column to the 200' column. At the same stations for the 100' span length, the increase is approximately 50%. Stations 1 and 3 are at the hinge location and the interior beam-column connection, respectively. It can be seen that as the span length increases, the reduced axial stiffness of the taller columns will produce higher maximum accelerations at Stations 1 and 3.

The variance of maximum acceleration is much less at the midspan of each of the beams. At Station 2 (Figures 4.12 (b) and 4.13 (b)), the maximum acceleration increases approximately 10% for the 100' span length and 30% for the 200' span length. At Station 4 (Figures 4.13 (d)), the maximum acceleration increases approximately 40% for the 100' span length, 75% for the hinged frame with the 200'

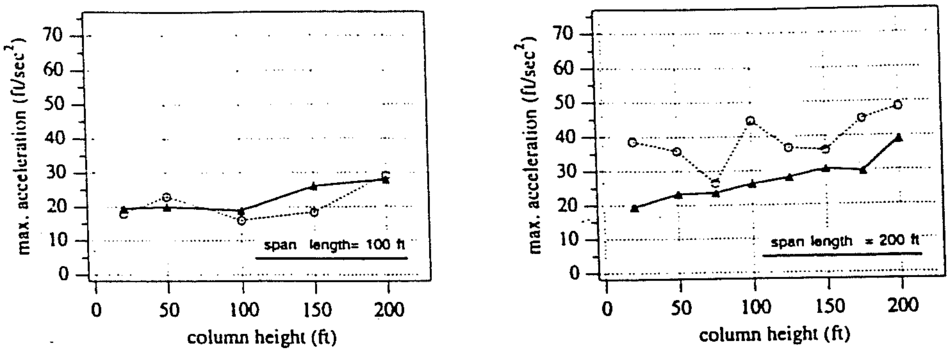

(a) - At 1/10th span (station - 1)

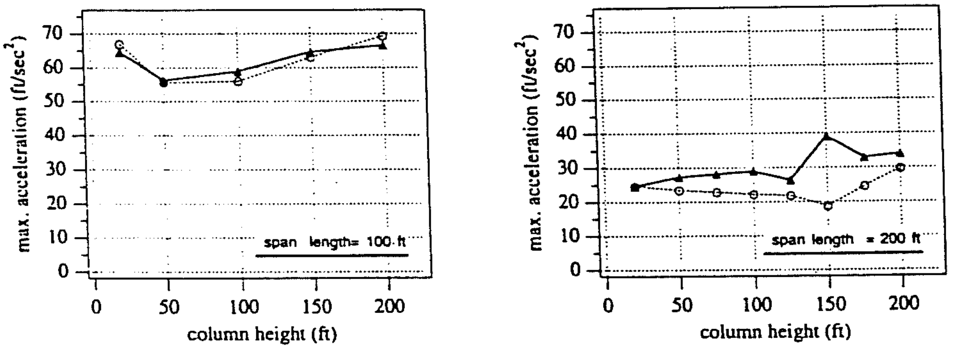

(b) - At mid-span (station - 2)

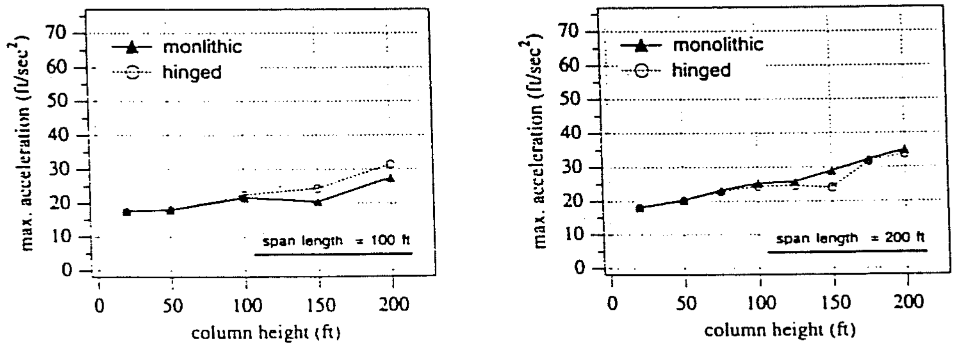

(c) - At interior beam-column connection (station - 3)

Figure 4.12 - Effect of column height on maximum accelerations at three different positions of the 2-span frames (span lengths = 100 feet and 200 feet)

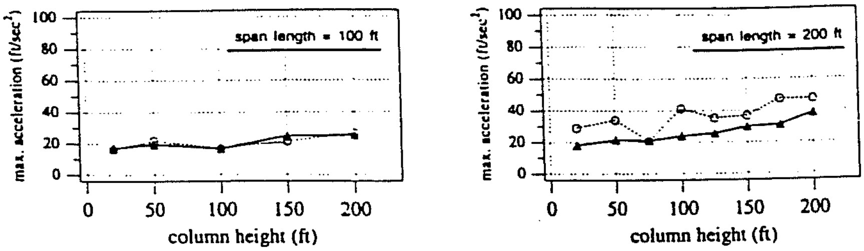

(a) - At 1/10th span (station - 1)

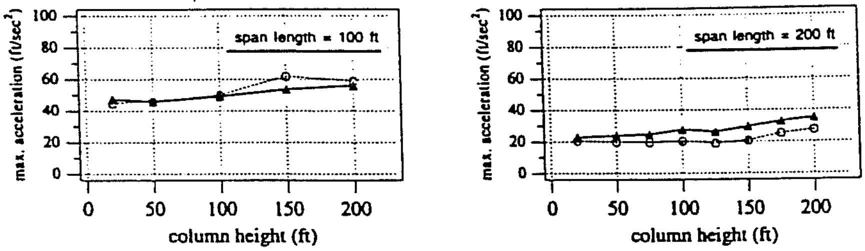

(b) - At mid-span of exterior beam (station - 2)

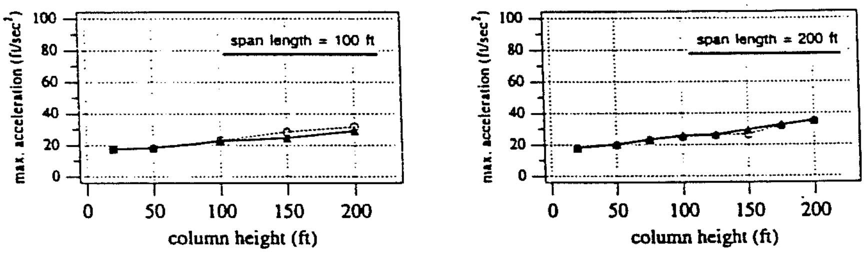

(c) - At interior column top (station - 3)

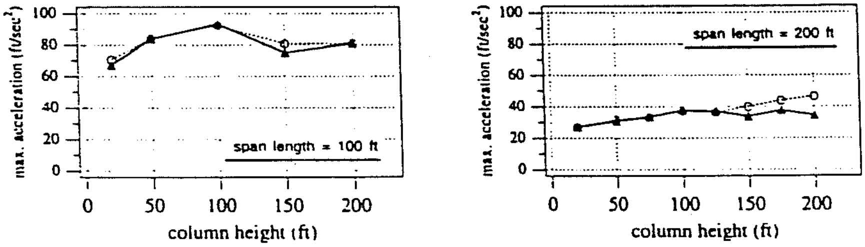

(d) - At mid-span of interior beam (station - 4)

—▲— monolithic ---○--- hinged

Figure 4.13 - Effect of column height on maximum accelerations at four different positions of the 3-span frames (span lengths = 100 feet and 200 feet)

span length, and 25% for the monolithic frame with the 200' span length.

The maximum acceleration curves look very similar for the hinged and monolithic cases with a 100' span length. The hinge makes a difference in the shape of the curves with the 200' span length. The accelerations become much greater at Station 1 in the hinged frame due to the increased flexibility of the beam when the hinge is added. The maximum acceleration percentage increase tends to not be as high as the increase in the monolithic models at Station 1.

Figures 4.14 and 4.15 show the transfer functions at the hinges and mid-span positions for the multi-span frames with column heights of 20'. The 100' span case has dominant frequencies close to the region of significant frequency components (6 Hz to 12 Hz) and thus high midspan accelerations. On the other hand, the 200' span case has its fundamental frequency near 2 Hz, which is not significant for this particular earthquake spectra.

From Figures 4.12 and 4.13, the monolithic frames and hinged frames with 100' span lengths experience comparable maximum accelerations for the different column heights and the various locations. However, in the cases with 200' span lengths, the hinged frame has larger accelerations than the monolithic frame at the 1/10th point (hinge), and lower accelerations at midpsan. This can be explained by examining the transfer functions of the hinged frames at the 1/10th point. A second vibration mode with a high amplitude appears at a lower frequency than for the monolithic frame (see Figure 4.14 and 4.15 -- upper right graphs). This significant peak occurs around 9 Hz. It corresponds to a vibration shape with large deformation at the hinge, and thus induces a considerable amount of acceleration at the hinges. This proves how important it is to understand the behavior of the bridge and the restrainer units located at the hinge.

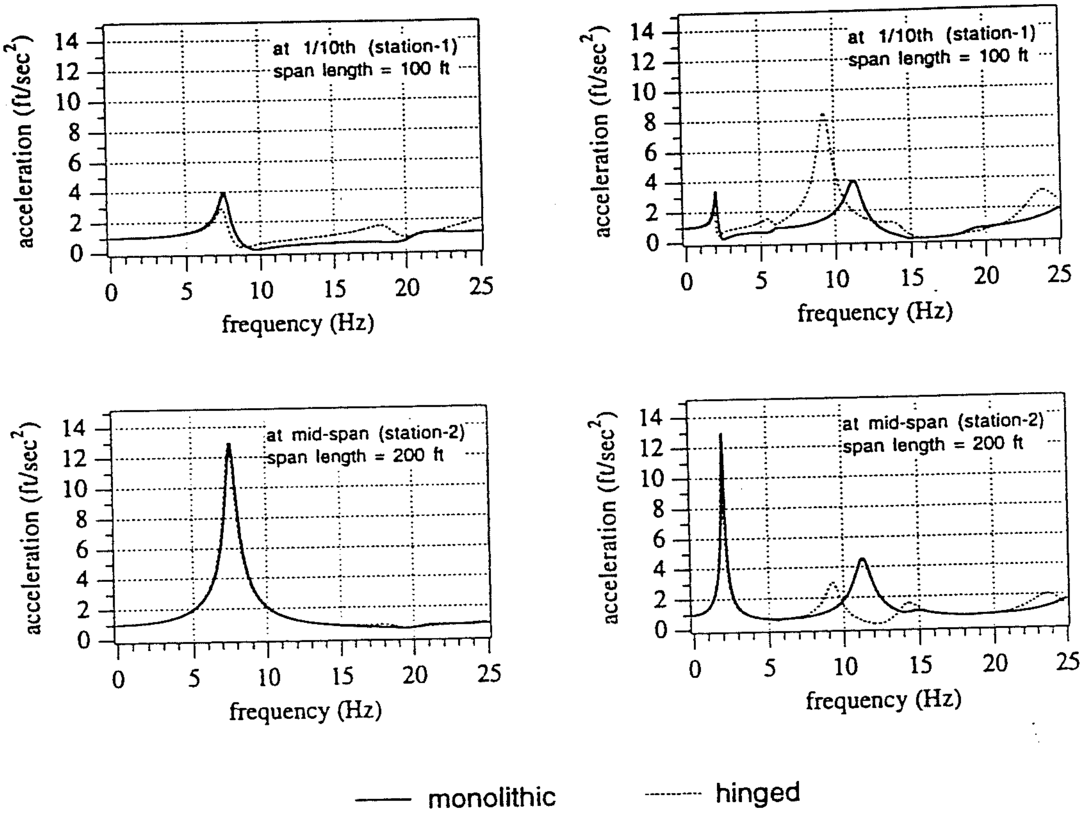

Figure 4.14 - Transfer functions for 2-span frame (column height = 20')

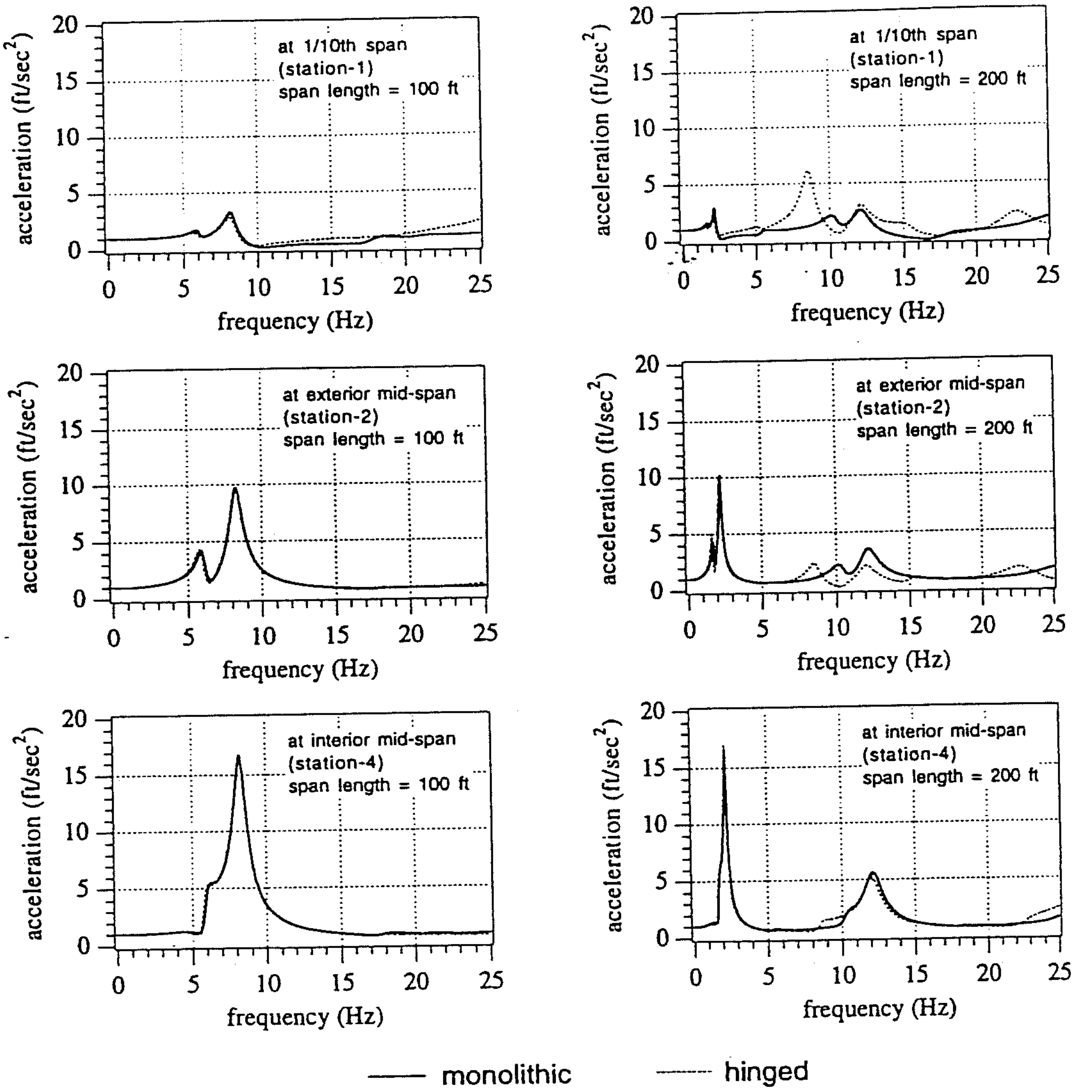

Figure 4.15 - Transfer functions for 3-span frames (column height = 20')

4.3.3 Deformed Shapes of Vibration

Figures 4.16 and 4.17 show the deformed shapes and amplitudes of the first few vibration modes of the multi-span frames with 200' spans. Upon comparing the results of the hinged and monolithic frames, it can be concluded that the two types of frames have similar mode shapes. The amplitude (dimensionless since it represents

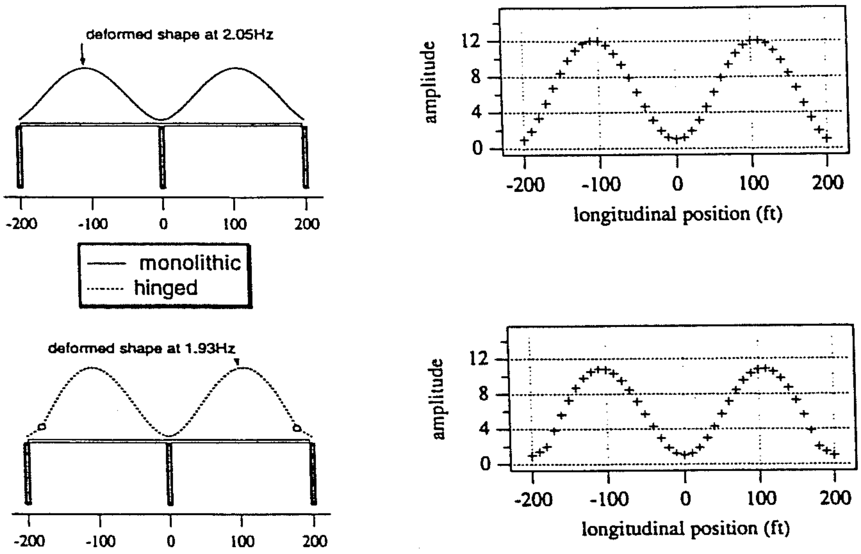

(a) - First mode

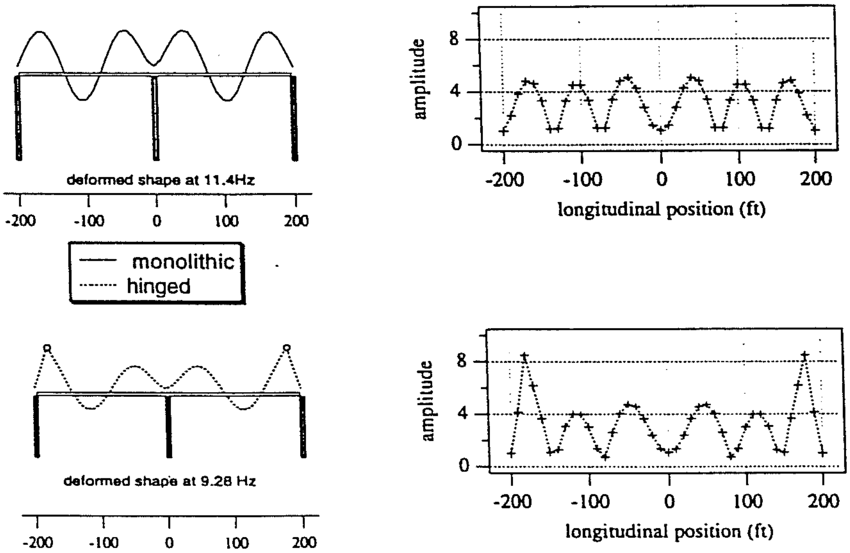

(b) - Second mode

Figure 4.16 - Vibration shapes and deformed amplitudes for a 2-span frame (column height = 20 feet, span length = 200 feet)

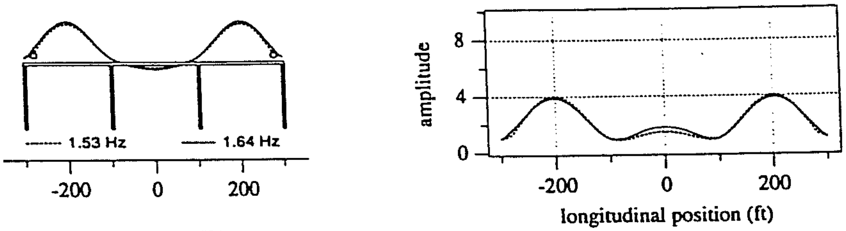

(a) - First mode

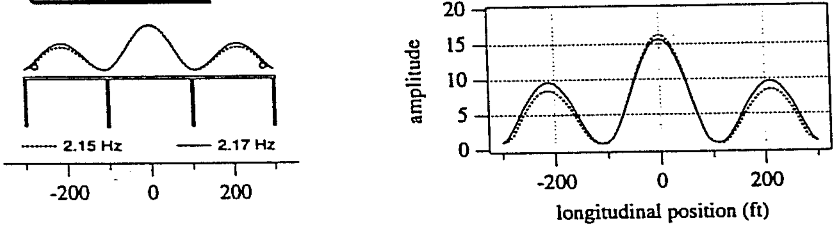

(b) - Second mode

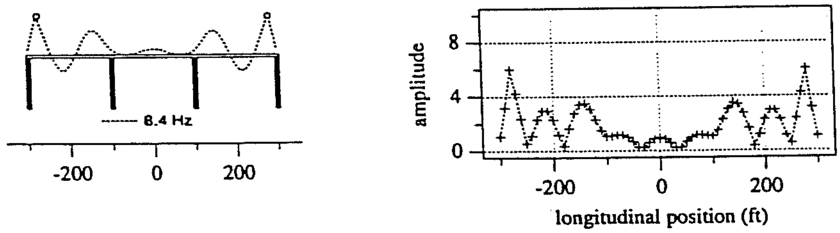

(c) - Third mode of hinged frame

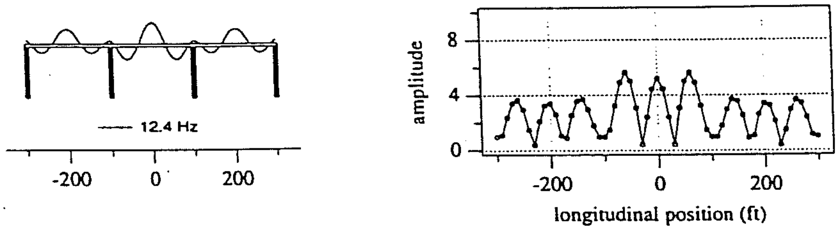

(d) - Third mode of monolithic frame

Figure 4.17 - Vibration shapes and deformed amplitudes for a 3-span frame (column height = 20 feet, span length = 200 feet)

magnification effects) is approximately the same as the amplitude in the monolithic frame. The addition of the hinge does not drastically affect the amplitudes in the deck. Higher vibration modes, especially the third mode for the 3-span case in Figure 4.16 (c), can result in high amplitudes at the hinge position. The hinge position is shown by the black dot. These figures again show the importance of the displacements that can occur at the hinges and the potential for an "unseating" faille at the hinge if the proper retrofitting is not done.

4.4 Summary of Parametric Studies

The magnitude of the induced vertical deck accelerations is a function of several variables, including the characteristics of ground motion, the dimensions and properties of the structural members, and the configuration of the bridge. The ground motion has some significant frequency components. Structural members with natural frequencies close to the significant ground frequencies are subjected to higher accelerations.

The sources of deck acceleration are the flexural vibration of the deck itself and the axial vibration of the columns. The axial vibration of the column is only important when the column is very long (over 150'). The flexural vibration of horizontal members is the primary source of vertical accelerations in the deck since the frequencies of the flexural vibration are comparable to the predominant frequencies of the ground motion.

For the single-span frames with a constant column height of 20', the maximum vertical acceleration reached a peak for a span length of 100' in the monolithic case and 75' for the hinged case (Table 4.1). The maximum accelerations then dropped and started increasing again as the span length approached 250'. This is because while the first mode of vibration was no longer in the dominant frequency range of the earthquake motion, the second and third modes were approaching this range.

Next, the column heights were varied from 20' to 250' for span lengths of 100' and 200'. The maximum accelerations at midspan of the beam of the hinged frames were smaller than those of the monolithically connected frames except for the 250' column height with a 200' span length (Table 4.2). For column heights above 100', the longer columns lead to higher maximum accelerations. This is due to the fact that the modes of column vibration moved into the dominant frequency region of the earthquake motion.

Finally, the effect of span length and column height was studied for two-span and three-span frames. When the column height was fixed at 20', the maximum acceleration at the hinge location increased as the span length increased above 150'. The maximum acceleration at midspan of the beam occurred at a span length of 100' for both the monolithic and hinged frame cases.

The column height for the two and three span frames was then varied from 20' to 200'. Frames with span lengths of 100' and 200' were evaluated. The general trend was that increasing the column height increased the maximum vertical accelerations, especially at Stations 1 and 3, the hinge and the interior beam-column connection. The percentage increase from the 20' column to the 200' column was approximately 100% in the 200' span length case and 50% in the 100' span length case. The variance was smaller at midspan of the beams. That is because the columns make much less of a contribution at midspan.

In the bridges examined in this study, the expansion joints, or hinges, are placed at or very near the 1/10th points of the span. Vertical accelerations at the hinges could become significant if the vibration frequencies of the higher modes approach the predominant frequencies of the ground motion. Consequently, the vertical ground motion could affect a pounding failure at a hinge.

4.5 Analysis of Draped Tendons

As seen from Sections 4.2 and 4.3, high vertical accelerations can occur in the bridge's superstructure as a result of vertical ground accelerations. When prestressed concrete girders have been designed using the "load balancing" method, a prestressing bending moment due to the prestressing force multiplied by the eccentricity is usually designed to balance approximately two-thirds of the bending moment due to the dead load. High vertical accelerations can reduce the "effective weight" of the superstructure, thus reducing the component of the bending moment due to the dead load. The opposite acting prestressing force bending moment could, as a result, cause tension cracks. This section investigates that possibility.

It is assumed for the following calculations that the bridge has no traffic and that the bridge superstructure experiences an upward vertical acceleration of 1g. This value is used since this situation results in the removal of all of the dead load. The only forces then acting on the bridge are the prestressing forces. The instantaneous dead load moment is thus effectively zero. In the calculations, the percentage of the normal (1g downward vertical acceleration) dead load moment which had been balanced by the prestressing moment has also been calculated. See Appendix D for a sample calculation.

4.5.1 Section Properties

In order to obtain section properties, the girder cross sections obtained from the as-built plans were input to AutoCAD® Release 12. AutoCAD calculated and output the cross-sectional area, the moment of inertia, and the location of the centroid. On most of the plans, the bottom soffit and the webs increased in thickness near the pier. The bottom soffit usually increased to 9" thick. As per CALTRANS procedure in the *Bridge Design Practice Manual,*[3] the structural effects due to the increase in web width were ignored. All of the dimensions are based on feet units.

4.5.1.1 North Connector Structure (Ramp C)

The data for the different cross sections of the north connector bridge are given in Table 4.3. The value for the centroid of the cross section calculated by AutoCAD® did not match the centroid of the prestressing tendons given in the drawings at the end of spans 4 and 5. The reason for this difference is not known.

The centroid of prestressing tendons is usually designed to be at the centroid of the cross section at the end of the spans. If it is not, additional prestressing moments result. This was the only case of the three bridges where this phenomenon occurred. Therefore, the calculations were done assuming that the location of the centroid of the prestressing tendons is the location of the centroid of the cross section.

Table 4.3 - Cross-section Properties for North Connector (Ramp C)

	Span 1 (midspan)	Span 1 (at bent)	Spans 4-5 (midspan - calculated)	Spans 4-5 (midspan - used)	Spans 4-5 (at bent)
Area (ft^2)	50.85	---	64.74	64.74	70.24
Moment of Inertia (ft^4)	413.55	---	541.02	541.02	605.64
$\bar{y}_{bot}$ (ft)	4.33	---	4.24	4.02	3.96
$\bar{y}_{top}$ (ft)	3.42	---	3.51	3.73	3.79
dead load (kips/ft)	8.25	---	10.5	10.5	11.5

4.5.1.2 Separation and Overhead Structure (Ramp M)

The data for the constant cross section of the separation and overhead are shown in Table 4.4. The value for the centroid of the cross section aligned with the centroid of the prestressing tendons at the endpoint. This means the values that AutoCAD output are reasonably accurate, since prestressed sections are usually designed with no eccentricity at the end of the span.

Table 4.4 - Cross-section Properties of Separation and Overhead (Ramp M)

	Spans 1-3, 5-6, and 9-10 (midspan)	Spans 1-3, 5-6, and 9-10 (at bent)
Area (ft^2)	94.5	104.25
Moment of Inertia (ft^4)	677.79	764.58
$\bar{y}_{bot}$ (ft)	3.79	3.49
$\bar{y}_{top}$ (ft)	3.21	3.51
dead load (kips/ft)	15	16.5

4.5.1.3 South Connector Structure (Ramp L)

The data for the constant cross section of the south connector are shown in Table 4.5. Again the value for the centroid of the cross section aligned with the centroid of the prestressing tendons at the end of the span.

Table 4.5 - Cross-section Properties of South Connector (Ramp L)

	Spans 3-4 and 6-8 (midspan)	Spans 3-4 and 6-8 (at bent)
Area (ft^2)	61.93	67.68
Moment of Inertia (ft^4)	429.24	482.12
$\bar{y}_{bot}$ (ft)	3.83	3.57
$\bar{y}_{top}$ (ft)	3.17	3.43
dead load (kips/ft)	10	11

4.5.2 Prestress Losses

Prestress losses were calculated in accordance with the CALTRANS *Bridge Design Practice Manual,*[3] the CALTRANS *Bridge Design Specifications,*[4] and general prestressed concrete engineering principles.

4.5.2.1 Friction and Curvature Losses

Friction losses were calculated according to Equation 4.1.

$$T_x = T_o\, e^{-(KL + \mu\alpha)} \tag{4.1}$$

The prestressing tendon is divided into segments where the eccentricity of the prestressing cable is known. T_o is the force at the known point O, T_x is the force at point X, K is the wobble coefficient in ft^{-1}, L is the distance in feet from point O to point X, μ is the friction coefficient, and α is the total angular change of the prestressing cable in radians. α is calculated according to the formulas,

$$\alpha = \sqrt{(\alpha_V)^2 + (\alpha_H)^2} \tag{4.2}$$

$$\alpha_V = \frac{2\delta}{L} \tag{4.3}$$

$$\alpha_H = \frac{L}{R} \tag{4.4}$$

where δ is the tendon drape (change in eccentricity) over the length L, and R is the radius of curvature for the bridge. For all of the spans on these bridges, it was assumed that K = 0.0002 ft^{-1} and $\mu = 0.25$ in accordance with the specifications on the bridge plans.

4.5.2.2 Anchor Set Losses

The effect of the anchor set on the cable stresses was computed according to the method given in the CALTRANS *Bridge Design Manual*[3] Section 3 and illustrated in Figure 4.18 below.

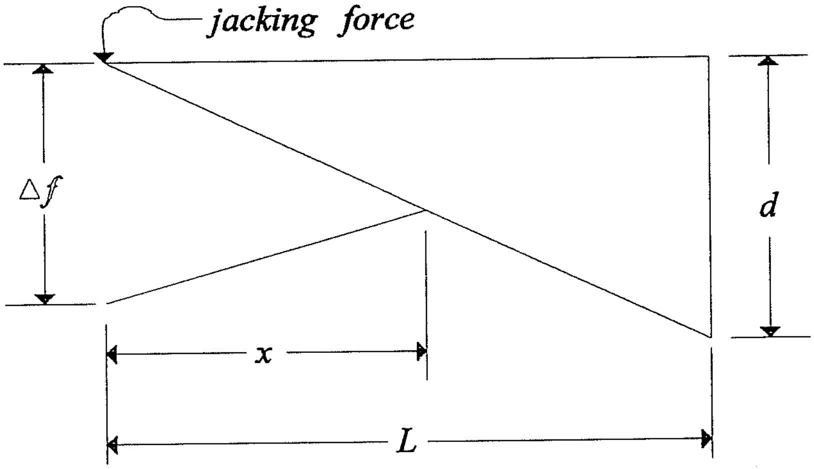

Figure 4.18 - Diagram for anchor set losses

The anchor set losses are calculated according to the following equations:

$$x = \sqrt{\frac{E(\Delta L)L}{12d}} \tag{4.5}$$

$$\Delta f = \frac{2dx}{L} \tag{4.6}$$

The variables in the diagram and Equations 4.5 and 4.6 are defined as follows:

Δf = change in stress due to anchor set (ksi)

x = length influenced by anchor set (ft)

d = friction loss in length L (ksi)

L = length to a point where loss is known (ft)

ΔL = anchor set (in)

E = modulus of elasticity for prestressed cables (ksi)

For the anchor set calculations, E was assumed to be 27,500 ksi and the anchor set ΔL was taken as ⅝" (as specified on the plans). For the calculations, a length L is chosen to which the friction losses d are known. The value of x is calculated. If the x is less than L, then the value for Δf can be calculated. If x is larger than L, a new value for L is chosen and x is recomputed.

4.5.2.3 Long Term Losses

In accordance with Table 9.16.2.2 of the CALTRANS *Bridge Design Specifications,*[4] the long term losses were taken as 20,000 ksi.

4.5.3 Resulting Stresses

The resulting top and bottom stresses for each of the bridges can be seen in Figures 4.18 through 4.23. Compressive stresses are positive and tensile stresses are

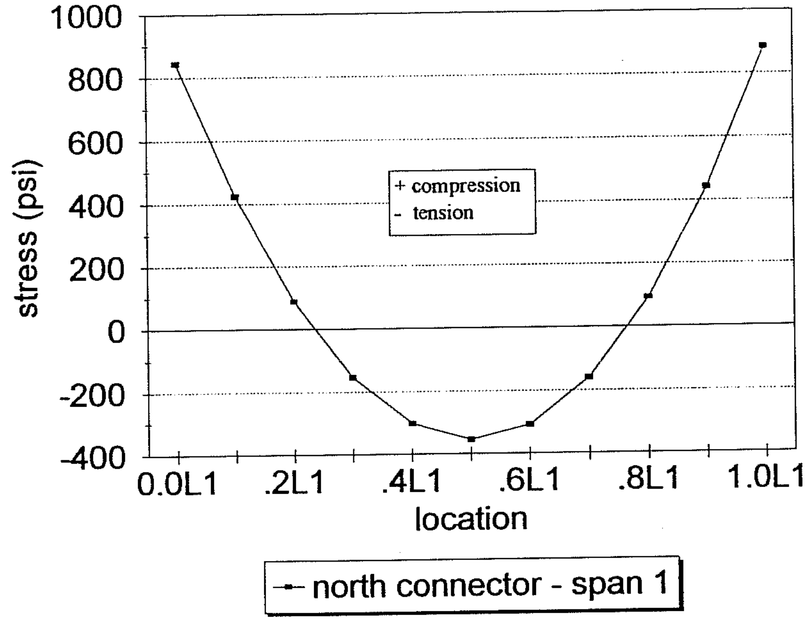

Figure 4.18 - Bottom fiber stress under "weightless" condition

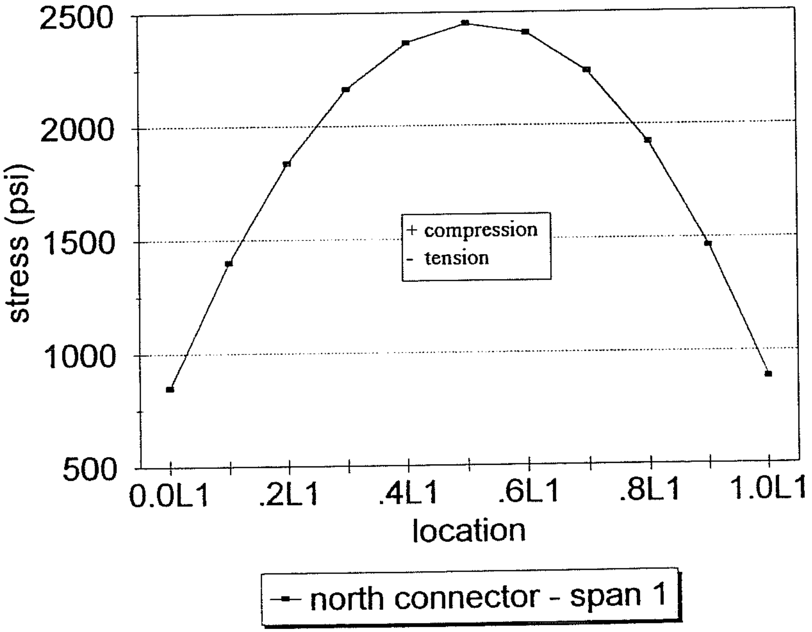

Figure 4.19 - Top fiber stress under "weightless" condition

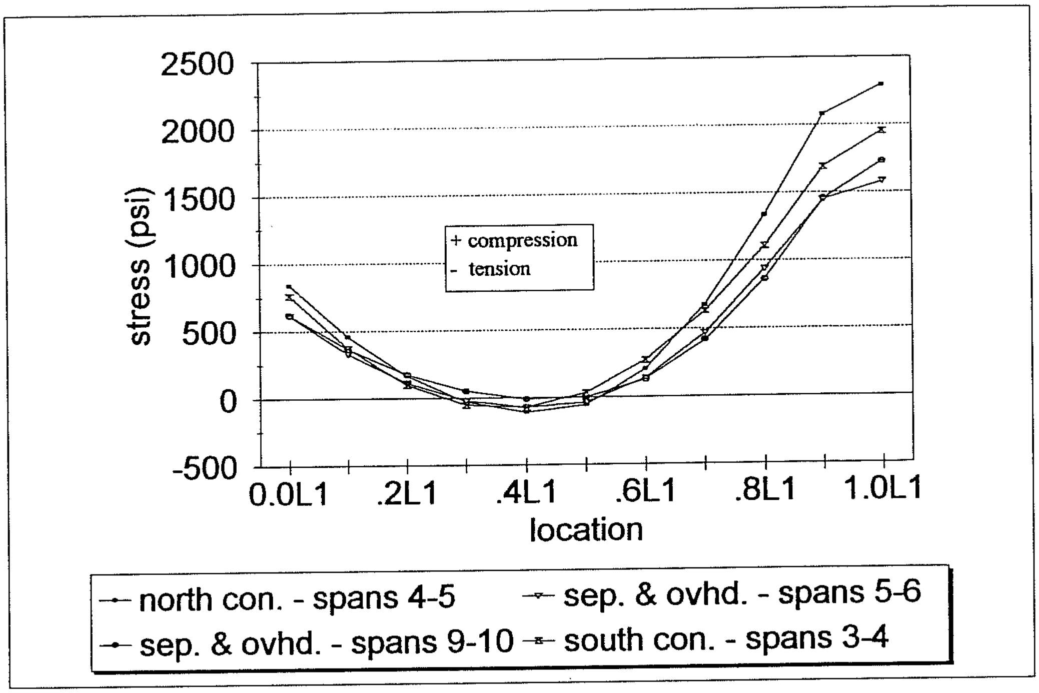

Figure 4.20 - Bottom fiber stress under "weightless" condition

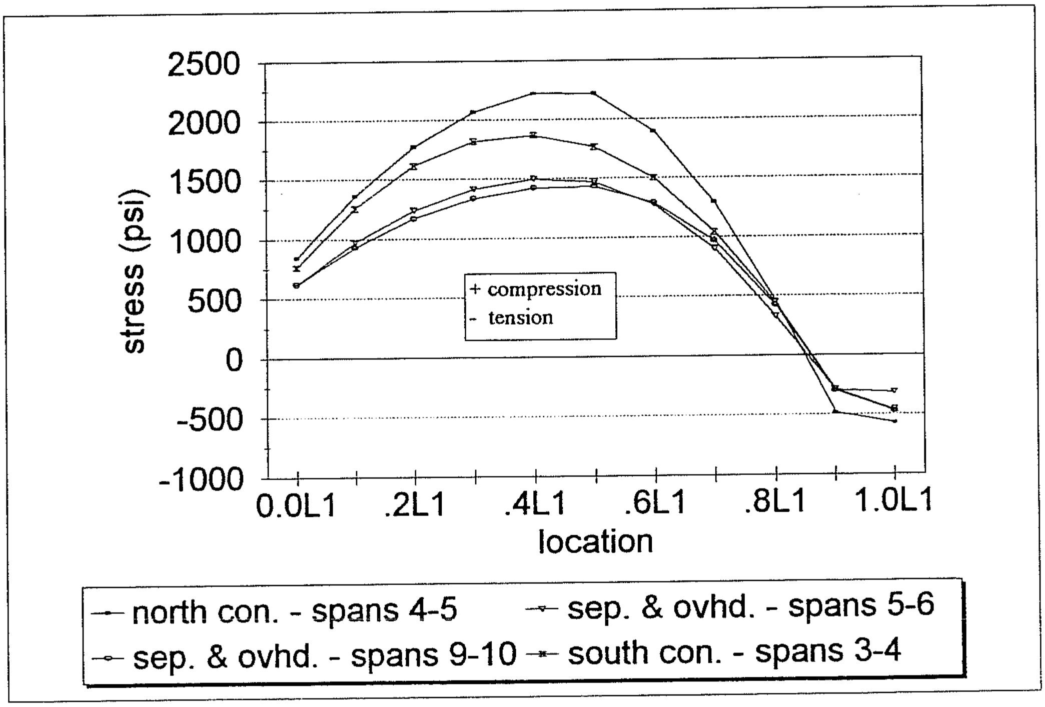

Figure 4.21 - Top fiber stress under "weightless" condition

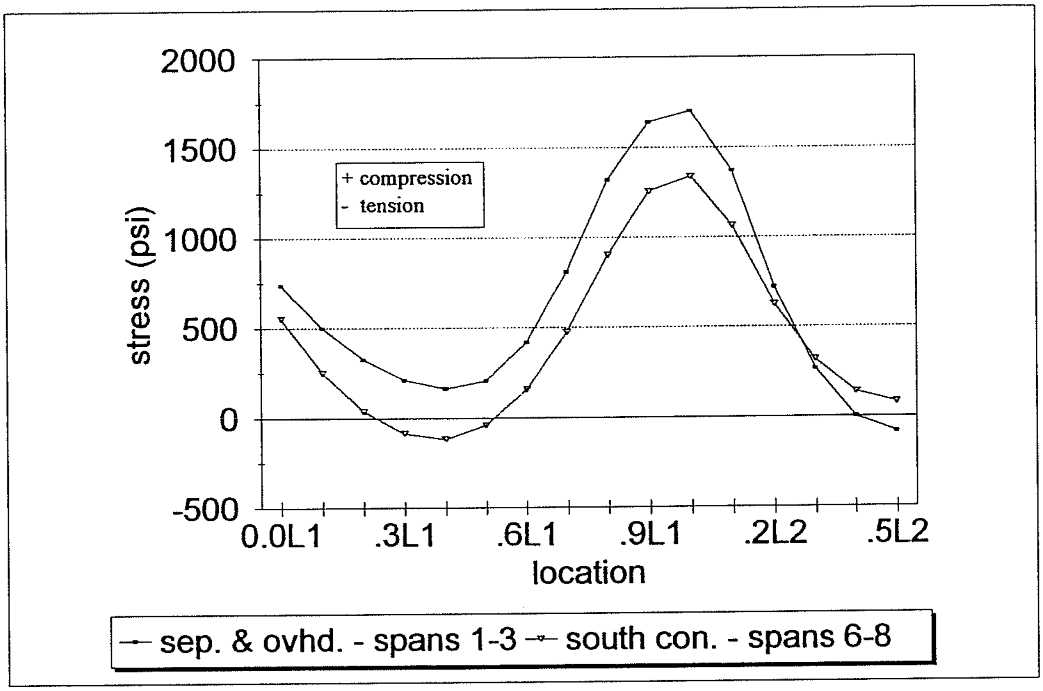

Figure 4.22 - Bottom fiber stress under "weightless" condition

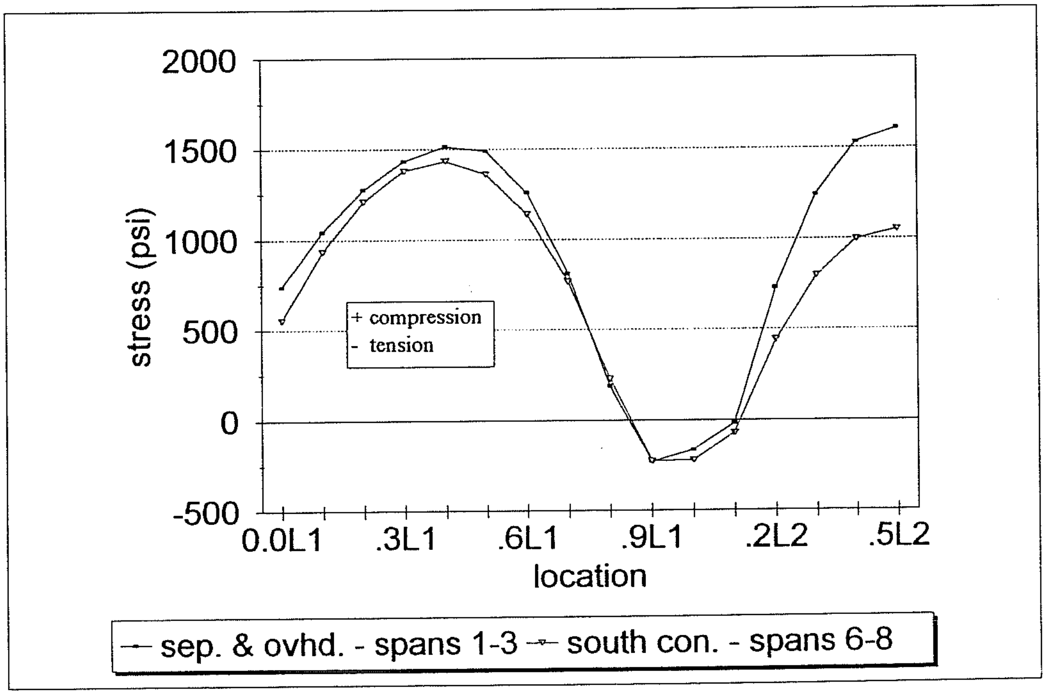

Figure 4.23 - Bottom fiber stress under "weightless" condition

negative. The AASHTO codes allows a maximum tensile stress of $0.190\sqrt{f'_c}$ in concrete.[1] With an assumed value of f'_c equal to 5 ksi, this means the allowable tensile stress is approximately 424 psi. The specified values of f'_c and the allowable tensile stress for each of the bridges is are shown in Table 4.6.

Table 4.6 - Maximum Allowable Tensile Stresses

bridge	spans	specified f'_c (ksi)	allowable tensile stress (psi)	tensile stress (psi)
north connector	1	4.5	402	355
north connector	4-5	3.6	360	640*
separation & overhead	1-3	3.5	355	284
separation & overhead	5-6	3.5	355	373*
separation & overhead	9-10	3.5	355	531*
south connector	3-4	4.0	379	523*
south connector	6-8	3.5	355	273

* exceeds allowable tensile stress

According to the calculations, the allowable tensile stress would be exceeded once in each of the north and south connectors and twice in the separation and overhead if these spans were weightless from the assumed 1g upward vertical acceleration. In all three cases the tensile stress exceeded the allowable tensile stress in the bottom fiber at the pier.

There are two reasons why these tensile stresses would probably not cause serious problems. The first is that the stresses listed above are instantaneous. The cracking mechanism probably would not be able to start in such a short amount of time since rapid loading rates generally result in higher levels of cracking stress. Second, these box girders contain continuous non-prestressed reinforcement so that any tensile cracks which did form could be controlled by the Grade 60 steel. Maximum compressive stresses are on the order of $0.4f'_c$ to $0.5f'_c$. These stress levels do not present a serious problem.

Also of interest is the question of how much of the nominal dead load is balanced by the prestress moment in these bridges along their spans. Figures 4.24 through 4.26 show the results of a study on typical single and multiple span bridges. As can be seen from Figure 4.24, the prestress force balances approximately two-thirds of the dead load moment in the single span bridge, which is what is generally assumed. In the two-span bridges, the variance is greater than for the single span bridges. In the first quarter of the beam 60%-80% of the dead load is balanced, but over the last three-quarters of the beam, closer to 80%-100% of the dead load moment is balanced. The spike in the separation and overhead frame 3 curve can be attributed to the fact that the dead load moment is very low at this point. This is approximately where the moment changes from positive to negative. Any assumptions that are slightly off, especially in regards to the dead load for this bridge, are magnified at this point. Figure 4.26 shows that for a three-span bridge, the prestress moment generally balances approximately 90%-95% of the dead load moment. The spikes in both curves can again be attributed to the fact that the dead

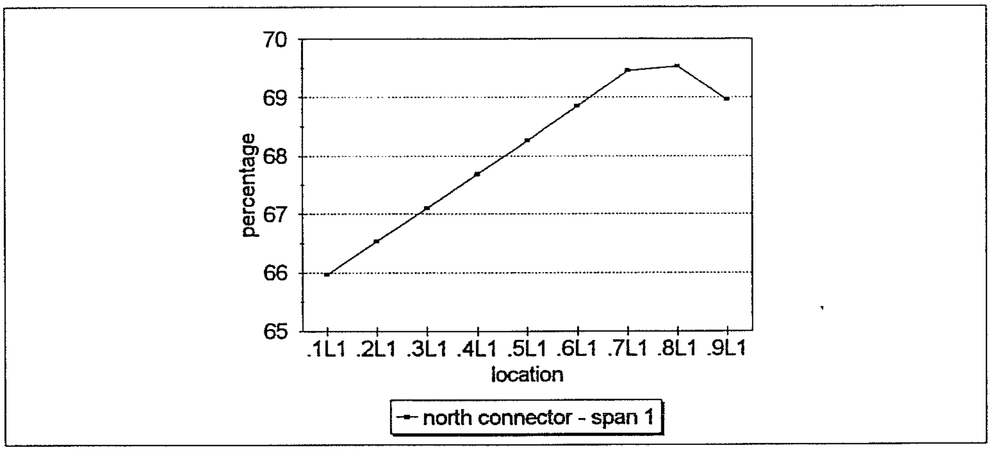

Figure 4.24 - Percentage of dead load moment balanced

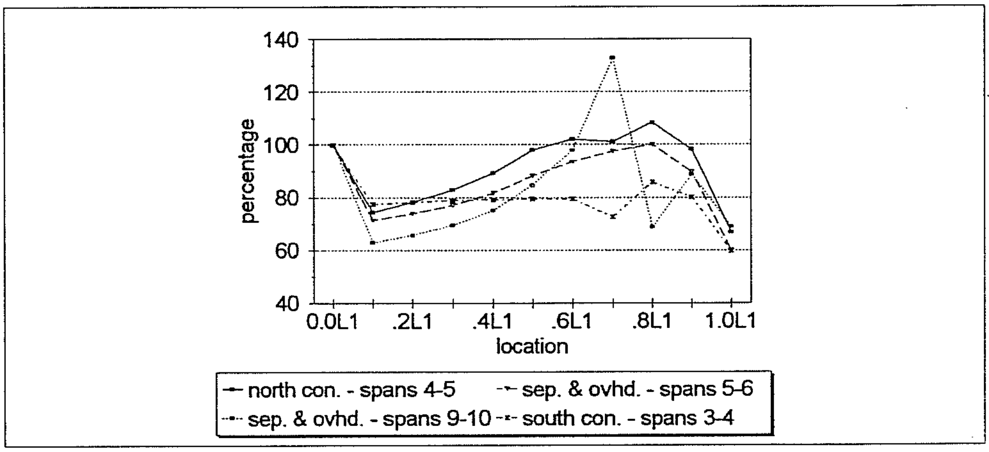

Figure 4.25 - Percentage of dead load moment balanced

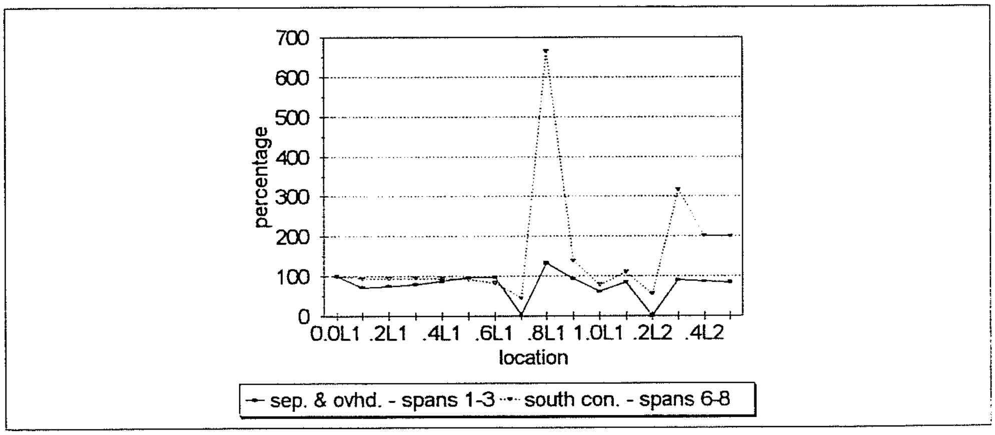

Figure 4.26 - Percentage of dead load moment balanced

load moments are very low at these points.

These results show that the "load balancing" method of design used for these typical bridges is very effective. In the multiple span cases, the dead load balances just under 100% of the dead load. This is an effective method of design, since the concrete will be under compressive stresses. The addition of live load will not cause excessive tension stresses.

4.5.4 Relationship to Parametric Studies

The stresses calculated in the previous section were the stresses with an upward vertical acceleration in the deck of 1g. This is effectively a weightless condition where the only stresses are due to the prestressing forces. However, this may not necessarily be the worst case scenario. In Sections 4.2 and 4.3, there were amplification factors that exceeded 3.0. While the computer model used is a linear elastic model and the results do not represent the true behavior of the bridge, these numbers show the importance of vertical acceleration. If the vertical acceleration of 0.56g from the Sylmar Hospital data is amplified by a factor of 3.0, this leads to accelerations in the deck of 1.7g upward. This is a net of 0.7g vertical acceleration acting upward. The dead load moment would then act in the reverse direction and the tension stresses would greatly increase. However, as mentioned previously, since these accelerations are instantaneous and there is additional Grade 60 reinforcement, this phenomenon should not cause considerable tension cracking. (See calculation in Appendix C.)

CHAPTER 5

ANALYSIS OF SUBSTRUCTURE

5.1 Introduction

Vertical accelerations may play an important role in the moment capacity of columns. The reduction of the axial force on the column due to a vertical acceleration can cause a lower moment capacity for the column. This can be seen on the moment interaction curve (Figure 5.1) as one moves from the balance point (A) to the pure moment point (A').

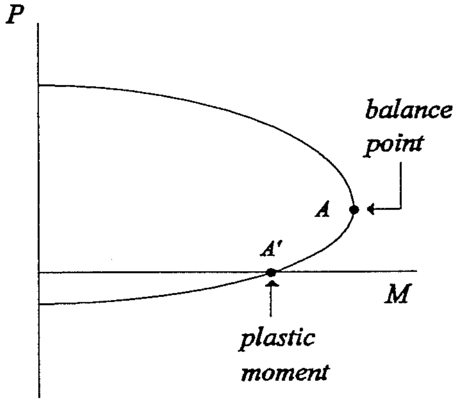

Figure 5.1 - Moment interaction diagram

For this phase of the study, the three bridges were subjected to three different earthquake inputs and the resulting moments were computed using the program BRIDGEQUAKE.[24] The three earthquakes that were input were the Sylmar Hospital records, the synthetic earthquake from Lamont-Doherty Observatory

(NCEER), and the UBC/AASHTO response spectrum. The resulting moments were compared to the moment capacities for each of the piers.

5.2 Column Interaction Diagrams

In order to account for the effects of the varying axial loads present on the columns due to the vertical accelerations, the column interaction curves were plotted for each of the piers. The interaction curves were computed assuming a maximum concrete compressive strain, ϵ_{cu}, of .003. An interaction curve example calculation is given in Appendix E. The interaction diagrams were drawn for the each of the piers. The moment was computed at both the top and the bottom of the piers. For the separation and overhead structure, since the pier is flared, the interaction diagrams were computed for the top of the flare and for the base of the flare. From the CALTRANS *Memo to Designers* Section 20-4 dated March 1995,[11] the flexural moment demand ratio, μ_F, is defined as:

$$\mu_F = \frac{M_{EQ} + M_D}{M_n} \tag{5.1}$$

where M_{EQ} is the moment due to the earthquake, M_D is the dead load moment, and M_n is the nominal moment at the appropriate level of axial force. A plastic hinge is assumed to form at any location where the moment ratio μ_F is greater than 1.5. For each of the piers in the three bridges, this ratio was calculated.

5.3 Sylmar Hospital Earthquake Results

The Sylmar Hospital records that were described in Chapter 1 and Chapter 3 were used as the ground motion input for the analysis of all three bridges. The total moment versus the axial load is plotted in each of Figures 5.2 through 5.15 with the results of the analysis superimposed with the column interaction diagrams.

5.3.1 North Connector (Ramp M)

The values that are of concern are those with very small axial loads which are near the plastic moment values. As can be seen from Figures 5.2 through 5.5 the highest axial loads on the piers are well below their axial capacity. In fact, all of the axial force values are well below the balance point. Table 5.1 gives the maximum in-plane moments and the flexural moment demand ratio in columns where μ_F exceeded 1.5.

Table 5.1 - In-plane Moment Results for North Connector

pier number	location	maximum moment from analysis (ft-kips)	nominal moment capacity (ft-kips)	moment demand ratio
3	top	26430	15977	1.65
7	top	33270	18529	1.80
9	top	31370	15291	2.05

Table 5.2 gives the same type of results for the out-of-plane bending moments.

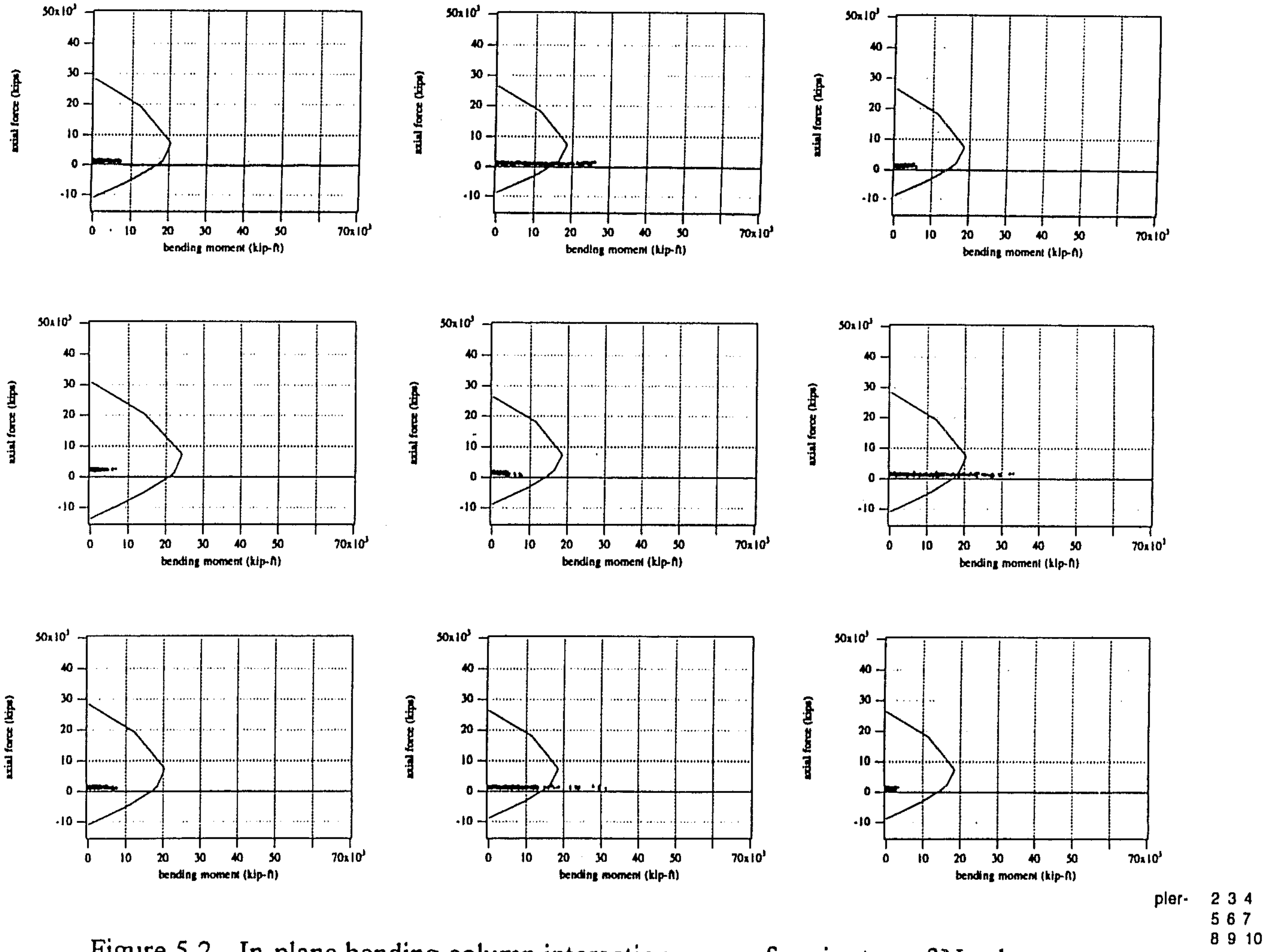

Figure 5.2 - In-plane bending column interaction curves for pier top of North Connector piers using Sylmar Hospital earthquake record

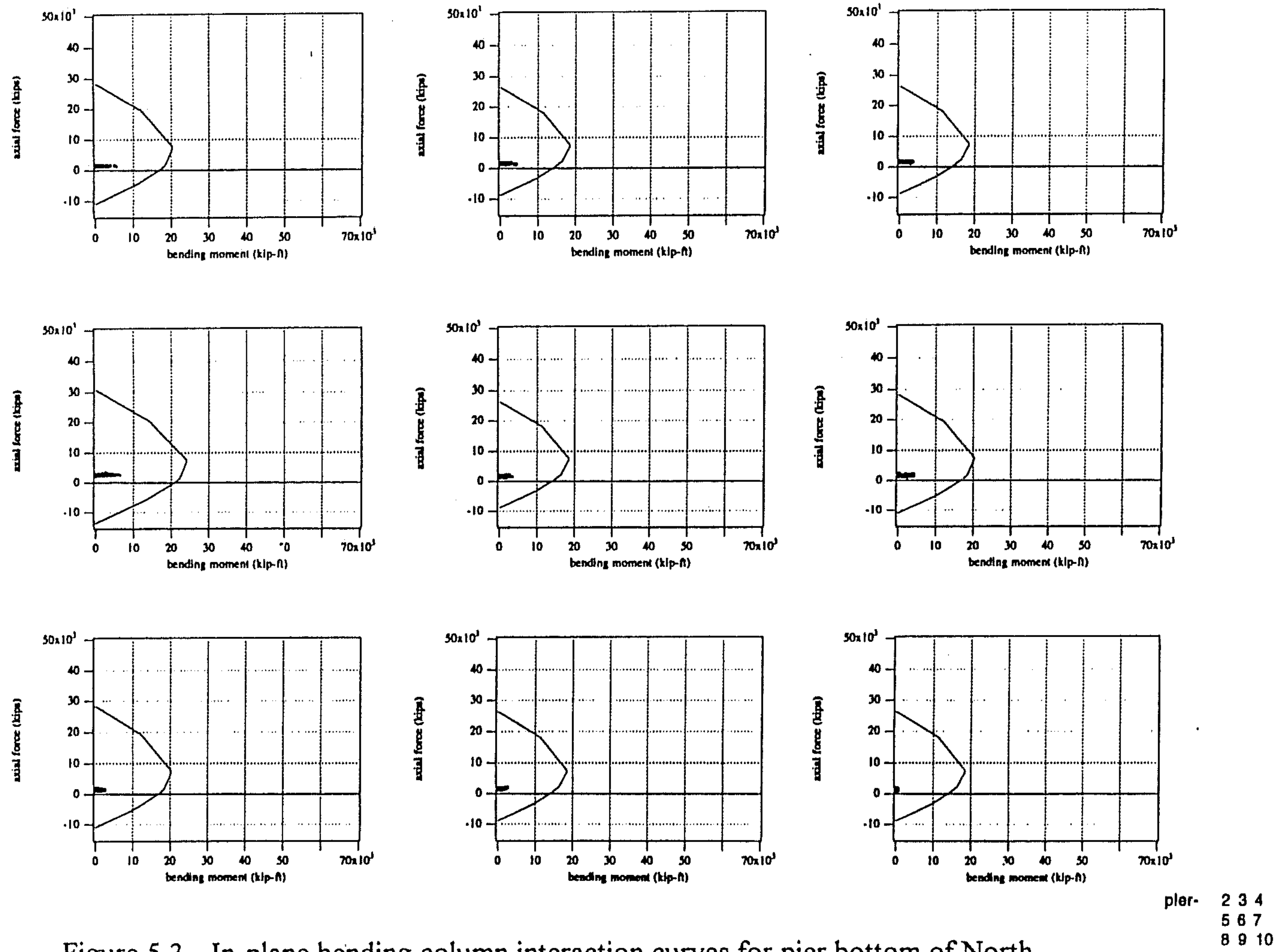

Figure 5.3 - In-plane bending column interaction curves for pier bottom of North Connector piers using Sylmar Hospital earthquake record

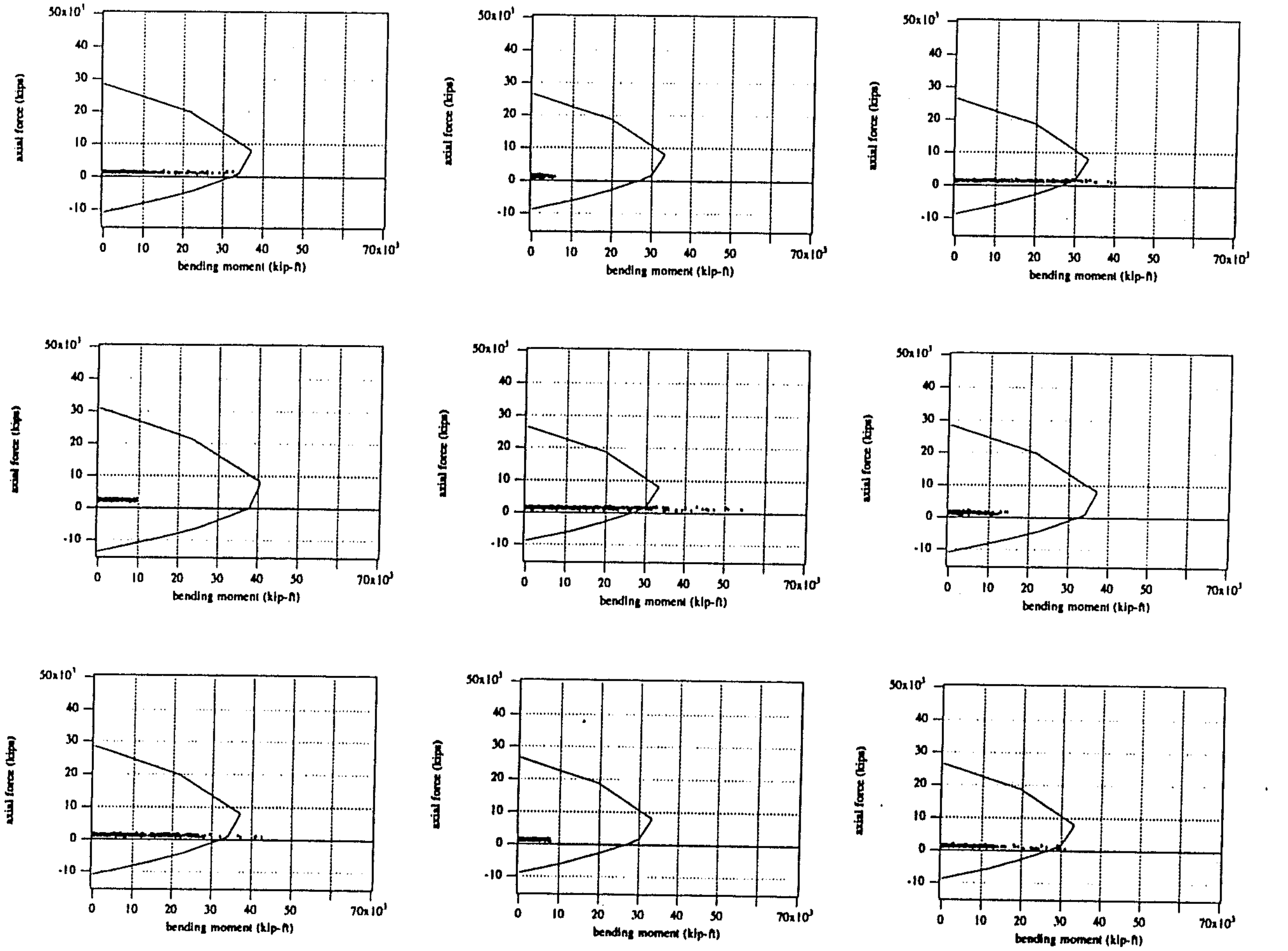

Figure 5.4 - Out-of-plane bending column interaction curves for pier top of North Connector piers using Sylmar Hospital earthquake record

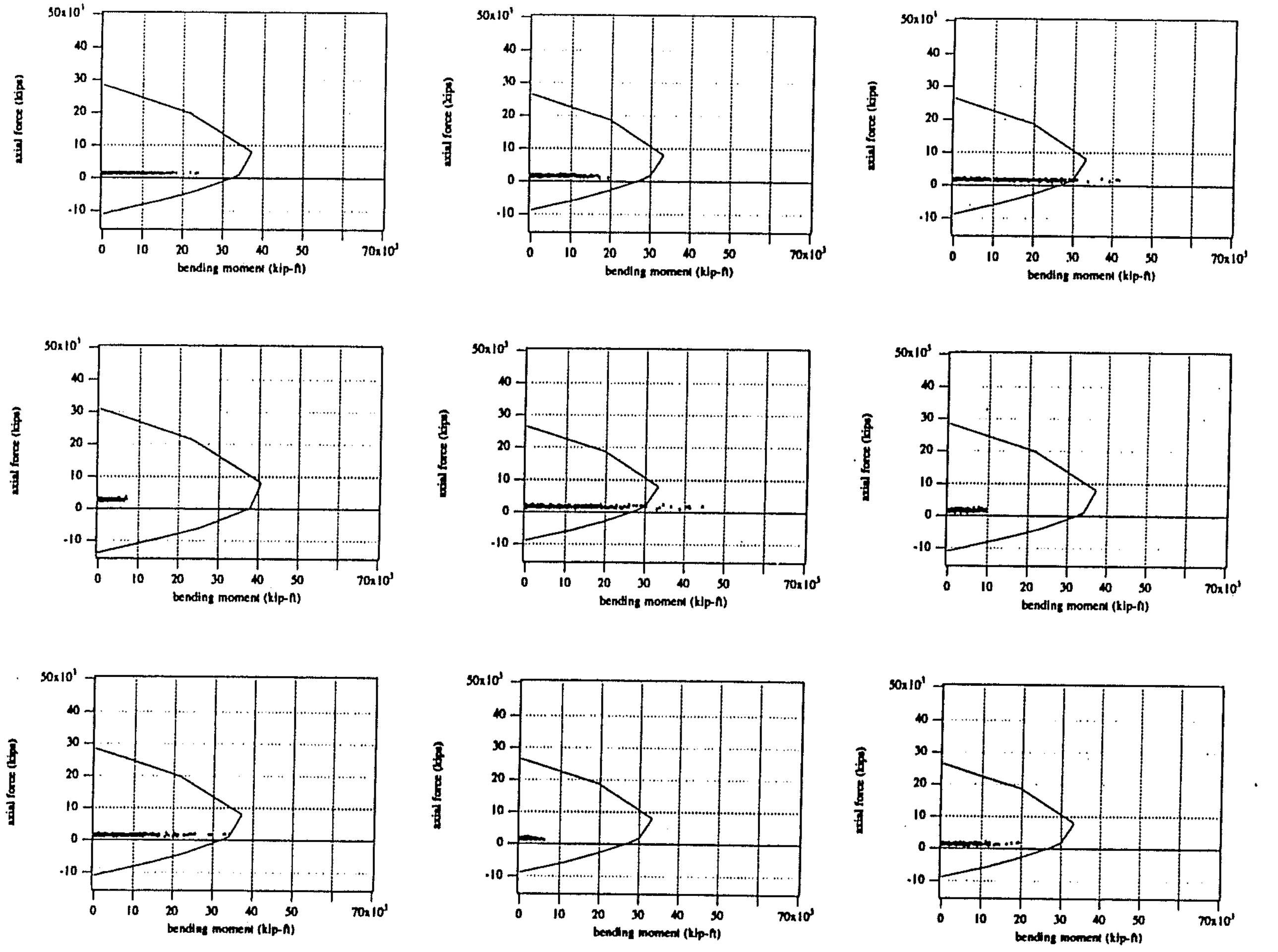

Figure 5.5 - Out-of-plane bending column interaction curves for pier bottom of North Connector piers using Sylmar Hospital earthquake record

Table 5.2 - Out-of-plane Moment Results for North Connector

pier number	location	maximum moment from analysis (ft-kips)	nominal moment capacity (ft-kips)	moment demand ratio
6	top	54250	29371	1.87

As can be seen from the results, piers #3, 6, 7, and 9 of the north connector were the piers where plastic hinges would form. In the out-of-plane direction, only pier #6 developed a hinge, whereas piers #3, 7, and 9 had hinges form in the in-plane direction. In all cases, the plastic hinges developed at the top of the pier.

5.3.2 Separation and Overhead (Pier C)

As can be seen from Figures 5.6 through 5.11, the highest axial loads on the piers were well below their balance point axial capacity. The flexural moment demand ratios were evaluated not only at the top and bottom of the piers (flare top), but also at the portion of the columns with a constant cross section (flare bottom) in accordance with recommendations from CALTRANS[19]. It is important for the evaluation of this type of bridge (flared column) to look at the bottom of the flare as well. The moments may be smaller than at the top of the pier, but the moment capacity, particularly in the transverse direction, is greatly reduced. While many of the piers experienced inelastic behavior, according to the CALTRANS flexural moment demand ratio, none of the piers developed plastic hinges.

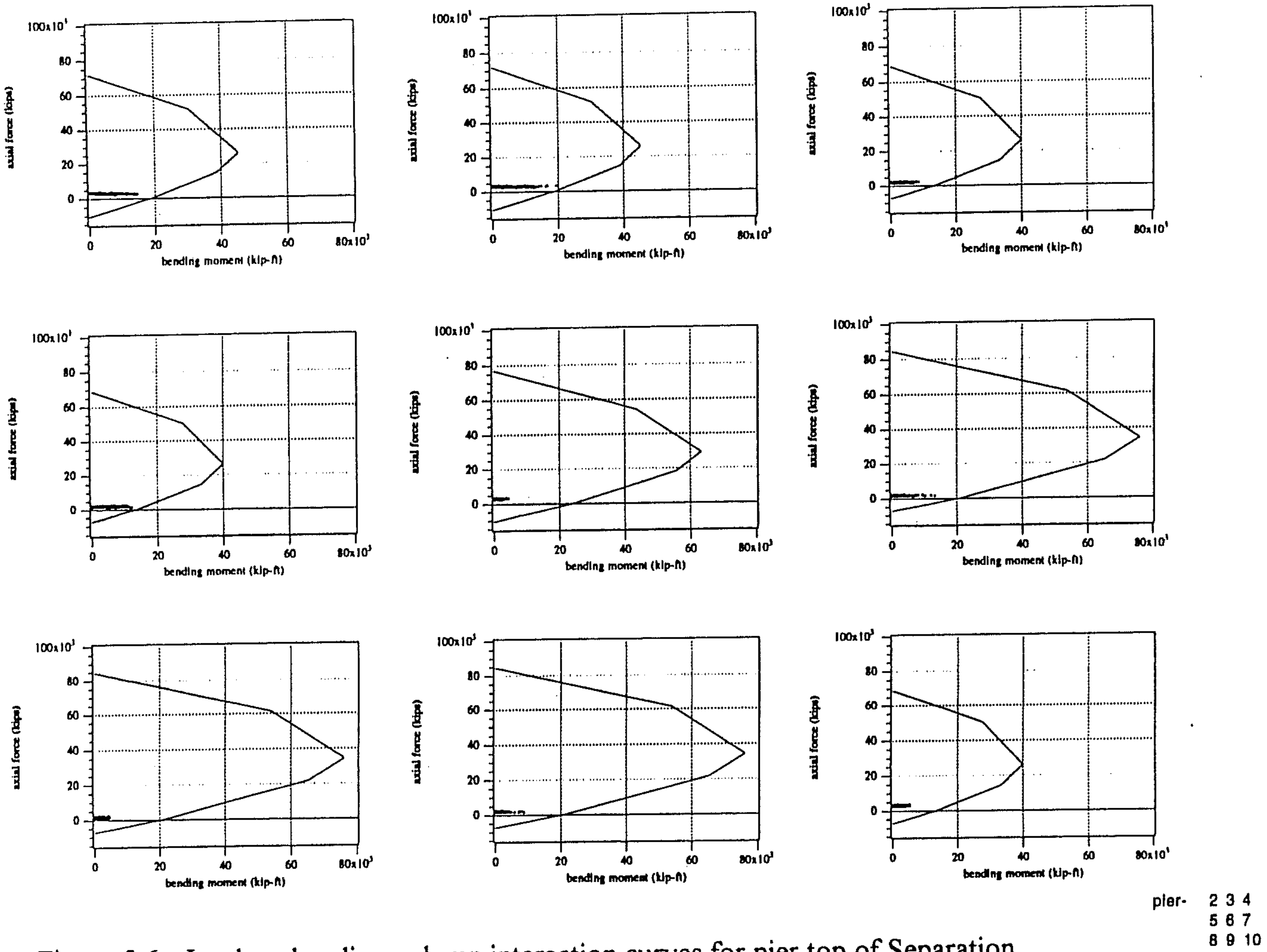

Figure 5.6 - In-plane bending column interaction curves for pier top of Separation and Overhead piers using Sylmar Hospital earthquake record

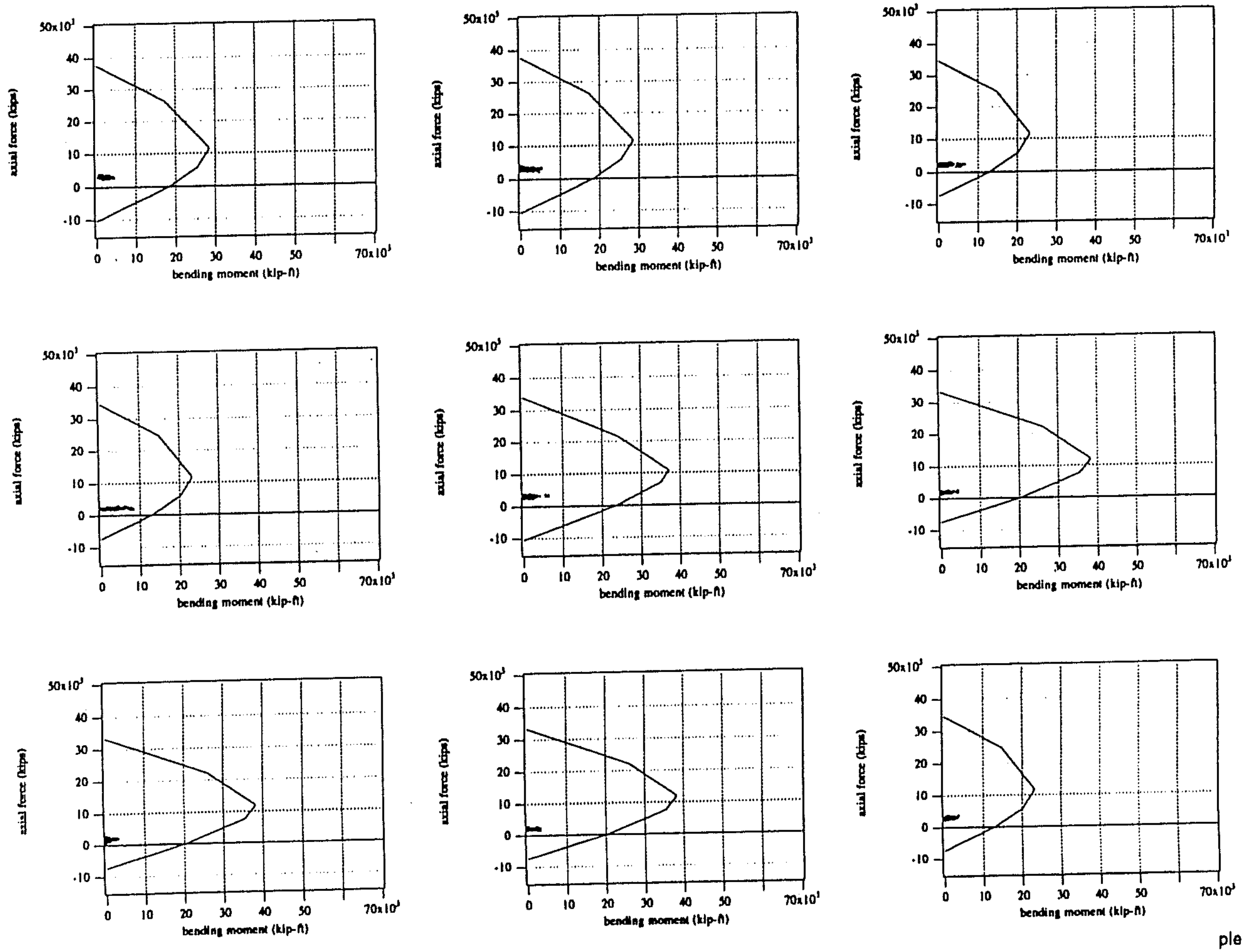

pier- 2 3 4
5 6 7
8 9 10

Figure 5.7 - In-plane bending column interaction curves for flare bottom of Separation and Overhead piers using Sylmar Hospital earthquake record

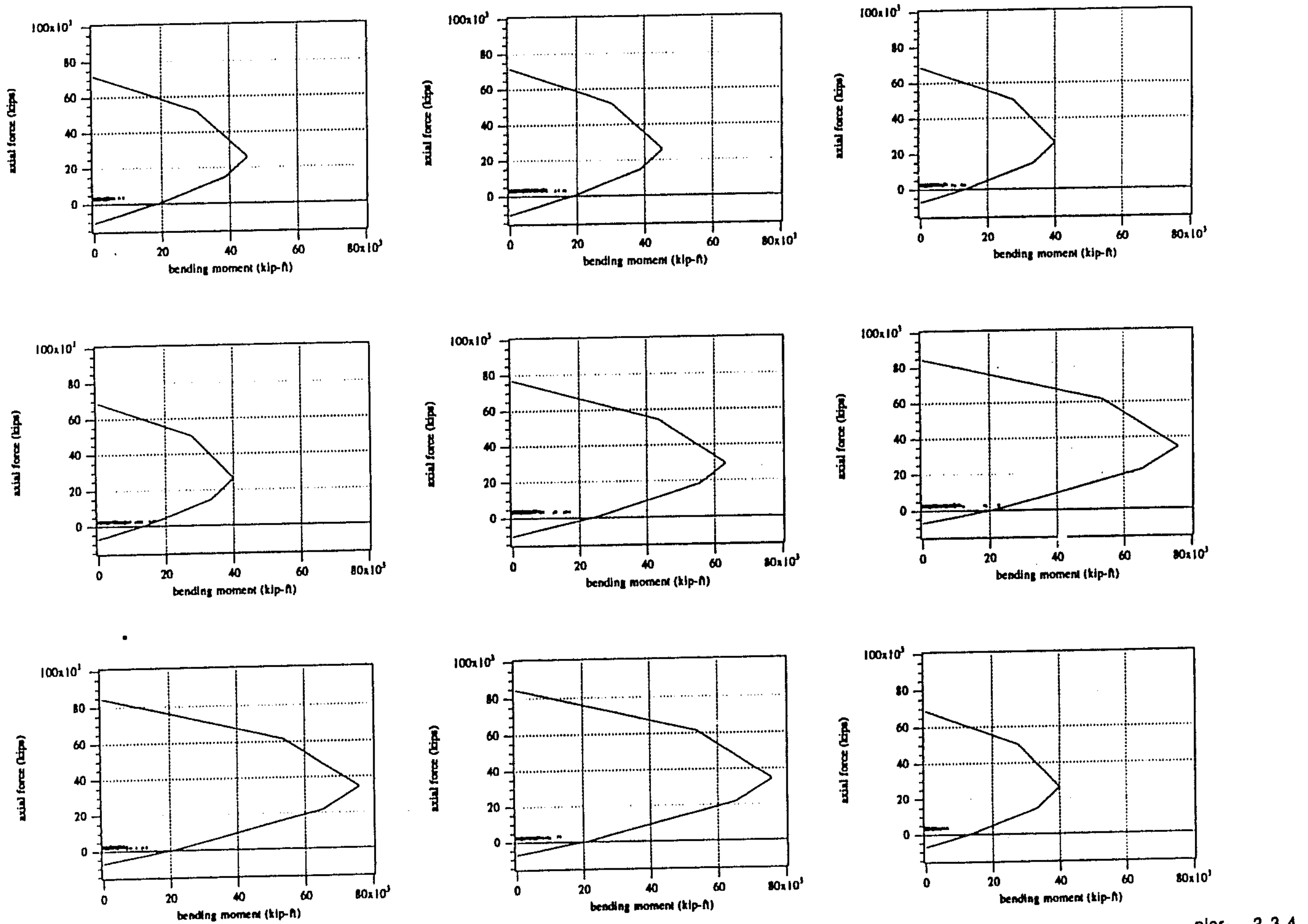

Figure 5.8 - In-plane bending column interaction curves for pier bottom of Separation and Overhead piers using Sylmar Hospital earthquake record

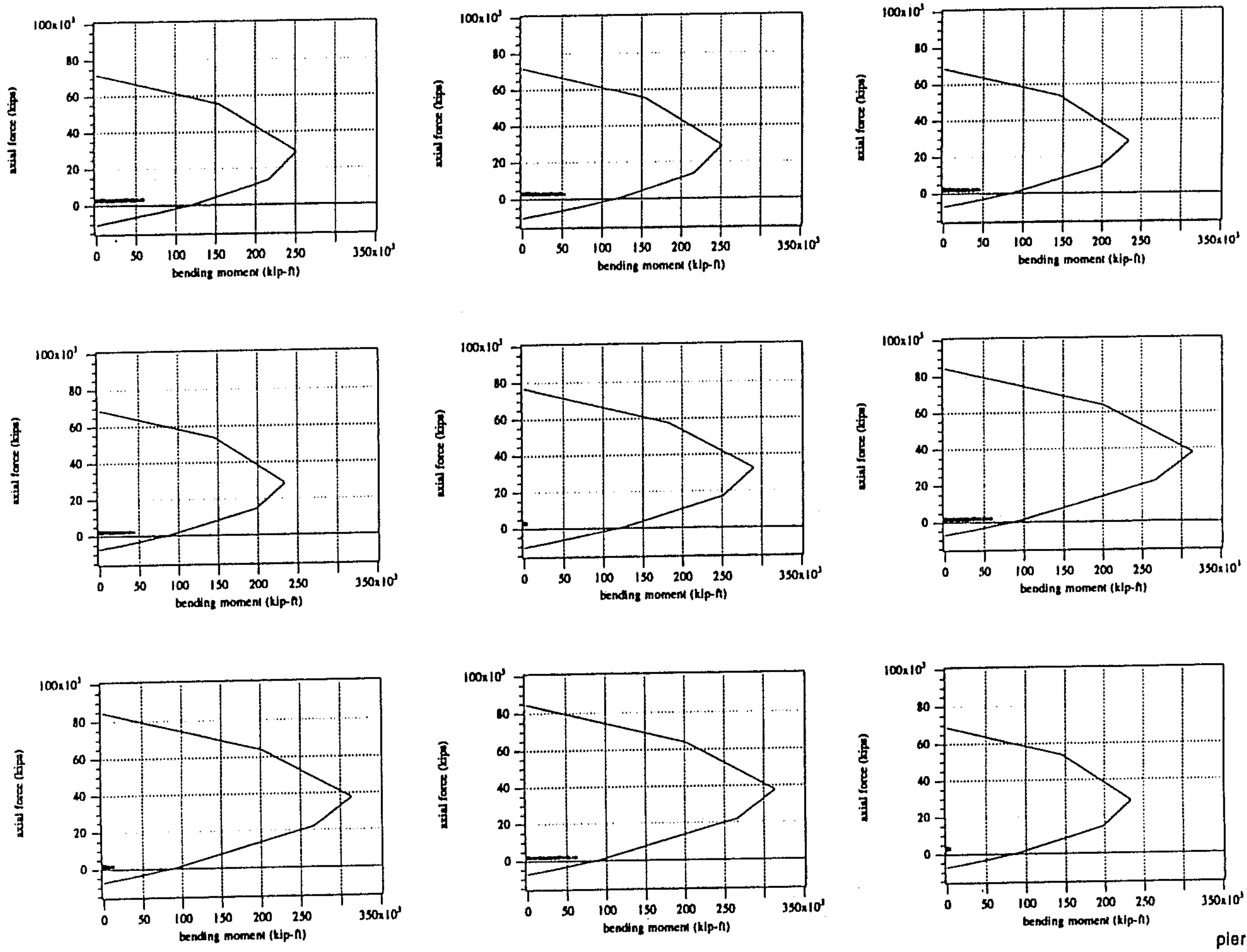

Figure 5.9 - Out-of-plane bending column interaction curves for pier top of Separation and Overhead piers using Sylmar Hospital earthquake record

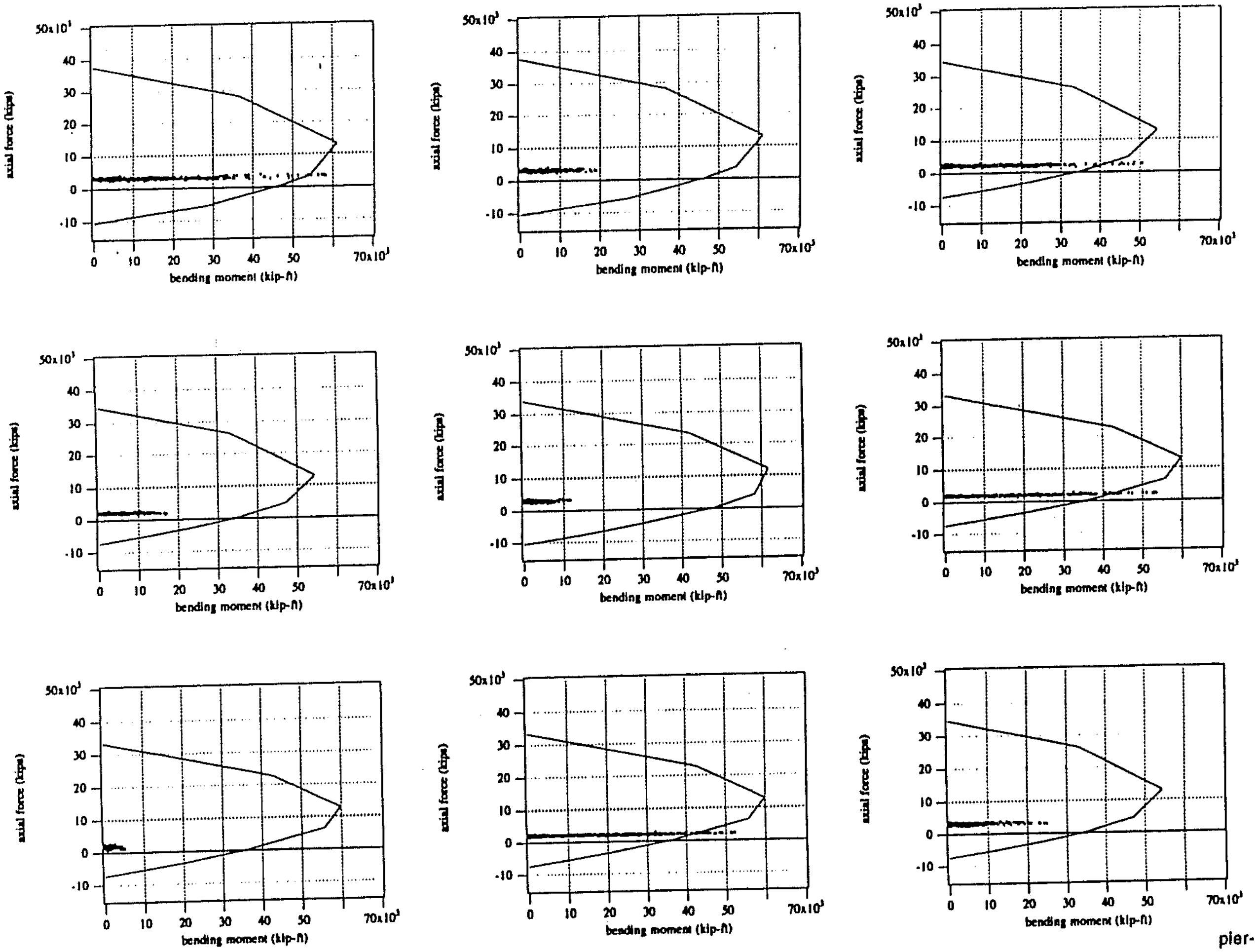

Figure 5.10 - Out-of-plane bending column interaction curves for flare bottom of Separation and Overhead piers using Sylmar Hospital earthquake record

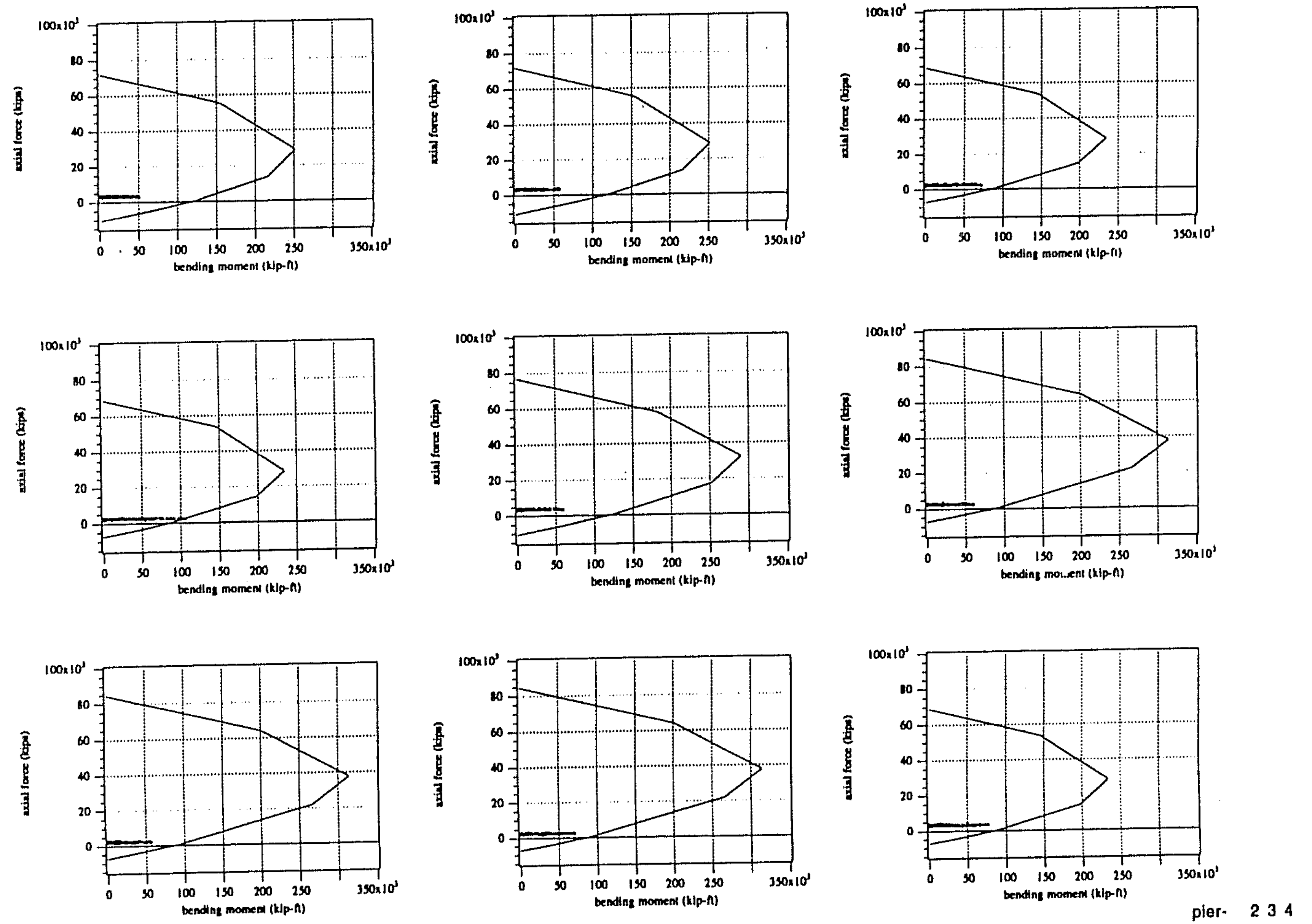

Figure 5.11 - Out-of-plane bending column interaction curves for pier bottom of Separation and Overhead piers using Sylmar Hospital earthquake record

5.3.3 South Connector Overcrossing (Ramp L)

The south connector follows the pattern of the other two bridges as well in that according to Figures 5.12 through 5.15, the highest axial load on the piers is well below their balance point axial capacity. Again, many of the piers experienced inelastic behavior. However, according to the CALTRANS flexural moment demand ratio, none of the piers developed plastic hinges.

5.4 Artificial Earthquake Results

5.4.1 North Connector (Ramp M)

The same type of analysis was run using the artificial earthquake from Lamont-NCEER as the input instead of the Sylmar Hospital record. Figures 5.16 through 5.19 show the results for the north connector structure using the artificial earthquake input. Table 5.9 lists all of the piers that had flexural moment demand ratios of greater than 1.5 in the in-plane direction.

Table 5.3 - In-Plane Moment Results for North Connector

pier number	location	maximum moment from analysis (ft-kips)	nominal moment capacity (ft-kips)	moment demand ratio
7	top	31057	18381	1.69

No piers in the north connector had $\mu_F > 1.5$ in the out-of-plane direction. Pier #7 also developed a plastic hinge under the Sylmar Hospital record with a moment demand ration of 1.80.

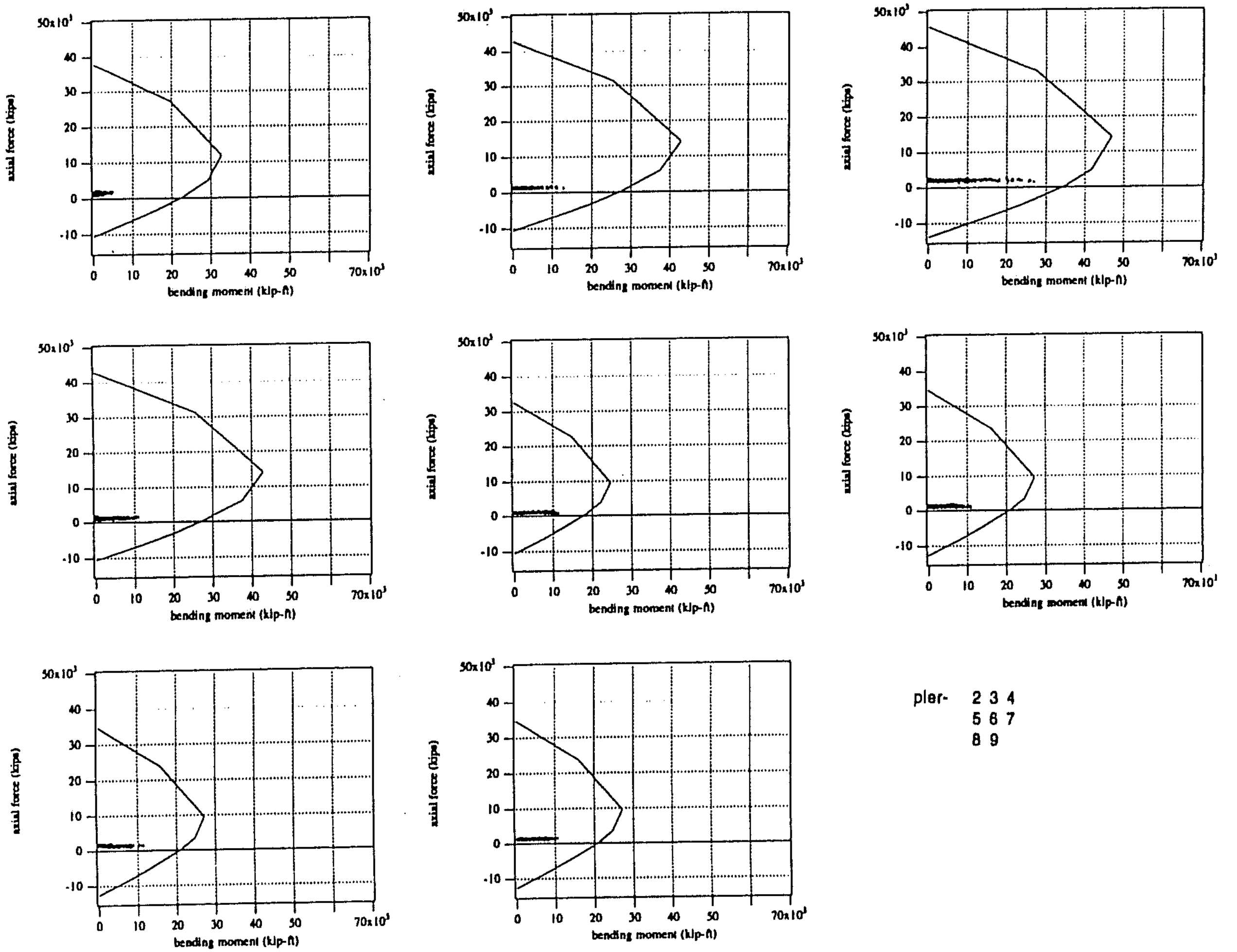

Figure 5.12 - In-plane bending column interaction curves for pier top of South Connector piers using Sylmar Hospital earthquake record

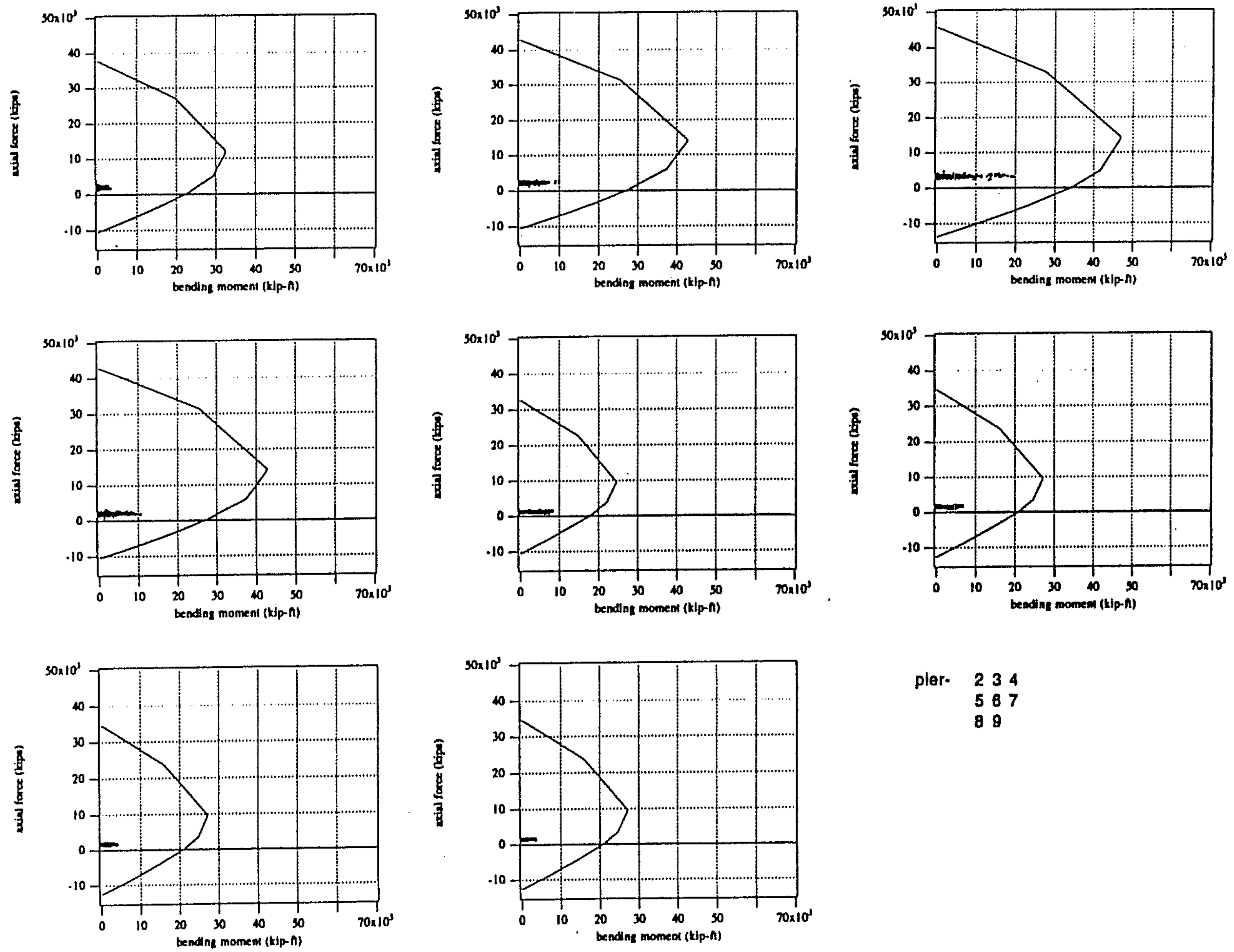

Figure 5.13 - In-plane bending column interaction curves for pier bottom of South Connector piers using Sylmar Hospital earthquake record

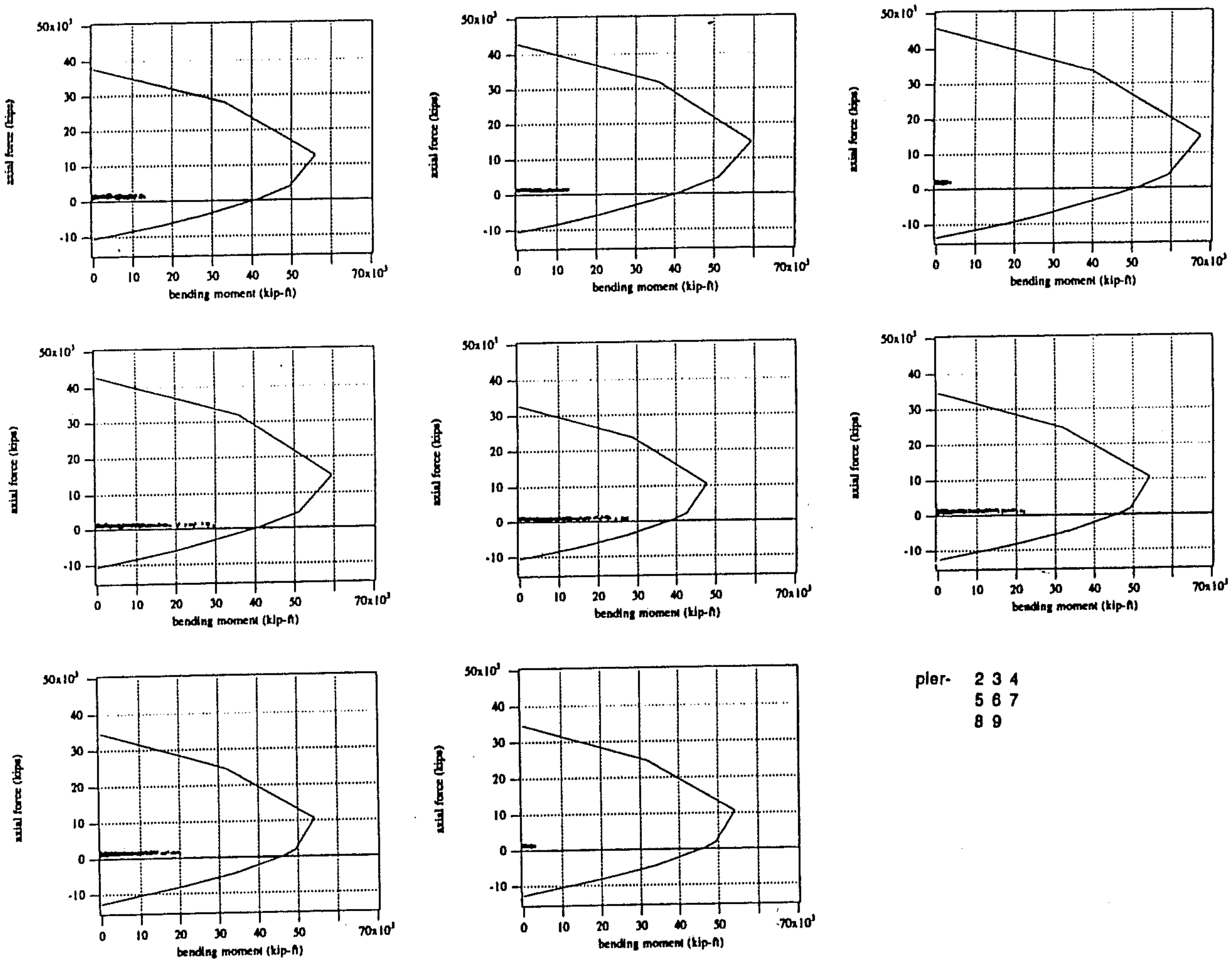

Figure 5.14 - Out-of-plane bending column interaction curves for pier top of South Connector piers using Sylmar Hospital earthquake record

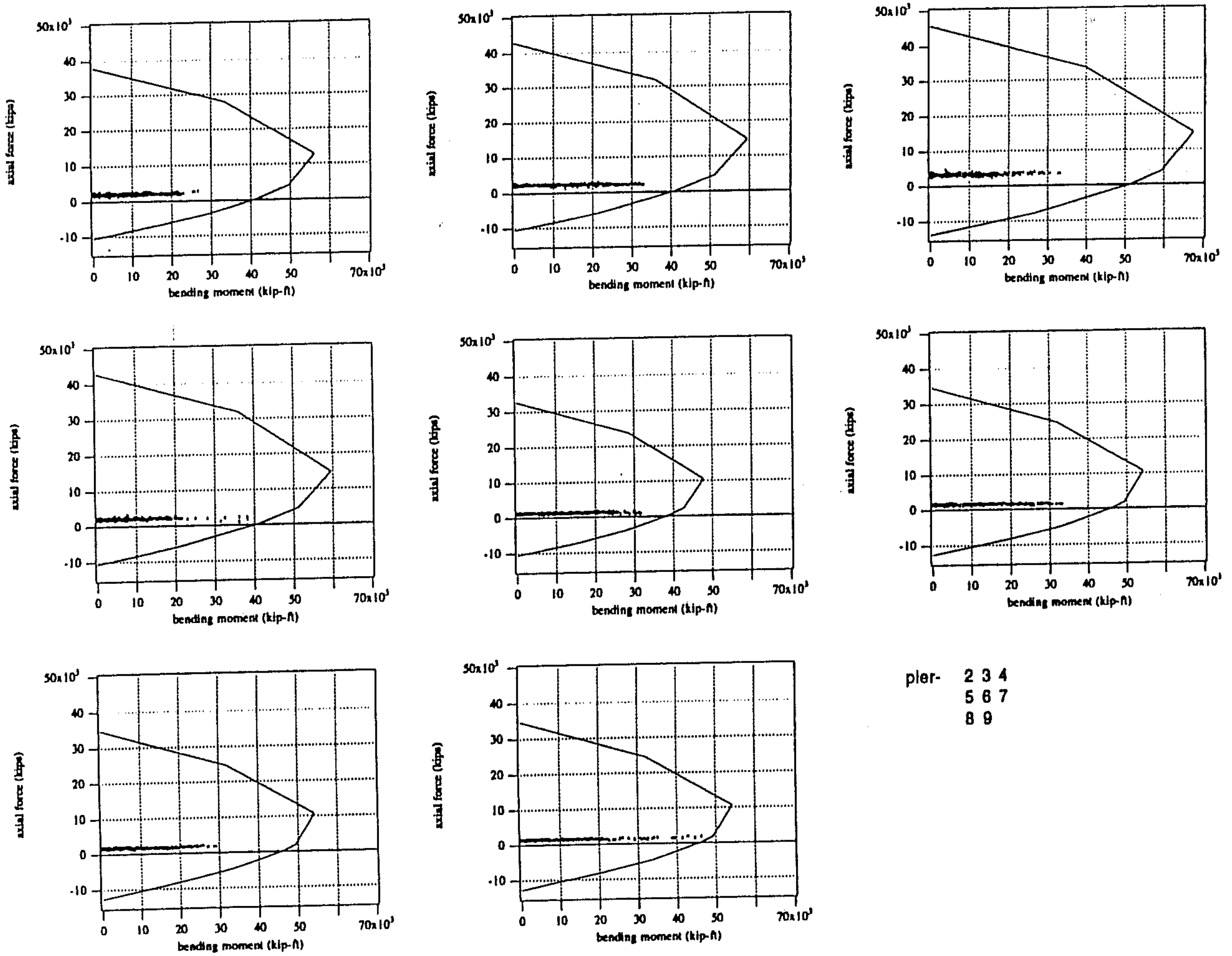

Figure 5.15 - Out-of-plane bending column interaction curves for pier bottom of South Connector piers using Sylmar Hospital earthquake record

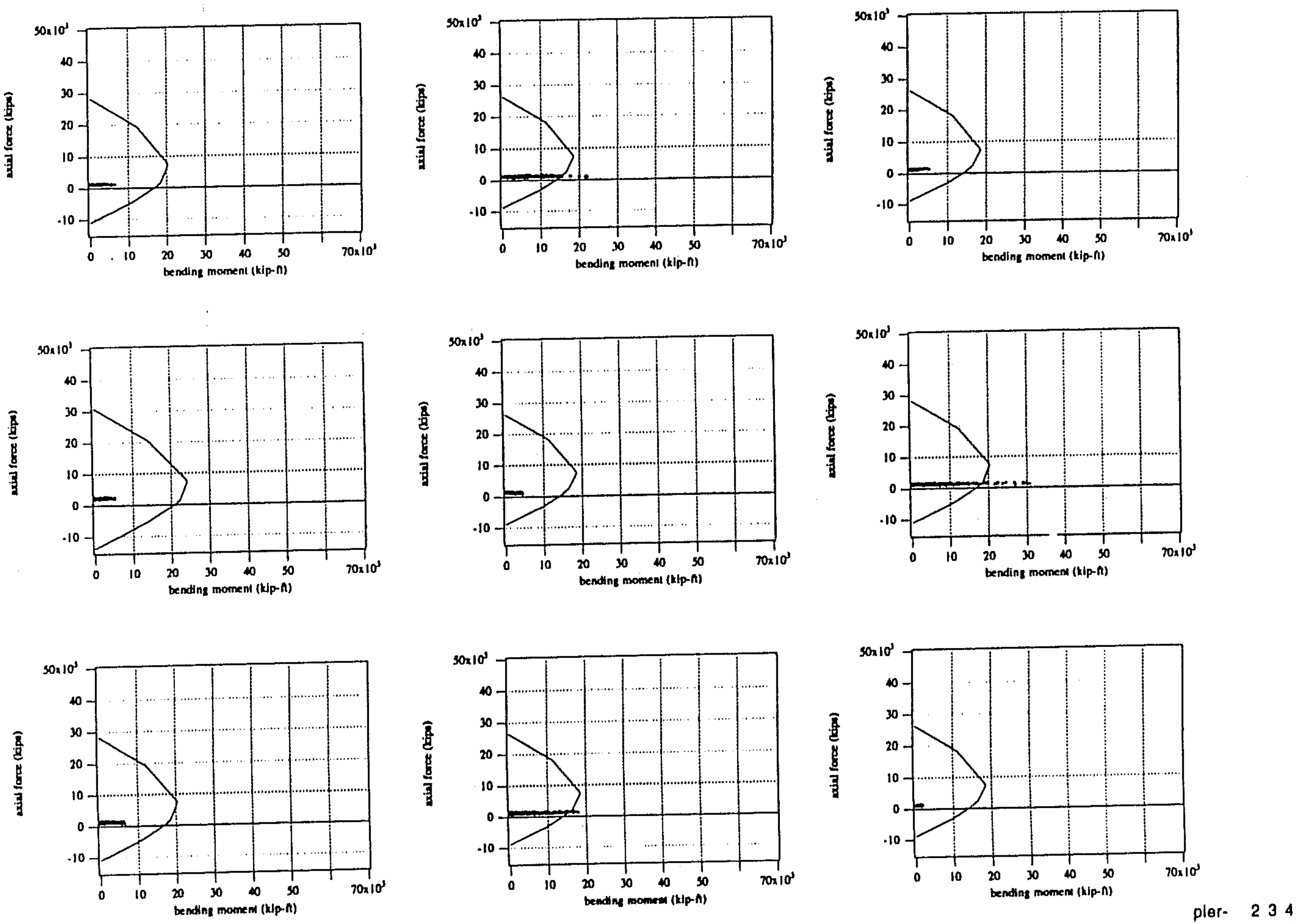

Figure 5.16 - In-plane bending column interaction curves for pier top of North Connector piers using NCEER artificial earthquake record

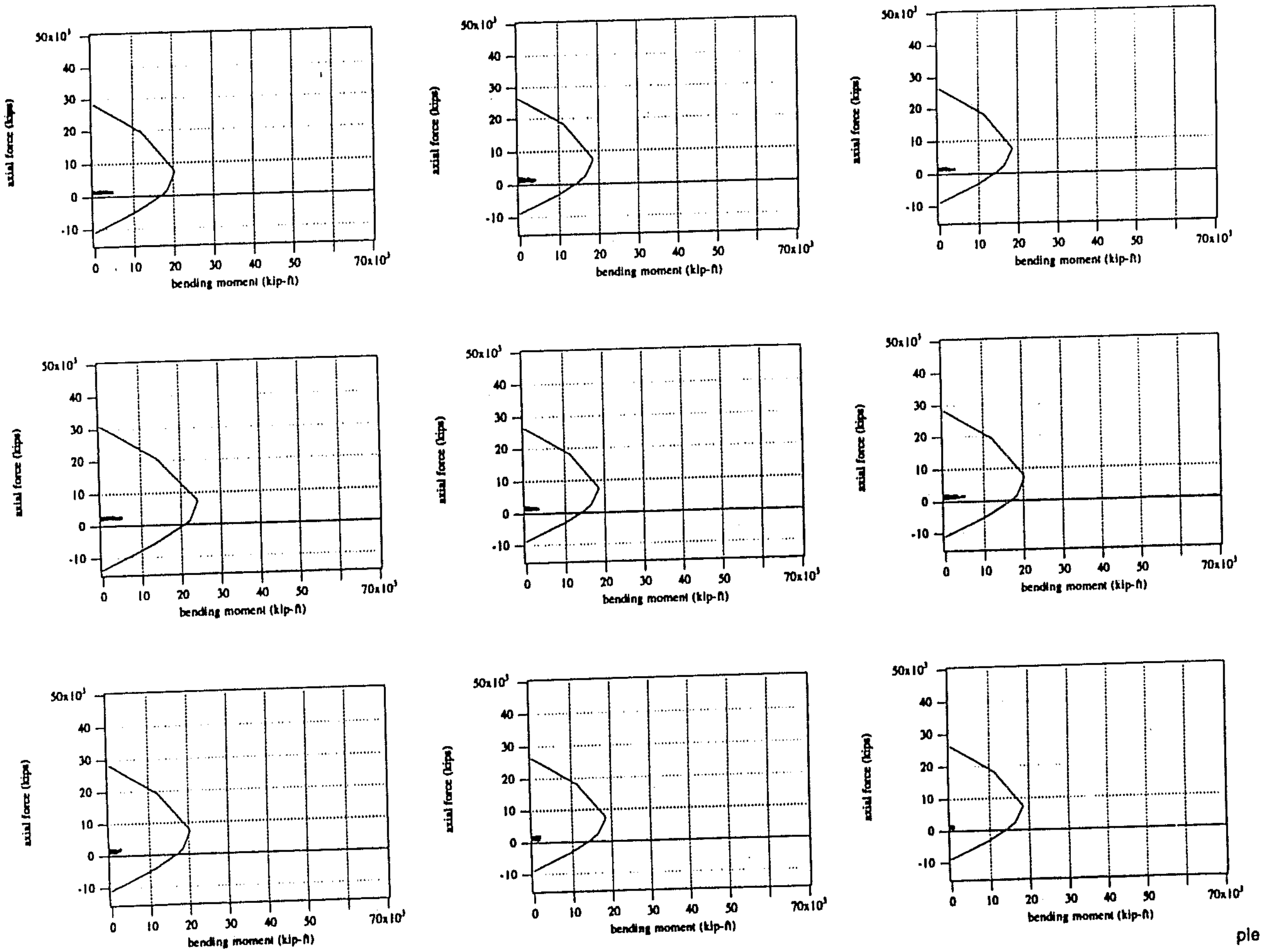

pier- 2 3 4
5 6 7
8 9 10

Figure 5.17 - In-plane bending column interaction curves for pier bottom of North Connector piers using NCEER artificial earthquake record

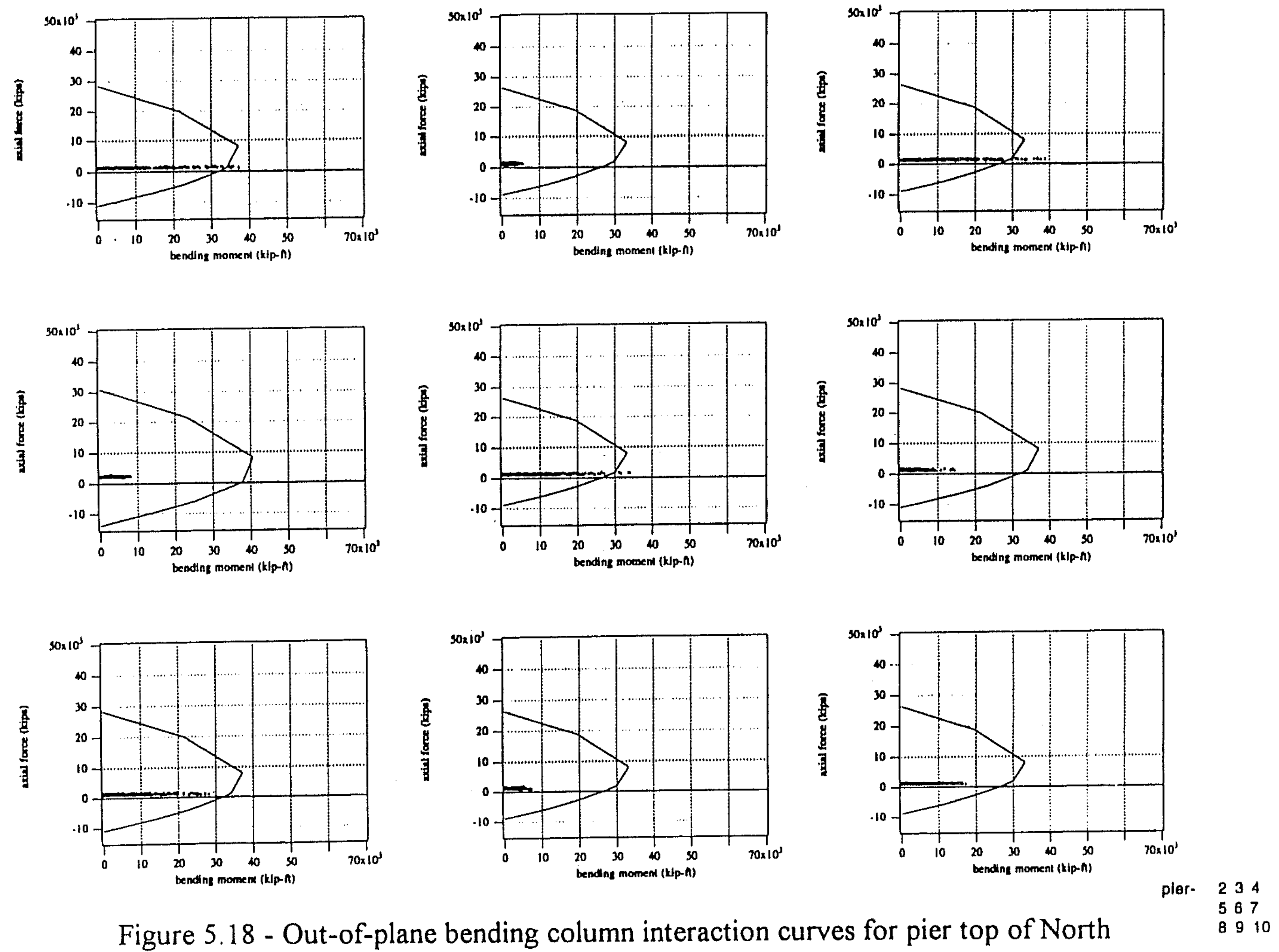

Figure 5.18 - Out-of-plane bending column interaction curves for pier top of North Connector piers using NCEER artificial earthquake record

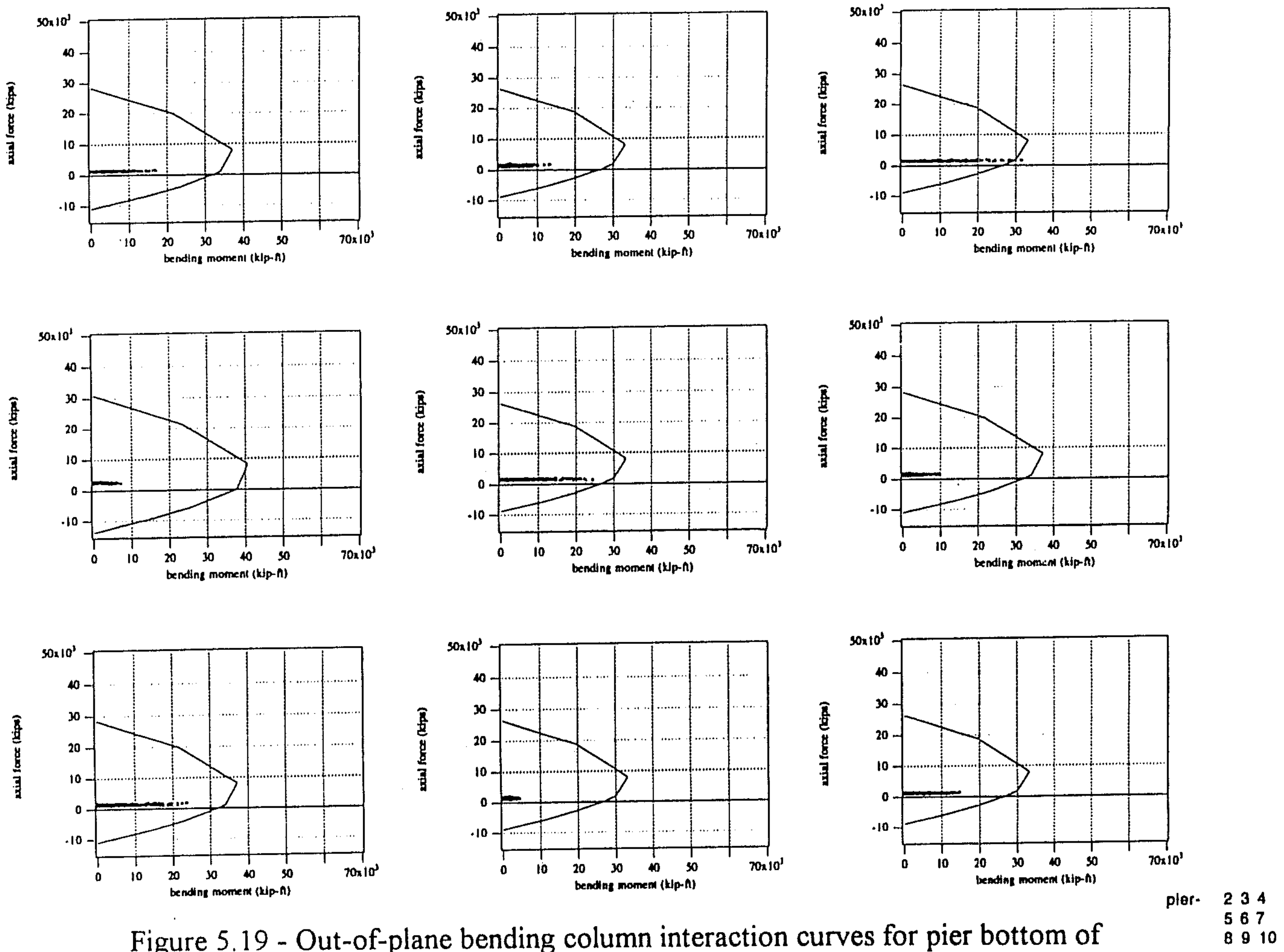

Figure 5.19 - Out-of-plane bending column interaction curves for pier bottom of North Connector piers using NCEER artificial earthquake record

5.4.2 Separation and Overhead (Ramp C)

As can be seen from Figures 5.20 through 5.25, the highest axial loads on the Ramp C piers again are well below their balance point axial capacity. The flexural moment demand ratios were evaluated at the top of the pier, at the flare bottom, and at the base of the pier, just as in the Sylmar Hospital case. Again, while many of the piers experienced inelastic behavior, according to the CALTRANS flexural moment demand ratio, none of the piers formed plastic hinges.

5.4.3 South Connector Overcrossing (Ramp L)

According to Figures 5.26 through 5.29, the highest axial load on the piers are well below their balance point capacity. Many of the piers experienced inelastic behavior. However, according to the CALTRANS flexural moment demand ratio, none of the piers developed plastic hinges. This is the same result obtained with the Sylmar Hospital earthquake used as the input record.

5.4.4 Comparisons to Sylmar Hospital Record

The results when the artificial earthquake is applied show some differences and similarities compared to those obtained with the Sylmar Hospital record. For both the artificial earthquake and the Sylmar Hospital record, the separation and overhead and the south connector had no piers with plastic hinges. The north connector had one pier (#7) that experienced hinging for the artificial earthquake. This pier, along with piers #3, 6, and 9 had hinges for the Sylmar Hospital case. The difference in the postulated earthquakes was enough to cause different behavior in

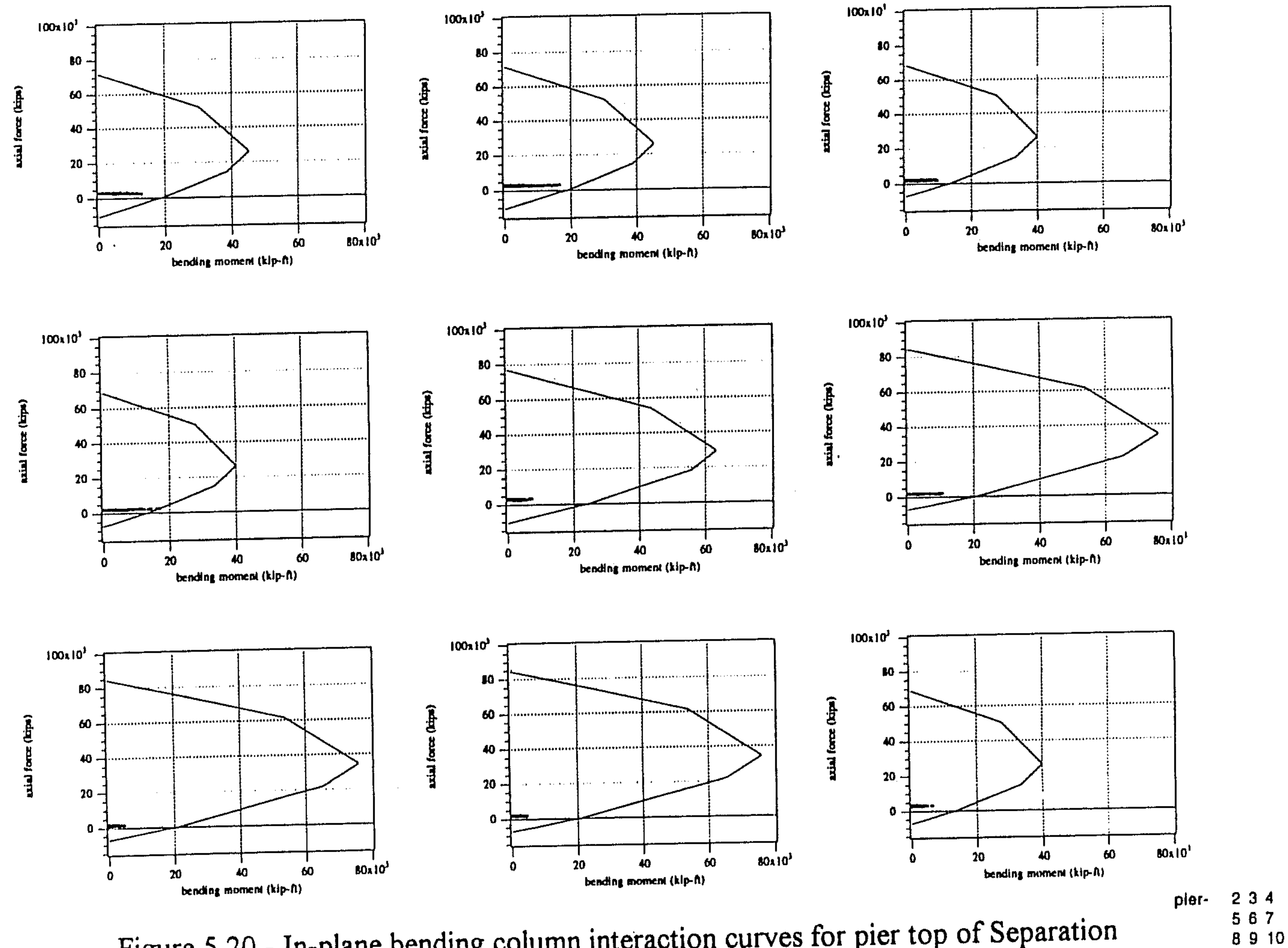

Figure 5.20 - In-plane bending column interaction curves for pier top of Separation and Overhead piers using NCEER artificial earthquake record

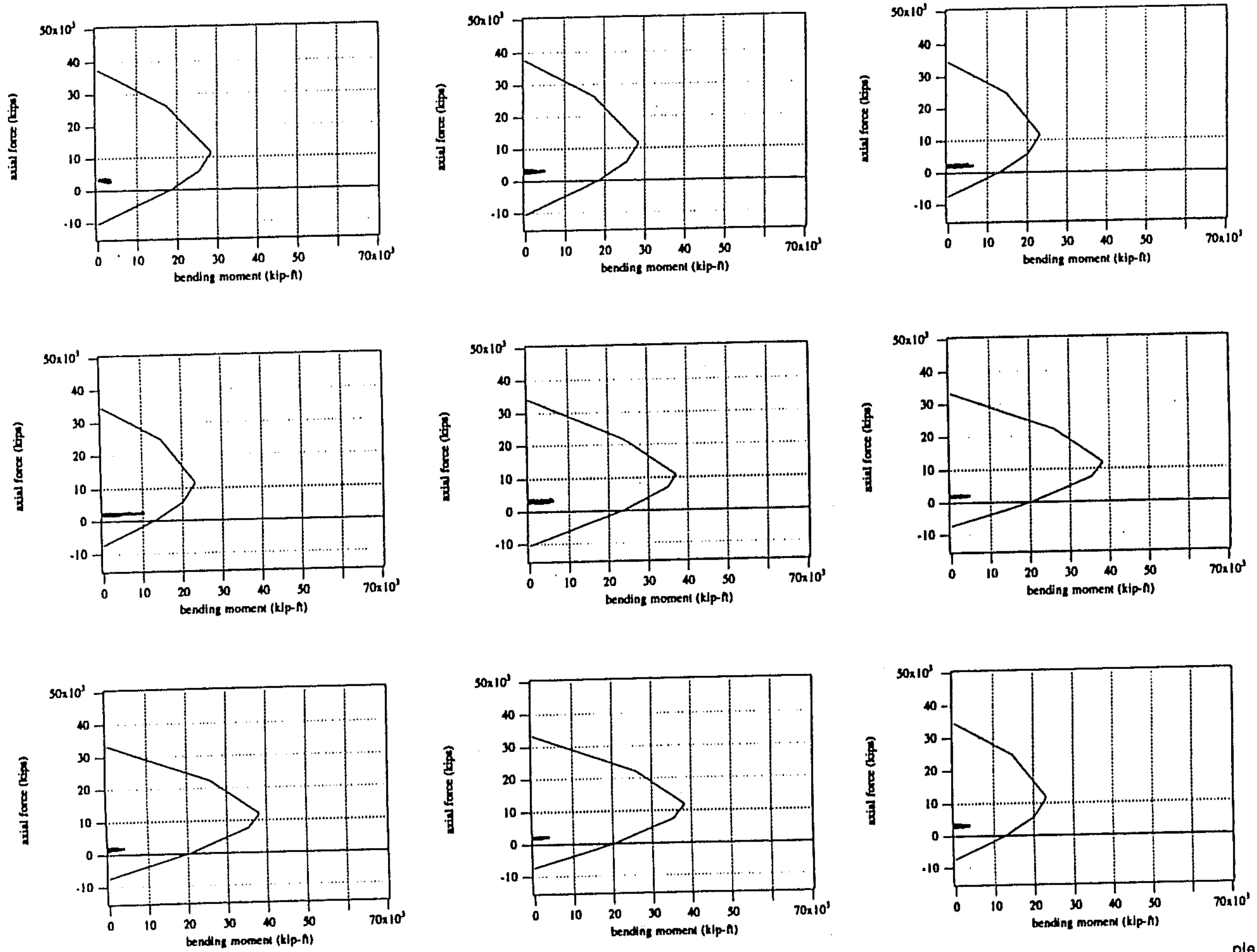

Figure 5.21 - In-plane bending column interaction curves for flare bottom of Separation and Overhead piers using NCEER artificial earthquake record

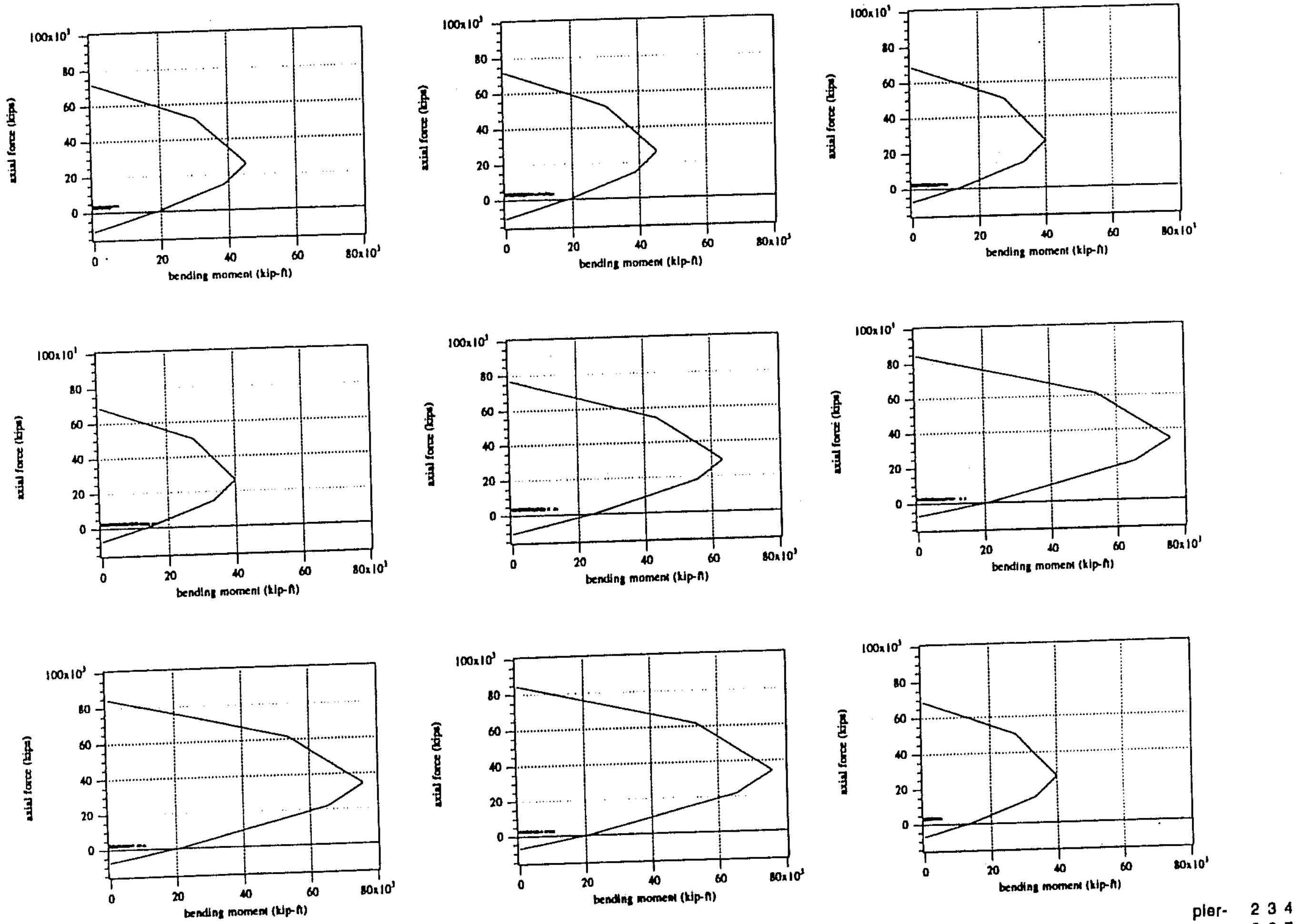

Figure 5.22 - In-plane bending column interaction curves for pier bottom of Separation and Overhead piers using NCEER artificial earthquake record

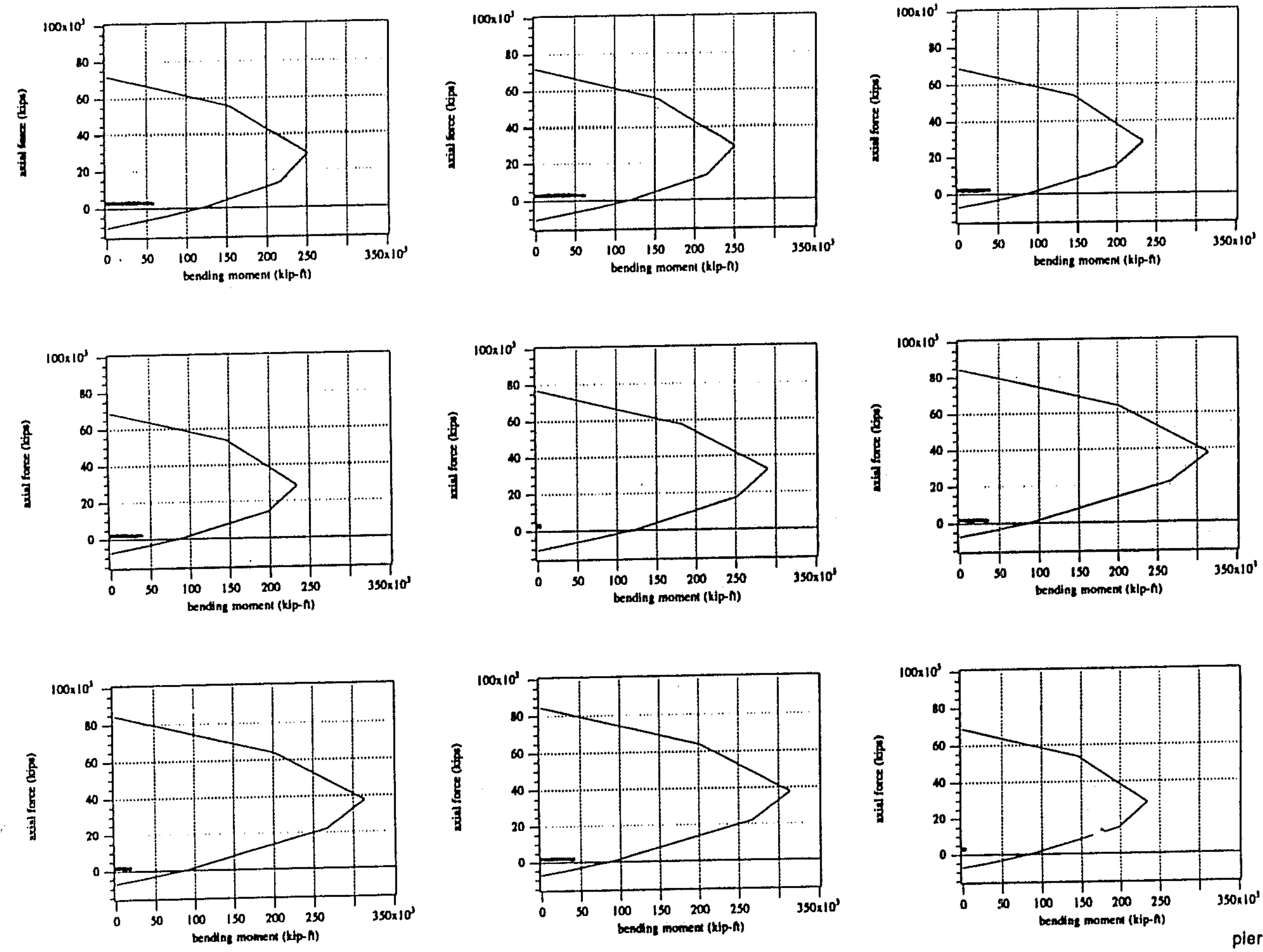

Figure 5.23 - Out-of-plane bending column interaction curves for pier top of Separation and Overhead piers using NCEER artificial earthquake record

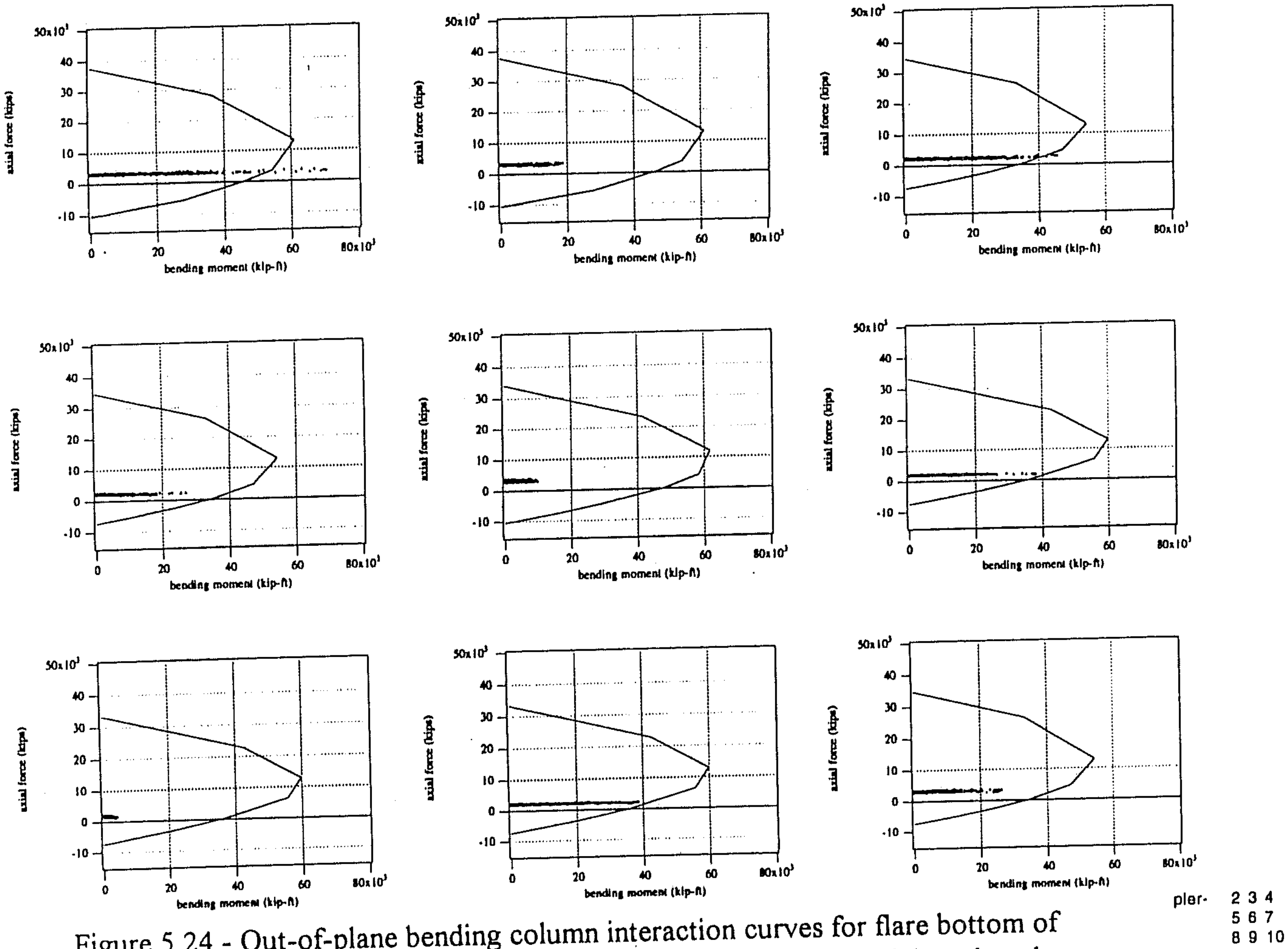

Figure 5.24 - Out-of-plane bending column interaction curves for flare bottom of Separation and Overhead piers using NCEER artificial earthquake record

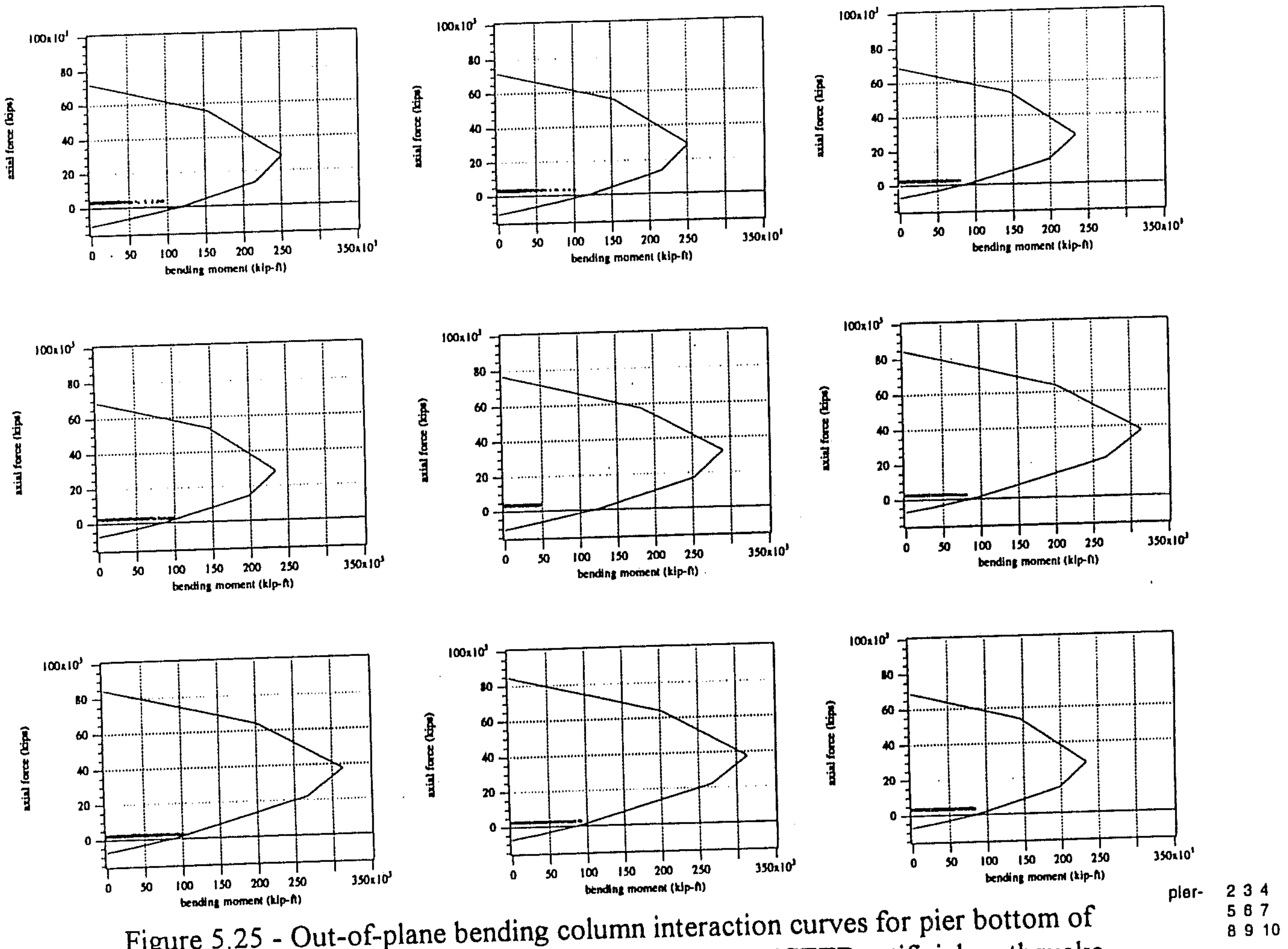

Figure 5.25 - Out-of-plane bending column interaction curves for pier bottom of Separation and Overhead piers using NCEER artificial earthquake record

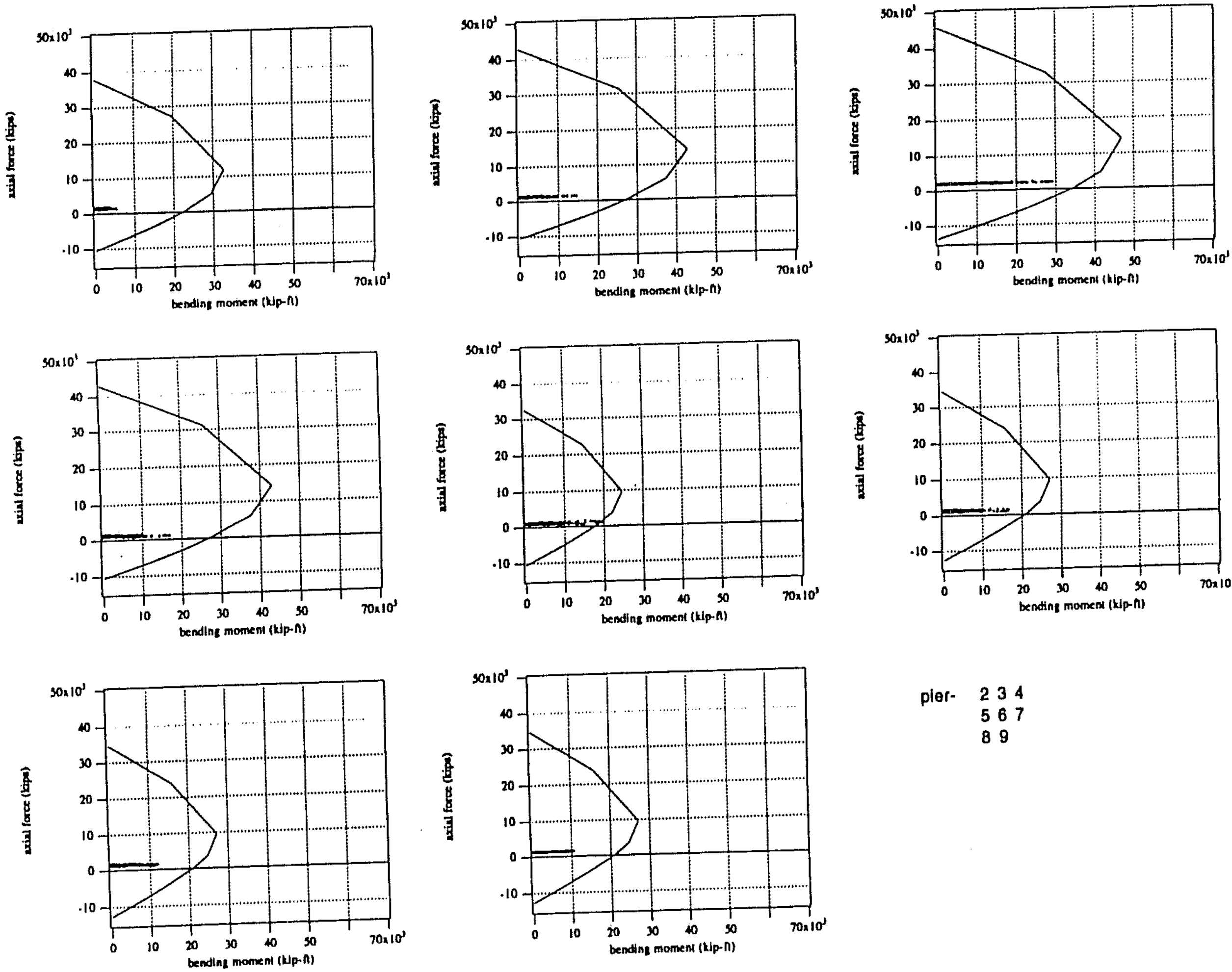

Figure 5.26 - In-plane bending column interaction curves for pier top of South Connector piers using NCEER artificial earthquake record

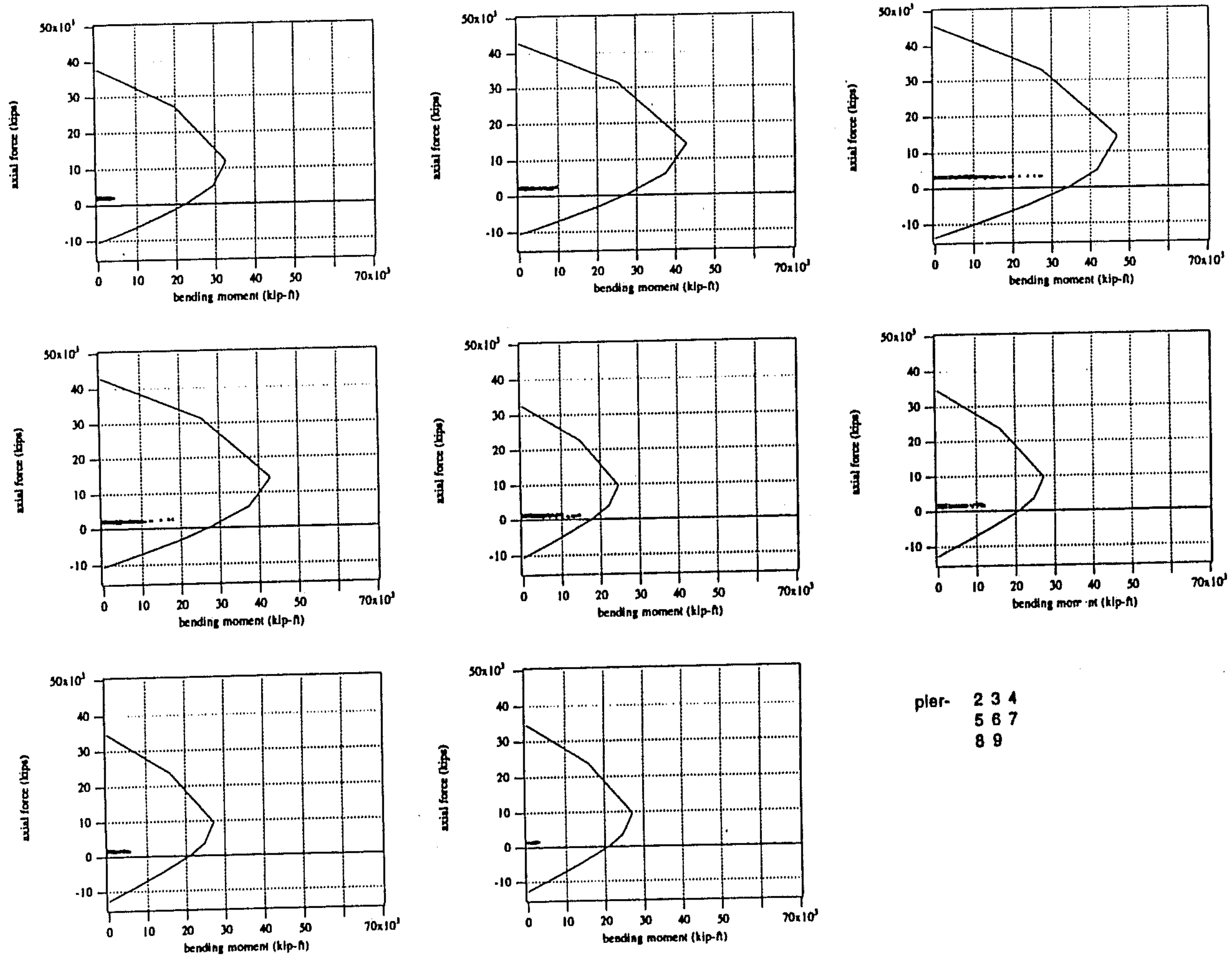

Figure 5.27 - In-plane bending column interaction curves for pier bottom of South Connector piers using NCEER artificial earthquake record

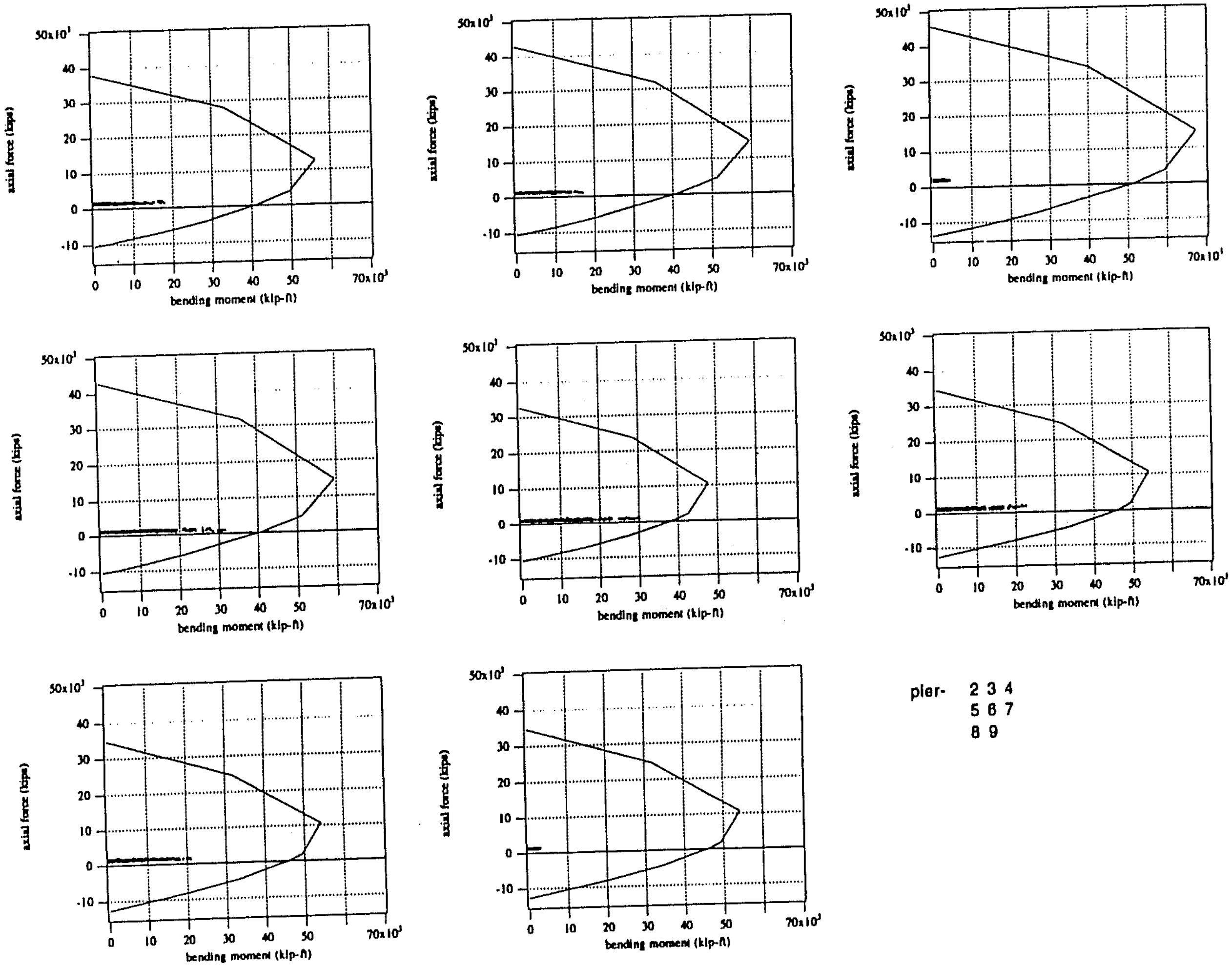

Figure 5.28 - Out-of-plane bending column interaction curves for pier top of South Connector piers using NCEER artificial earthquake record

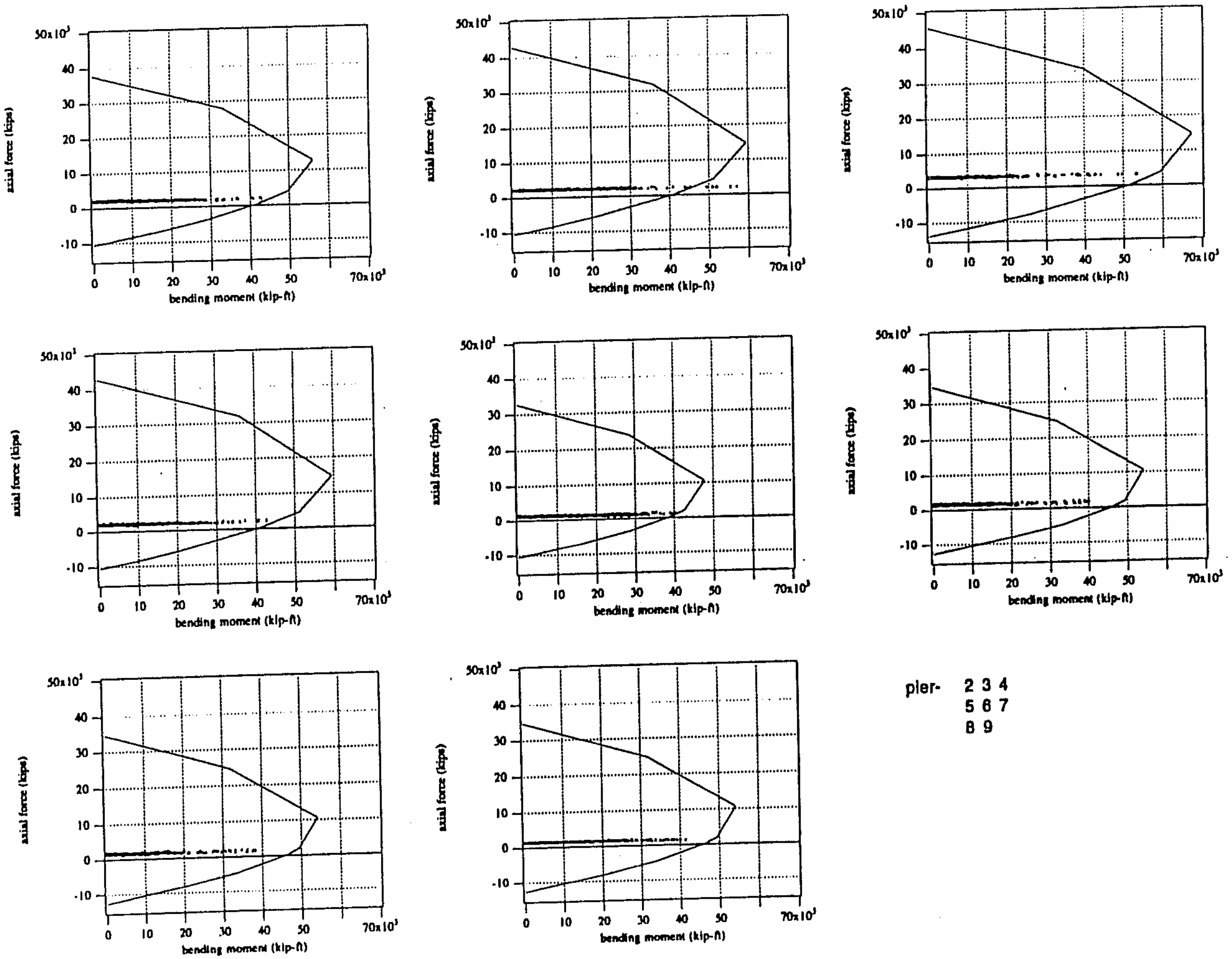

Figure 5.29 - Out-of-plane bending column interaction curves for pier bottom of South Connector piers using NCEER artificial earthquake record

these two cases. The bridges obviously responded differently (less plastic hinges were formed) for the lower accelerations of the NCEER artificial earthquake.

5.5 UBC/AASHTO Analysis

The final analyses conducted in this part of the study were performed using a motion consistent with the UBC/AASHTO design spectrum as the input. California is in a Zone 4 earthquake region. The soil type was assumed to be an S_3 type. The spectrum that was used is given in Figure 5.30.

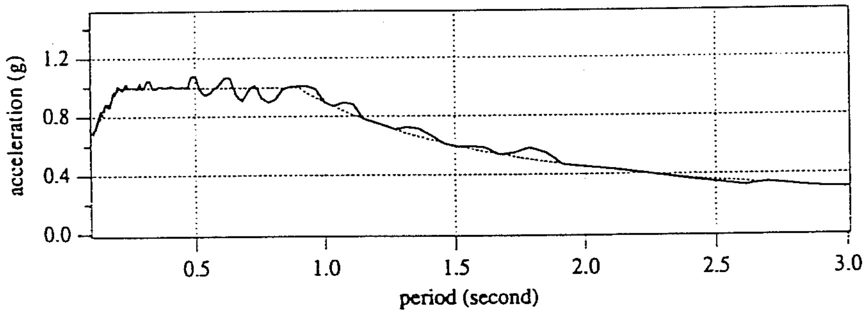

Figure 5.30 - UBC/AASHTO design spectrum

Using this spectrum, 3 artificial earthquakes (one for each axis of motion) were developed using the program SIMQUAKE. The actual spectrum corresponding to these synthetic motions is also shown in Figure 5.30. In order to simulate the earthquakes, a hypothetical up-time (5 seconds) and lag-time (2 seconds) are needed. These values were obtained from the Sylmar Hospital records as an approximation for the bridge site. The time histories for these artificial earthquakes based on the UBC/AASHTO spectrum are given in Figure 5.31.

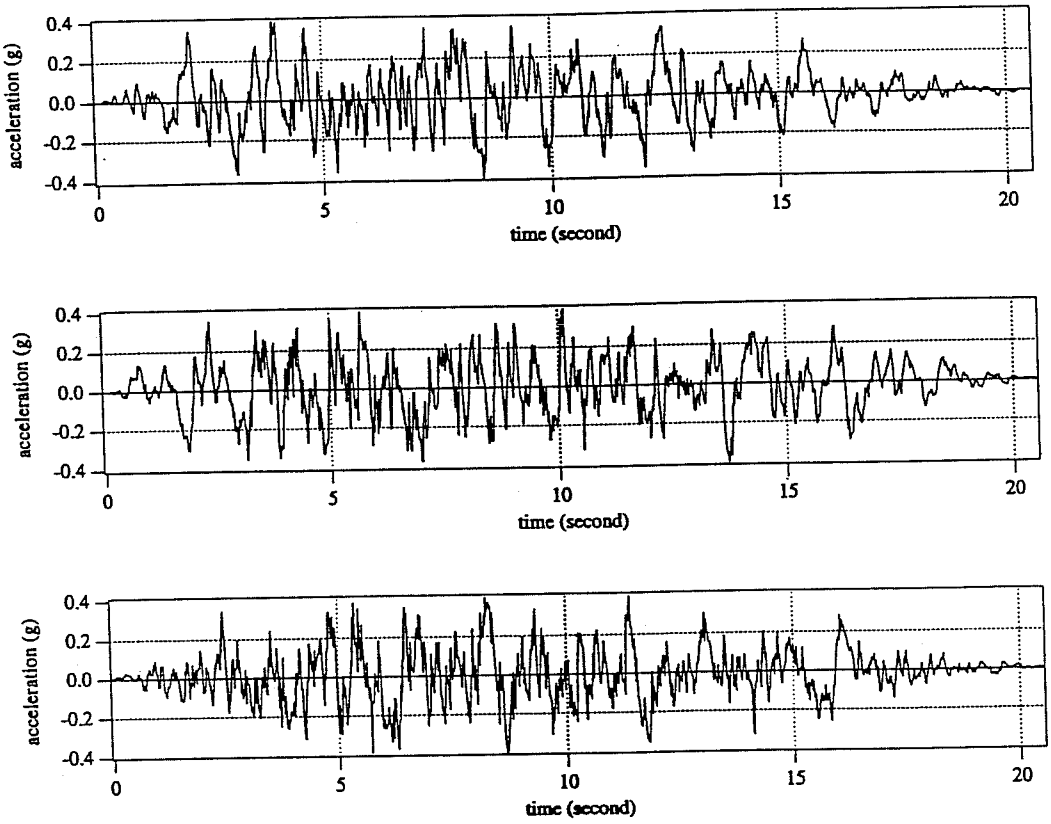

Figure 5.31 - Simulated earthquake time histories

Using these time histories and the same computer program as before, each of the bridges was again analyzed with three components of acceleration. The vertical ground motion accelerations were taken as two-thirds of the horizontal accelerations as per the UBC.

5.5.1 North Connector (Ramp M)

The piers that are of concern are those with very small axial loads so that

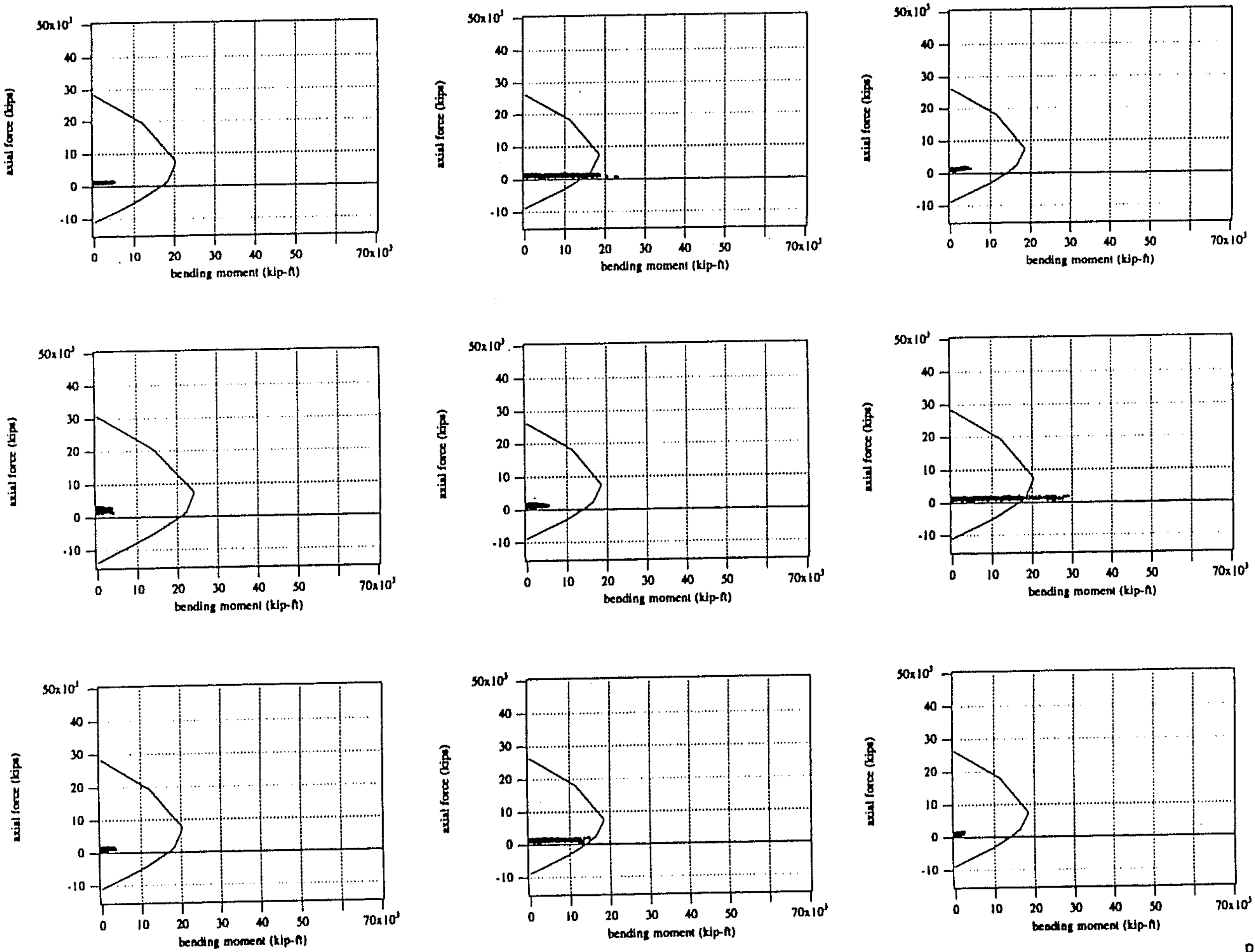

Figure 5.32 - In-plane bending column interaction curves for pier top of North Connector piers using UBC/AASHTO earthquake record

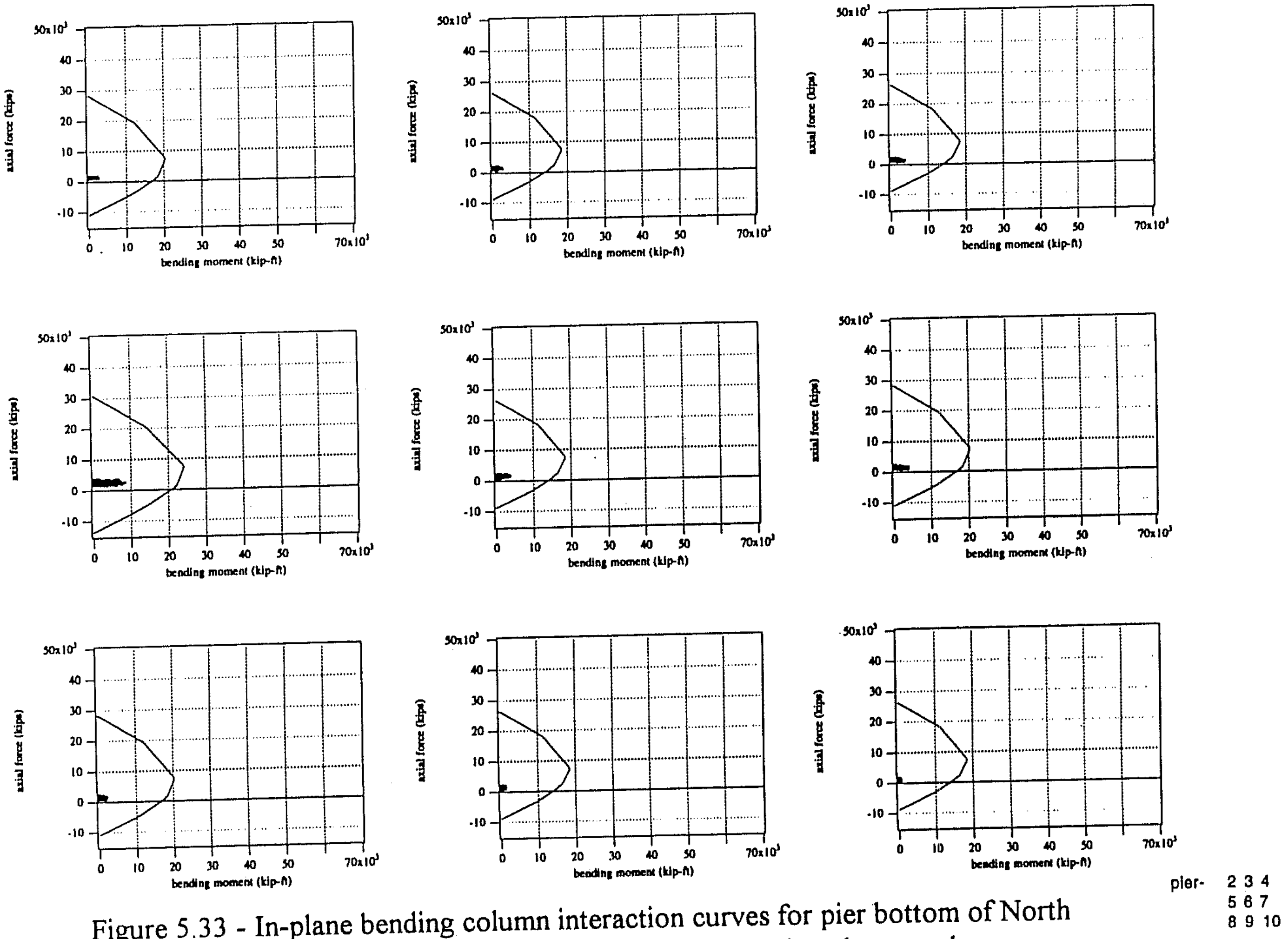

Figure 5.33 - In-plane bending column interaction curves for pier bottom of North Connector piers using UBC/AASHTO earthquake record

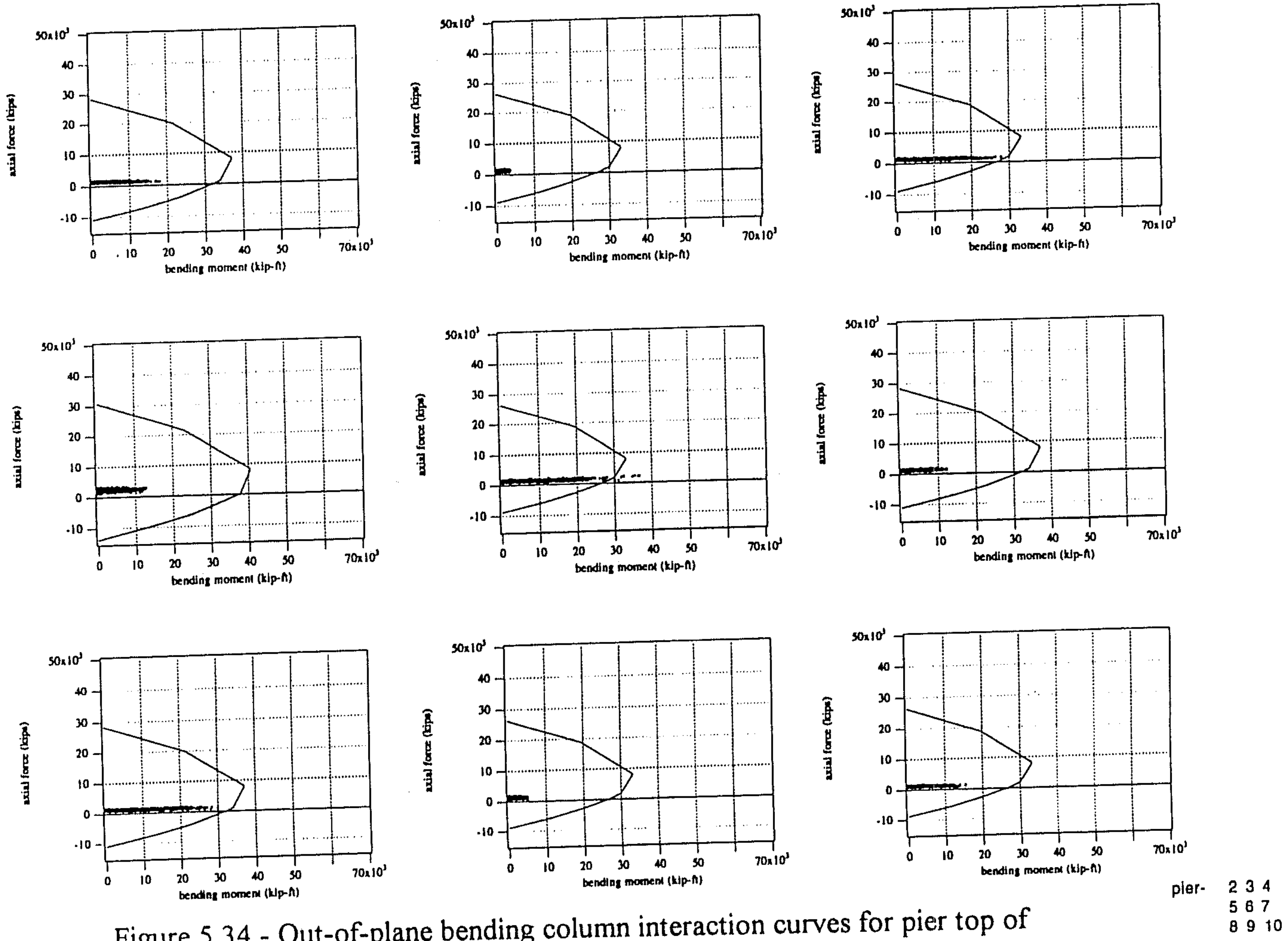

Figure 5.34 - Out-of-plane bending column interaction curves for pier top of North Connector piers using UBC/AASHTO earthquake record

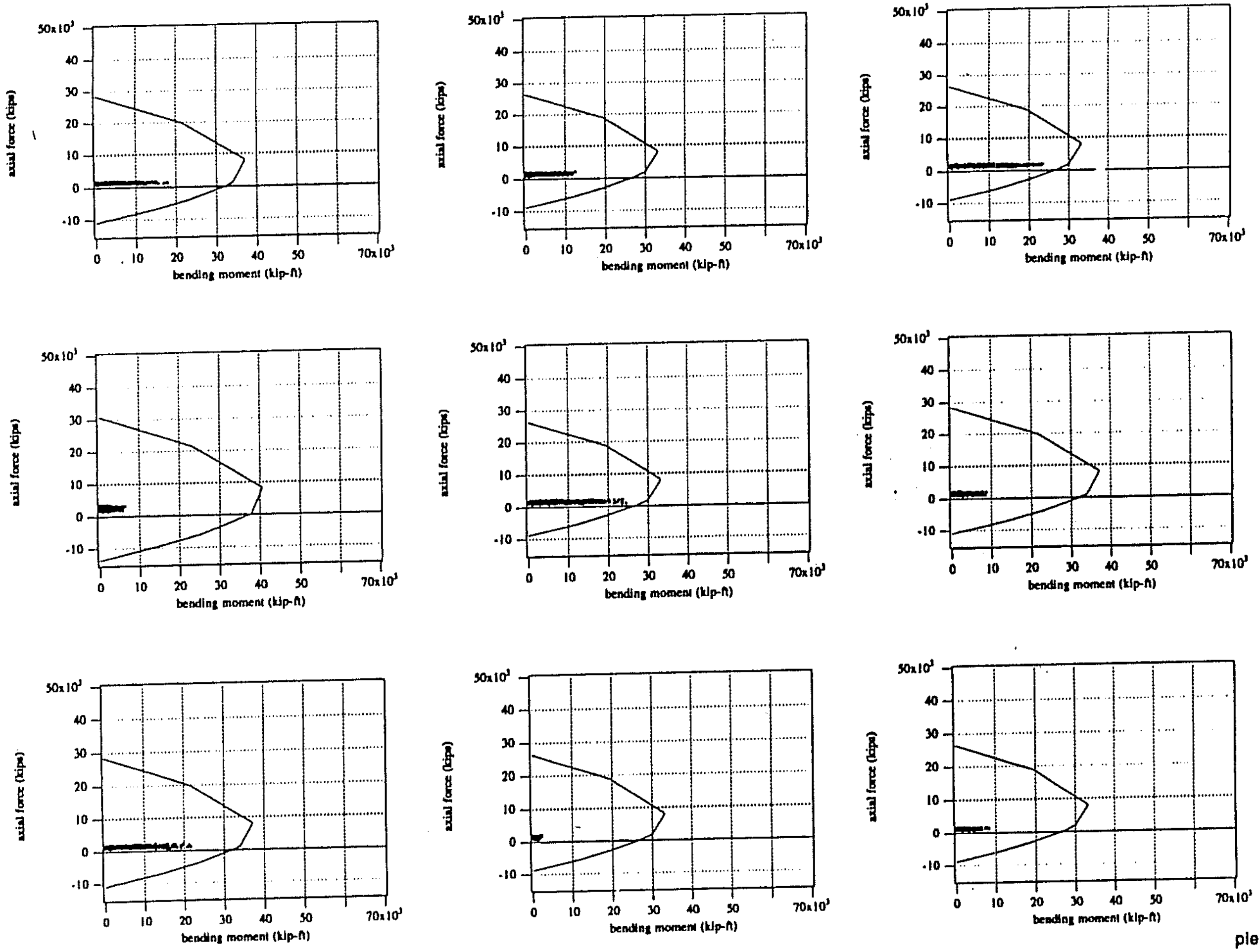

Figure 5.35 - Out-of-plane bending column interaction curves for pier bottom of North Connector piers using UBC/AASHTO earthquake record

their moment capacity is near the plastic moment. As can be seen from Figures 5.32 through 5.35 the highest axial loads on the piers are well below the balance point.

Table 5.4 gives the maximum in-plane moments and the flexural moment demand ratio in columns where μ_F exceeded 1.5.

Table 5.4 - In-plane Moment Results for North Connector

pier number	location	maximum moment from analysis (ft-kips)	nominal moment capacity (ft-kips)	moment demand ratio
3	top	22980	14776	1.56
7	top	29220	18529	1.58

No piers in the north connector had $\mu_F > 1.5$ in the out-of-plane direction. Pier #7 also had a plastic hinge form for each of the other two earthquakes. The moment demand ratios were 1.80 and 1.69 for the other two input earthquakes. Pier #3 formed a plastic hinge in the Northridge earthquake analysis.

5.5.2 Separation and Overhead (Ramp C)

As can be seen from Figures 5.36 through 5.41, the highest axial loads on the piers again are well below their balance point capacity. The flexural moment demand ratios were evaluated at the top of the pier, at the flare bottom, and at the base of the pier, just as for the Sylmar Hospital and Lamont-NCEER artificial earthquakes. No piers in the in-plane direction had values of $\mu_F > 1.5$, but Table 5.5 lists the numerous columns which formed plastic hinges in the out-of-plane direction.

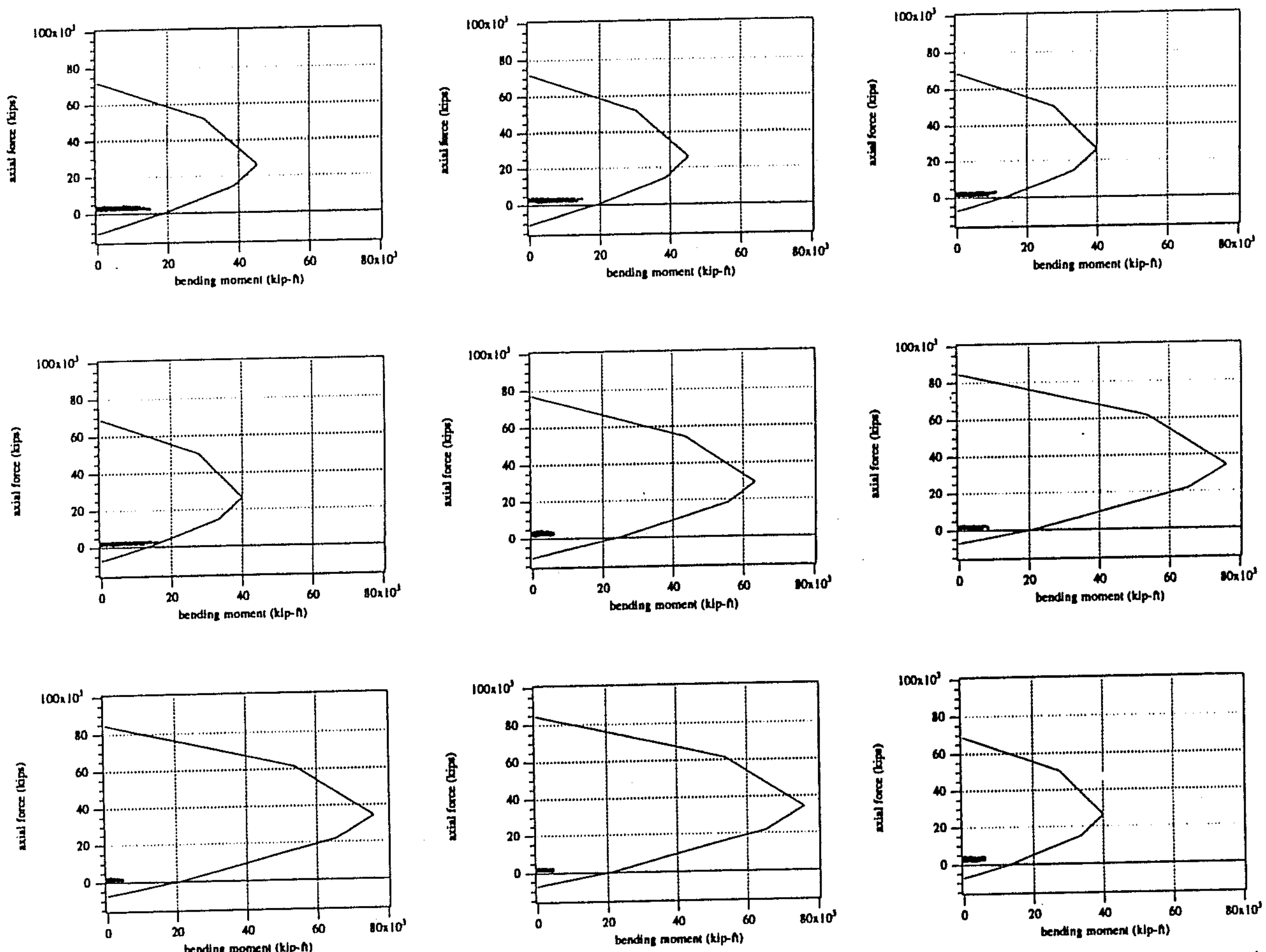

Figure 5.36 - In-plane bending column interaction curves for pier top of Separation and Overhead piers using UBC/AASHTO earthquake record

pier- 2 3 4
5 6 7
8 9 10

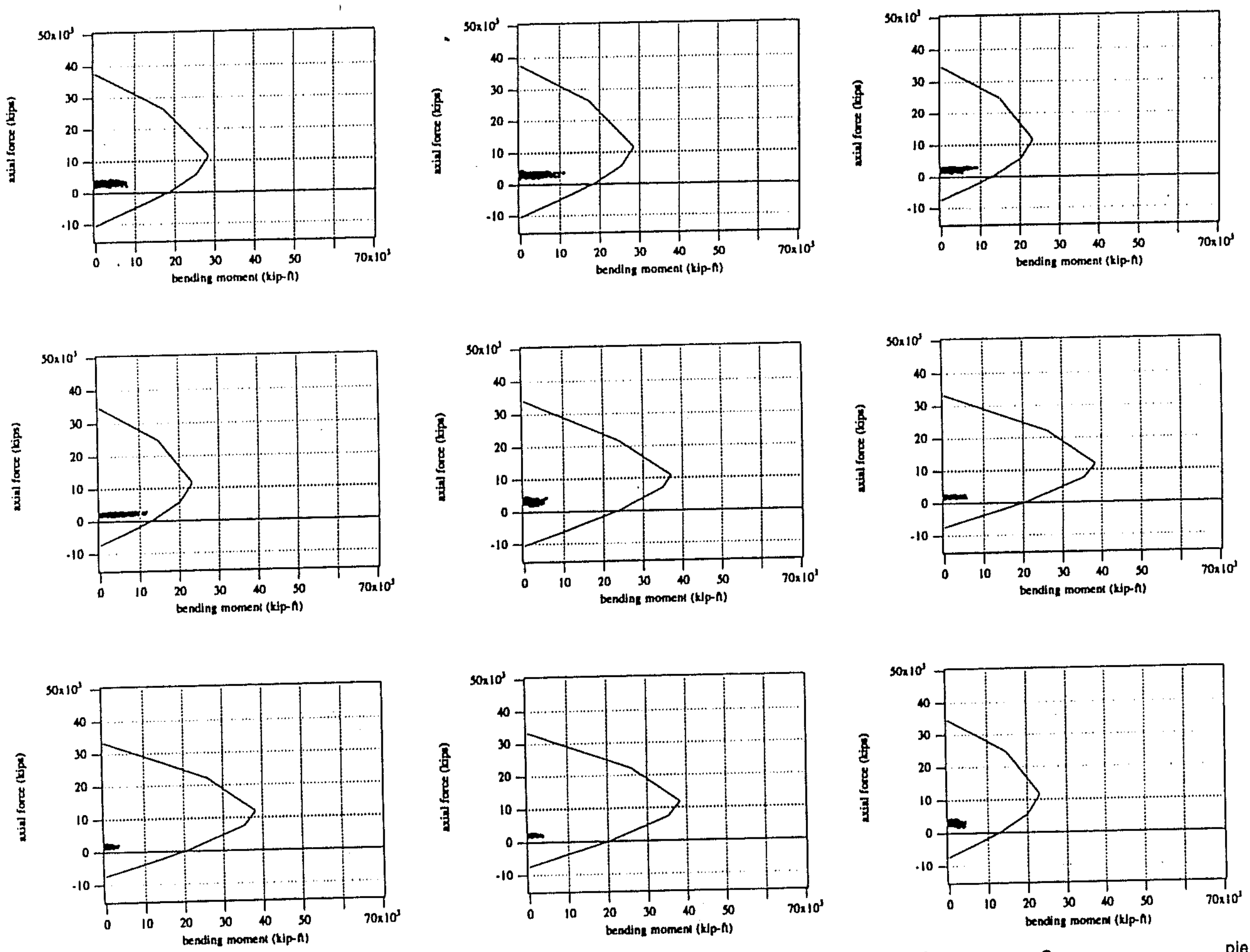

Figure 5.37 - In-plane bending column interaction curves for flare bottom of Separation and Overhead piers using UBC/AASHTO earthquake record

pier- 2 3 4
5 6 7
8 9 10

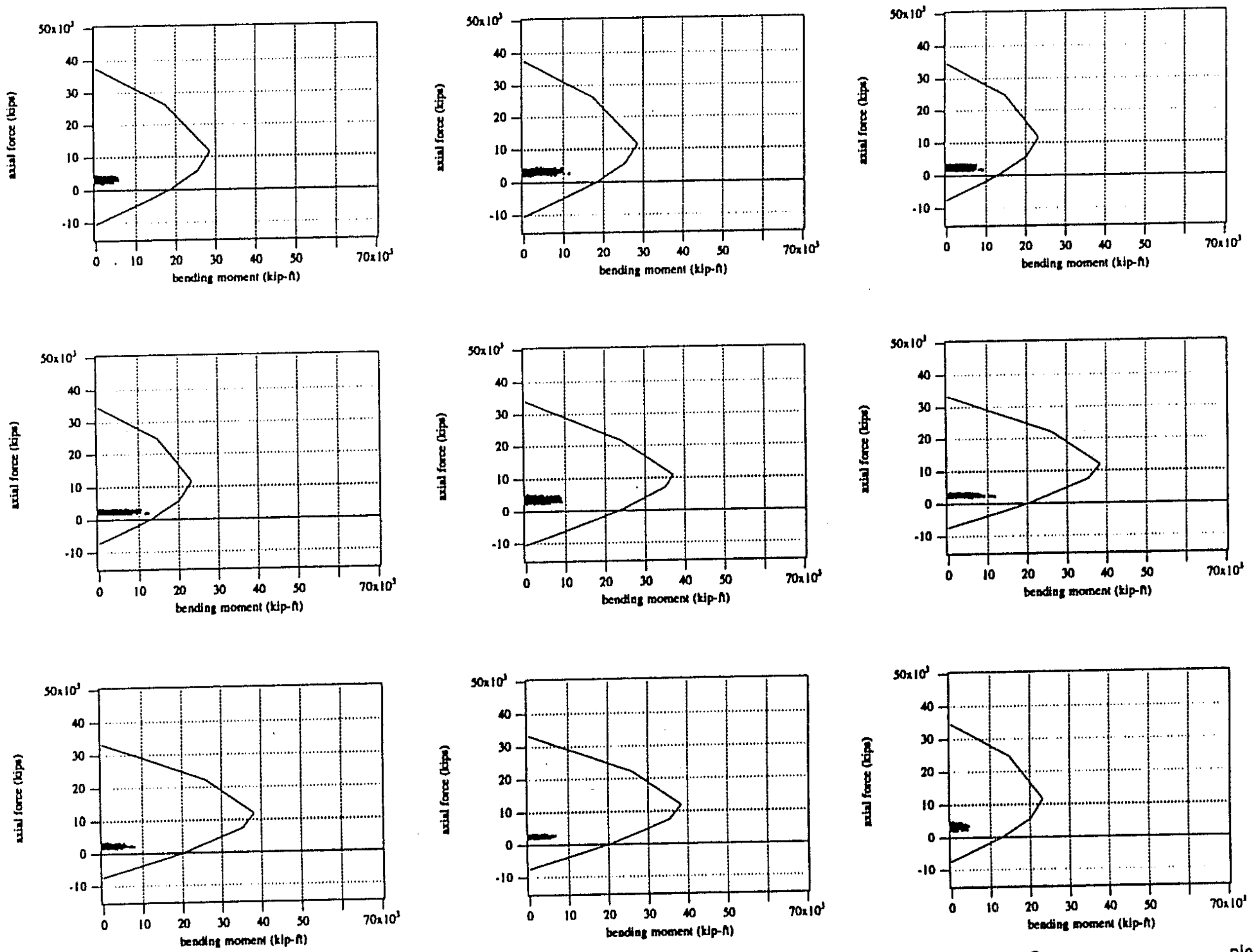

Figure 5.38 - In-plane bending column interaction curves for pier bottom of Separation and Overhead piers using UBC/AASHTO earthquake record

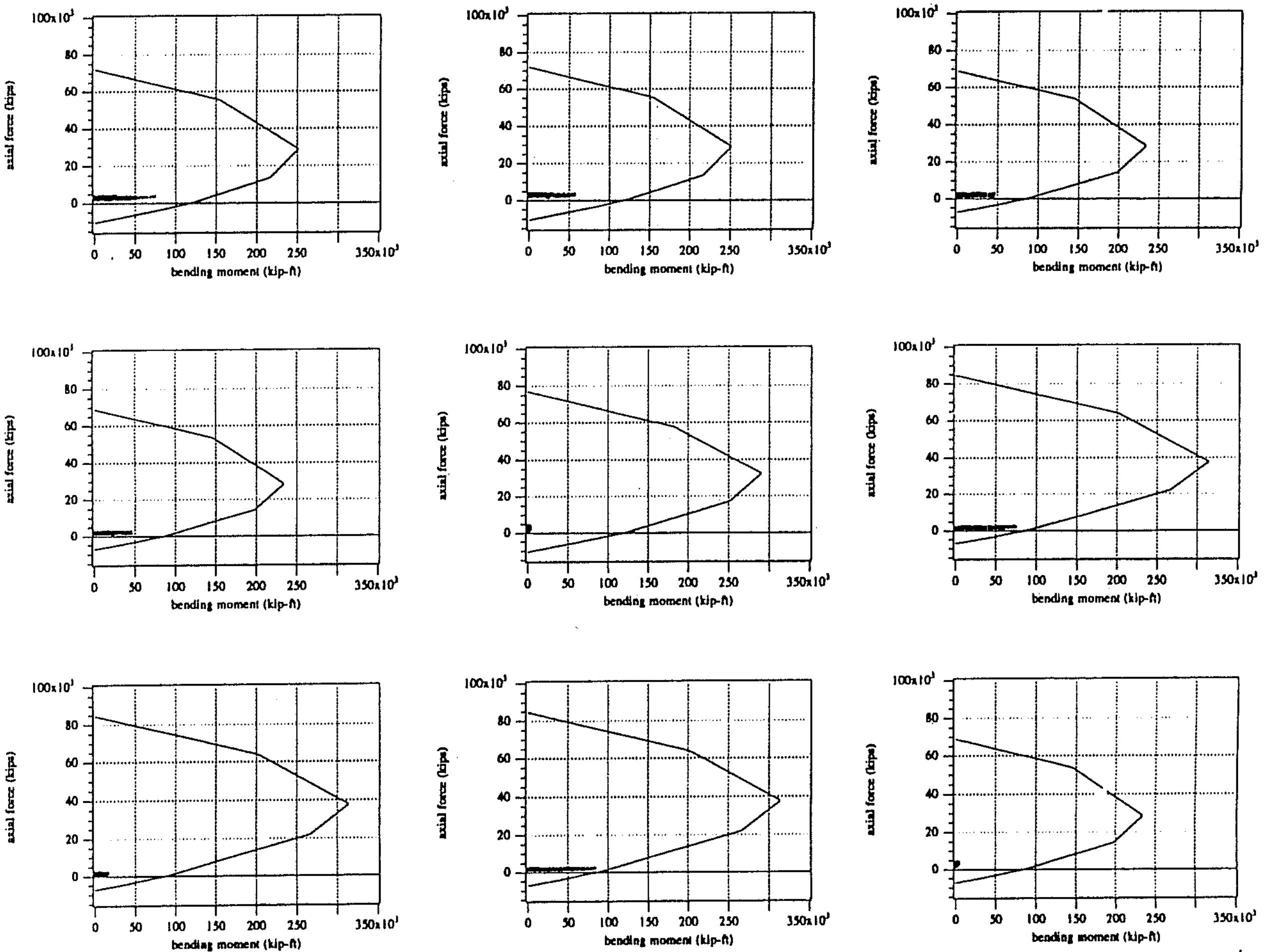

Figure 5.39 - Out-of-plane bending column interaction curves for pier top of Separation and Overhead piers using UBC/AASHTO earthquake record

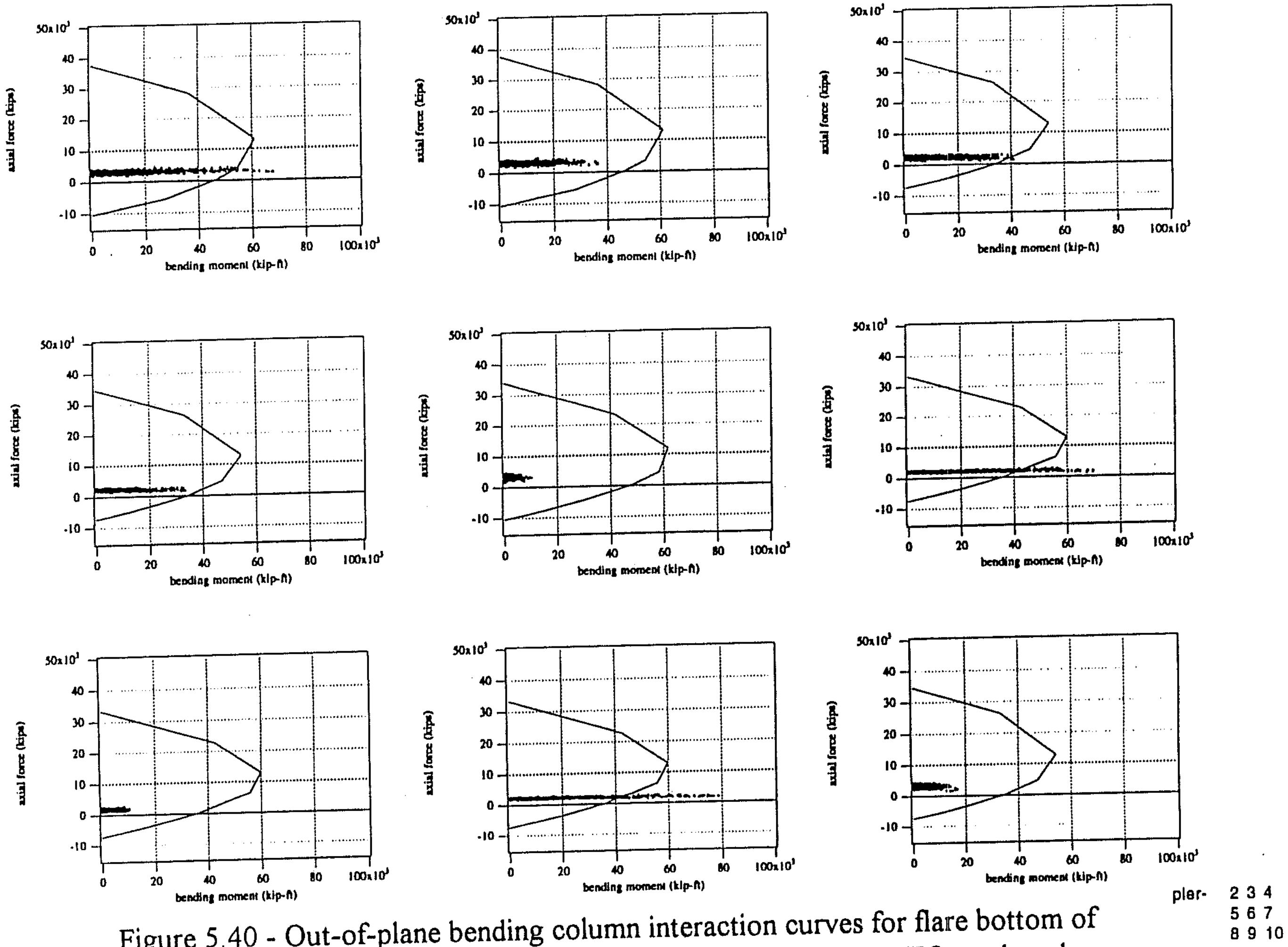

Figure 5.40 - Out-of-plane bending column interaction curves for flare bottom of Separation and Overhead piers using UBC/AASHTO earthquake record

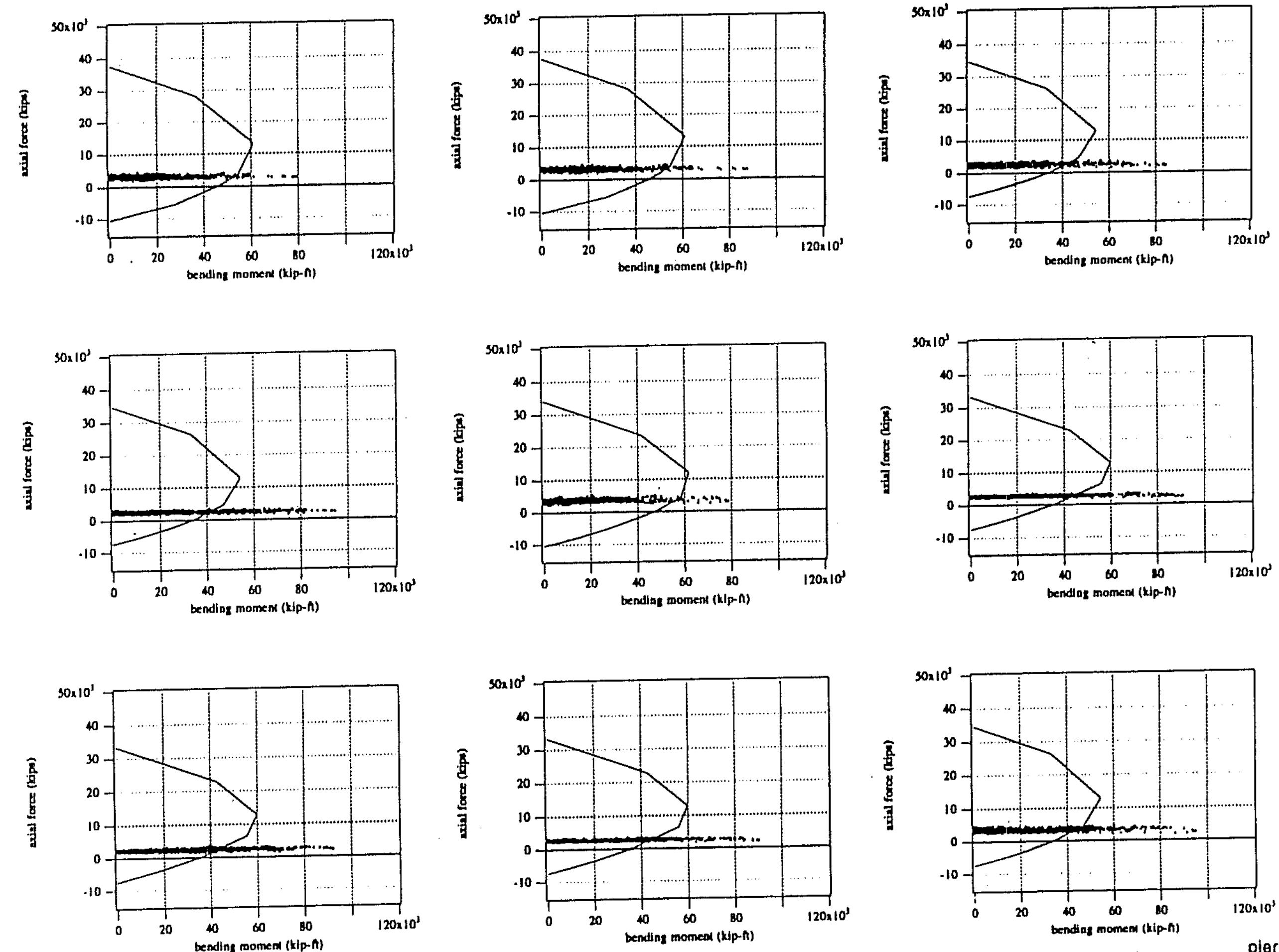

Figure 5.41 - Out-of-plane bending column interaction curves for pier bottom of Separation and Overhead piers using UBC/AASHTO earthquake record

Table 5.5 - Out-of-plane Moment Results for Separation and Overhead

pier number	location	maximum moment from analysis (ft-kips)	nominal moment capacity (ft-kips)	moment demand ratio
3	bottom	90890	53794	1.69
4	bottom	85510	40393	2.12
5	bottom	93460	41076	2.28
7	flare bottom	69070	41285	1.67
7	bottom	91100	43301	2.10
8	bottom	92240	42293	2.18
9	flare bottom	78970	41789	1.89
9	bottom	90480	42545	2.13
10	bottom	95300	42439	2.25

As can be seen from these results, plastic hinges would develop in the separation and overhead structure for all of the piers except #2 and #6. The UBC/AASHTO earthquake caused serious problems in the out-of-plane direction. This supports the fact that for curved overpasses like this, the out-of-plane direction controls the design.[11]

5.5.3 South Connector Overcrossing (Ramp L)

As shown in Figures 5.42 through 5.45, the highest axial load on the piers is again well below their balance point axial capacity. Many of the piers experienced

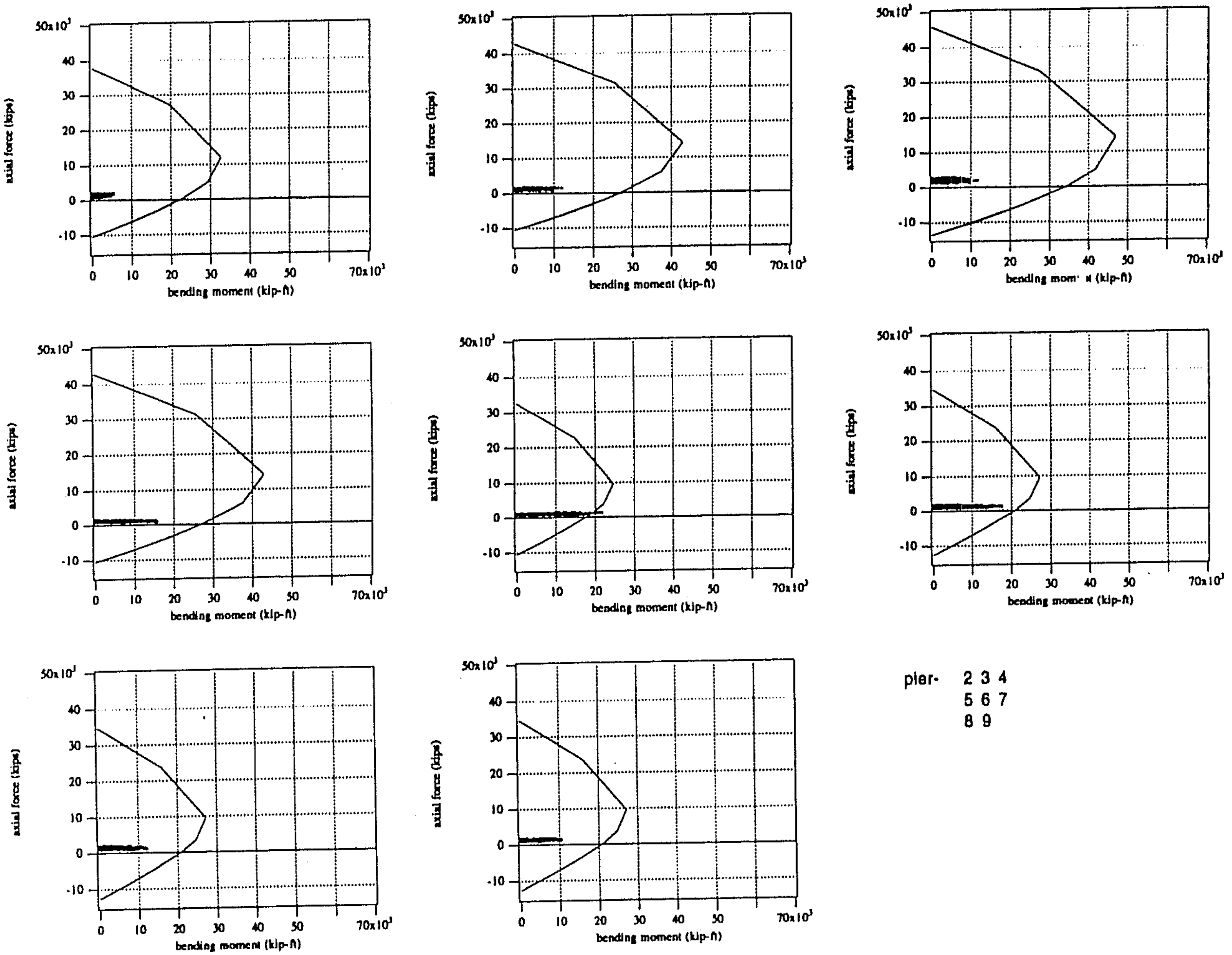

Figure 5.42 - In-plane bending column interaction curves for pier top of South Connector piers using UBC/AASHTO earthquake record

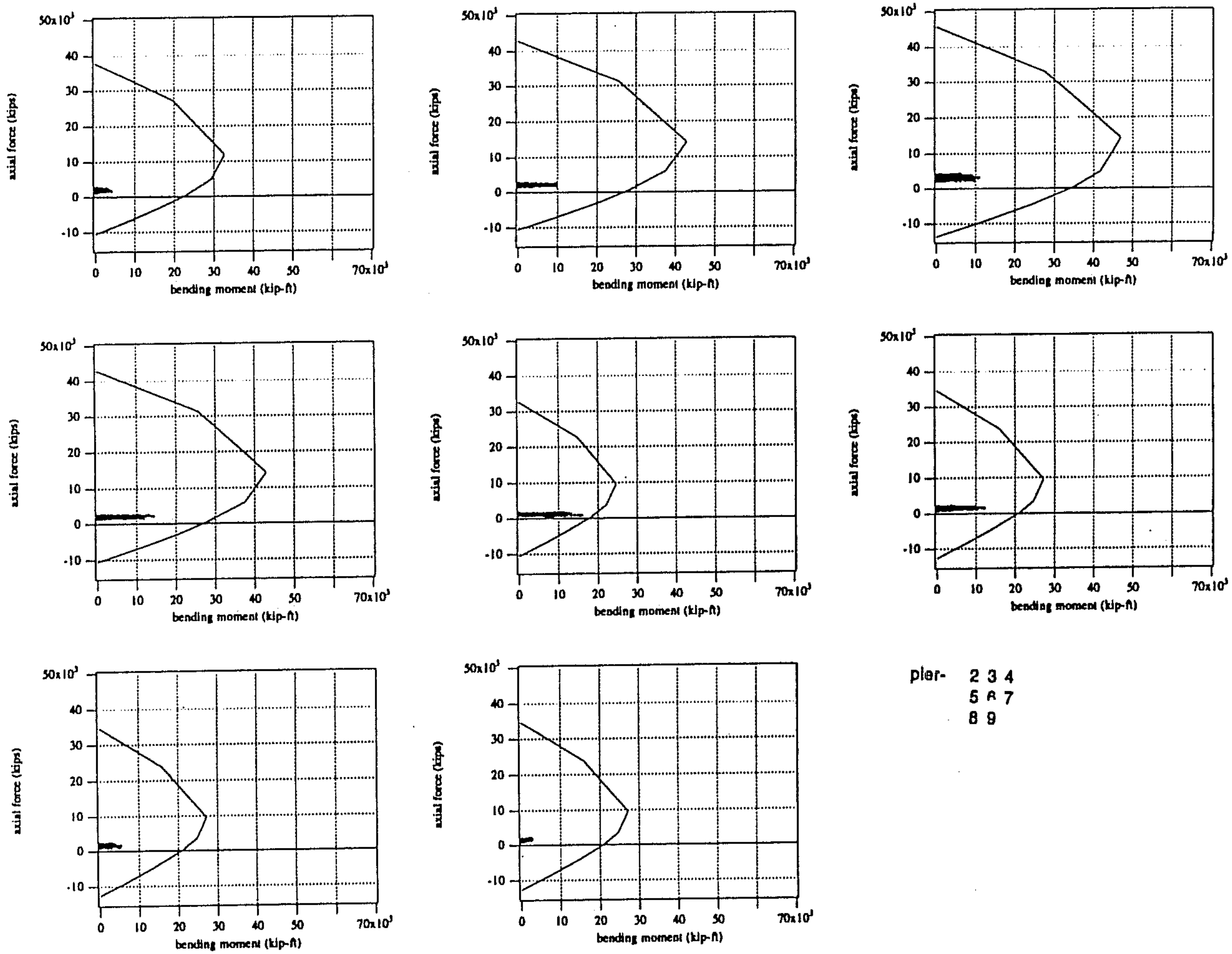

Figure 5.43 - In-plane bending column interaction curves for pier bottom of South Connector piers using UBC/AASHTO earthquake record

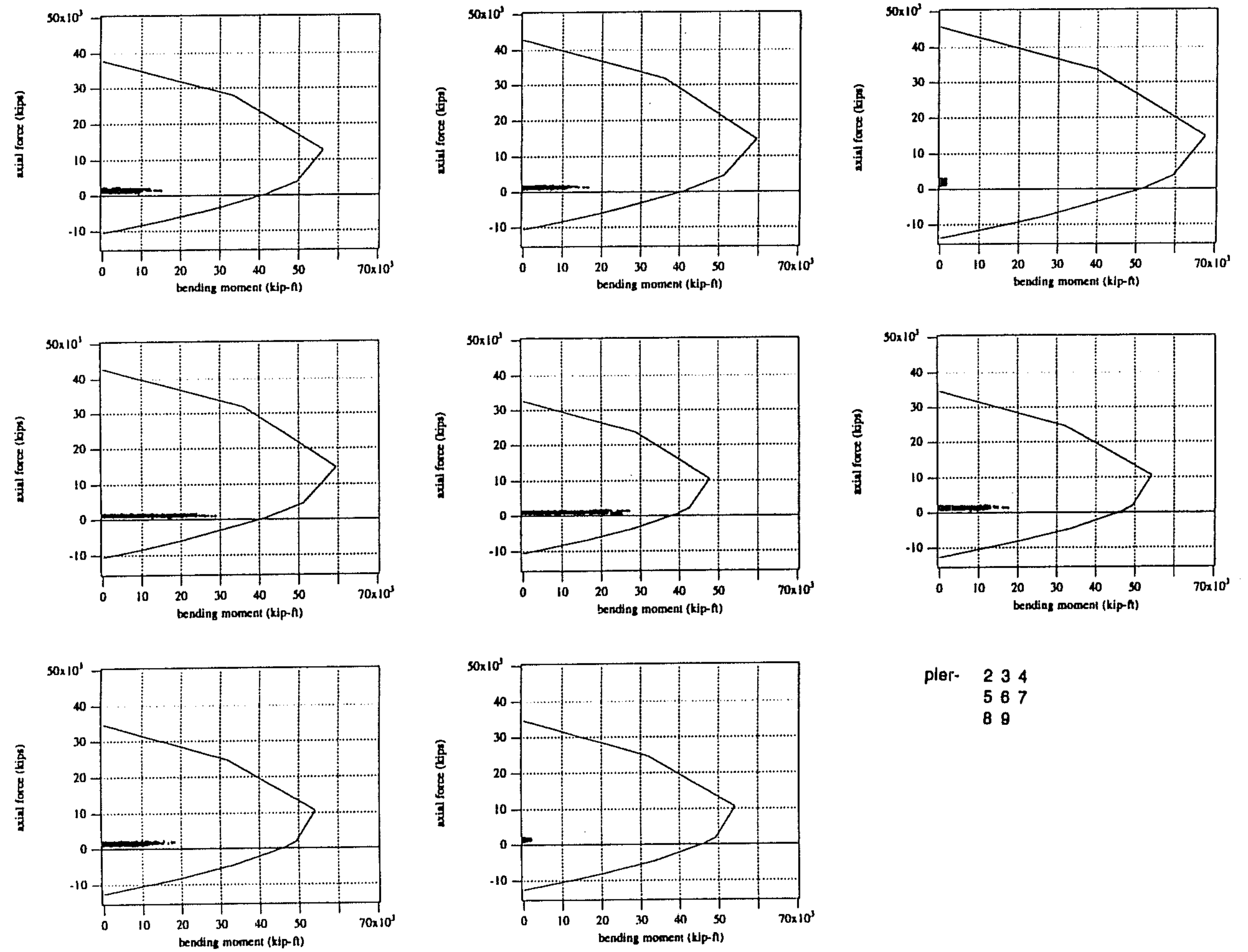

Figure 5.44 - Out-of-plane bending column interaction curves for pier top of South Connector piers using UBC/AASHTO earthquake record

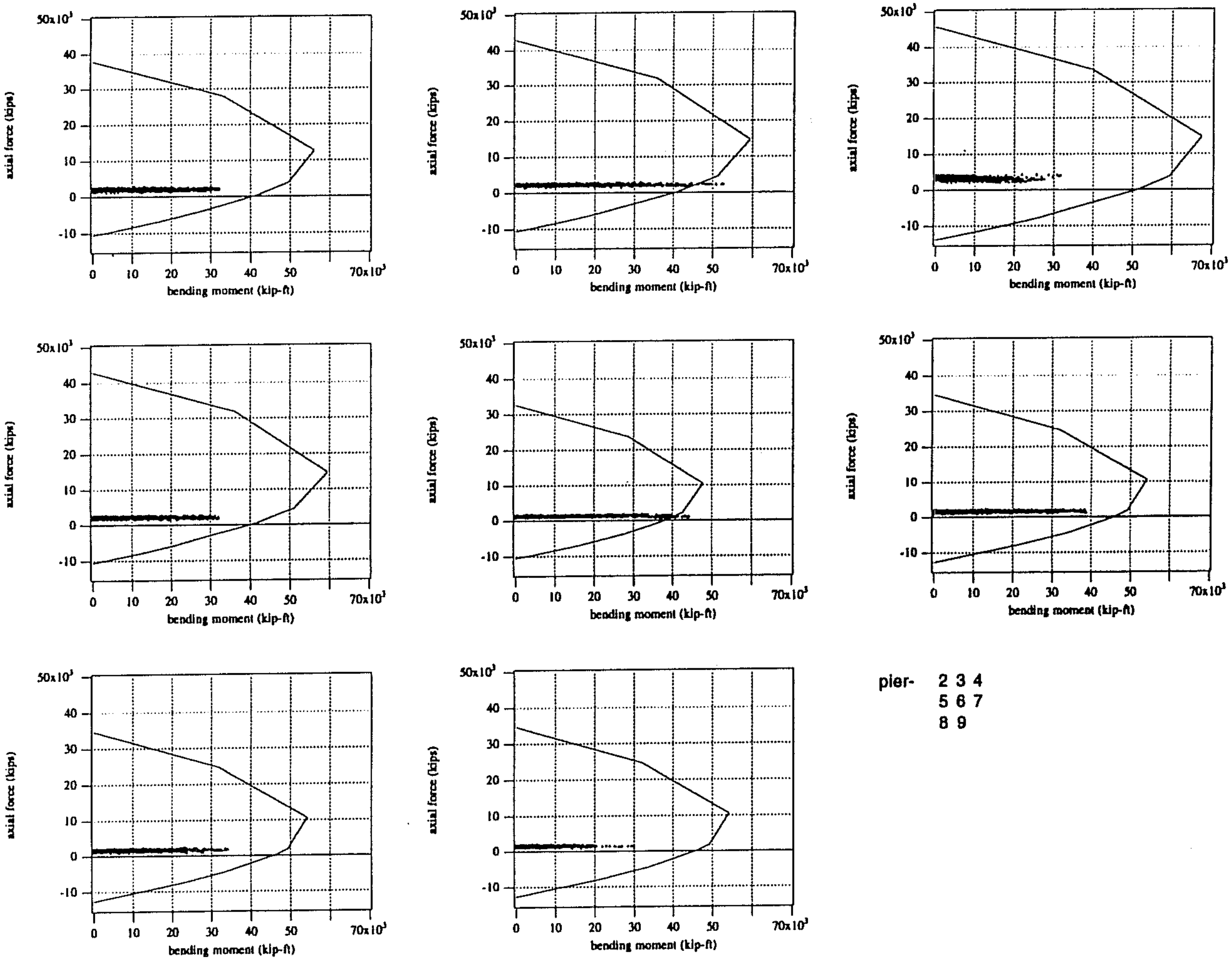

Figure 5.45 - Out-of-plane bending column interaction curves for pier bottom of South Connector piers using UBC/AASHTO earthquake record

inelastic behavior. However, according to the CALTRANS flexural moment demand ratio, none of the piers formed plastic hinges. This is the same result obtained with the other two input earthquakes.

5.6 Two Components of Acceleration vs. Three Components of Acceleration

The question arises as to what effect the vertical acceleration had on the moments in the columns. Table 5.6 lists the data from the south connector for the "UBC/AASHTO" earthquake. The moments listed are at the pier top in the in-plane and out-of-plane directions. The ratio of the moments (M3/M2) was also calculated. M2 is the moment when two directions of horizontal acceleration are input, and M3 is the moment when the vertical acceleration component is added.

Table 5.6 - Results of Adding Vertical Acceleration for Ramp L

	in-plane direction			out-of-plane direction		
pier	M3	M2	ratio	M3	M2	ratio
2	5049	4493	1.12	15320	15330	1.00
3	10520	9443	1.11	16100	16060	1.00
4	11850	11610	1.02	1591	1488	1.07
5	15200	13840	1.10	28610	28820	0.99
6	21760	22240	0.98	27460	27680	0.99
7	15940	16250	0.98	17360	17520	0.99
8	12720	12350	1.03	18420	18600	0.99
9	8607	6152	1.40	2112	1320	1.60
in-plane - $\bar{x} = 1.09$				out-of-plane - $\bar{x} = 1.08$		
in-plane - $\sigma = 0.13$				out-of-plane - $\sigma = 0.20$		

Table 5.7 lists the same type of data for the north connector structure using the UBC/AASHTO earthquake.

Table 5.7 - Results of Adding Vertical Acceleration for Ramp M

	in-plane direction			out-of-plane direction		
pier	M3	M2	ratio	M3	M2	ratio
2	4522	3481	1.30	18290	18130	1.01
3	23140	23100	1.00	3210	3432	0.94
4	4335	3557	1.22	27480	26960	1.02
5	4302	4107	1.05	13270	13240	1.00
6	4344	3728	1.17	35300	34690	1.02
7	28960	28870	1.00	12710	12310	1.03
8	3701	3994	0.93	29320	29330	1.00
9	14880	14920	1.00	5397	5682	0.95
10	2127	1383	1.54	15390	15430	1.00
in-plane - $\bar{x} = 1.13$				out-of-plane - $\bar{x} = 1.00$		
in-plane - $\sigma = 0.18$				out-of-plane - $\sigma = 0.03$		

Finally, Table 5.8 lists the same type of data for the separation and overhead structure using the UBC/AASHTO earthquake.

Table 5.8 - Results of Adding Vertical Acceleration for Ramp C

	in-plane direction			out-of-plane direction		
pier	M3	M2	ratio	M3	M2	ratio
2	9992	6092	1.64	69350	68510	1.01
3	15340	13080	1.17	62420	62700	1.00
4	9327	6899	1.35	45640	45250	1.01
5	12440	10260	1.21	44170	44510	0.99
6	5999	5974	1.00	4602	4580	1.00
7	8511	7144	1.19	76290	76510	1.00
8	4389	4536	0.97	16320	16430	0.99
9	4741	3819	1.24	83460	83340	1.00
10	4388	4213	1.04	4652	4571	1.02
in-plane - $\bar{x} = 1.22$				out-of-plane - $\bar{x} = 1.00$		
in-plane - $\sigma = 0.21$				out-of-plane - $\sigma = 0.01$		

The averages tat are listed above are not as important, however, as the 95% confidence limits. The separation and overhead (Ramp C) had the largest spread in confidence limit in the in-plane direction (1.08, 1.35). The south connector (Ramp L) had the largest spread in confidence limit in the out-of-plane direction (0.94, 1,22). When all of the bridges are placed in the same statistical data pool, the confidence limit for the ratio M3/M2 is (1.07, 1.21) in the in-plane direction and (0.97, 1.07) in the out-of-plane direction is 1.02. Overall, putting all 52 data in the same statistical sample, the 95% confidence limit is (1.04, 1.12).

While the bending moment in the piers is caused primarily by horizontal acceleration, this data shows that the vertical acceleration affects the moments in the piers to some degree, increasing them when vertical acceleration is added by an overall average of 5-10%. This is because as the vertical acceleration is applied piers will become more flexible and more stiff as the axial load changes. As the stiffness of the piers changes, they will attract more or less of the horizontal load, which will in turn affect the bending moment in the pier.

5.7 Correlation to Observed Damage After Northridge Earthquake

It seems as though the damage that was reported after the Northridge earthquake was not the same type of damage that would be caused by the formation of plastic hinges predicted by the computer model. The computer model, while limited because of its linear elastic modelling technique, predicted plastic hinges to form in four of the piers of the north connector (Ramp L). These piers all experienced little or no damage during the earthquake. The most likely failure scenario, the failure of pier #2 in shear, is outlined in Chapter 2.

CHAPTER 6

ANALYSIS OF HINGES

The last portion of the analysis for this project involved the behavior and effectiveness of the hinge restrainers. Before 1971, the typical hinge restrainers were those shown in Figures 6.1 and 6.2. Figure 6.1 is known as a "movement-equalizer" bolt and Figure 6.2 is known as a hinge extender. After the San Fernando earthquake in 1971, many of the bridges in the Los Angeles area were retrofitted with cable hinge restrainers typical of those shown in Figure 6.3. Many of the previous hinge types failed during the San Fernando earthquake. Most of the cable hinge restrainers are made from a galvanized aluminum metal with an E = 14,000 ksi before yielding and E = 18,000 ksi after yielding. The typical cable has a ¾" nominal diameter.[10] The cables are connected to 1" diameter regular strength bolts at the cable ends. These restrainers were installed as shown in Figure 6.3 to help tie the structure together during an earthquake. The cables generally reach across a diaphragm at the hinge, but can stretch from the hinge to a diaphragm located near the pier. They are easier to install at the hinge diaphragm than at the diaphragm near the pier.[14] This portion of the thesis studies the action, movement, and effectiveness of the hinge restrainers during an earthquake. If the restrainer allows a girder to move more than the bearing seat width, major problems will occur. This can be seen in the schematic diagram of Figure 6.4.

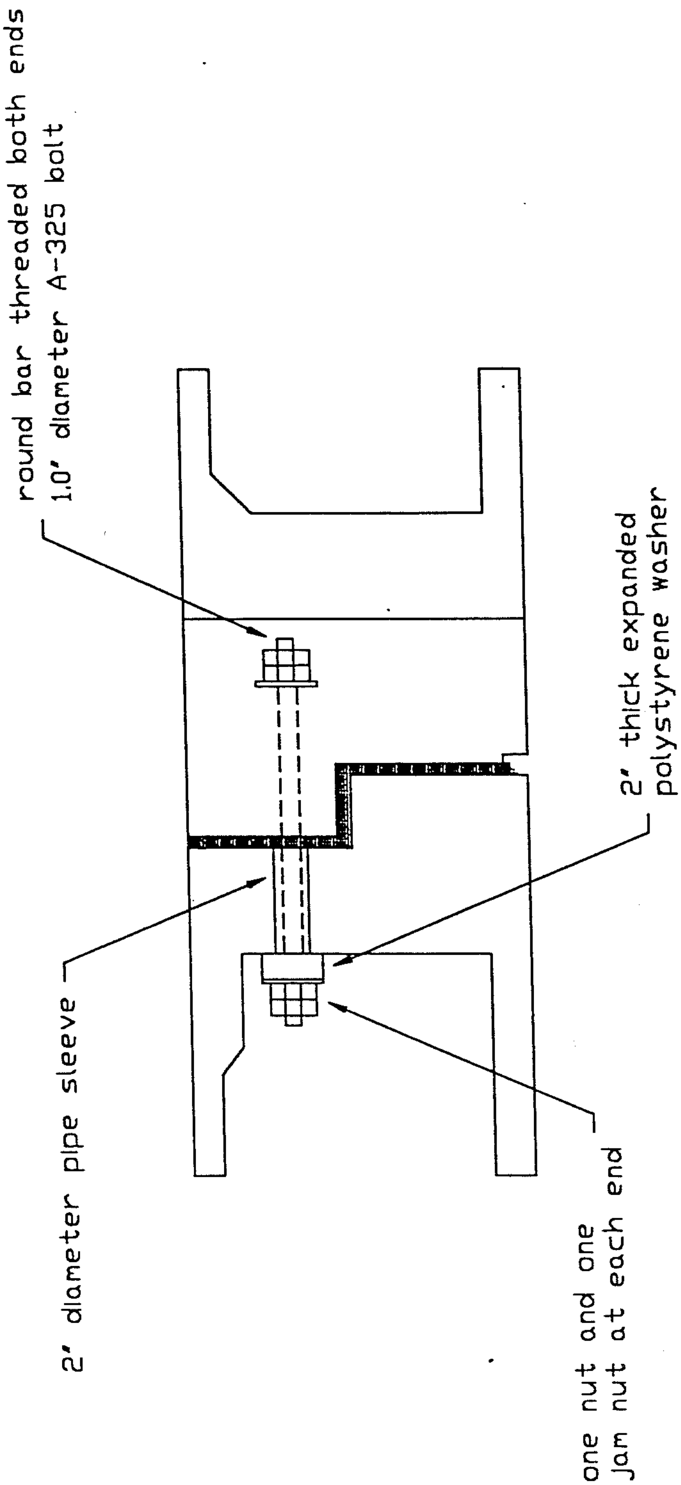
round bar threaded both ends
1.0" diameter A-325 bolt
2" thick expanded
polystyrene washer
2" diameter pipe sleeve
one nut and one
Jam nut at each end

Figure 6.1 - Movement-equalizer bolt

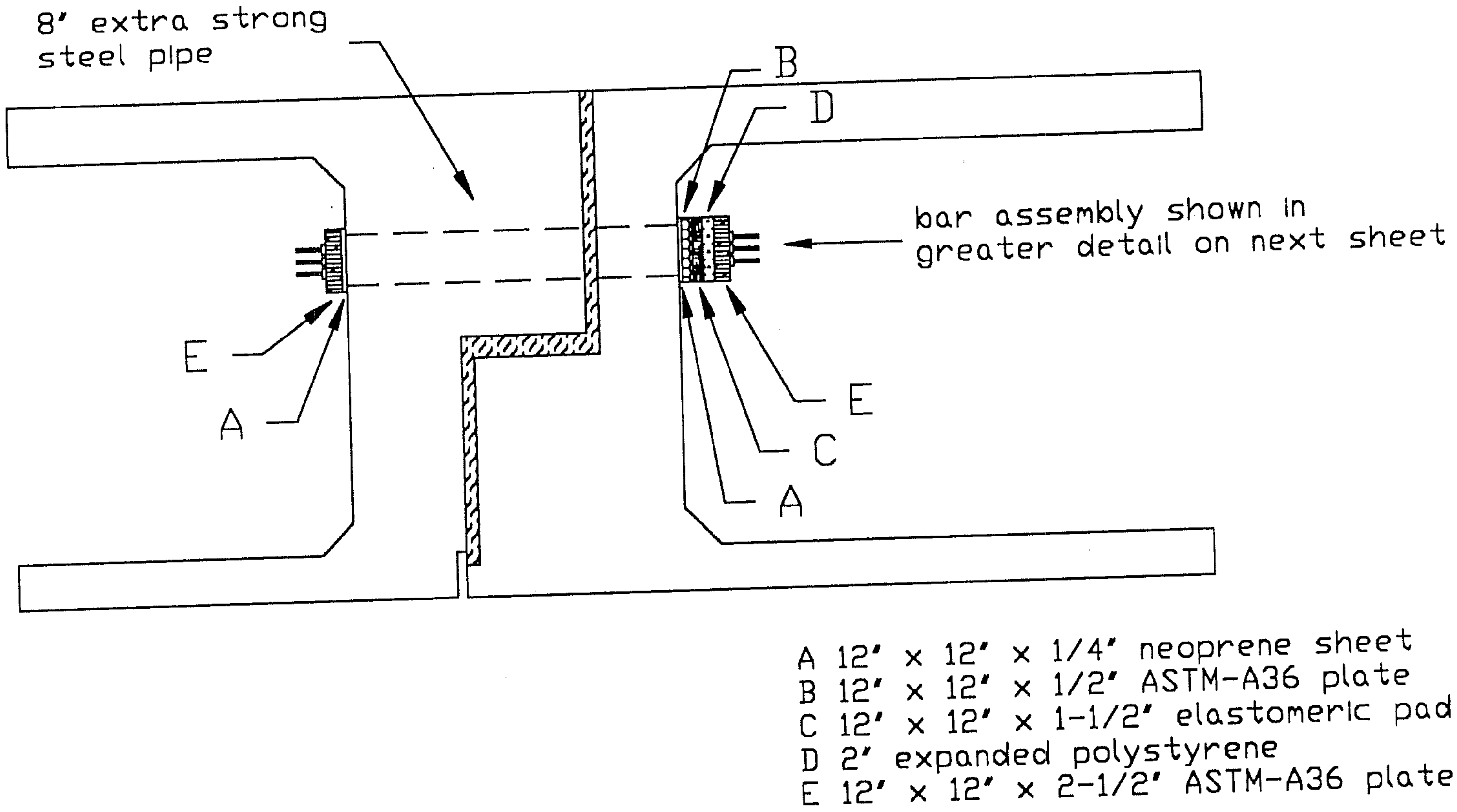
8' extra strong
steel pipe
B
D
bar assembly shown in
greater detail on next sheet
E
A
E
C
A
A 12' x 12' x 1/4' neoprene sheet
B 12' x 12' x 1/2' ASTM-A36 plate
C 12' x 12' x 1-1/2' elastomeric pad
D 2' expanded polystyrene
E 12' x 12' x 2-1/2' ASTM-A36 plate

Figure 6.2(a) - Overview of bar assembly

Figure 6.2 - Hinge restrainer detail (using bars)

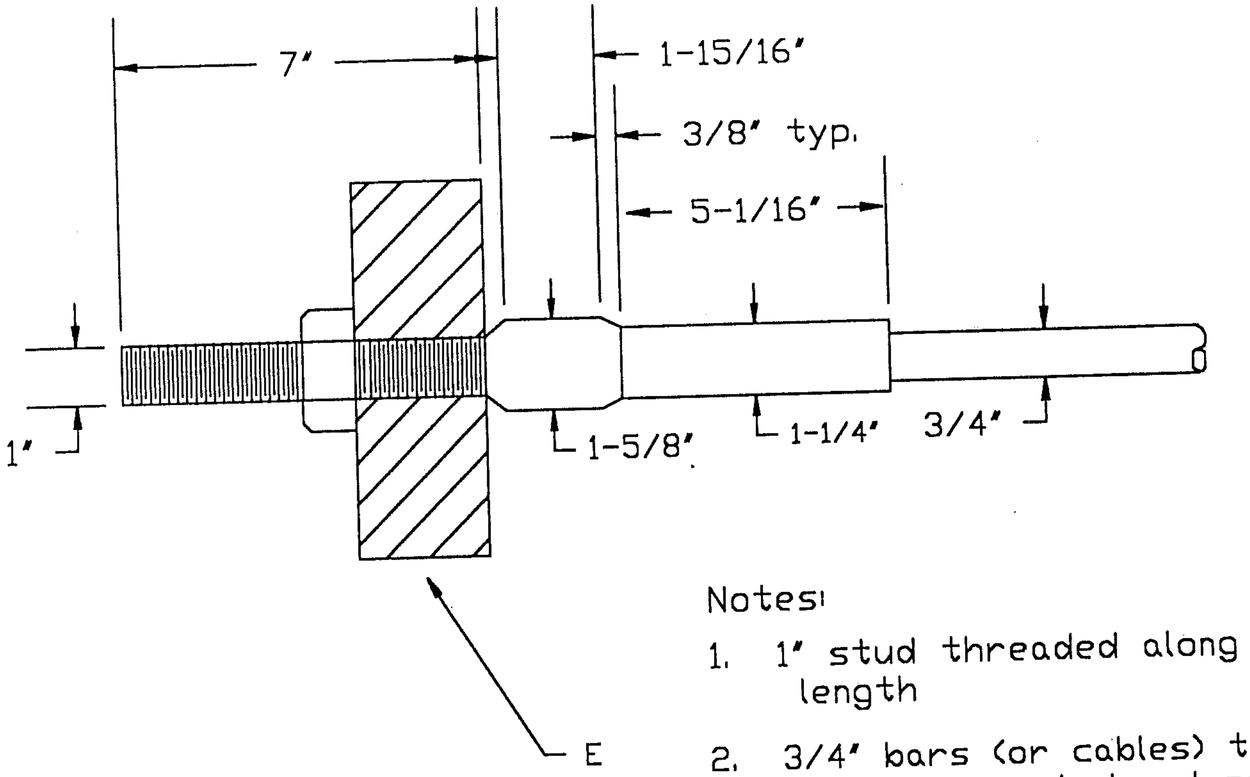
7"
1-15/16"
3/8" typ.
5-1/16"
1"
1-5/8"
1-1/4"
3/4"
E

Notes:

1. 1" stud threaded along entire length
2. 3/4" bars (or cables) to be swage connected and seal wrapped with duct tape or equal

Figure 6.2(b) - Detail of bar assembly

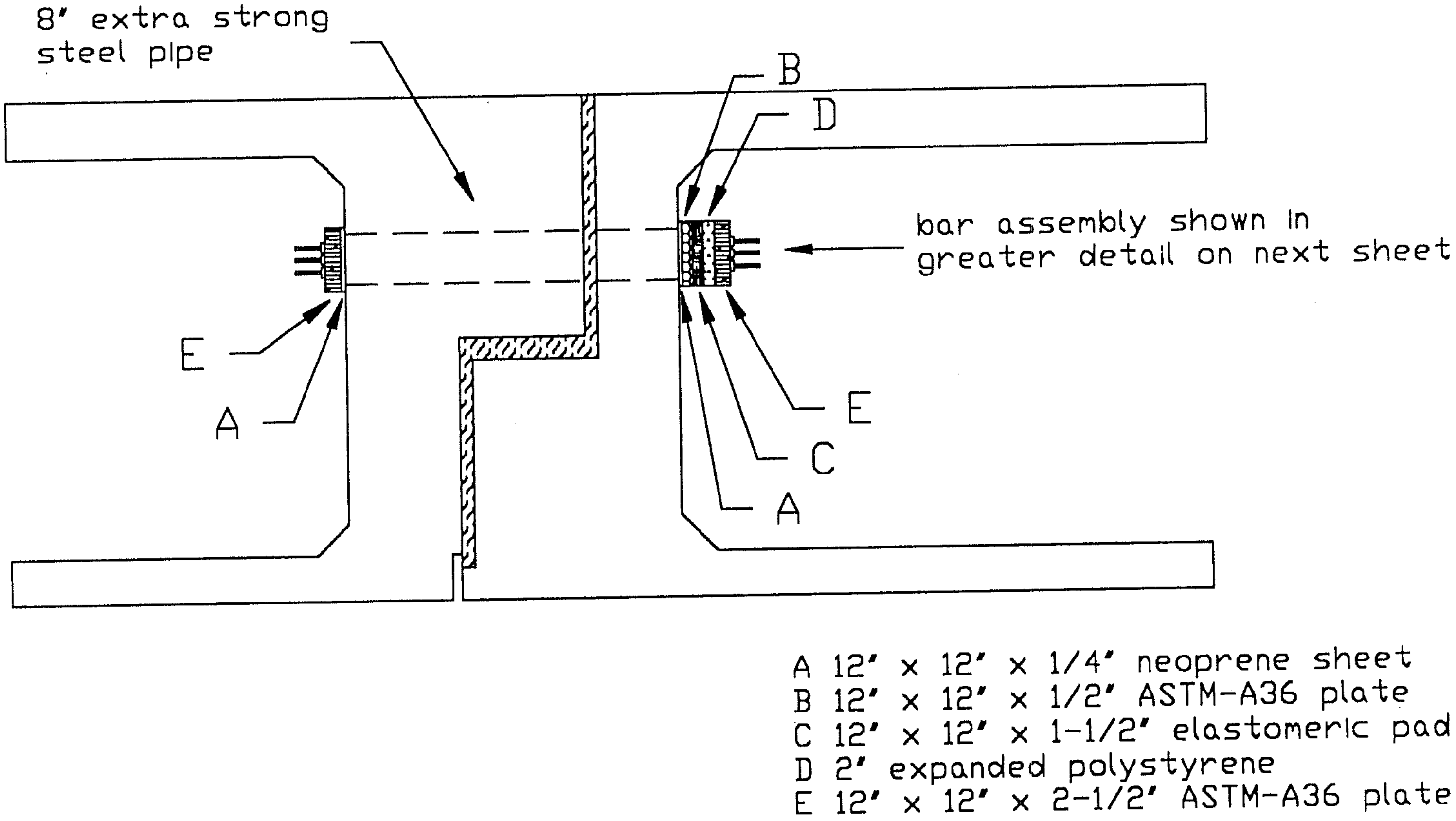
8″ extra strong steel pipe
B
D
bar assembly shown in greater detail on next sheet
E
A
E
C
A
A 12″ x 12″ x 1/4″ neoprene sheet
B 12″ x 12″ x 1/2″ ASTM-A36 plate
C 12″ x 12″ x 1-1/2″ elastomeric pad
D 2″ expanded polystyrene
E 12″ x 12″ x 2-1/2″ ASTM-A36 plate

Figure 6.3(a) - Overview of cable assembly

Figure 6.3 - Hinge restrainer detail (using cables)

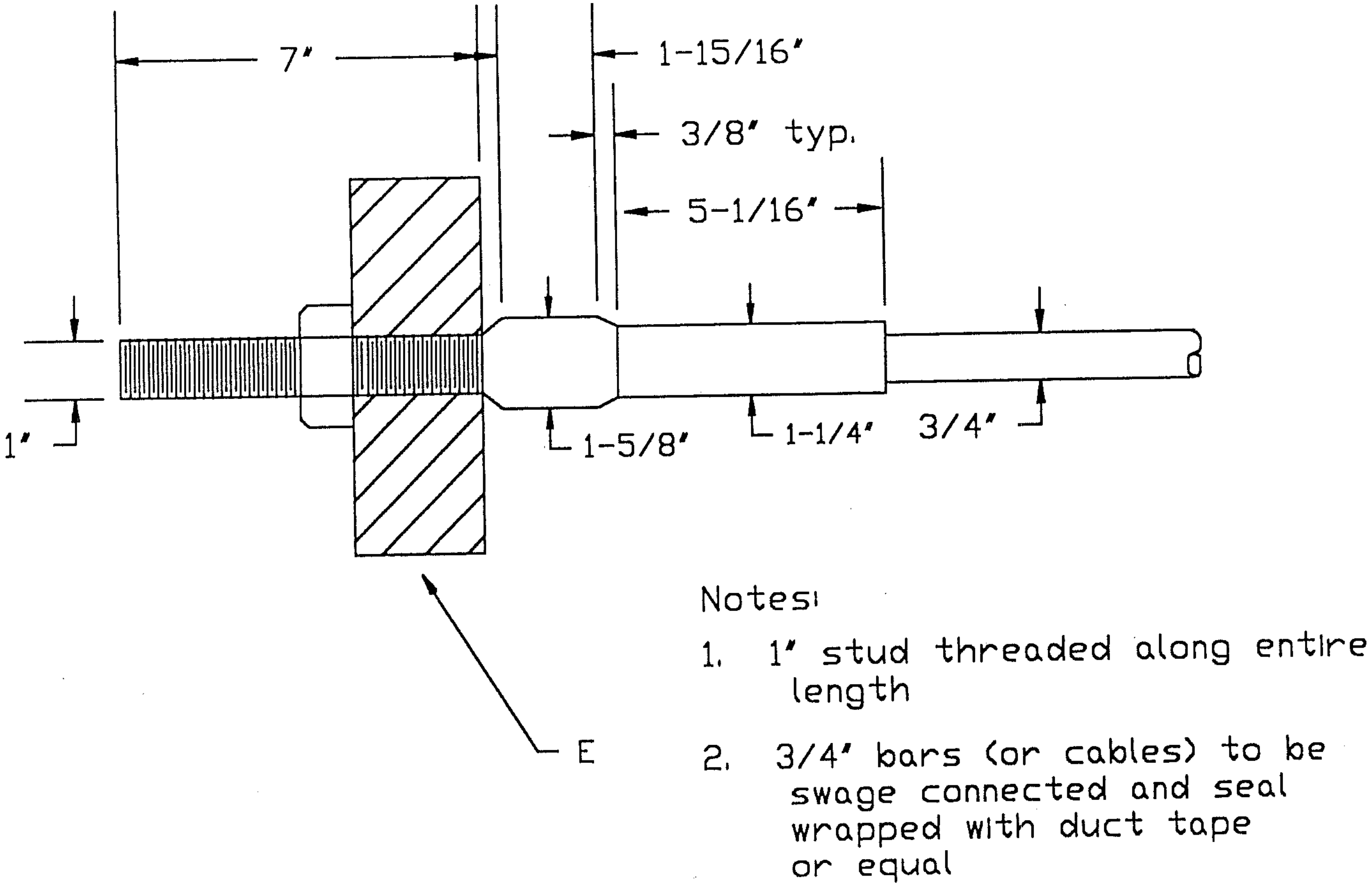
7"
1-15/16"
3/8" typ.
5-1/16"
1"
1-5/8"
1-1/4"
3/4"
E

Notes:

1. 1" stud threaded along entire length

2. 3/4" bars (or cables) to be swage connected and seal wrapped with duct tape or equal

Figure 6.3(b) - Detail of cable assembly

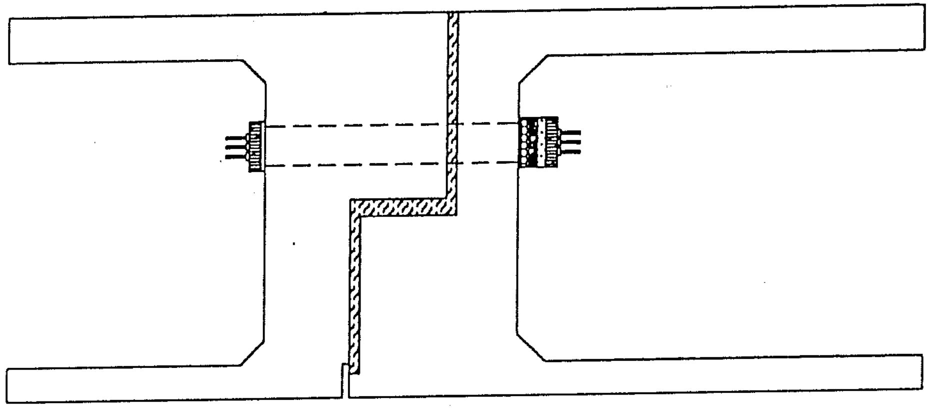

Figure 6.4(a) - Hinge restrainer before earthquake

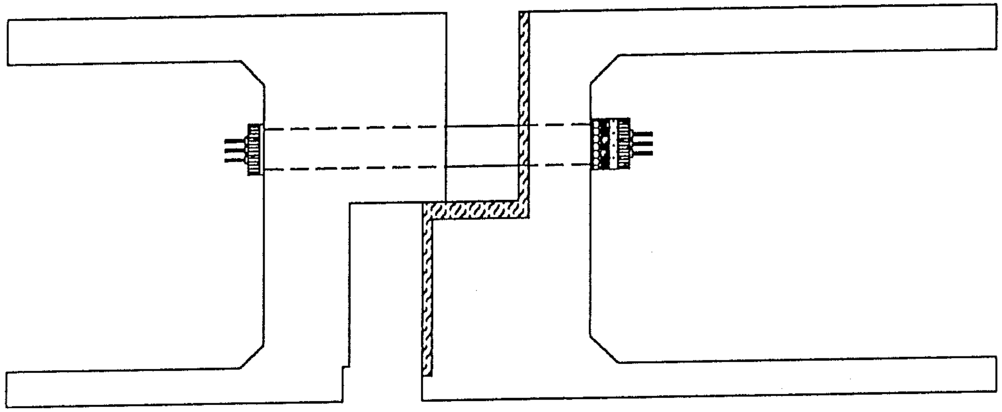

Figure 6.4(b) - Hinge restrainer stretches but keeps bridge together at hinge

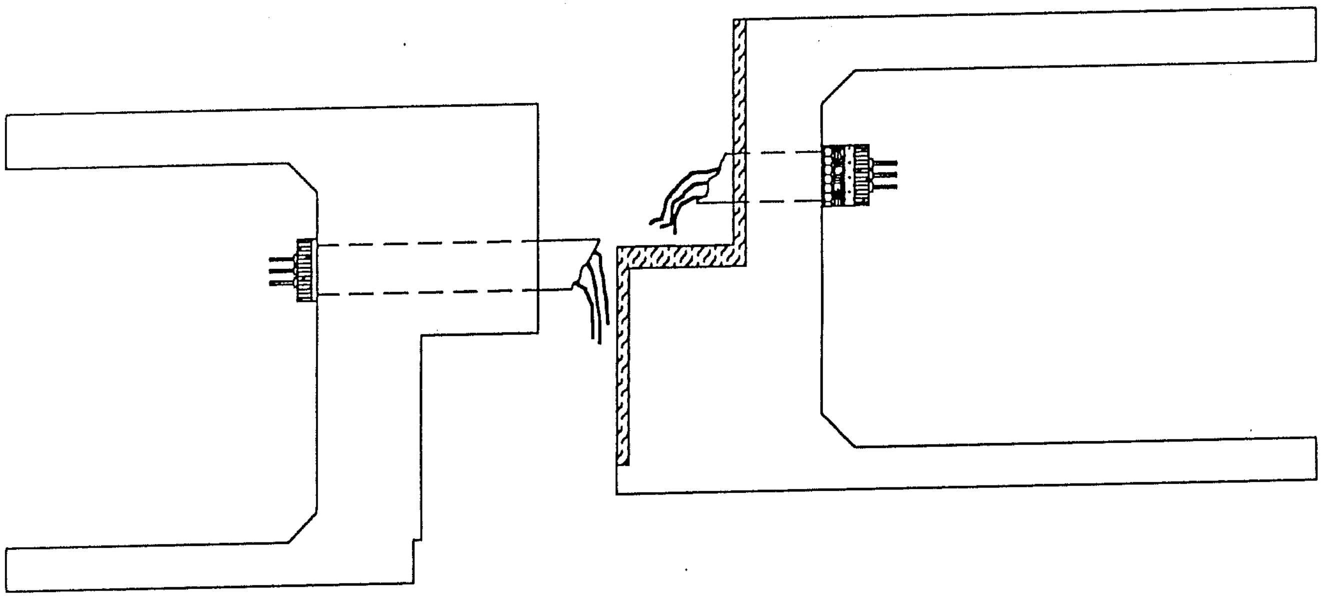

Figure 6.4(c) - If deflection is too big, the steel pipe could crack and the restrainers could rupture, resulting in the girder unseating

Figure 6.4 - Schematic showing failure of hinge restrainer assembly

6.1 Hinge Restrainer Stiffness

One of the most important factors when studying the cable hinge restrainers is the calculation of their stiffness. The procedure utilized herein follows the recommendations of the CALTRANS *Bridge Design Aids Manual* Section 14-12.[2]

The maximum allowable restrainer deflection is defined as:

$$D_r = D_y + D_g \tag{6.1}$$

$$D_y = \frac{F_y L}{E} \tag{6.2}$$

where D_r is the maximum allowable deflection, D_y is the deflection at yield, D_g is the gap in the restrainer system, F_y is the yield stress of the restrainers (176 ksi), L is the length of the restrainers, and E is Young's modulus (10,000 ksi before initial stretching).[21] Gaps are generally left in the system to account for thermal expansion, prestress shortening, and shrinkage. The gaps can be provided in different ways. First, the hinge seat can have a gap between the two adjacent spans as seen in Figure 6.5.

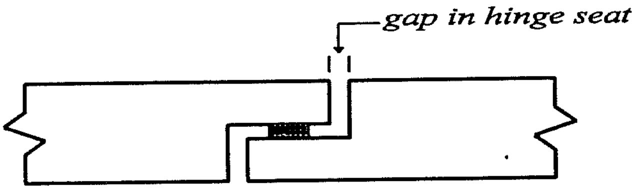

Figure 6.5 - Example of gap in hinge seat

This hinge seat often has elastomeric bearing pads and/or expanded polystyrene to provide additional stiffness and prevent pounding damage. The second way that the gap can be utilized is in the cable units themselves as shown in Figure 6.3. The cable restrainers are first tightened to a specified amount and then released so that they will contain a predetermined slack. The units used in the bridges in this study were initially tightened to 45 foot-pounds of torque and then released 1.25". This 1.25" is the maximum additional amount that the hinge joint is expected to open due to temperature, prestress shortening, shrinkage, and creep.

After the gaps have been calculated, the overall stiffness of the cable restrainer units can be calculated as:

$$K_{restrainer} = \frac{F_y N_r A_r}{D_r} \tag{6.3}$$

N_r is the number of restrainers and A_r is the area per restrainer, which is 0.222 in^2 for the three bridges in this study. This formula is not entirely accurate since D_r will continue to increase as the cable is stretched, but it is the best estimate for an elastic model.

In additional to the cable restrainer units, "movement-equalizer bolts" and bars are located at some of the hinges. These bolts and bars also help to hold the structure together during an earthquake, but are not included in any stiffness calculations. The bars experienced some drastic failures in the San Fernando earthquake, and therefore this detail is generally no longer used.

6.2 Stiffnesses for Structures Studied

The restrainer stiffnesses at each of the hinges was calculated using Equations 6.1 to 6.3. Table 6.1 describes the type of restrainer units for each bridge.

Table 6.1 - Restrainer Units for Each Bridge

bridge	restrainer unit type
north connector	3 restrainers consisting of 7-¾" bars 5 4-bar restrainer assemblies
separation and overhead	3 1" diameter movement-equalizing bolts 5 4-bar restrainer assemblies
south connector	3 1" diameter movement-equalizing bolts 5 4-bar restrainer assemblies

The value of the length of the cable hinge restrainers is assumed to be 48". This value was taken from the Priestly report[13] and a conversation with Mr. James Wright.[14] The value for D_g was taken as 1" since the hinges had 1" of expanded polystyrene. The 1.25" of "slack" in the cable is not included here as per CALTRANS recommendations since this slack is taken up by temperature, prestress shortening, shrinkage, and creep. The values for the stiffnesses of individual hinges are summarized in Table 6.2.

Table 6.2 - Cable Restrainer Unit Stiffnesses

bridge	stiffness (k/in)
north connector	781
separation and overhead	781
south connector	781

With these stiffnesses, computer analyses using BRIDGEQUAKE were made using the Sylmar Hospital earthquake records. For each bridge, the analysis was made with the vertical accelerations included. The time history for the displacement at each joint was obtained. Figures 6.6 to 6.8 show the results of these analyses.

6.3 Joint Displacement Results

As can be seen from Figures 6.6 to 6.8, the displacement at the joints was less than 4" except in the separation and overhead structure (Ramp C) hinges 2 and 4. Hinge 2 had a displacement of approximately 6.9" and hinge 4 had a displacement

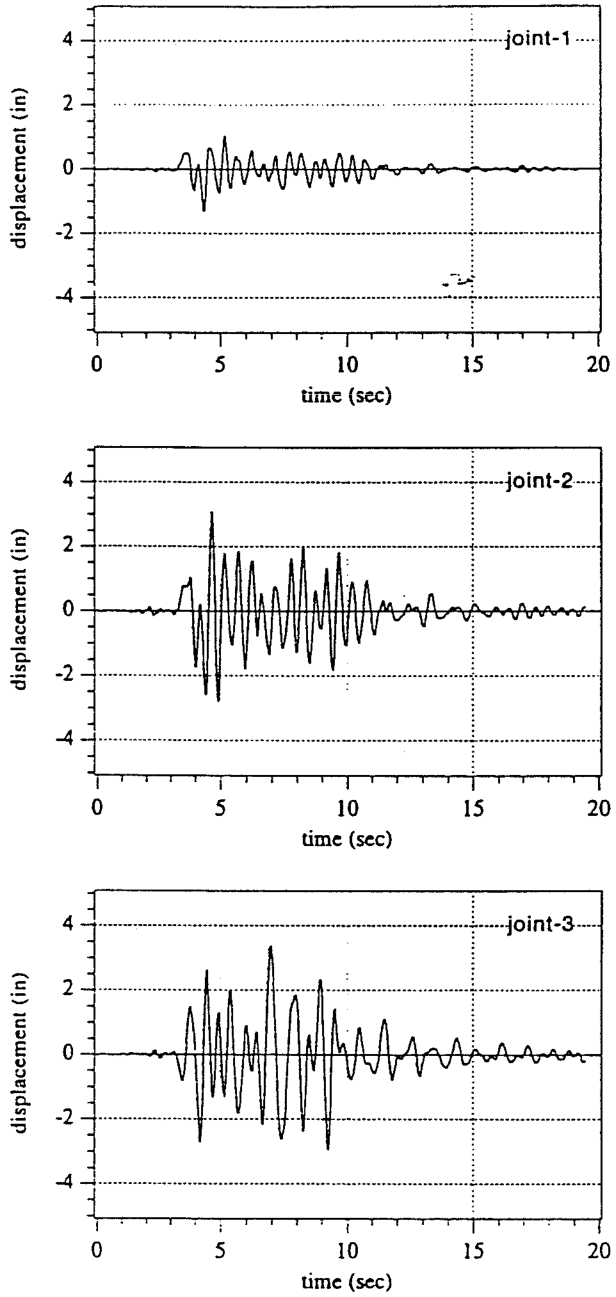

Figure 6.6 - Joint displacements for North Connector

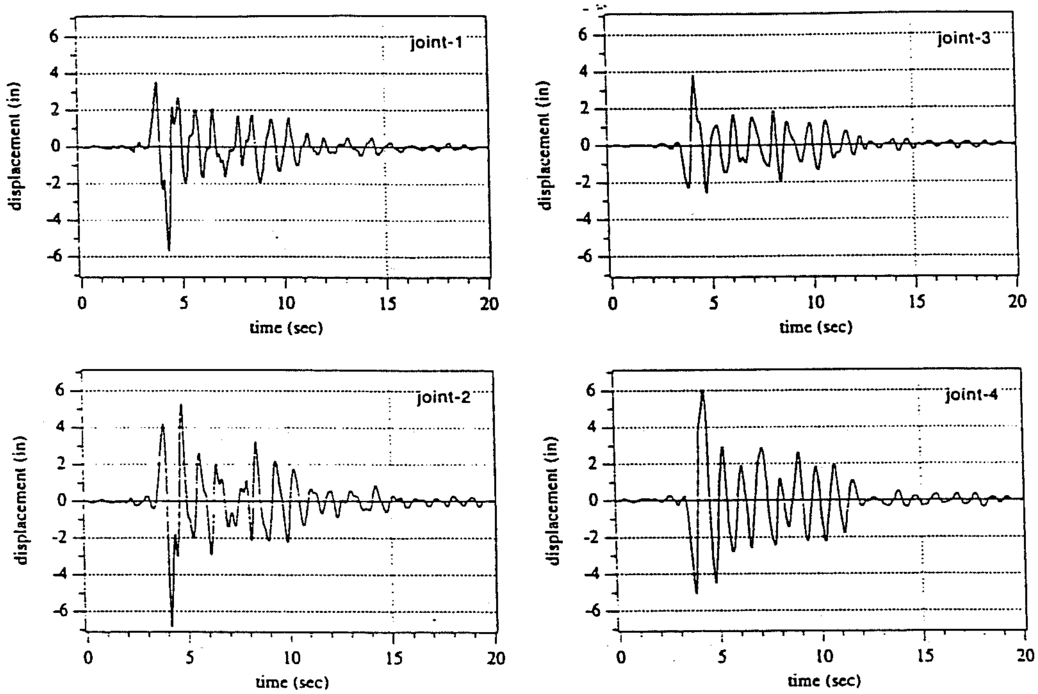

Figure 6.7 - Joint displacements for Separation and Overhead

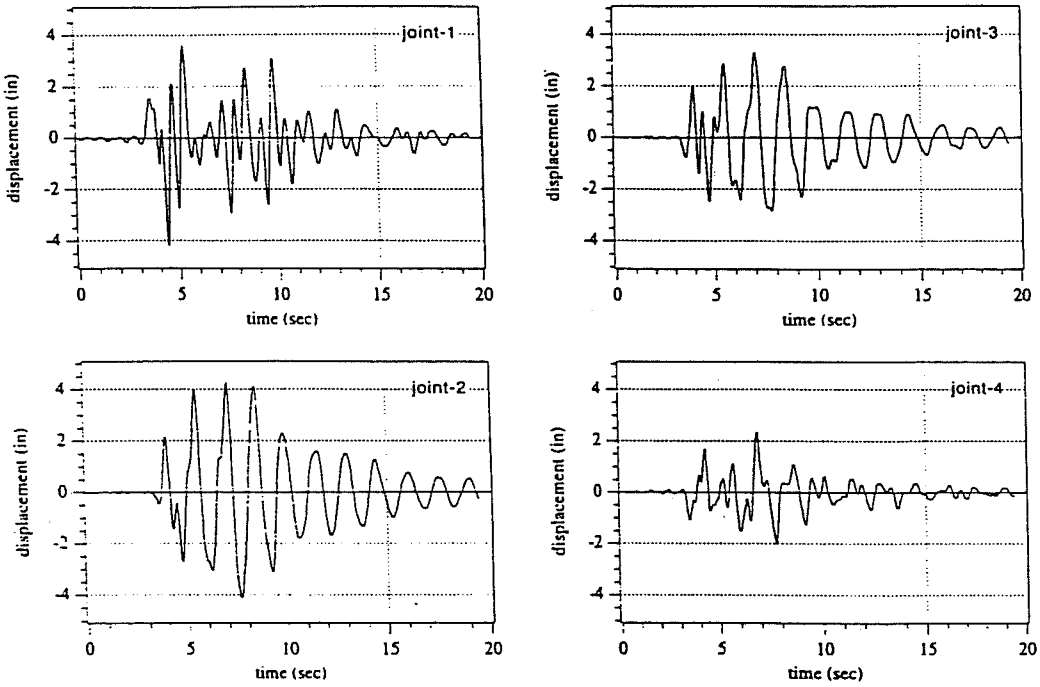

Figure 6.8 - Joint displacements for South Connector

of 6". All these displacements are satisfactory since they are less than the hinge seat width of 14" to 16". Some of the older bridges have bearing seat widths of 8". The displacements are satisfactory for these bridges as well. These results show that the current design and construction practices of CALTRANS are a definite improvement over the hinge restrainers that have failed in the past. Work needs to continue to be done to improve the performance of the bridges at the hinges.

The behavior of the bridges at the hinges could have been more accurately modeled using a non-linear behavior program for two reasons. First, the hinge restrainers act differently in tension than in compression because the hinge can only compress so far before it is pressing against the thin expanded polystyrene layer. Secondly, Equation 3 is really a non-linear equation that changes as the hinge expands.

CHAPTER 7

CONCLUSIONS

Major damage occurred to many highway bridges during the Northridge earthquake in January of 1994. High ground accelerations, both horizontal and vertical, led many to reevaluate various parts of the design process for typical freeway bridges in earthquake prone regions. Of particular interest in this study was the response of highway bridges to vertical accelerations when combined with the components of horizontal ground motion. The objectives of this study were:

- to analytically investigate the potential effects of vertical accelerations on the seismic response and performance of bridge structures when combined with the two horizontal components of motion.
- to correlate the prediction of the computer model to actual damage observed during the Northridge earthquake.
- to examine the different designs of post-tensioned bridges damaged in this earthquake to determine the levels of "load balancing" used by designers and the effects of vertical accelerations on these "load-balanced" structures.
- to assess the adequacy of present bridge design provisions which generally ignore vertical accelerations.

These objectives were reached by the use of a linear elastic computer program for all of the analyses. This chapter summarizes the findings relating to these objectives, makes recommendations for the present design codes, and proposes ideas for future research in these areas.

7.1 Summary of Findings

7.1.1 "Load-Balancing" Techniques

For this portion of the project, vertical accelerations of 1g were initially assumed so that the instantaneous effect of the dead load would be absent in the stress calculations. Prestress losses due to friction, anchor set, and long term losses were evaluated and the resulting stresses in the top and bottom fibers of the box girders were computed. With an assumed value of f'_c of 5000 psi, it was determined that tension cracks in the concrete would form at approximately 424 psi. This value was only exceeded three times, once in each of the bridges. Using the specified values of f'_c, the allowable tensile stress was exceeded four times, one time each in the north and south connectors and twice in the separation and overhead. All of these high tensile stresses occurred in the bottom fiber over the piers.

However, the vertical acceleration of 1g was not necessarily the worst case scenario for the bridges. In many cases, the vertical accelerations in the ground were amplified by a factor of 3.0 in the deck. Vertical accelerations of approximately 1.7g, a net of 0.7g acceleration upward, were recorded. This would cause the dead load to act in the opposite direction and further increase the tensile stresses.

The "load-balancing" technique is very effective for the design of box girders. After losses the prestress force balances approximately 67% of the dead load in one-span frames, approximately 80%-100% of the dead load moment in two-span frames, and approximately 90%-95% of the dead load moment in three-span frames. Any tensile cracks that may possibly occur due to the effect of the vertical accelerations are not a major problem since present design practice is to provide continuous reinforcing bars located in the top of the girders over the piers and at the bottom of the girders at midspan. (See Appendix C.)

7.1.2 Flexural Moment Demand Ratio

Using recommendation from the CALTRANS Memo to Designers manual, the flexural moment demand ratio, μ_F, was evaluated for each of the bridge piers. The flexural moment demand ratio is the ratio of the moment in the pier due to an earthquake to the nominal moment capacity of the pier. If the value of μ_F is greater than 1.5, it is assumed that the column has formed a plastic hinge. This calculation was done using the linear elastic computer program BRIDGEQUAKE. Three different inputs were used for the analyses of the bridges -- the Sylmar Hospital records, the artificial earthquake for the bridge site from Lamont-NCEER, and an artificial earthquake developed from the UBC/AASHTO spectrum.

Of the twenty-six piers that were evaluated, 4 (15%) developed plastic hinges under the Sylmar Hospital record case, 1 (4%) formed plastic hinges for the Lamont-NCEER artificial earthquake case, and 9 (35%) formed plastic hinges for the UBC/AASHTO case. The separation and overhead structure performed particularly poorly for the UBC/AASHTO earthquake with all of the piers but two developing plastic hinges due to moments in the out-of-plane direction.

7.1.3 Hinge Restrainers

The hinge restrainers now used in the retrofit of the bridges in the California area performed well using the linear elastic model. None of the hinge restrainers elongated an amount greater than the hinge seat. According to these calculations, the failure of these bridges was not because the box girders fell off at the hinge. The largest displacement was 6.9", which is much less than the 14" to 16" hinge seats that are provided in current design practice.

7.2 Conclusions

Based on the results of this study, a number of conclusions can be made. The first concerns the computer program that was used. While the frequency based, linear elastic computer program was efficient, a non-linear computer program would have provided more accurate results. The behavior of the bridge at the hinges could have been more accurately modeled. A nonlinear model would have also provided more accurate results for behavior of the piers, since a nonlinear model would have allowed displacement or curvature ductility to be computed for the piers. However, the fact that a linear elastic program was used does not invalidate the results. It provides some idea of the magnitude of the moments that the piers experience during an earthquake. The flexural moment demand ratio used the linear elastic model to provide some feeling of where the piers would form plastic hinges. The linear model also helped to show that the addition of vertical accelerations did not cause any of the piers to go into tension. This was seen in all of the diagrams of Chapter 5.

Second, it can be concluded that the "load-balancing" technique for designing post-tensioned members is an accurate and effective method. The tension stresses that resulted from the vertical accelerations occurred only at isolated instants of time. Thus, the cracking mechanism does not have time to even get started. This can be evidenced by the fact that there really was no serious tensile cracking reported near the piers of these three bridges after the Northridge earthquake. The non-prestressed reinforcement that is in the girders also helps control the tensile cracks.

It is important that vertical accelerations be included in the design of the piers. The moments applied to the pier can increase slightly by the application of vertical accelerations (more in the in-plane direction than in the out-of-plane direction). The piers had moments that increased on the average by a factor of 1.08 (95% confidence limit = (1.04, 1.12)) when the three components of motion were applied instead of just two components of motion. In isolated instances, two piers increased by factors of 1.54 and 1.64.

Third, the type of behavior that was exhibited by the columns in this study is not the type of behavior that would have caused the collapse of the bridges during the Northridge earthquake. The probable cause of failure mentioned by Priestly in his report[2], the short piers failing in shear and spans subsequently collapsing due to negative moment failures, is a much more likely scenario than vertical accelerations being the cause.

Fourth, as mentioned previously, the hinge restrainers that are now used in the retrofit of the bridges in the California area performed well. None of the hinge restrainers elongated an amount greater than the hinge seat.

7.3 Design Recommendations

As mentioned in the previous section, the major design recommendation that results from this report is that vertical accelerations need to be considered in the design of the piers. Increased moments on the piers as a result of vertical accelerations can cause major problems if the pier is underdesigned. While a time domain analysis of every bridge is probably unfeasible and uneconomical, the moments in the pier could be multiplied by a factor (possibly 1.1)

A second recommendation coming from this study is the amount of regular continuous reinforcement that is in the prestressed concrete sections of the bridge. If high vertical accelerations do occur, this reinforcement could be required to close tensile cracks and carry the moment. Currently, there is not much conventional reinforcement in these prestressed sections.

7.4 Possible Future Research

There are some definite areas where future research can be done with respect to vertical accelerations.

(1) A more accurate computer model needs to be developed. A time-domain program that includes non-linear effects on the piers and hinge restrainers would improve the results.

(2) With retrofitting becoming a viable economical option, the behavior of piers under axial load and bending that have been retrofit with steel jackets or isolation silos is a definite area in need of research.

(3) A more accurate model for the hinge needs to be developed. The behavior of the hinge is completely different if the cables are in tension or compression and if there is a filler material or not in the hinge. A linear elastic model of this hinge is not sufficiently accurate.

(4) Tests that study the effects of vertical accelerations on the reactions at the bearing pads supporting the box girders can be run. This requires a time domain computer program rather than the frequency domain computer used in this study. This type of study could also be done with an actual physical model.

Appendix A

CALTRANS Bridge Plans

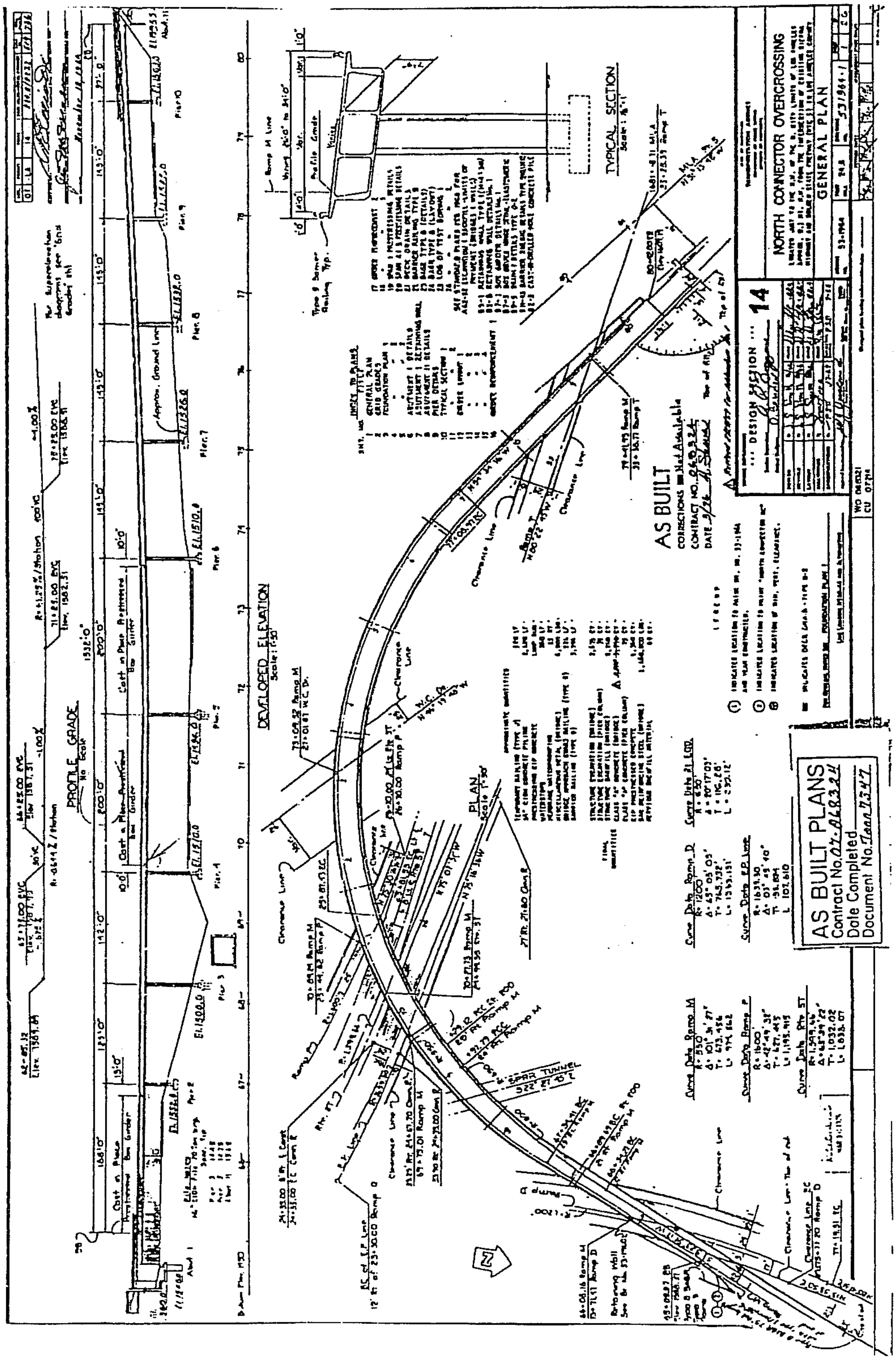
PROFILE GRADE
DEVELOPED ELEVATION
PLAN
TYPICAL SECTION
AS BUILT
AS BUILT PLANS
NORTH CONNECTOR OVERCROSSING
GENERAL PLAN
14

Figure A.1 - North Connector general plan

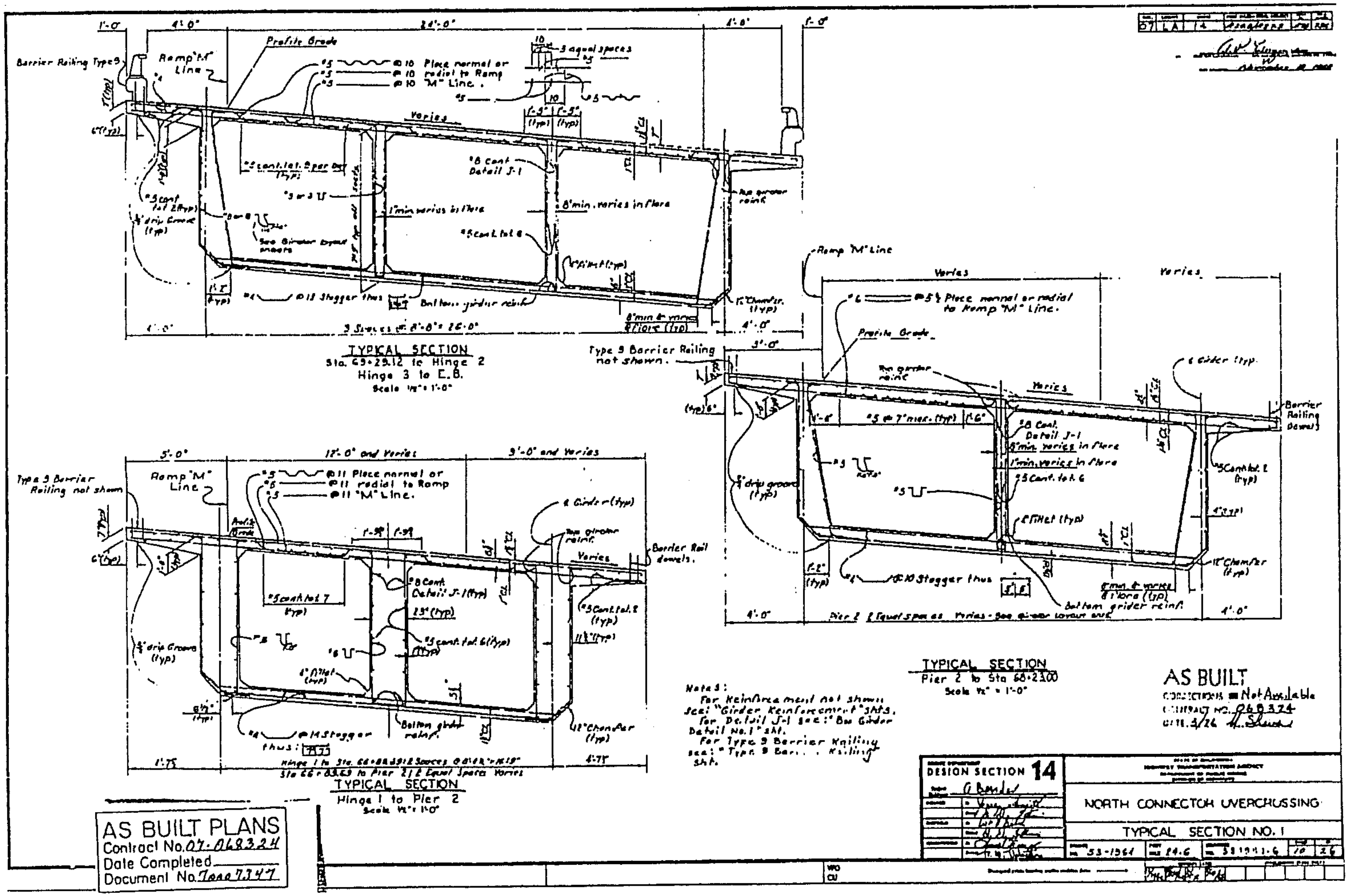
TYPICAL SECTION
Sta. 63+29.12 to Hinge 2
Hinge 3 to E.B.
Scale ½" = 1'-0"
TYPICAL SECTION
Pier 2 to Sta 68+23.00
Scale ½" = 1'-0"
TYPICAL SECTION
Hinge 1 to Pier 2
Scale ½" = 1'-0"
Barrier Railing Type 9
Ramp "M" Line
Profile Grade
Varies
Type 9 Barrier Railing not shown.
Barrier Rail dowels.
Notes:
For Reinforcement not shown see: "Girder Reinforcement" shts.
For Detail J-1 see: "Box Girder Detail No. 1" sht.
For Type 9 Barrier Railing see: "Type 9 Barrier Railing" sht.
AS BUILT
AS BUILT PLANS
Contract No. 07-068324
Date Completed
Document No.
DESIGN SECTION 14
NORTH CONNECTOR OVERCROSSING
TYPICAL SECTION NO. 1

Figure A.2 - North Connector typical section No. 1

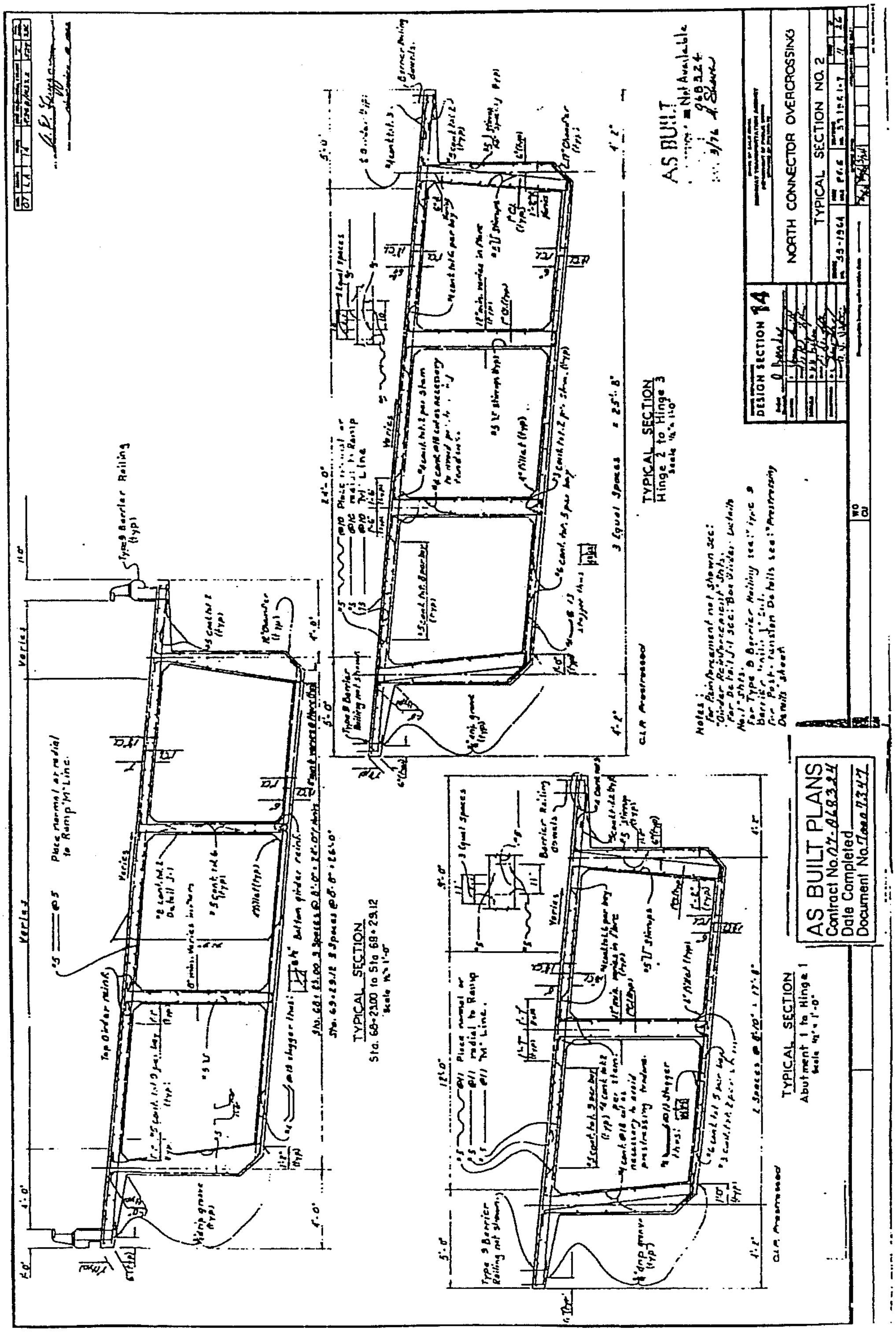
TYPICAL SECTION
Sta. 68+23.00 to Sta 69+29.12
TYPICAL SECTION
Hinge 2 to Hinge 3
TYPICAL SECTION
Abutment 1 to Hinge 1
AS BUILT
AS BUILT PLANS
Contract No.
Date Completed
Document No.
DESIGN SECTION 14
NORTH CONNECTOR OVERCROSSING
TYPICAL SECTION NO. 2

Figure A.3 - North Connector typical section No. 2

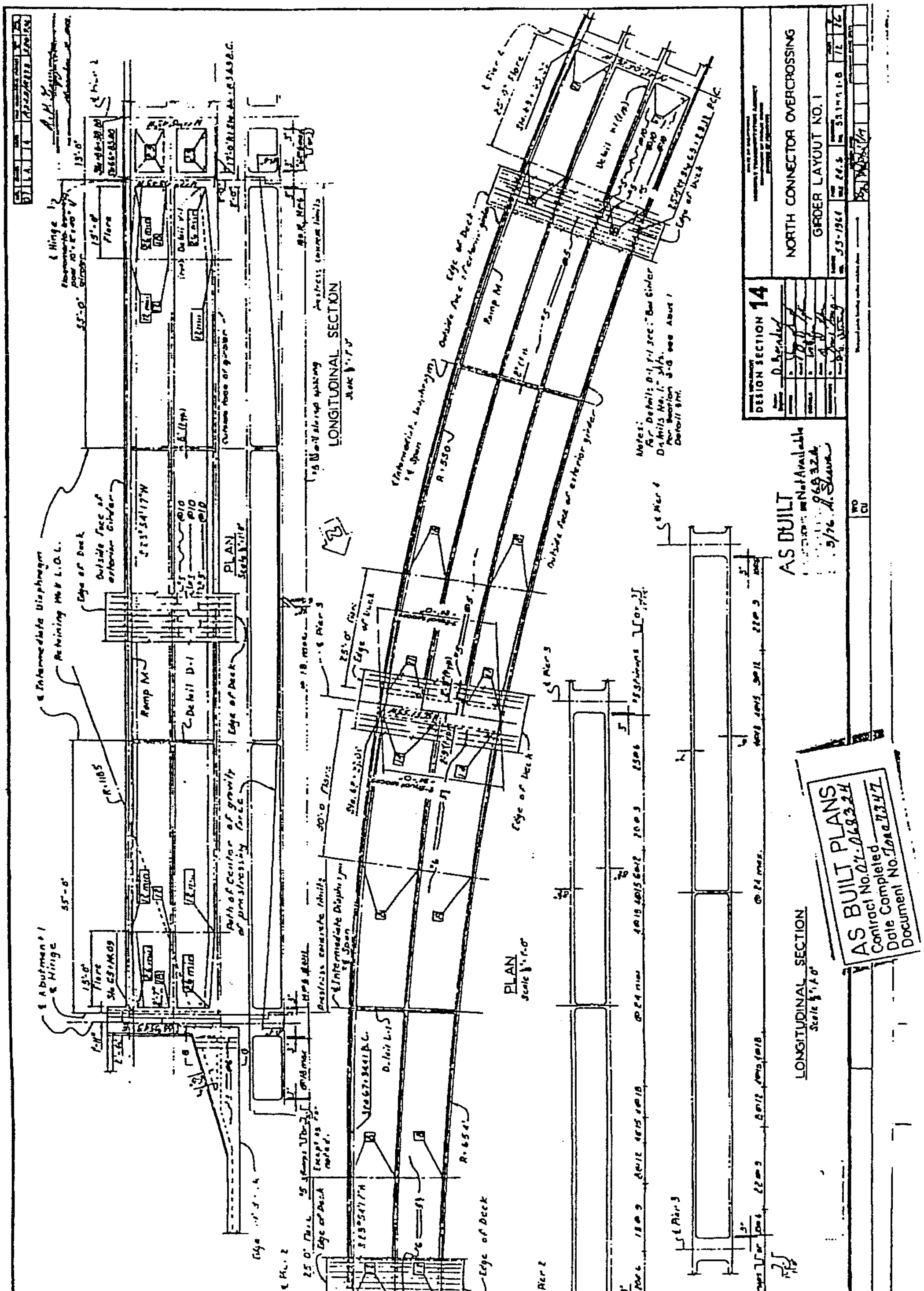
NORTH CONNECTOR OVERCROSSING
GIRDER LAYOUT NO. 1
DESIGN SECTION 14
AS BUILT
AS BUILT PLANS
Contract No.
Date Completed
Document No.
PLAN
LONGITUDINAL SECTION
Ramp M
Edge of Deck
R=550
R=1105
55'-0"
15'-0"
25'-0"

Figure A.4 - North Connector girder layout No. 1

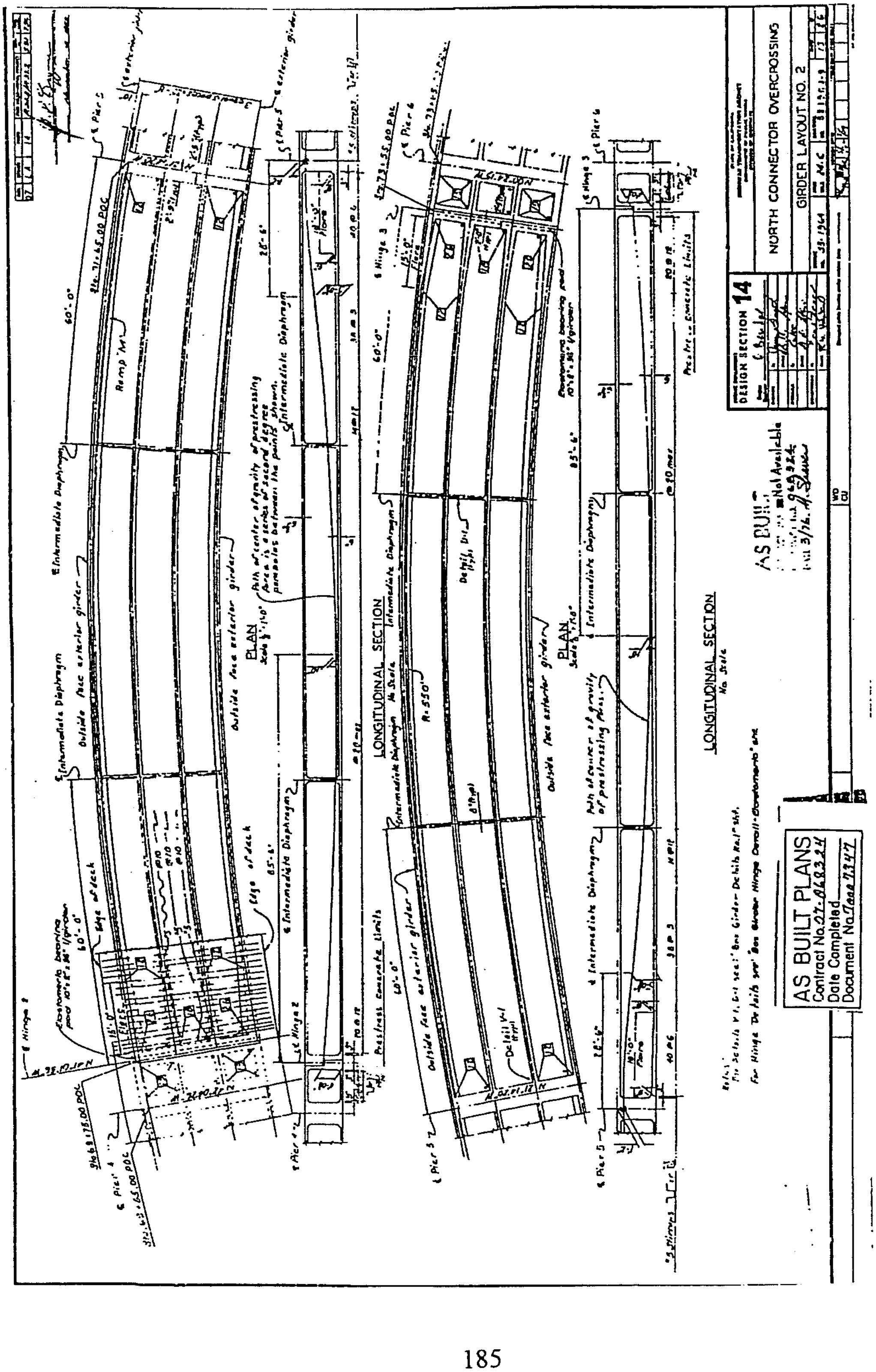
NORTH CONNECTOR OVERCROSSING
GIRDER LAYOUT NO. 2
DESIGN SECTION 14
PLAN
LONGITUDINAL SECTION
Ramp 'M'
Outside face exterior girder
Intermediate Diaphragm
Prestress concrete limits
Edge of deck
60'-0"
85'-6"
R=550'
AS BUILT PLANS
Contract No.
Date Completed
Document No.

Figure A.5 - North Connector girder layout No. 2

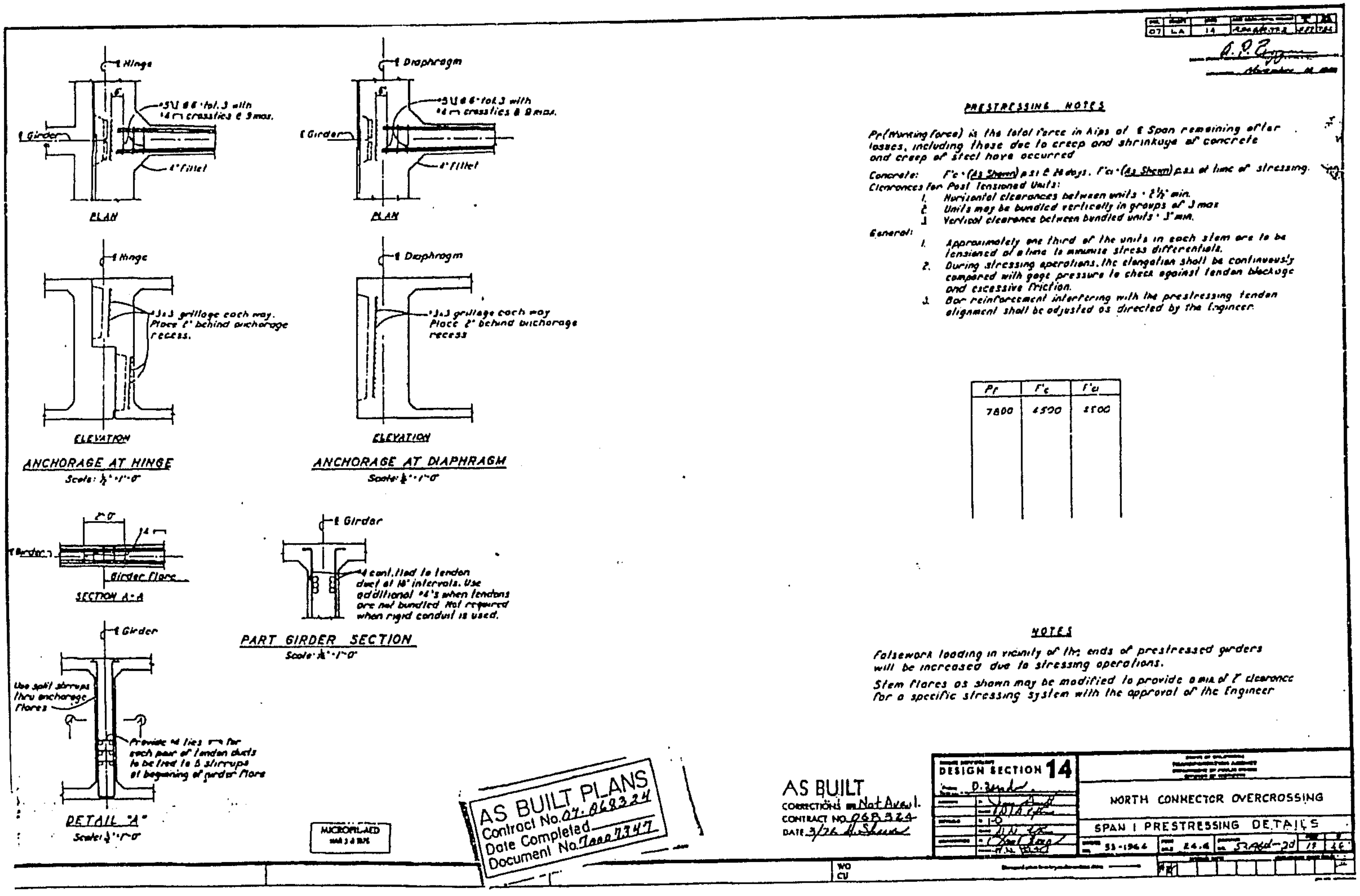
07
LA
14
℄ Hinge
#5 ⊔ @ 6" tot. 3 with
#4 ⌐ crossties @ 9 max.
℄ Girder
4" fillet
PLAN
℄ Diaphragm
#5 ⊔ @ 6" tot. 3 with
#4 ⌐ crossties @ 9 max.
℄ Girder
4" fillet
PLAN
℄ Hinge
#3 x 3 grillage each way.
Place 2" behind anchorage recess.
ELEVATION
ANCHORAGE AT HINGE
Scale: ½" = 1'-0"
℄ Diaphragm
#3 x 3 grillage each way
Place 2" behind anchorage recess
ELEVATION
ANCHORAGE AT DIAPHRAGM
Scale: ½" = 1'-0"
2'-0"
#4 ⌐
℄ Girder
Girder flare
SECTION A-A
℄ Girder
#4 cont. tied to tendon duct at 18" intervals. Use additional #4's when tendons are not bundled. Not required when rigid conduit is used.
PART GIRDER SECTION
Scale: ½" = 1'-0"
℄ Girder
Use split stirrups thru anchorage flares
A
A
Provide #4 ties ⌐ for each pair of tendon ducts to be tied to 5 stirrups at beginning of girder flare
DETAIL "A"
Scale: ½" = 1'-0"
MICROFILMED
DESIGN SECTION 14
D. [illegible]
1-0
NORTH CONNECTOR OVERCROSSING
SPAN 1 PRESTRESSING DETAILS
53-1964
24.4
53-[illegible]-20
WO
CU

PRESTRESSING NOTES

Pr (Working force) is the total force in kips of ℄ Span remaining after losses, including those due to creep and shrinkage of concrete and creep of steel have occurred

Concrete: f'c = (As Shown) psi @ 28 days. f'ci = (As Shown) psi at time of stressing.

Clearances for Post Tensioned Units:
1. Horizontal clearances between units = 1½" min.
2. Units may be bundled vertically in groups of 3 max
3. Vertical clearance between bundled units = 3" min.

General:
1. Approximately one third of the units in each stem are to be tensioned at a time to minimize stress differentials.
2. During stressing operations, the elongation shall be continuously compared with gage pressure to check against tendon blockage and excessive friction.
3. Bar reinforcement interfering with the prestressing tendon alignment shall be adjusted as directed by the Engineer.

Pr	f'c	f'ci
7800	4500	3500

NOTES

Falsework loading in vicinity of the ends of prestressed girders will be increased due to stressing operations.

Stem flares as shown may be modified to provide a min. of 1" clearance for a specific stressing system with the approval of the Engineer

AS BUILT PLANS
Contract No. 07-068324
Date Completed
Document No. 7000 7347

AS BUILT
CORRECTIONS Not Avail.
CONTRACT NO. 068324
DATE 3/76

Figure A.6 - North Connector span 1 prestressing details

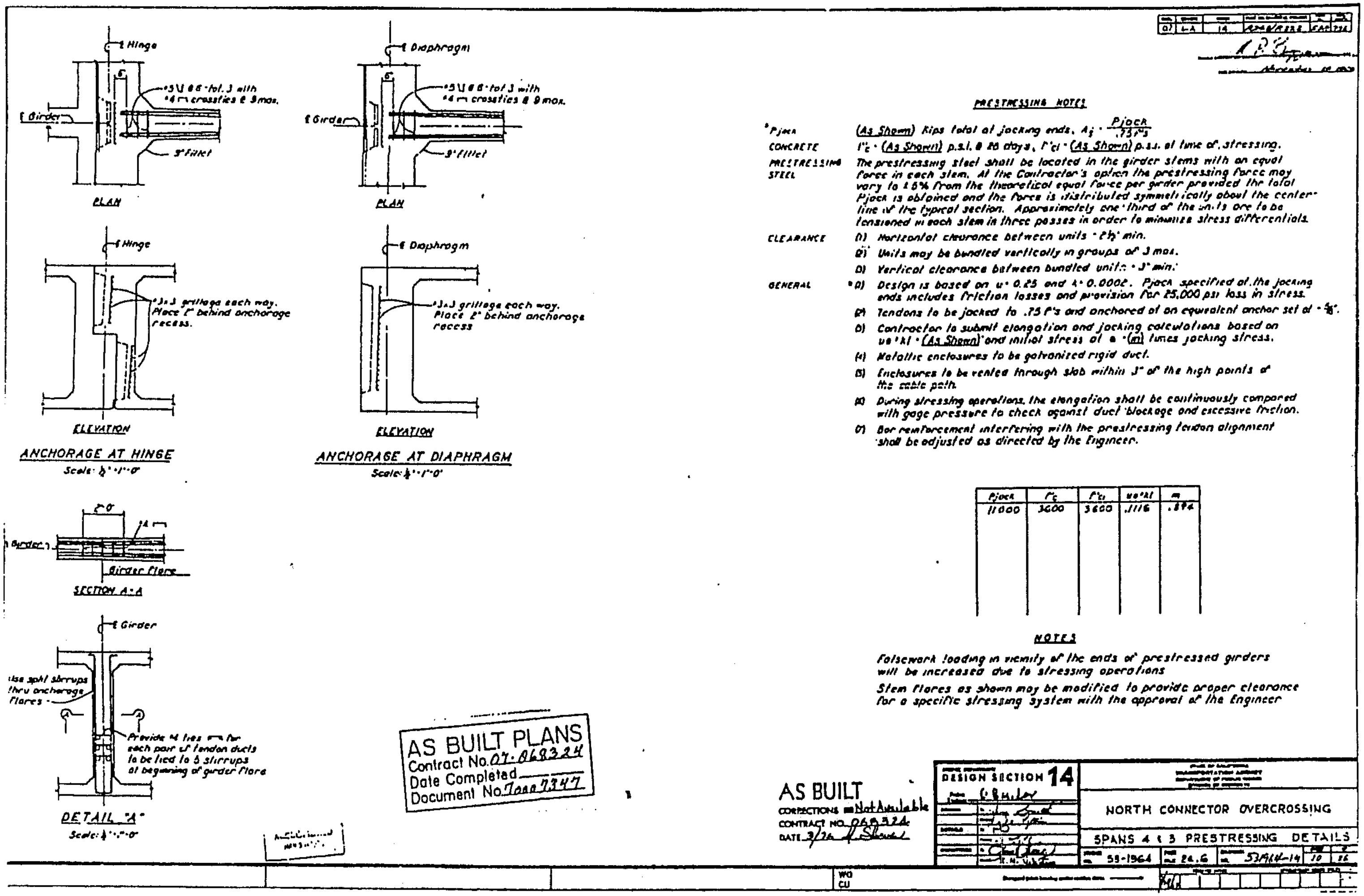
℄ Hinge
#5 ⊔ @ 6" tot. 3 with #4 ⊓ crossties @ 9 max.
℄ Girder
9" fillet
PLAN
℄ Diaphragm
#5 ⊔ @ 6" tot 3 with #4 ⊓ crossties @ 9 max.
℄ Girder
9" fillet
PLAN
℄ Hinge
#3×3 grillage each way. Place 2" behind anchorage recess.
ELEVATION
ANCHORAGE AT HINGE
Scale: ½" = 1'-0"
℄ Diaphragm
#3×3 grillage each way. Place 2" behind anchorage recess
ELEVATION
ANCHORAGE AT DIAPHRAGM
Scale: ½" = 1'-0"
2'-0"
#4 ⊓
℄ Girder
Girder Flare
SECTION A-A
℄ Girder
Use split stirrups thru anchorage flares
A
A
Provide #4 ties ⊓ for each pair of tendon ducts to be tied to 5 stirrups at beginning of girder flare
DETAIL "A"
Scale: ½" = 1'-0"
DESIGN SECTION 14
NORTH CONNECTOR OVERCROSSING
SPANS 4 & 5 PRESTRESSING DETAILS
53-1964
24.6
53/1964-14
10
16
WO
CU

PRESTRESSING NOTES

*Pjack (As Shown) Kips total at jacking ends. $A_s = \frac{P_{jack}}{.75f'_s}$

CONCRETE f'_c = (As Shown) p.s.i. @ 28 days, f'_{ci} = (As Shown) p.s.i. at time of stressing.

PRESTRESSING STEEL The prestressing steel shall be located in the girder stems with an equal force in each stem. At the Contractor's option the prestressing force may vary to ±5% from the theoretical equal force per girder provided the total Pjack is obtained and the force is distributed symmetrically about the center-line of the typical section. Approximately one-third of the units are to be tensioned in each stem in three passes in order to minimize stress differentials.

CLEARANCE
1) Horizontal clearance between units = 1½" min.
2) Units may be bundled vertically in groups of 3 max.
3) Vertical clearance between bundled units = 3" min.

GENERAL
*1) Design is based on u = 0.25 and k = 0.0002. Pjack specified at the jacking ends includes friction losses and provision for 25,000 psi loss in stress.
2) Tendons to be jacked to .75 f's and anchored at an equivalent anchor set of = ⅝".
3) Contractor to submit elongation and jacking calculations based on uα+kl = (As Shown) and initial stress at a = (m) times jacking stress.
4) Metallic enclosures to be galvanized rigid duct.
5) Enclosures to be vented through slab within 3" of the high points of the cable path.
6) During stressing operations, the elongation shall be continuously compared with gage pressure to check against duct blockage and excessive friction.
7) Bar reinforcement interfering with the prestressing tendon alignment shall be adjusted as directed by the Engineer.

Pjack	f'_c	f'_{ci}	uα+kl	m
11000	3600	3600	.1116	.894

NOTES

Falsework loading in vicinity of the ends of prestressed girders will be increased due to stressing operations

Stem flares as shown may be modified to provide proper clearance for a specific stressing system with the approval of the Engineer

AS BUILT PLANS
Contract No. 07-068324
Date Completed
Document No. 7000 7347

AS BUILT
CORRECTIONS Not Available
CONTRACT NO. 068324
DATE 3/76

Figure A.7 - North Connector spans 4 & 5 prestressing details

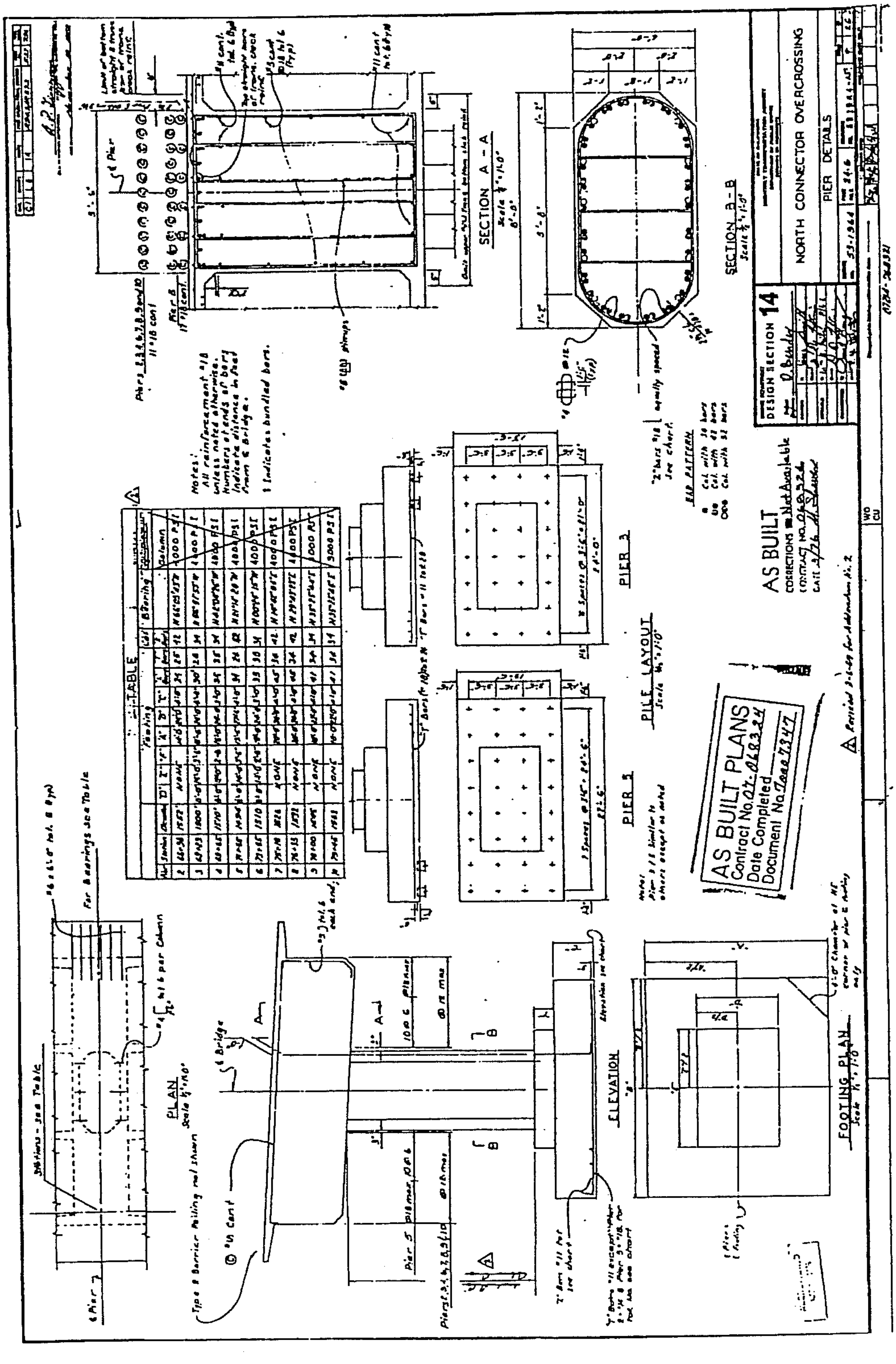
NORTH CONNECTOR OVERCROSSING
PIER DETAILS
DESIGN SECTION 14
SECTION A - A
SECTION B - B
PILE LAYOUT
PIER 3
PIER 5
ELEVATION
FOOTING PLAN
PLAN
TABLE
Notes:
AS BUILT
AS BUILT PLANS
Contract No.
Date Completed
Document No.

Figure A.8 - North Connector pier details

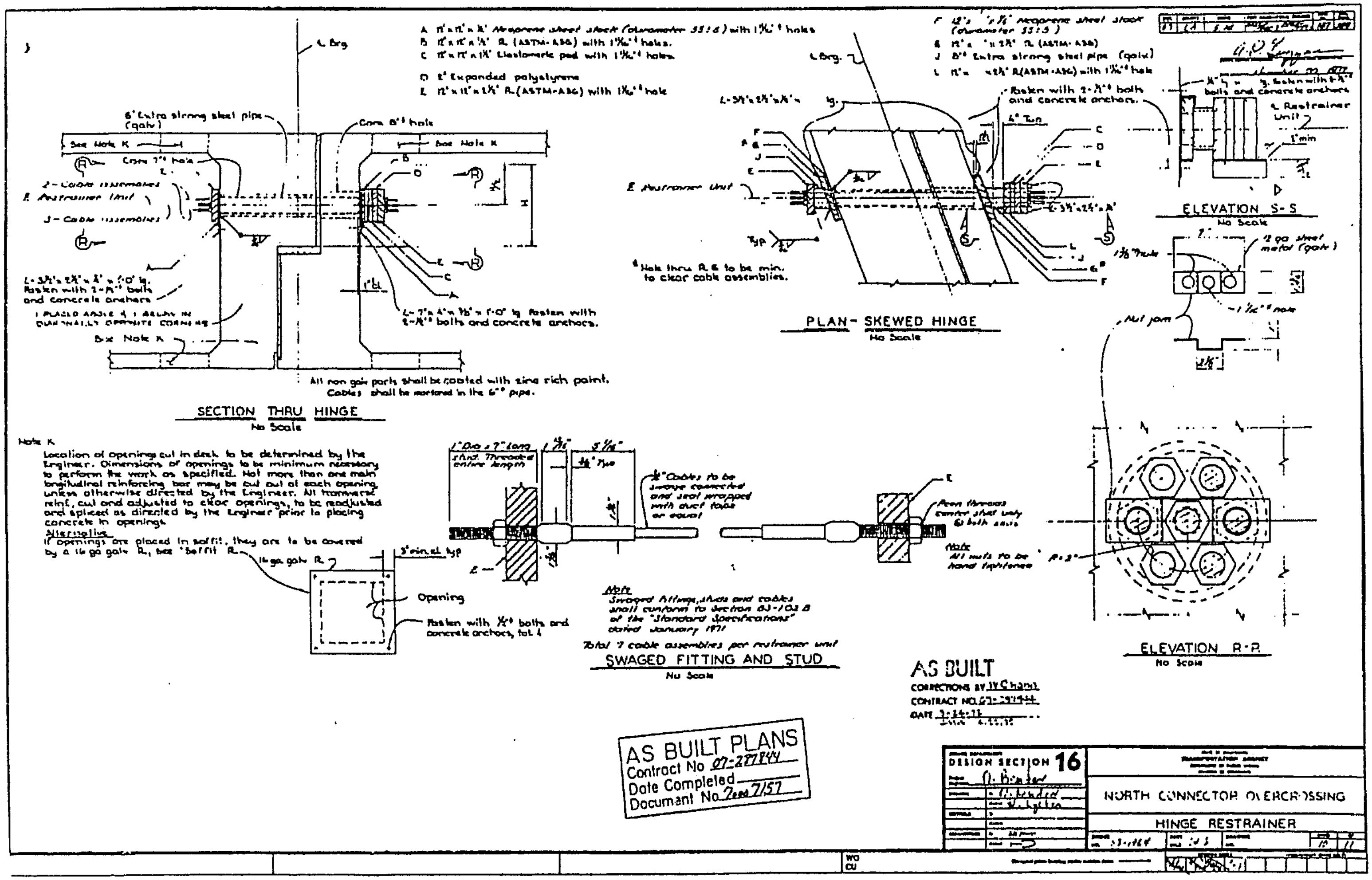

A 11"x11"x 3/4" Neoprene sheet stock (durometer 55±5) with 1 5/16" holes
B 11"x11"x 1/2" PL (ASTM-A36) with 1 5/16" holes.
C 11"x11"x 1 1/2" Elastomeric pad with 1 5/16" holes.
D 2" Expanded polystyrene
E 11"x11"x 1 1/2" PL (ASTM-A36) with 1 5/16" hole
F 12"x 1 1/2" Neoprene sheet stock (durometer 55±5)
G 11"x 2 1/2" PL (ASTM-A36)
J 8" Extra strong steel pipe (galv)
L 11"x 2 1/2" PL (ASTM-A36) with 1 5/16" hole
SECTION THRU HINGE
No Scale
6" Extra strong steel pipe (galv)
See Note K
Core 7" hole
Core 8" hole
2 - Cable assemblies
℄ Restrainer Unit
3 - Cable assemblies
℄ Brg
L - 3 1/2" x 2 1/2" x 3/8" x 1'-0" lg. Fasten with 2 - 3/4" bolts and concrete anchors
L - 7" x 4" x 1/2" x 1'-0" lg. Fasten with 2 - 3/4" bolts and concrete anchors.
All non galv parts shall be coated with zinc rich paint. Cables shall be mortared in the 6" pipe.
Note K
Location of openings cut in deck to be determined by the Engineer. Dimensions of openings to be minimum necessary to perform the work as specified. Not more than one main longitudinal reinforcing bar may be cut out of each opening, unless otherwise directed by the Engineer. All transverse reinf. cut and adjusted to clear openings, to be readjusted and spliced as directed by the Engineer prior to placing concrete in openings.
Alternative
If openings are placed in soffit, they are to be covered by a 16 ga galv PL, see "Soffit PL"
16 ga. galv PL
Opening
Fasten with 3/8" bolts and concrete anchors, tot 4
PLAN - SKEWED HINGE
No Scale
℄ Brg.
℄ Restrainer Unit
* Hole thru PL G to be min. to clear cable assemblies.
Fasten with 2 - 3/4" bolts and concrete anchors.
4" Turn
ELEVATION S-S
No Scale
12 ga sheet metal (galv)
1 5/16" hole
Nut jam
℄ Restrainer Unit
1" min
ELEVATION R-R
No Scale
1" Dia x 7" Long stud. Threaded entire length
5 1/16"
3/4" Cables to be swage connected and seal wrapped with duct tape or equal
Peen threads center stud only @ both ends
Note
All nuts to be hand tightened
Note
Swaged fittings, studs and cables shall conform to Section 63-10.2 B of the "Standard Specifications" dated January 1971
Total 7 cable assemblies per restrainer unit
SWAGED FITTING AND STUD
No Scale
AS BUILT
CORRECTIONS BY IYChang
CONTRACT NO. 07-297944
DATE 3-24-75
AS BUILT PLANS
Contract No 07-297944
Date Completed
Document No. 2007/57
DESIGN SECTION 16
NORTH CONNECTOR OVERCROSSING
HINGE RESTRAINER

Figure A.9 - North Connector hinge restrainer

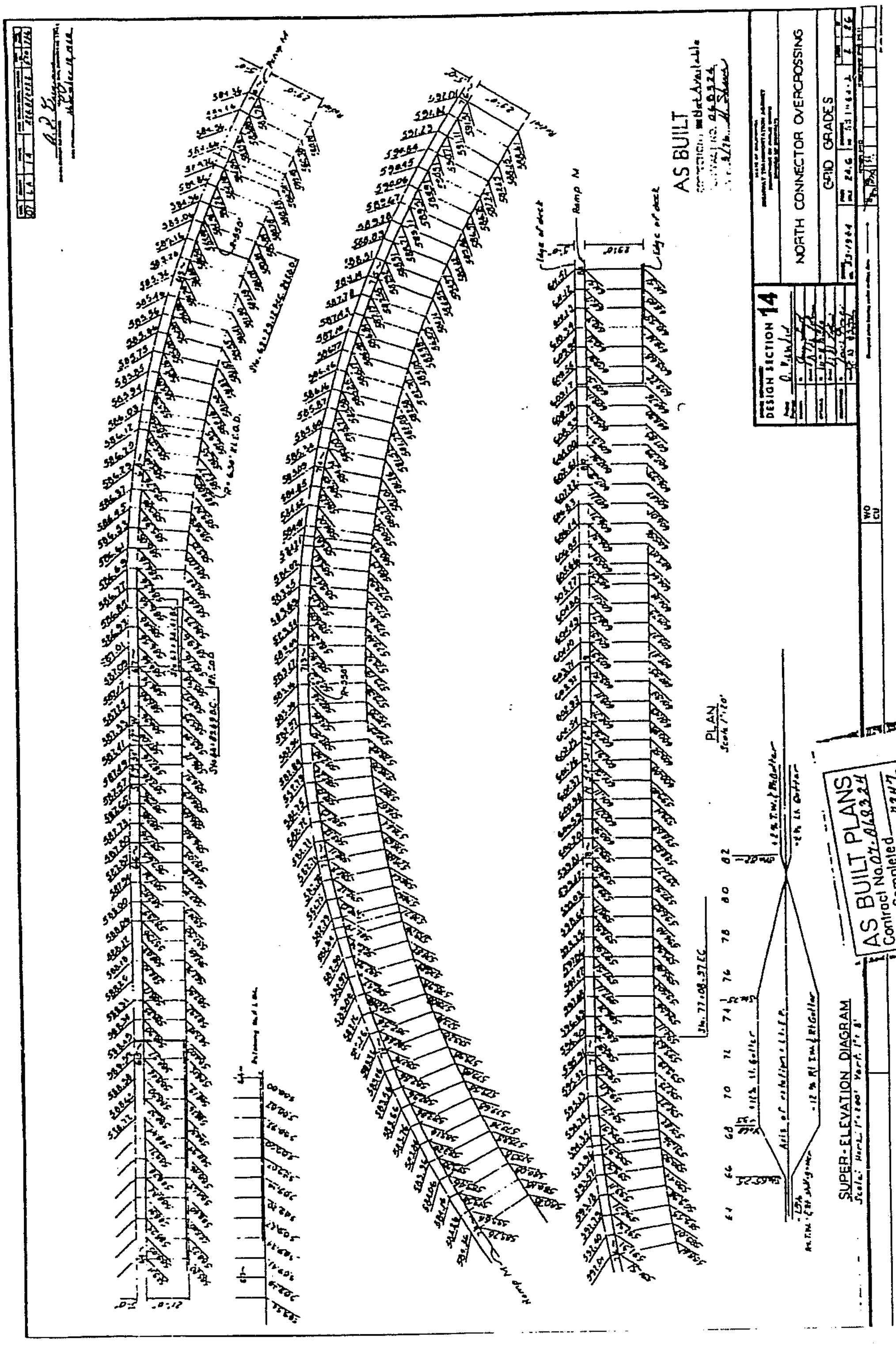
AS BUILT
DESIGN SECTION 14
NORTH CONNECTOR OVERCROSSING
GRID GRADES
Ramp M
Edge of deck
PLAN
SUPER-ELEVATION DIAGRAM
AS BUILT PLANS
Contract No. 04-018324
Date Completed
Document No.

Figure A.10 - North Connector grid grades

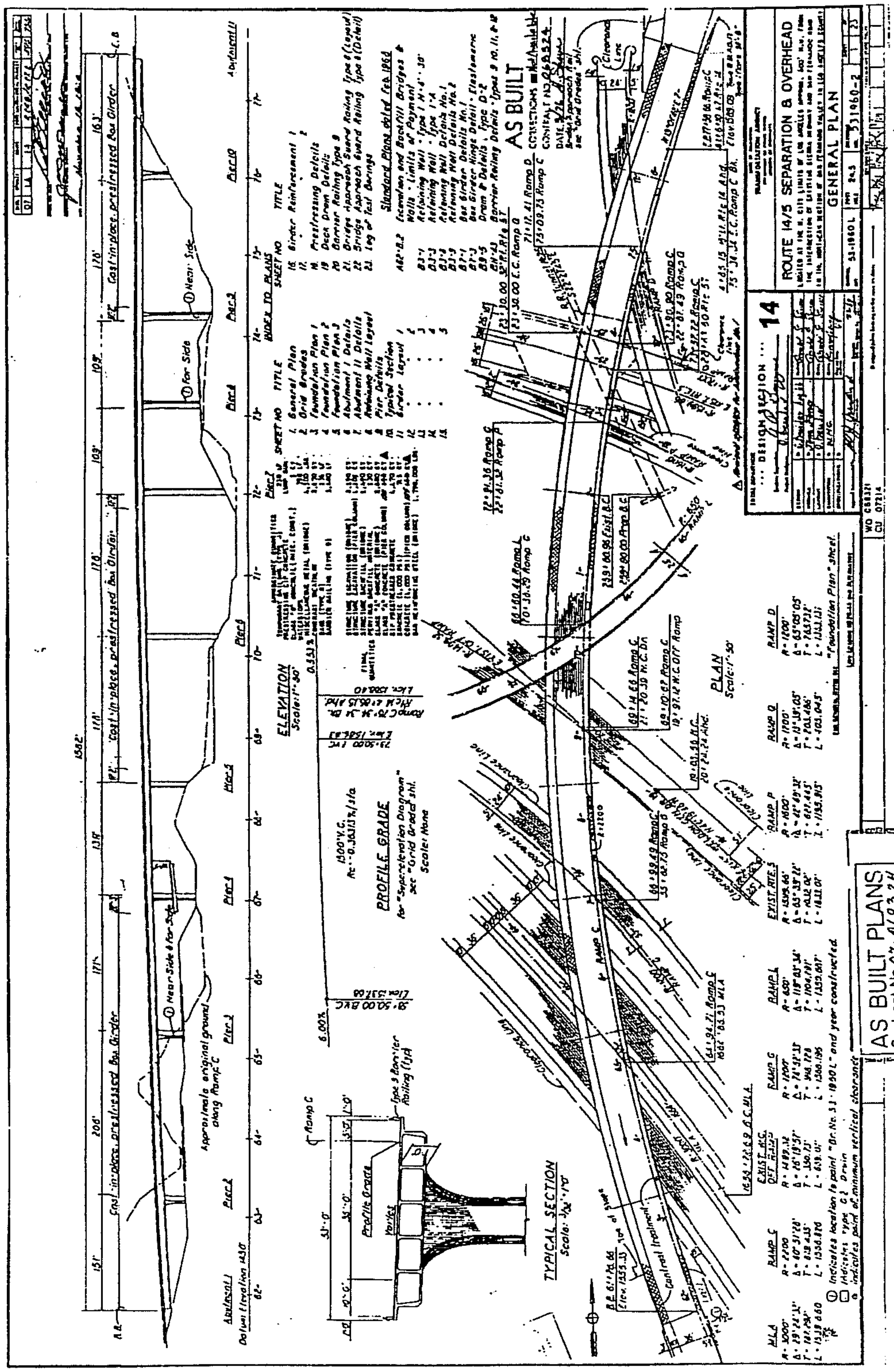
ROUTE 14/5 SEPARATION & OVERHEAD
GENERAL PLAN
AS BUILT
AS BUILT PLANS
ELEVATION
Scale: 1" = 30'
PLAN
Scale: 1" = 30'
PROFILE GRADE
TYPICAL SECTION
INDEX TO PLANS
Abutment 1
Pier 2
Pier 3
Pier 4
Pier 5
Pier 6
Pier 7
Pier 8
Pier 9
Abutment 10
Cast-in-place, prestressed Box Girder
Ramp C
Ramp D
Ramp G
Ramp L
Ramp P
Ramp Q
53-1960 L

Figure A.11 - Separation and Overhead general plan

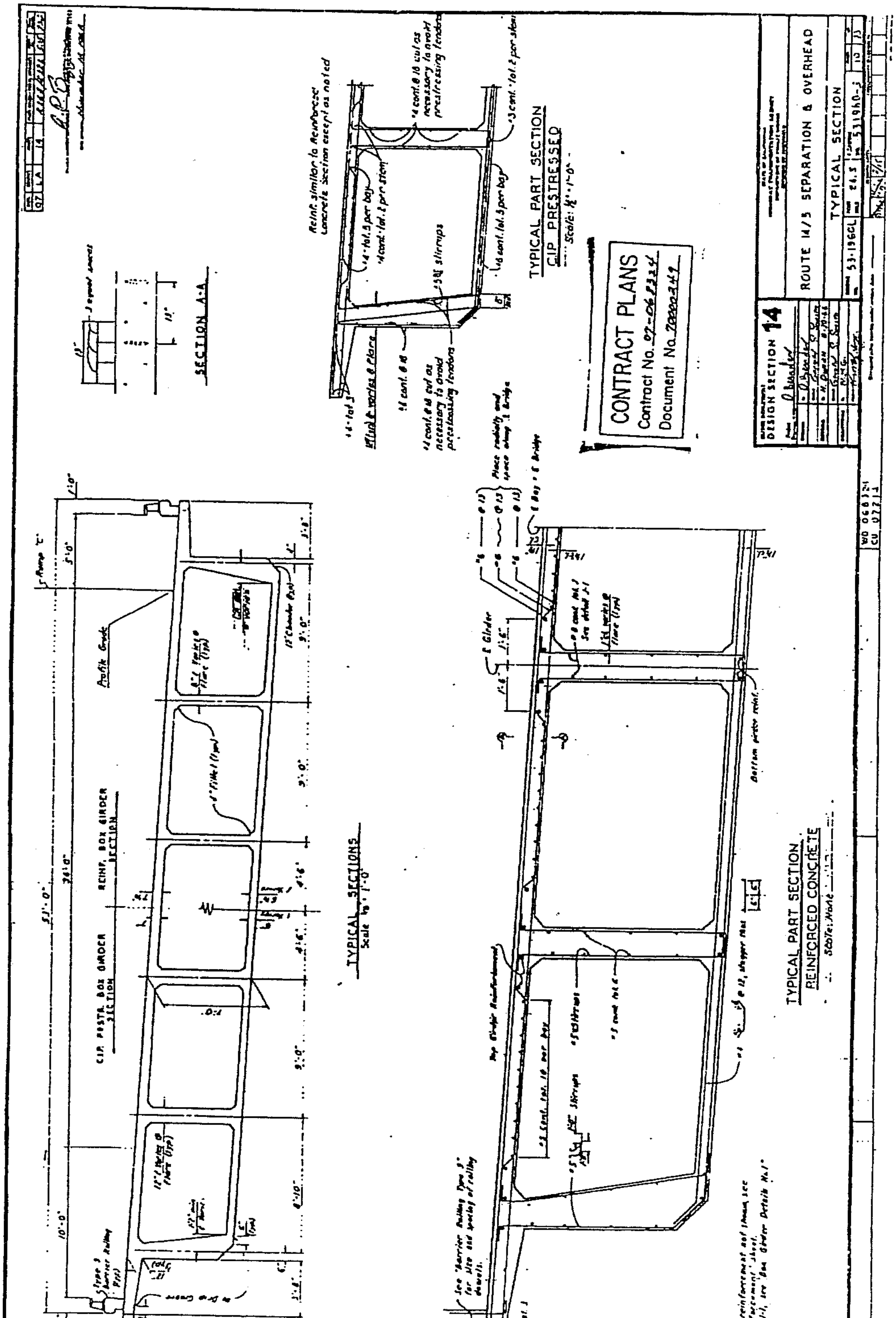
TYPICAL SECTIONS
CIP PRSTR. BOX GIRDER SECTION
REINF. BOX GIRDER SECTION
SECTION A-A
TYPICAL PART SECTION
CIP PRESTRESSED
TYPICAL PART SECTION
REINFORCED CONCRETE
CONTRACT PLANS
DESIGN SECTION 14
ROUTE 14/5 SEPARATION & OVERHEAD
TYPICAL SECTION
53-1960L
53-1960-3

Figure A.12 - Separation and Overhead typical section

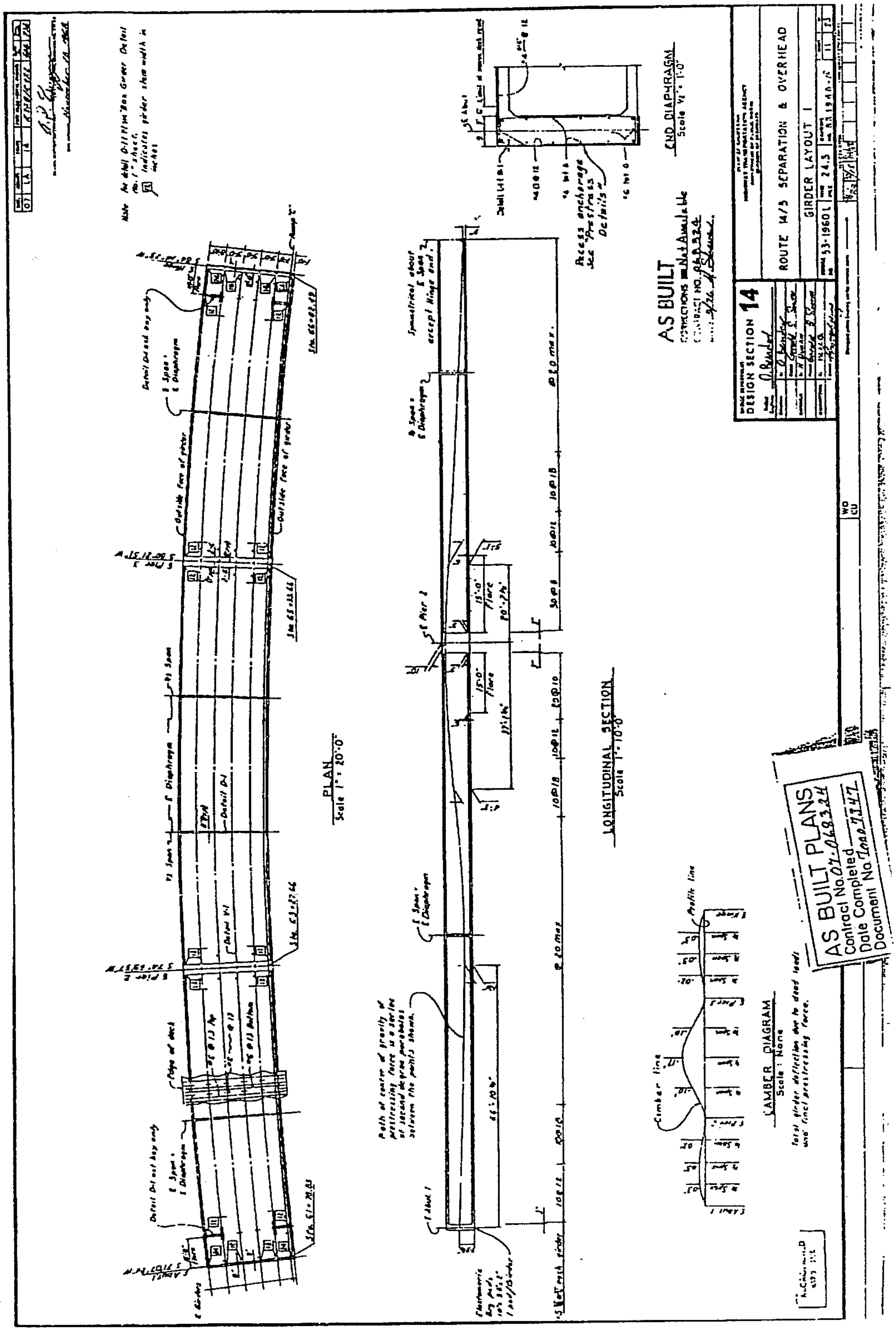
PLAN
Scale 1" = 20'-0"
LONGITUDINAL SECTION
Scale 1" = 10'-0"
END DIAPHRAGM
Scale ½" = 1'-0"
CAMBER DIAGRAM
Scale: None
Camber line
Profile line
AS BUILT
DESIGN SECTION 14
ROUTE 14/5 SEPARATION & OVERHEAD
GIRDER LAYOUT 1
AS BUILT PLANS
Contract No. 07-068324
Date Completed
Document No

Figure A.13 - Separation and Overhead girder layout 1

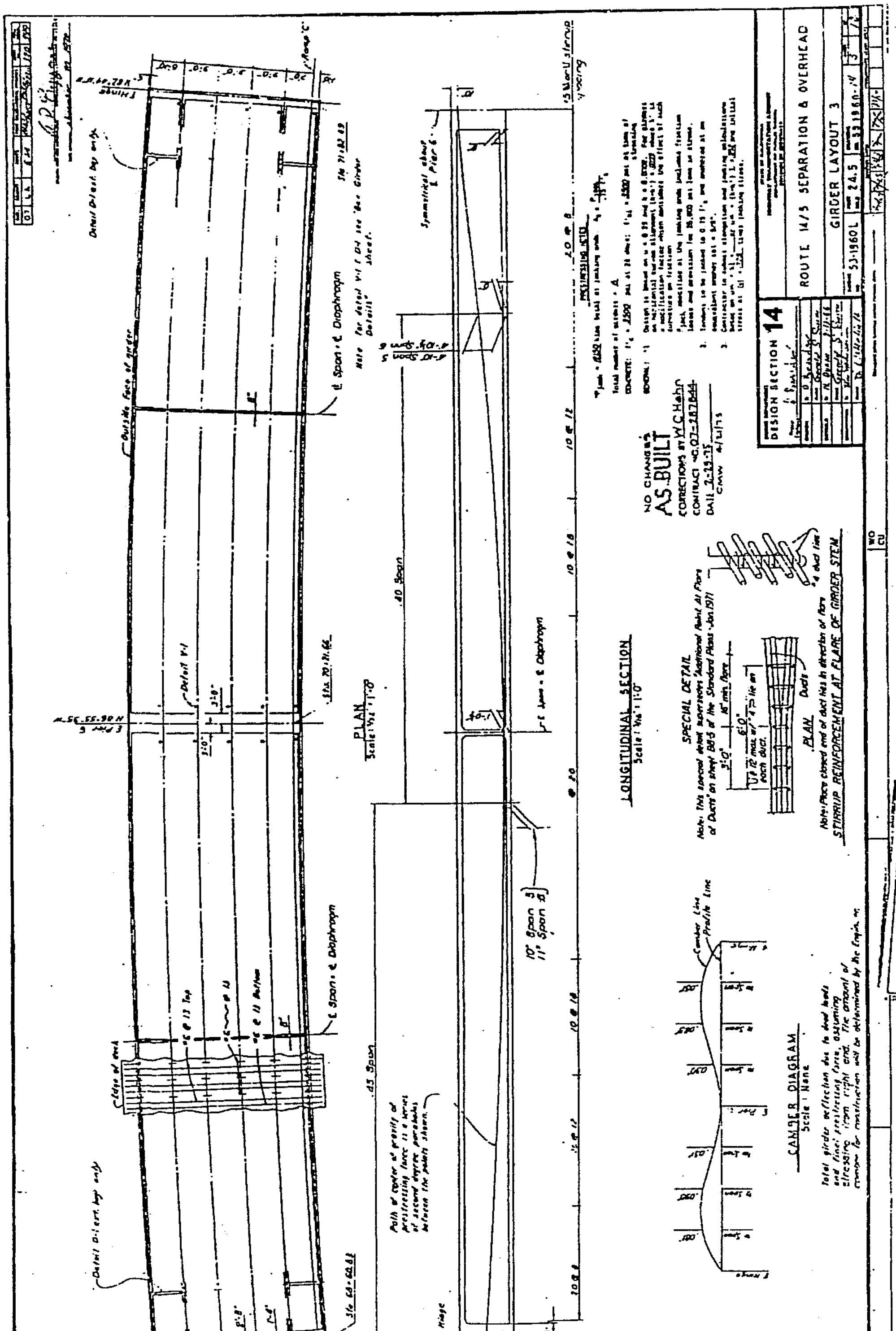
PLAN
LONGITUDINAL SECTION
SPECIAL DETAIL
STIRRUP REINFORCEMENT AT FLARE OF GIRDER STEM
CAMBER DIAGRAM
NO CHANGES
AS BUILT
DESIGN SECTION 14
ROUTE 14/5 SEPARATION & OVERHEAD
GIRDER LAYOUT 3
AS BUILT PLANS

Figure A.14 - Separation and Overhead girder layout 3

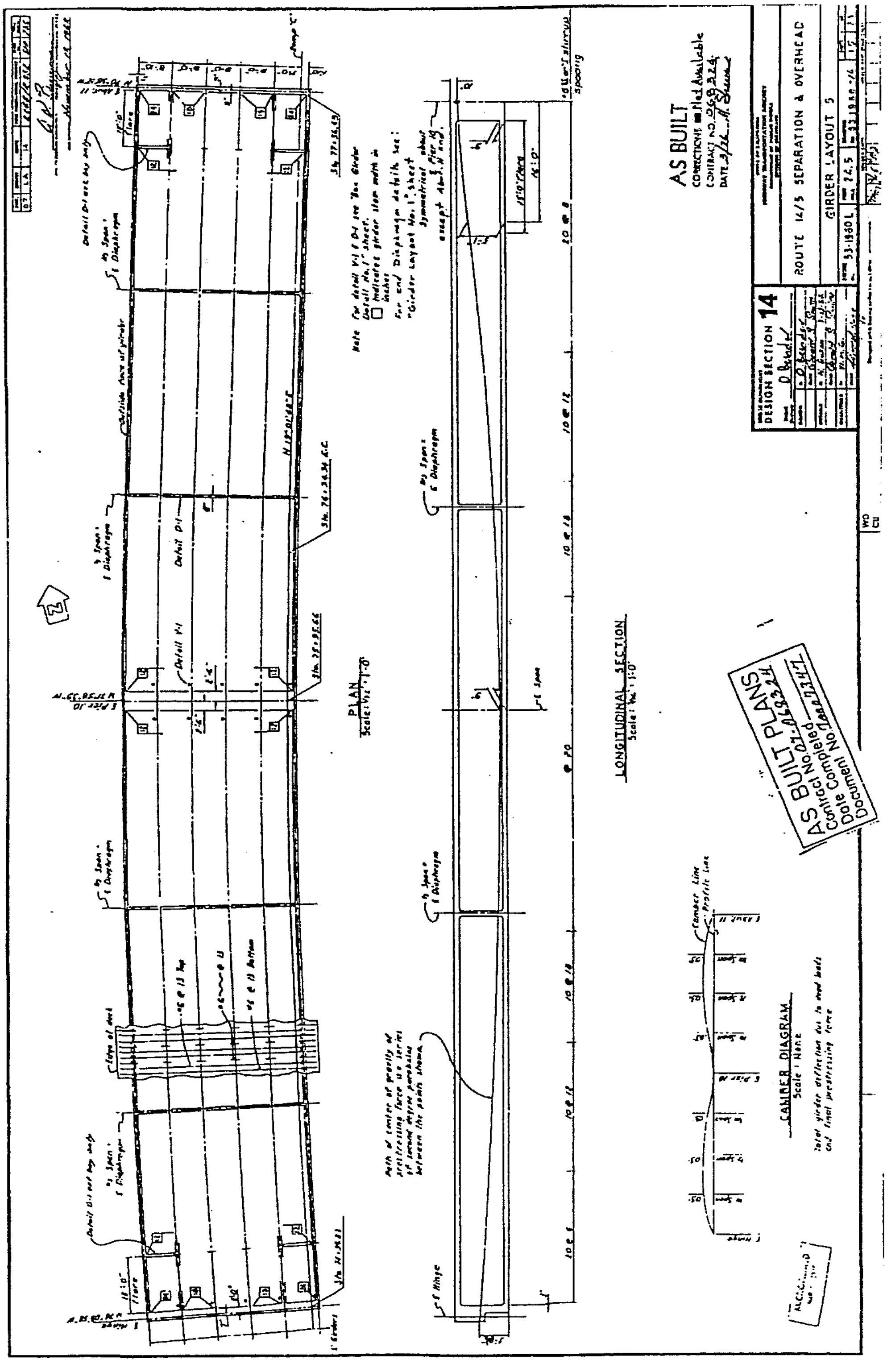
AS BUILT
PLAN
LONGITUDINAL SECTION
CAMBER DIAGRAM
DESIGN SECTION 14
ROUTE 14/5 SEPARATION & OVERHEAD
GIRDER LAYOUT 5
AS BUILT PLANS

Figure A.15 - Separation and Overhead girder layout 5

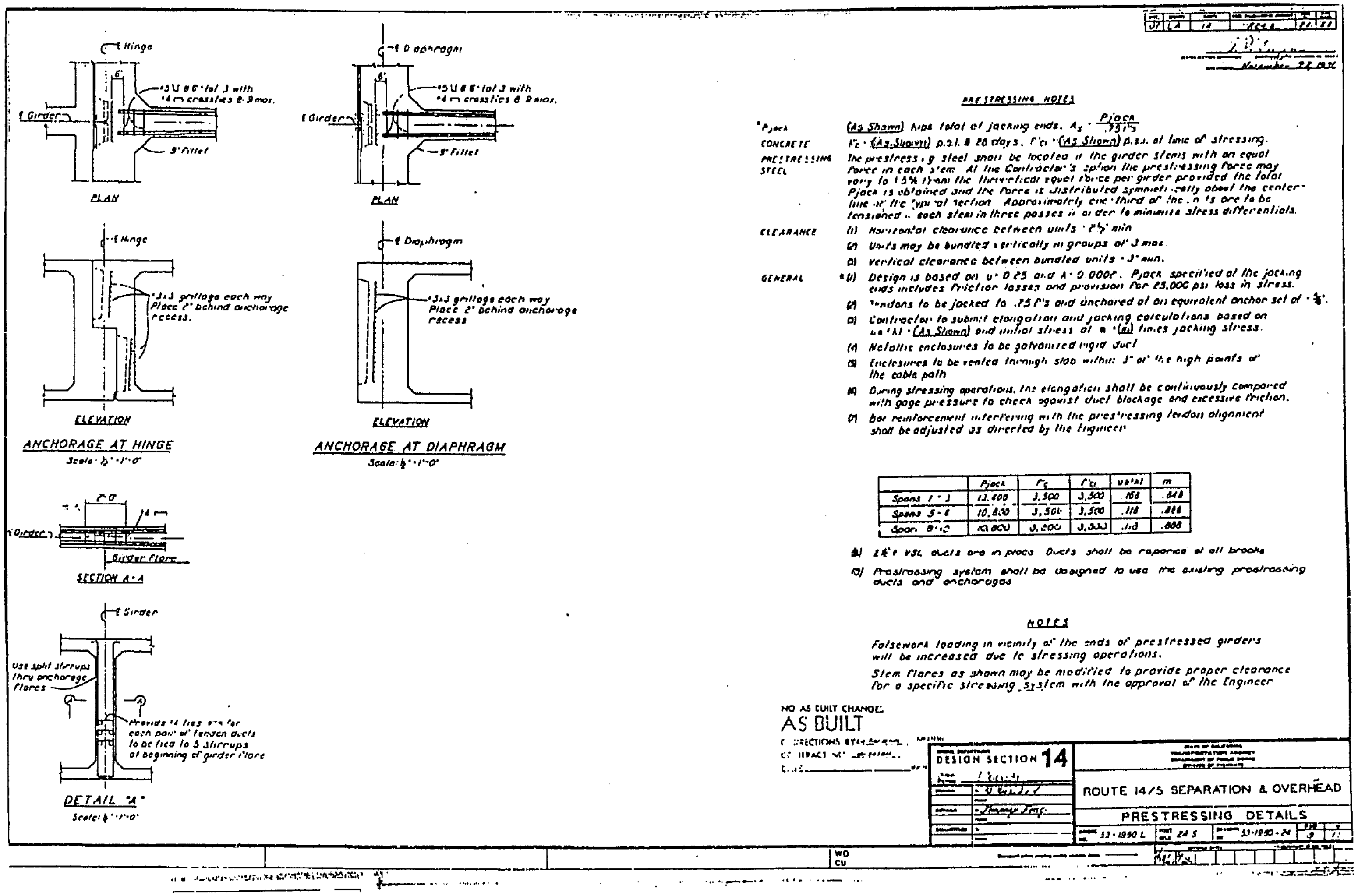
℄ Hinge
℄ Girder
#5 U @ 6" tot 3 with #4 ⊓ crossties @ 9 max.
9" Fillet
6"
PLAN
℄ Diaphragm
ELEVATION
#3x3 grillage each way Place 2" behind anchorage recess.
ANCHORAGE AT HINGE
Scale ½" = 1'-0"
ANCHORAGE AT DIAPHRAGM
Scale ½" = 1'-0"
2'-0"
Girder Flare
SECTION A-A
℄ Girder
Use split stirrups thru anchorage flares
Provide #4 ties @ for each pair of tendon ducts to be tied to 5 stirrups at beginning of girder flare
DETAIL "A"
Scale ½" = 1'-0"
November 22 19

PRESTRESSING NOTES

*Pjack (As Shown) kips total at jacking ends. $A_s = \frac{P_{jack}}{.75 f'_s}$

CONCRETE f'c = (As Shown) p.s.i. @ 28 days, f'ci = (As Shown) p.s.i. at time of stressing.

PRESTRESSING STEEL The prestressing steel shall be located in the girder stems with an equal force in each stem. At the Contractor's option the prestressing force may vary to 15% from the theoretical equal force per girder provided the total Pjack is obtained and the force is distributed symmetrically about the centerline of the typical section. Approximately one-third of the units are to be tensioned in each stem in three passes in order to minimize stress differentials.

CLEARANCE
(1) Horizontal clearance between units = 2½" min
(2) Units may be bundled vertically in groups of 3 max.
(3) Vertical clearance between bundled units = 3" min.

GENERAL
*(1) Design is based on μ = 0.25 and K = 0.0002. Pjack specified at the jacking ends includes friction losses and provision for 25,000 psi loss in stress.
(2) Tendons to be jacked to .75 f's and anchored at an equivalent anchor set of = [illegible].
(3) Contractor to submit elongation and jacking calculations based on μα+KL = (As Shown) and initial stress of = (.8) times jacking stress.
(4) Metallic enclosures to be galvanized rigid duct
(5) Enclosures to be vented through slab within 3' of the high points of the cable path
(6) During stressing operations, the elongation shall be continuously compared with gage pressure to check against duct blockage and excessive friction.
(7) Bar reinforcement interfering with the prestressing tendon alignment shall be adjusted as directed by the Engineer

	Pjack	f'c	f'ci	μα+KL	m
Spans 1-3	13,400	3,500	3,500	.168	.848
Spans 5-8	10,800	3,500	3,500	.118	.888
Span 8-10	10,800	3,200	3,330	.118	.888

(8) 2⅝" φ VSL ducts are in place. Ducts shall be repaired at all breaks
(9) Prestressing system shall be designed to use the existing prestressing ducts and anchorages

NOTES

Falsework loading in vicinity of the ends of prestressed girders will be increased due to stressing operations.

Stem flares as shown may be modified to provide proper clearance for a specific stressing system with the approval of the Engineer

NO AS BUILT CHANGES
AS BUILT

DESIGN SECTION 14

ROUTE 14/5 SEPARATION & OVERHEAD
PRESTRESSING DETAILS
53-1950 L
24.5
53-1950-24

Figure A.16 - Separation and Overhead prestressing details

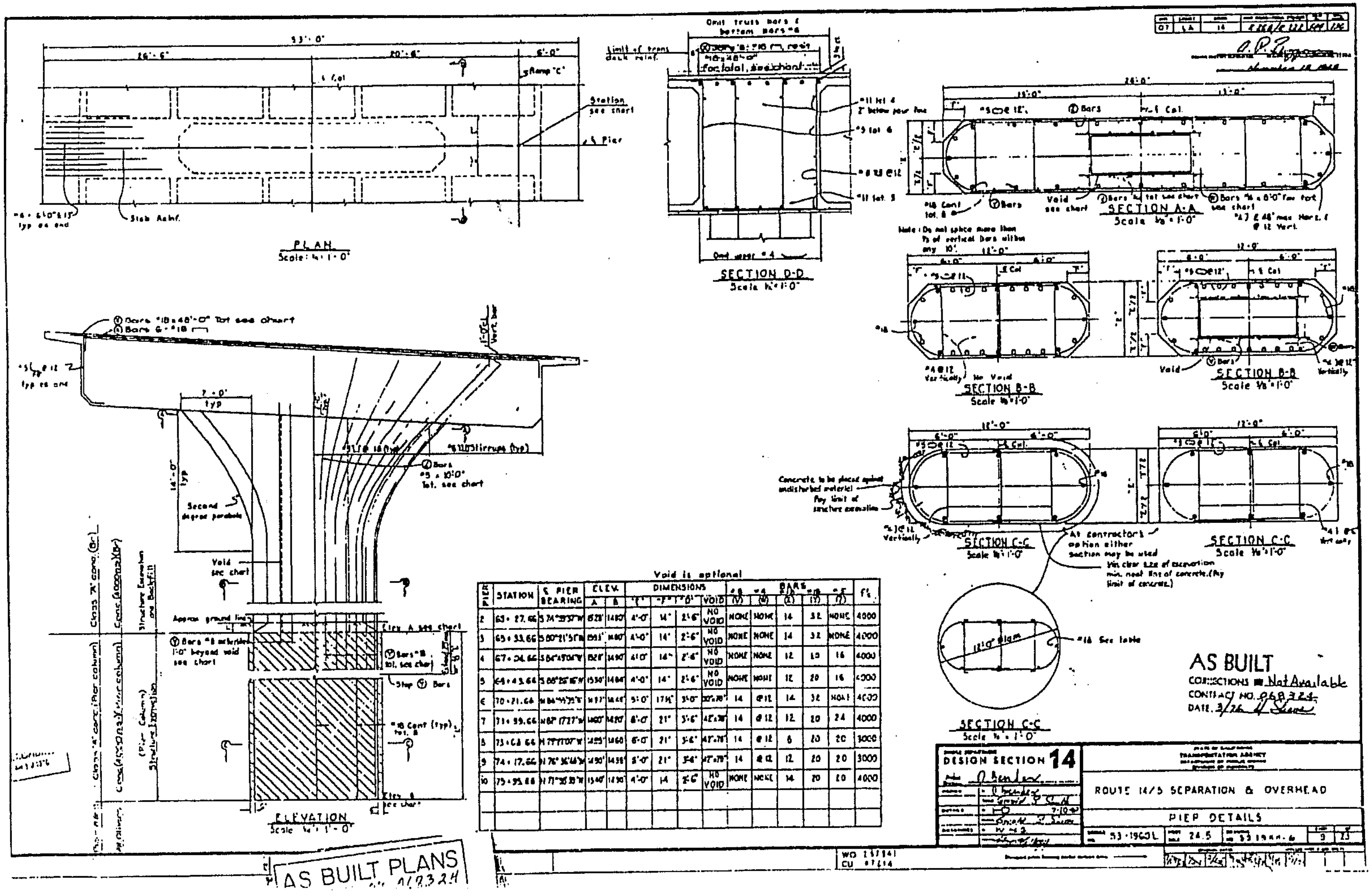
PLAN
Scale: ¼" = 1'-0"
53'-0"
26'-6"
20'-6"
6'-0"
Station see chart
℄ Pier
Slab Reinf.
ELEVATION
Scale ¼" = 1'-0"
Second degree parabola
Void see chart
SECTION D-D
Scale ½" = 1'-0"
SECTION A-A
Scale ⅛" = 1'-0"
SECTION B-B
Scale ⅛" = 1'-0"
SECTION C-C
Scale ⅛" = 1'-0"
SECTION C-C
Scale ¼" = 1'-0"
At contractor's option either section may be used
AS BUILT PLANS
AS BUILT
CORRECTIONS Not Available
CONTRACT NO. 068324
DESIGN SECTION 14
ROUTE 14/5 SEPARATION & OVERHEAD
PIER DETAILS
53-1960L
24.5
WO 137141
CU 07614

Void is optional

PIER	STATION	℄ PIER BEARING	ELEV. A	ELEV. B	DIMENSIONS "E"	DIMENSIONS "F"	DIMENSIONS "D"	DIMENSIONS VOID	BARS (V)	BARS (W)	BARS (X)	BARS (Y)	BARS (Z)	f'c
2	63+27.66	S 74°33'37"W	1528'	1480'	4'-0"	14"	2'-6"	NO VOID	NONE	NONE	14	32	NONE	4000
3	65+33.66	S 80°21'51"W	1531'	1480'	4'-0"	14"	2'-6"	NO VOID	NONE	NONE	14	32	NONE	4000
4	67+24.66	S 84°15'07"W	1528'	1490'	4'-0"	14"	2'-6"	NO VOID	NONE	NONE	12	10	16	4000
5	69+43.66	S 88°25'16"W	1530'	1484'	4'-0"	14"	2'-6"	NO VOID	NONE	NONE	12	20	16	4000
6	70+71.66	N 84°55'25"W	1477'	1441'	5'-0"	17½"	3'-0"	30"x70"	14	@12	14	32	NONE	4000
7	71+99.66	N 82°17'27"W	1460'	1420'	8'-0"	21"	3'-6"	42"x78"	14	@12	12	20	24	4000
8	73+68.66	N 77°11'07"W	1455'	1460'	6'-0"	21"	3'-6"	47"x78"	14	@12	6	20	20	3000
9	74+17.66	N 76°36'48"W	1450'	1438'	5'-0"	21"	3'-4"	47"x78"	14	@12	12	20	20	3000
10	75+95.66	N 71°35'35"W	1540'	1490'	4'-0"	14	2'-6"	NO VOID	NONE	NONE	14	20	20	4000

Figure A.17 - Separation and Overhead pier details

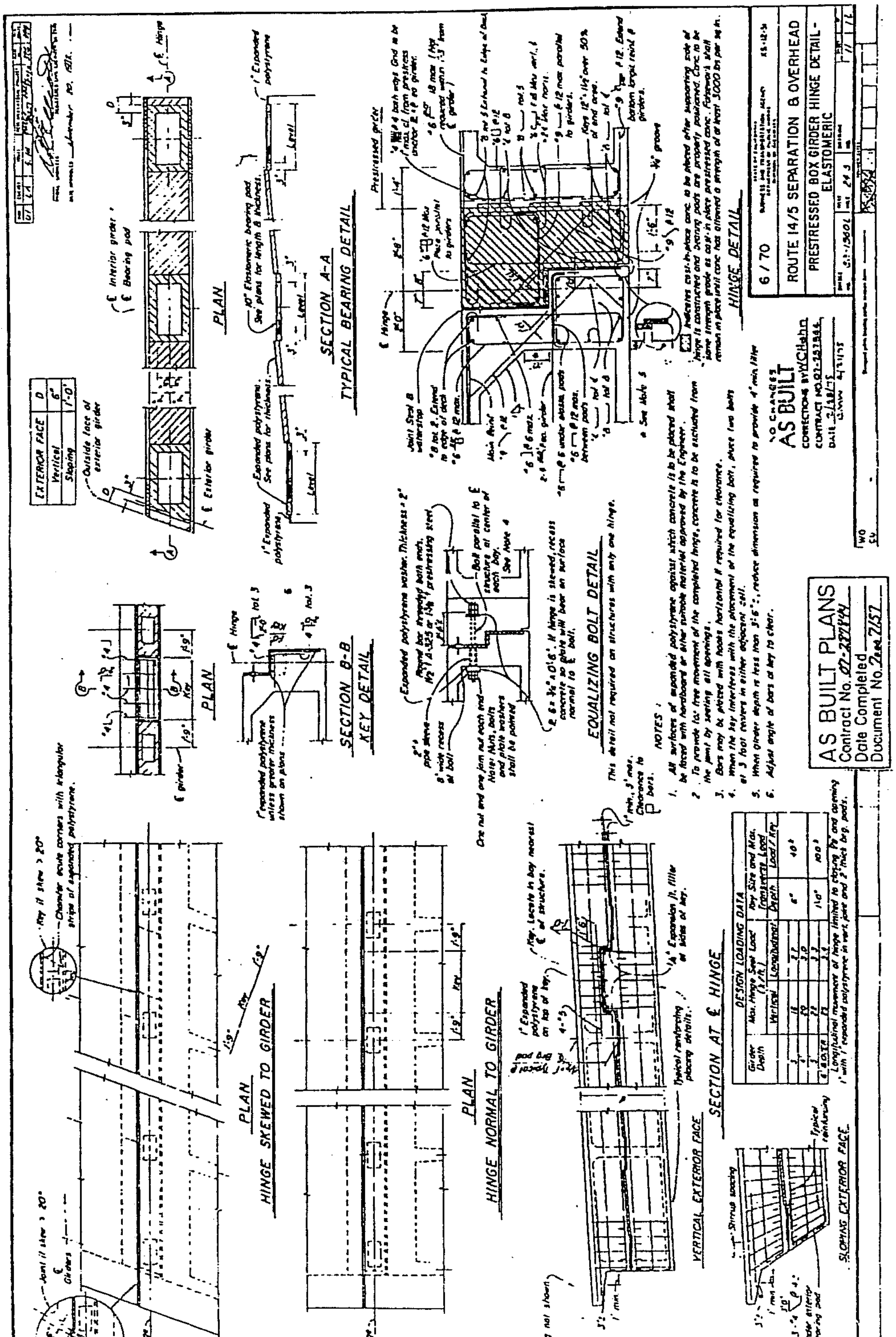
PLAN
HINGE SKEWED TO GIRDER
PLAN
HINGE NORMAL TO GIRDER
SECTION AT ℄ HINGE
VERTICAL EXTERIOR FACE
SLOPING EXTERIOR FACE
DESIGN LOADING DATA
PLAN
SECTION B-B
KEY DETAIL
EQUALIZING BOLT DETAIL
NOTES :
AS BUILT PLANS
Contract No.
Date Completed
Document No.
EXTERIOR FACE
Vertical
Sloping
PLAN
SECTION A-A
TYPICAL BEARING DETAIL
HINGE DETAIL
NO CHANGES
AS BUILT
ROUTE 14/5 SEPARATION & OVERHEAD
PRESTRESSED BOX GIRDER HINGE DETAIL - ELASTOMERIC

Figure A.18 - Separation and Overhead prestressed box girder hinge detail - elastomeric

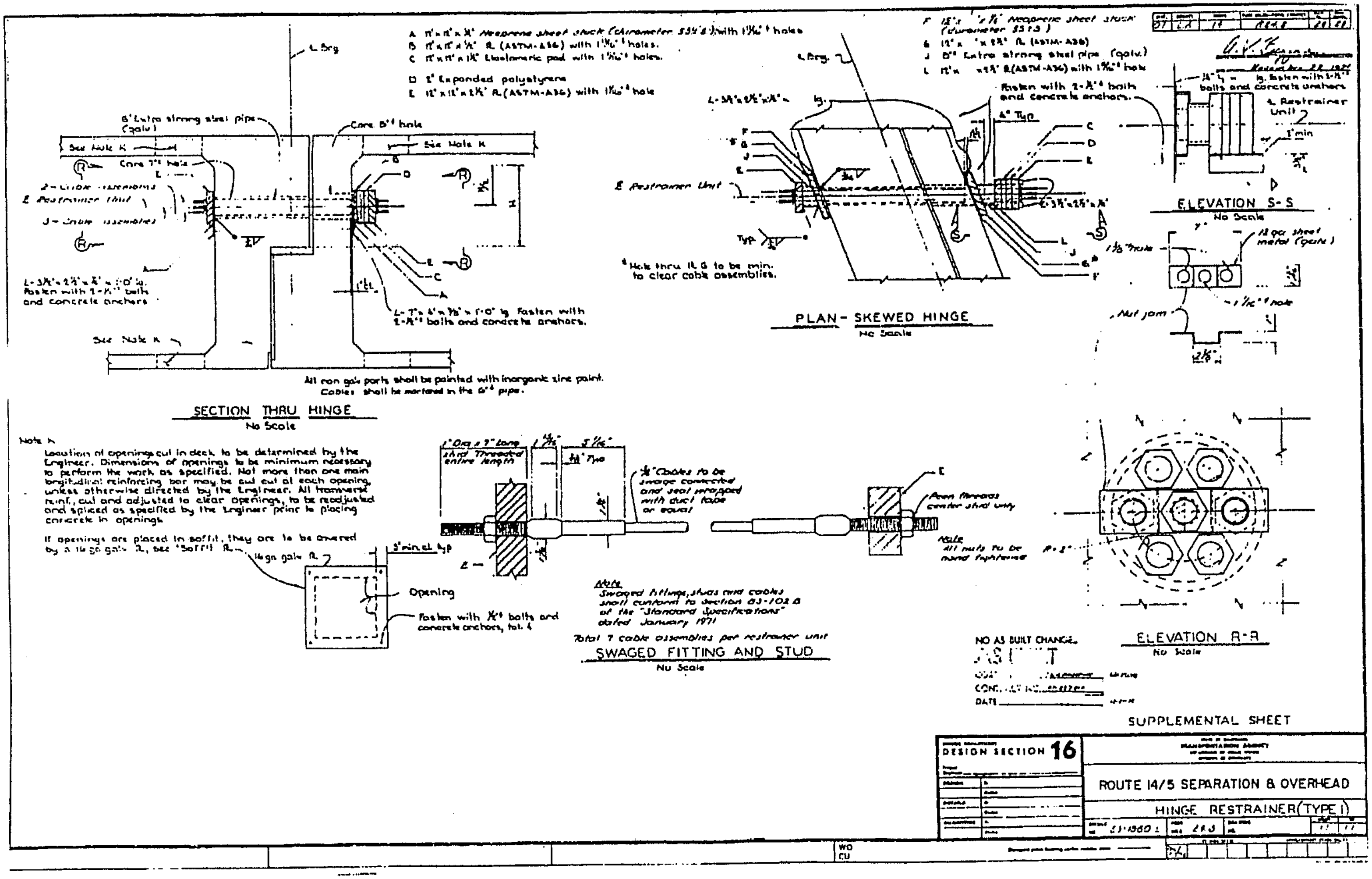

A 11" x 11" x ¾" Neoprene sheet stock (durometer 55±5) with 1⅜" holes
B 11" x 11" x ½" ℞ (ASTM-A36) with 1⅜" holes.
C 11" x 11" x 1¾" Elastomeric pad with 1⅜" holes.
D 2" Expanded polystyrene
E 11" x 11" x 1¾" ℞ (ASTM-A36) with 1⅜" hole
F 15" x ¾" Neoprene sheet stock (durometer 55±5)
G 15" x 2½" ℞ (ASTM-A36)
J 8" Extra strong steel pipe (galv.)
L 15" x 2½" ℞ (ASTM-A36) with 1⅜" hole
6" Extra strong steel pipe (galv.)
Core 8" hole
Core 7" hole
See Note K
2 - Cable assemblies
℄ Restrainer Unit
3 - Cable assemblies
L - 3½" x 2½" x ¾" x 1'-0" lg. Fasten with 2 - ¾" bolts and concrete anchors
L - 7" x 4" x ⅞" x 1'-0" lg. Fasten with 2 - ¾" bolts and concrete anchors.
℄ Brg.
All non galv parts shall be painted with inorganic zinc paint.
Cables shall be mortared in the 8" pipe.
SECTION THRU HINGE
No Scale
Note K
Location of openings cut in deck to be determined by the Engineer. Dimensions of openings to be minimum necessary to perform the work as specified. Not more than one main longitudinal reinforcing bar may be cut out at each opening, unless otherwise directed by the Engineer. All transverse reinf., cut and adjusted to clear openings, to be readjusted and spliced as specified by the Engineer prior to placing concrete in openings.
If openings are placed in soffit, they are to be covered by a 16 ga galv ℞, see "Soffit ℞".
16 ga galv ℞
3" min cl typ
Opening
Fasten with ⅜" bolts and concrete anchors, tot. 4
L - 3½" x 2½" x ¾" x
℄ Restrainer Unit
Hole thru ℞ G to be min. to clear cable assemblies.
Typ
4" Typ
Fasten with 2 - ¾" bolts and concrete anchors.
PLAN - SKEWED HINGE
No Scale
Fasten with 2 - ¾" bolts and concrete anchors
℄ Restrainer Unit
1" min
ELEVATION S - S
No Scale
12 ga sheet metal (galv.)
1⅝" hole
1⅛" hole
Nut jam
1" Dia x 7" Long stud Threaded entire length
¾" Typ
¾" Cables to be swage connected and seal wrapped with duct tape or equal
Peen threads center stud only
Note
All nuts to be hand tightened
Note
Swaged fittings, studs and cables shall conform to section 83-102.8 of the "Standard Specifications" dated January 1971
Total 7 cable assemblies per restrainer unit
SWAGED FITTING AND STUD
No Scale
ELEVATION R - R
No Scale
NO AS BUILT CHANGE
CONT. NO.
DATE
SUPPLEMENTAL SHEET
DESIGN SECTION 16
ROUTE 14/5 SEPARATION & OVERHEAD
HINGE RESTRAINER (TYPE 1)
53-1960 L
WO
CU

Figure A.19 - Separation and Overhead hinge restrainer (Type 1)

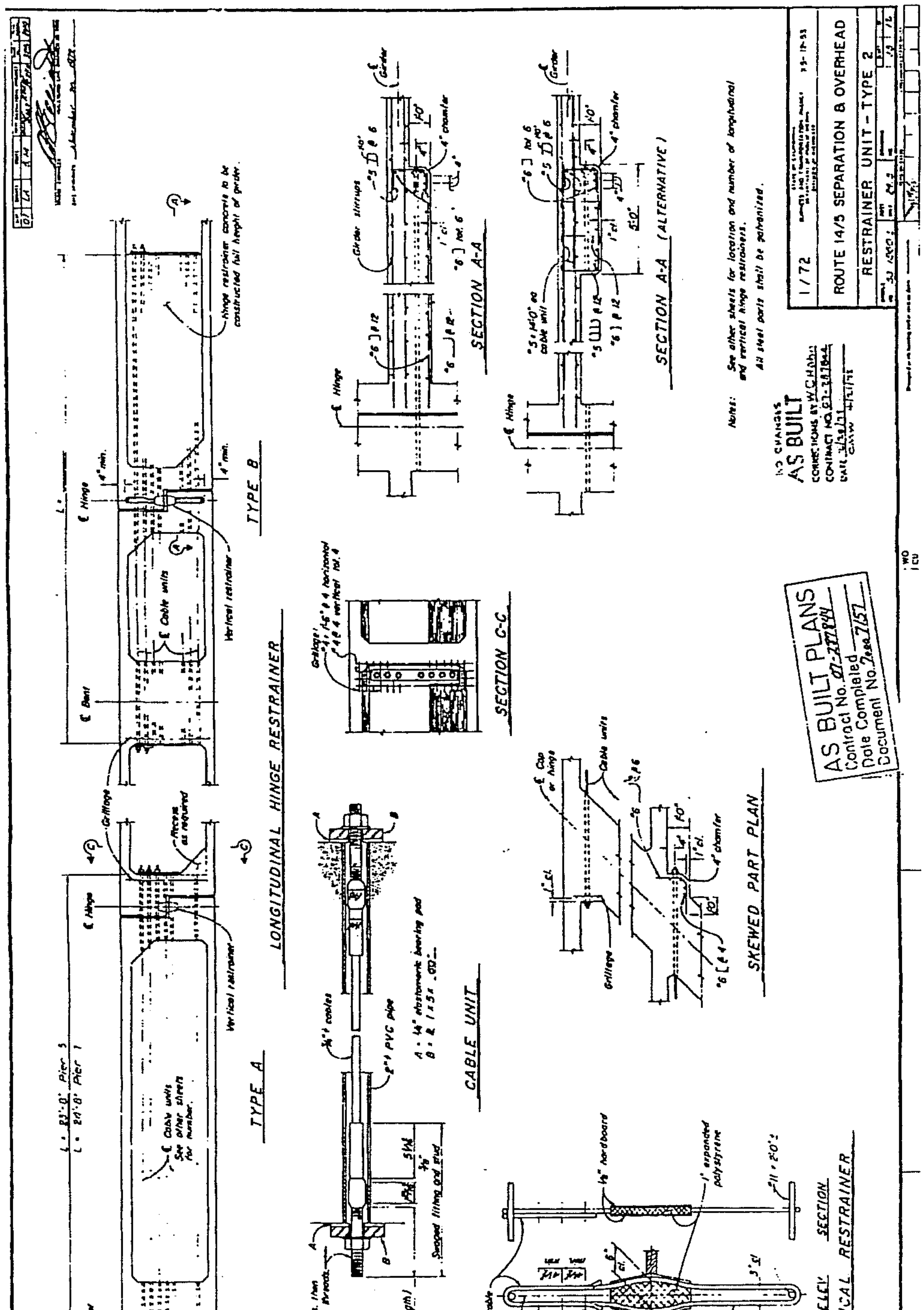

LONGITUDINAL HINGE RESTRAINER
TYPE A
TYPE B
CABLE UNIT
SECTION C-C
SECTION A-A
SECTION A-A (ALTERNATIVE)
SKEWED PART PLAN
ELEV. SECTION
VERTICAL RESTRAINER
ROUTE 14/5 SEPARATION & OVERHEAD
RESTRAINER UNIT - TYPE 2
AS BUILT
AS BUILT PLANS
Contract No.
Date Completed
Document No.

Figure A.20 - Separation and Overhead restrainer unit (Type 2)

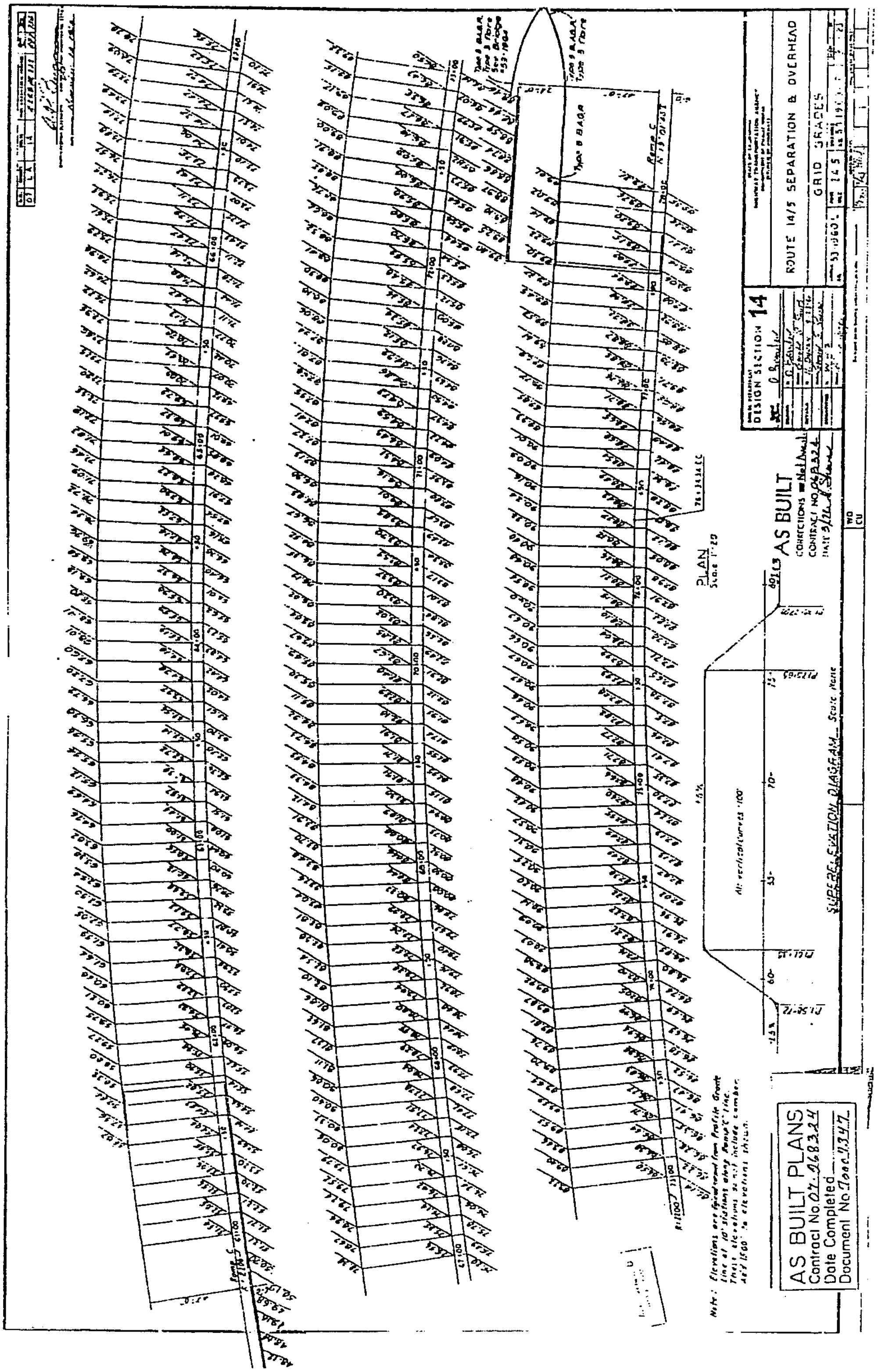
ROUTE 14/5 SEPARATION & OVERHEAD
GRID GRADES
DESIGN SECTION 14
AS BUILT
PLAN Scale 1"=20'
SUPERELEVATION DIAGRAM Scale: None
AS BUILT PLANS
Contract No
Date Completed
Document No

Figure A.21 - Separation and Overhead grid grades

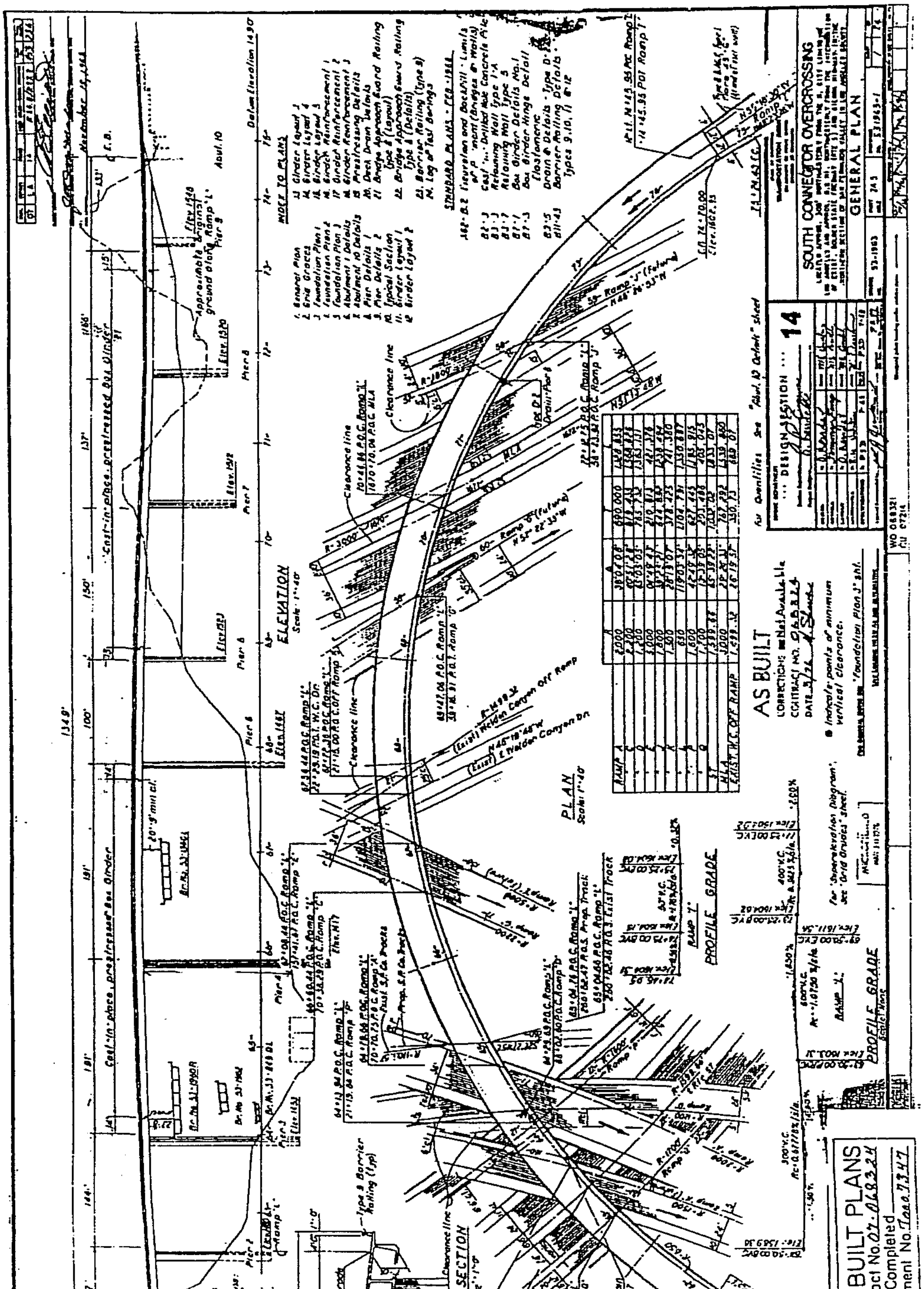
ELEVATION
PLAN
TYPICAL SECTION
PROFILE GRADE
INDEX TO PLANS
AS BUILT
AS BUILT PLANS
Contract No. 07-068324
Date Completed
Document No.
SOUTH CONNECTOR OVERCROSSING
GENERAL PLAN

Figure A.22 - South Connector general plan

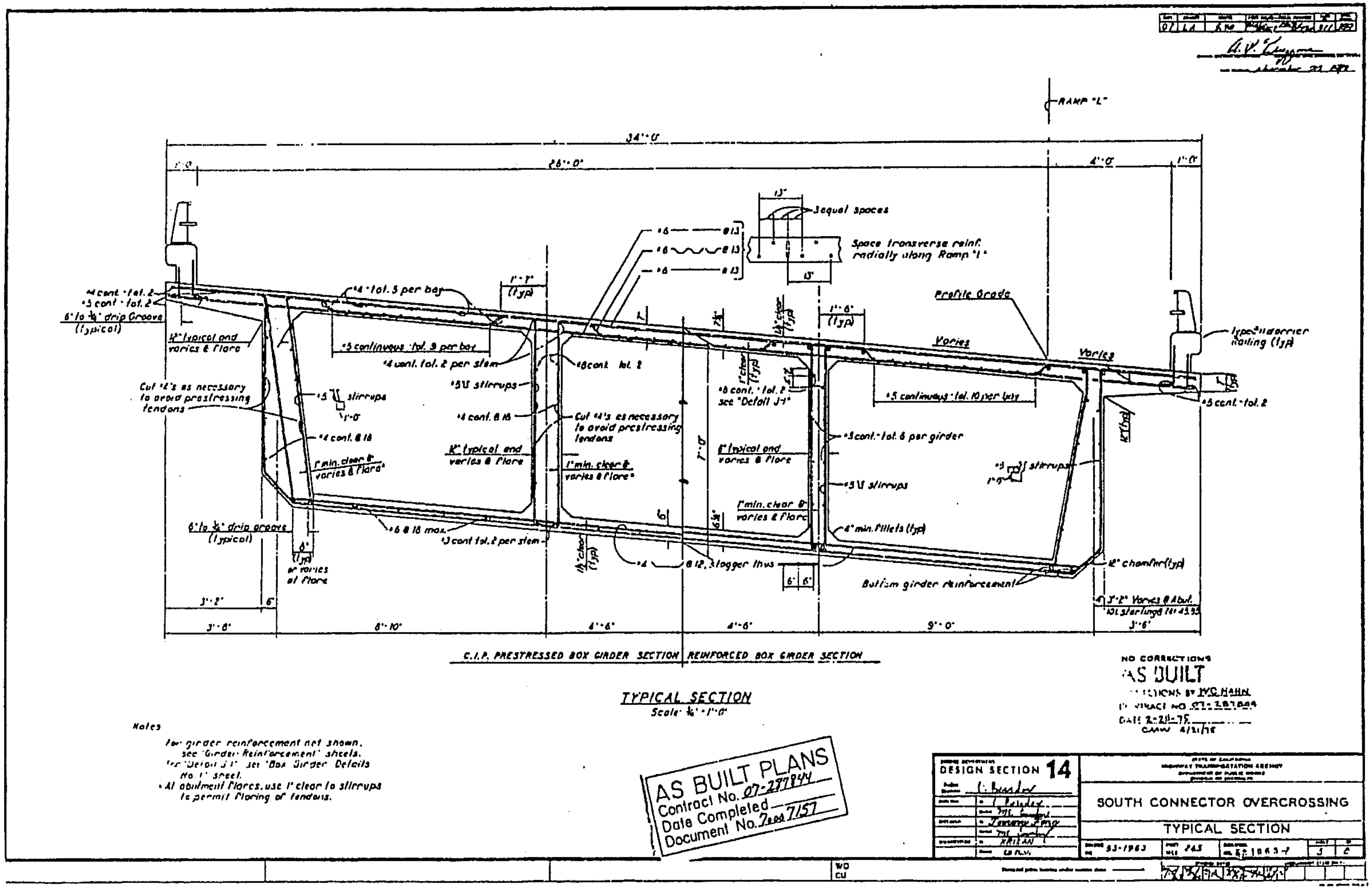
RAMP "L"
34'-0"
28'-0"
1'-0"
4'-0"
1'-0"
13"
3 equal spaces
#6 @ 13
#6 @ 13
#6 @ 13
13"
Space transverse reinf. radially along Ramp "L"
Profile Grade
Varies
Varies
Type 9 barrier Railing (Typ)
#4 cont - tot. 2
#3 cont - tot. 2
6" to 3/4" drip Groove (typical)
1/2" typical and varies @ flare
#4 - tot. 5 per bay
1'-1" (Typ)
#5 continuous - tot. 9 per bay
#4 cont. tot. 2 per stem
#8 cont. tot. 2
#5 U stirrups
#5 stirrups
1'-0"
Cut #4's as necessary to avoid prestressing tendons
#4 cont. @ 18
#4 cont. @ 18
1/2" typical and varies @ flare
1" min. clear & varies & flare*
1" min. clear & varies & flare*
7'-0"
1 1/2" clear (Typ)
1" clear (Typ)
#6 cont. - tot. 2 see "Detail J-1"
1'-6" (Typ)
#5 continuous - tot. 10 per bay
#5 cont. - tot. 6 per girder
8" typical and varies @ flare
#5 U stirrups
#5 U stirrups
1'-0"
1" min. clear & varies & flare
4" min. fillets (typ)
#5 cont. - tot. 2
12" chamfer (typ)
Bottom girder reinforcement
6" to 3/4" drip groove (typical)
8" (Typ) or varies at flare
#6 @ 18 max.
#3 cont tot. 2 per stem
#4 @ 12, stagger thus
6" 6"
3'-2"
6"
3'-2" Varies @ Abut.
3'-6"
8'-10"
4'-6"
4'-6"
9'-0"
3'-6"
C.I.P. PRESTRESSED BOX GIRDER SECTION
REINFORCED BOX GIRDER SECTION
TYPICAL SECTION
Scale: 1/4" = 1'-0"
Notes
For girder reinforcement not shown, see 'Girder Reinforcement' sheets.
For 'Detail J-1' see 'Box Girder Details No. 1' sheet.
* At abutment flares, use 1" clear to stirrups to permit flaring of tendons.
NO CORRECTIONS
AS BUILT
CORRECTIONS BY W.C. HAHN
CONTRACT NO. 07-287844
DATE 2-21-75
AS BUILT PLANS
Contract No. 07-277844
Date Completed
Document No. 7157
DESIGN SECTION 14
SOUTH CONNECTOR OVERCROSSING
TYPICAL SECTION
53-1963
245
WO
CU

Figure A.23 - South Connector typical section

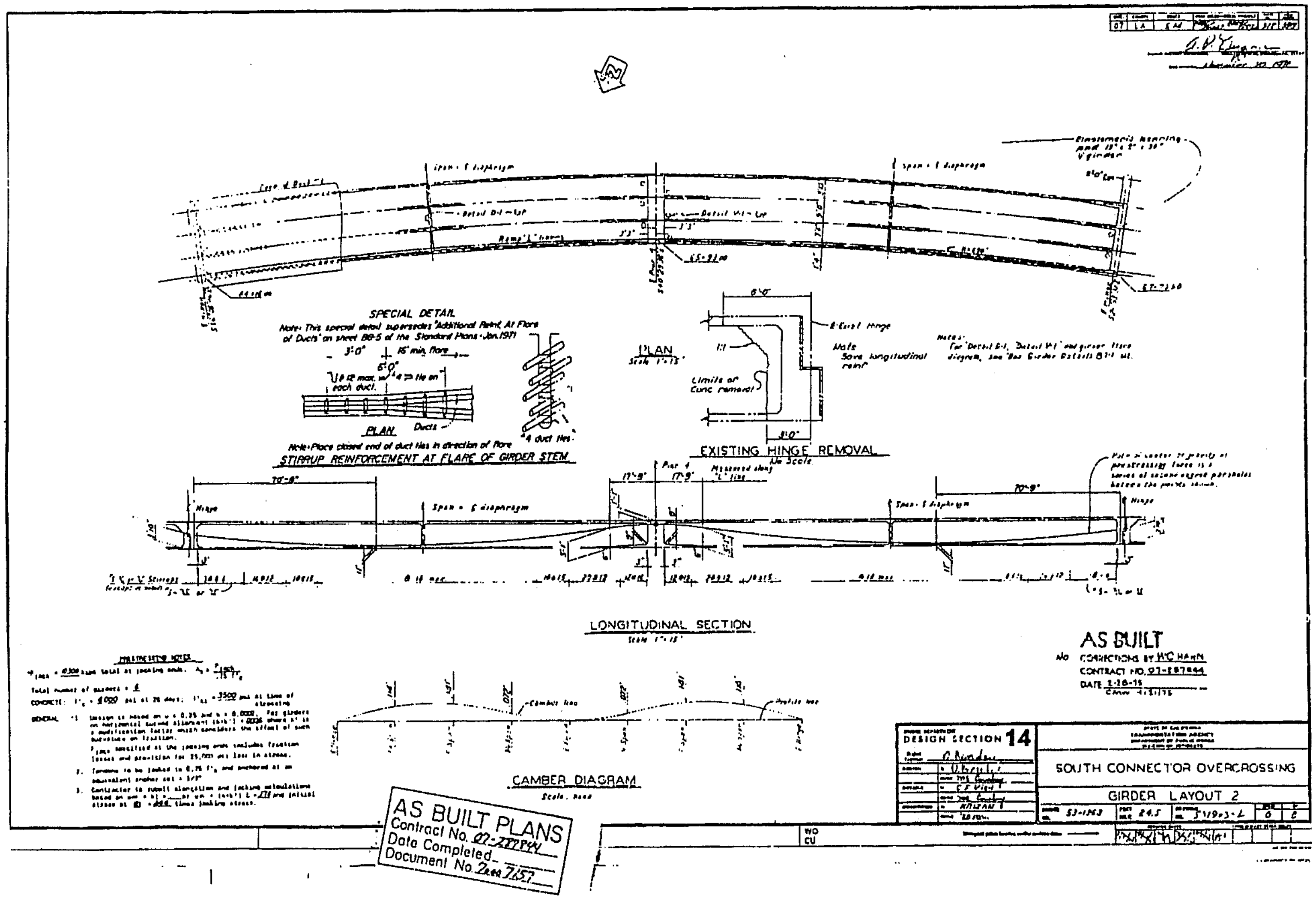
SPECIAL DETAIL
Note: This special detail supersedes "Additional Reinf. At Flare of Ducts" on sheet B8-5 of the Standard Plans - Jan. 1971
3'-0"
16' min. flare
6'-0"
#4 ⊃ tie on each duct.
PLAN
Ducts
#4 duct ties
Note: Place closed end of duct ties in direction of flare
STIRRUP REINFORCEMENT AT FLARE OF GIRDER STEM
PLAN
Limits of Conc removal
Existing Hinge
Note
Save longitudinal reinf.
6'-0"
3'-0"
EXISTING HINGE REMOVAL
No Scale
Span ℄ diaphragm
Hinge
70'-9"
17'-9"
LONGITUDINAL SECTION
CAMBER DIAGRAM
Camber line
Profile line
PRESTRESSING NOTES
AS BUILT
No CORRECTIONS BY W.C. HAHN
CONTRACT NO. 07-287944
DATE 2-26-75
DESIGN SECTION 14
SOUTH CONNECTOR OVERCROSSING
GIRDER LAYOUT 2
53-1353
24.5
AS BUILT PLANS
Contract No. 07-287944
Data Completed
Document No. 2aa 7157

Figure A.24 - South Connector girder layout 2

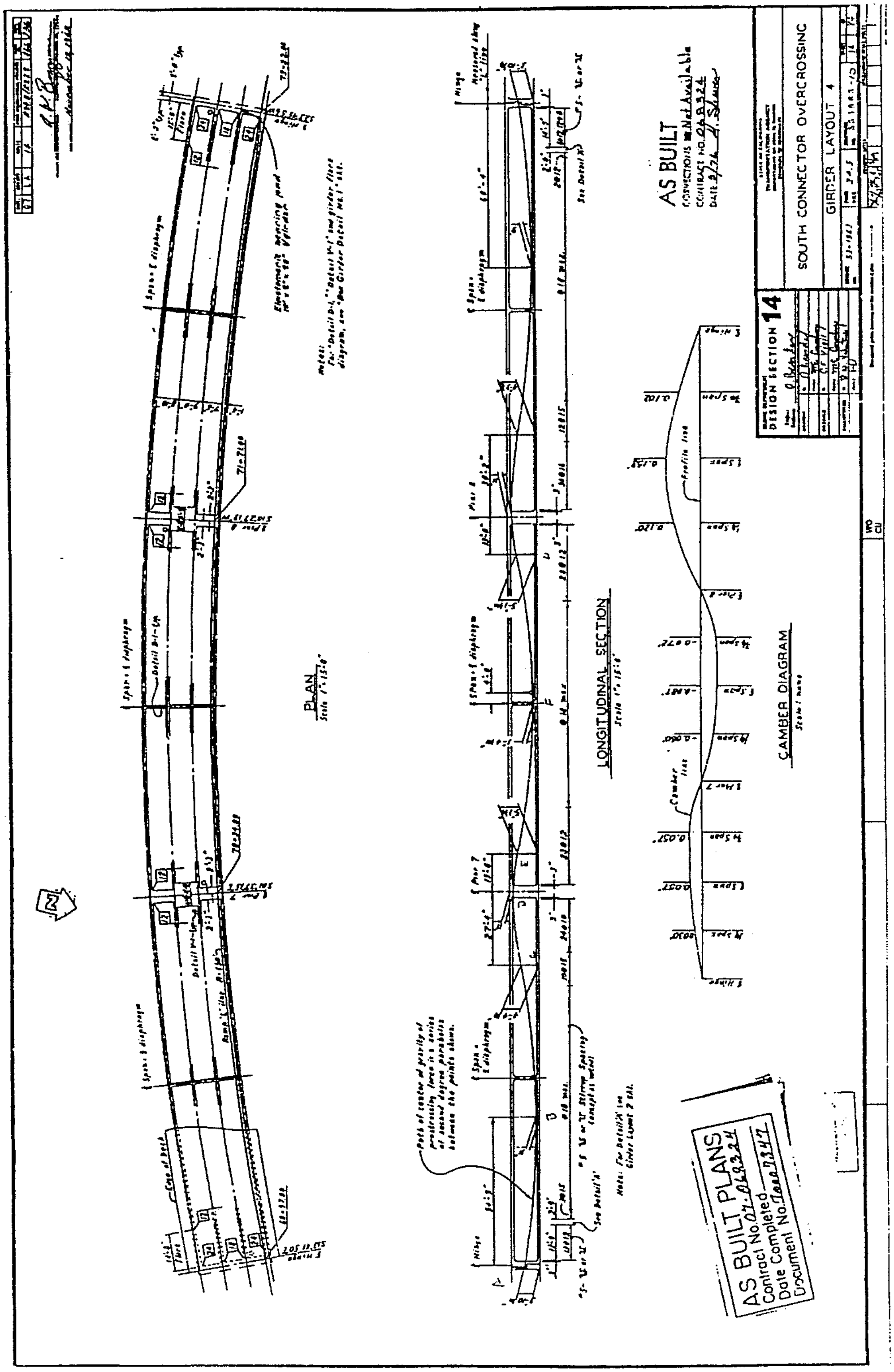
PLAN
LONGITUDINAL SECTION
CAMBER DIAGRAM
AS BUILT
DESIGN SECTION 14
SOUTH CONNECTOR OVERCROSSING
GIRDER LAYOUT 4
AS BUILT PLANS
Contract No.
Date Completed
Document No.

Figure A.25 - South Connector girder layout 4

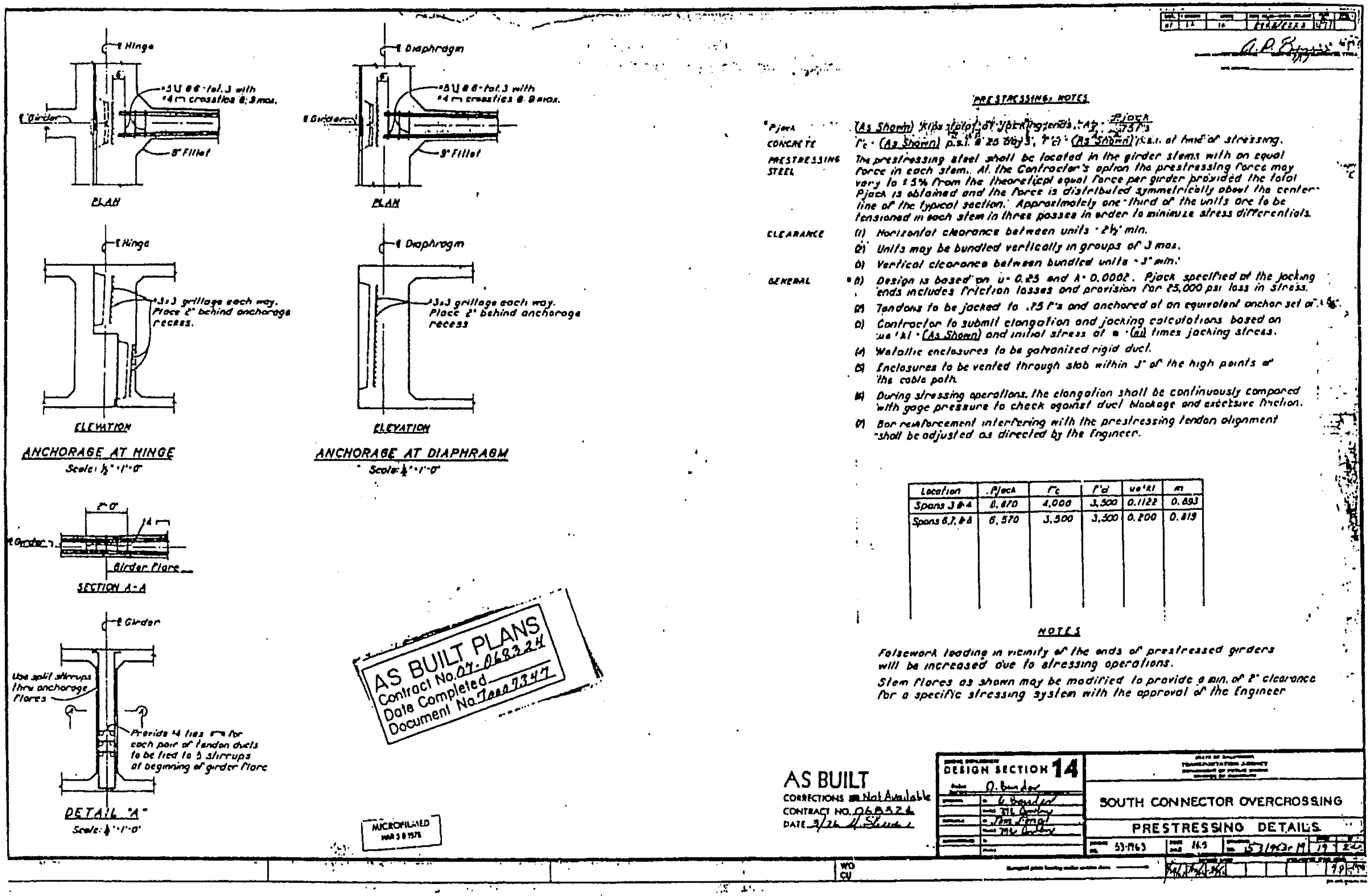
℄ Hinge
℄ Girder
*5 U 8 6-tol.3 with *4 ▭ crossties @ 3 max.
8" Fillet
PLAN
ELEVATION
3x3 grillage each way. Place 2" behind anchorage recess.
ANCHORAGE AT HINGE
Scale: ½" = 1'-0"
℄ Diaphragm
ANCHORAGE AT DIAPHRAGM
Scale: ½" = 1'-0"
℄ Girder
Girder Flare
SECTION A-A
Use split stirrups thru anchorage flares
Provide 4 ties for each pair of tendon ducts to be tied to 5 stirrups at beginning of girder flare
DETAIL "A"
Scale: ½" = 1'-0"
AS BUILT PLANS
Contract No. 07-068324
Date Completed
Document No. 7347
MICROFILMED
DESIGN SECTION 14
SOUTH CONNECTOR OVERCROSSING
PRESTRESSING DETAILS
53-1163
WO
CU

PRESTRESSING NOTES

*Pjack (As Shown) Kips total at jacking ends. As = Pjack / .75f's

CONCRETE f'c = (As Shown) p.s.i. @ 28 days, f'ci = (As Shown) p.s.i. at time of stressing.

PRESTRESSING STEEL The prestressing steel shall be located in the girder stems with an equal force in each stem. At the Contractor's option the prestressing force may vary to ±5% from the theoretical equal force per girder provided the total Pjack is obtained and the force is distributed symmetrically about the centerline of the typical section. Approximately one-third of the units are to be tensioned in each stem in three passes in order to minimize stress differentials.

CLEARANCE
(1) Horizontal clearance between units = 2½" min.
(2) Units may be bundled vertically in groups of 3 max.
(3) Vertical clearance between bundled units = 3" min.

GENERAL
*(1) Design is based on u = 0.25 and k = 0.0002. Pjack specified at the jacking ends includes friction losses and provision for 25,000 psi loss in stress.
(2) Tendons to be jacked to .75 f's and anchored at an equivalent anchor set of ⅜".
(3) Contractor to submit elongation and jacking calculations based on uα+kl = (As Shown) and initial stress of = (m) times jacking stress.
(4) Metallic enclosures to be galvanized rigid duct.
(5) Enclosures to be vented through slab within 3' of the high points of the cable path.
(6) During stressing operations, the elongation shall be continuously compared with gage pressure to check against duct blockage and excessive friction.
(7) Bar reinforcement interfering with the prestressing tendon alignment shall be adjusted as directed by the Engineer.

Location	Pjack	f'c	f'ci	uα+kl	m
Spans 3 & 4	8,870	4,000	3,500	0.1122	0.893
Spans 6,7,& 8	6,570	3,500	3,500	0.200	0.819

NOTES

Falsework loading in vicinity of the ends of prestressed girders will be increased due to stressing operations.

Stem flares as shown may be modified to provide a min. of 2" clearance for a specific stressing system with the approval of the Engineer

AS BUILT
CORRECTIONS Not Available
CONTRACT NO. 068324
DATE 3/26

Figure A.26 - South Connector prestressing details

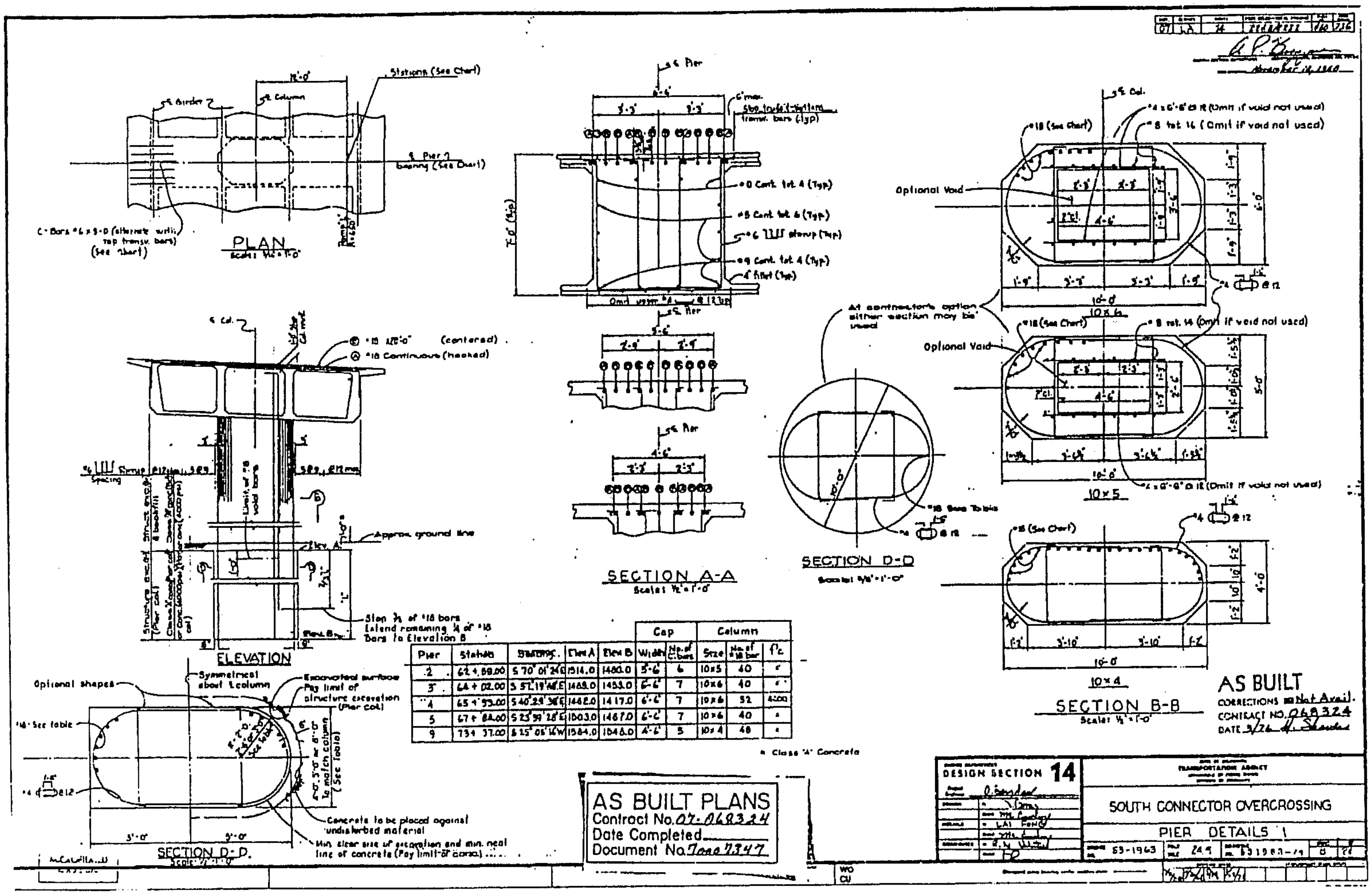
PLAN
ELEVATION
SECTION A-A
Scale: ½" = 1'-0"
SECTION D-D
SECTION B-B
Optional Void
Optional shapes
Approx. ground line
Pier | Station | Bearing | Elev A | Elev B | Cap Width | Cap No. of C bars | Column Size | Column No. of #18 bar | f'c
2 | 62+88.00 | S 70° 01' 24" E | 1514.0 | 1480.0 | 5'-6" | 6 | 10×5 | 40 | *
3 | 64+02.00 | S 57° 19' 46" E | 1469.0 | 1453.0 | 6'-6" | 7 | 10×6 | 40 | *
4 | 65+93.00 | S 40° 29' 36" E | 1448.0 | 1417.0 | 6'-6" | 7 | 10×6 | 52 | 4000
5 | 67+84.00 | S 23° 39' 28" E | 1003.0 | 1467.0 | 6'-6" | 7 | 10×6 | 40 | *
9 | 73+37.00 | S 25° 05' 16" W | 1584.0 | 1046.0 | 4'-6" | 5 | 10×4 | 48 | *
* Class 'A' Concrete
AS BUILT PLANS
Contract No. 07-068324
Date Completed
Document No. 7346
AS BUILT
CONTRACT NO. 068324
DESIGN SECTION 14
SOUTH CONNECTOR OVERCROSSING
PIER DETAILS 1

Figure A.27 - South Connector pier details 1

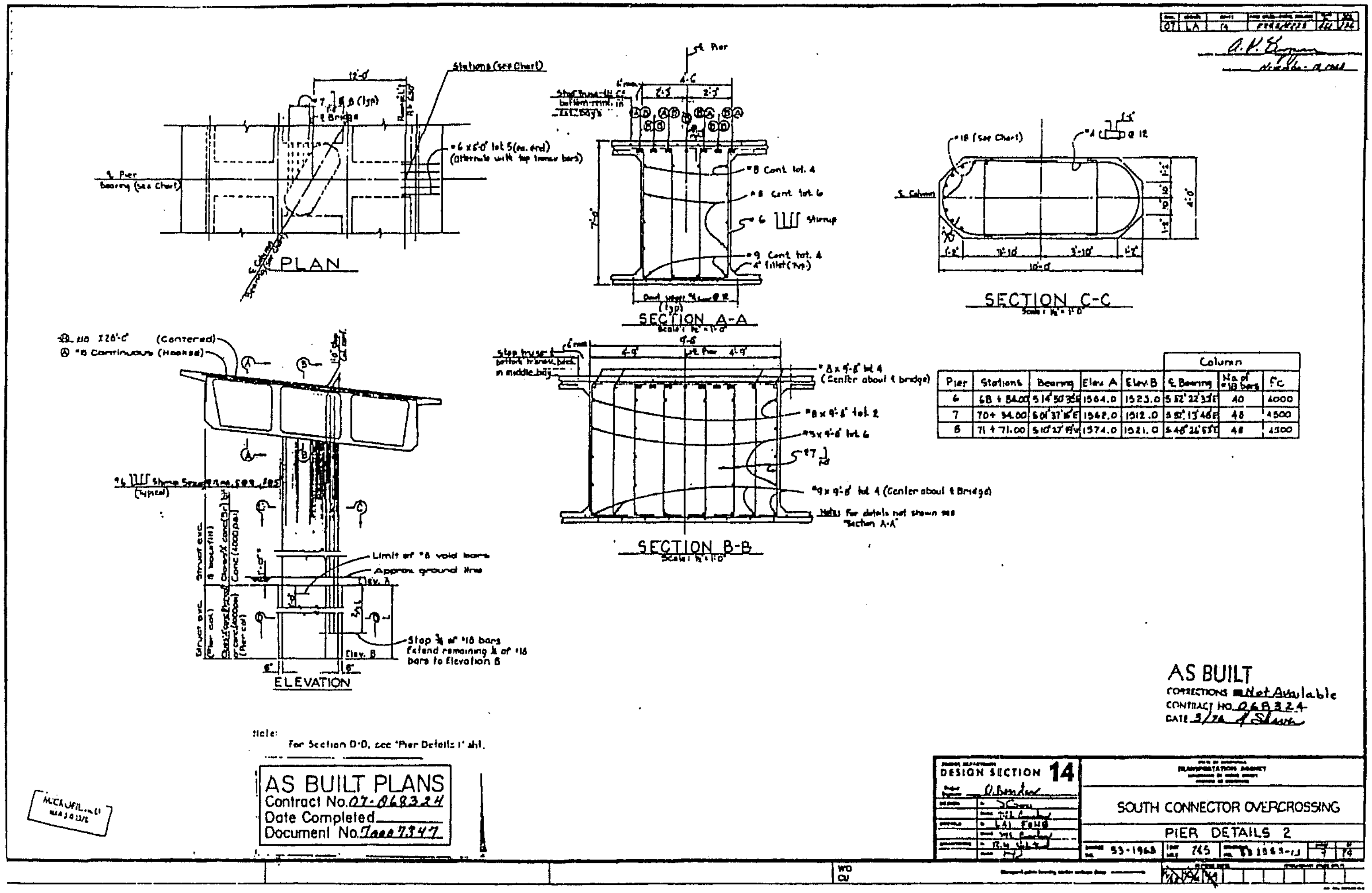
PLAN
Stations (see Chart)
12'-0"
℄ Bridge
℄ Pier Bearing (see Chart)
#6 x 5'-0" tot. 5 (ea. end) (Alternate with top transv. bars)
SECTION A-A
℄ Pier
4'-6"
2'-3"
2'-3"
#8 Cont tot. 4
#8 Cont tot. 6
#6 Stirrup
#9 Cont tot. 4
4" fillet (typ)
7'-0"
SECTION C-C
Scale: ½" = 1'-0"
#18 (see Chart)
#4 @ 12
℄ Column
10'-0"
3'-10"
3'-10"
1'-2"
4'-0"
ELEVATION
#18 @ 1'-0" (Centered)
#8 Continuous (Hooked)
Limit of #8 void bars
Approx. ground line
Elev. A
Elev. B
Stop ¾ of #18 bars Extend remaining ¼ of #18 bars to Elevation B
Struct exc.
SECTION B-B
9'-6"
4'-9"
4'-9"
#8 x 4'-6" tot 4 (Center about ℄ bridge)
#8 x 4'-6" tot. 2
#5 x 4'-6" tot. 6
#7
#9 x 9'-6" tot. 4 (Center about ℄ Bridge)
Note: For details not shown see "Section A-A"
Note:
For Section D-D, see "Pier Details 1" sht.
AS BUILT PLANS
Contract No. 07-068324
Date Completed
Document No.
AS BUILT
CORRECTIONS Not Available
CONTRACT NO. 068324
DESIGN SECTION 14
SOUTH CONNECTOR OVERCROSSING
PIER DETAILS 2
53-1968
265

					Column		
Pier	Stations	Bearing	Elev A	Elev B	℄ Bearing	No. of #18 bars	f'c
6	68 + 84.00	S 14° 50' 35" E	1564.0	1523.0	S 52° 22' 35" E	40	4000
7	70 + 34.00	S 01° 37' 16" E	1542.0	1512.0	S 52° 13' 46" E	48	4500
8	71 + 71.00	S 10° 27' 19" W	1574.0	1521.0	S 48° 26' 53" E	48	4500

Figure A.28 - South Connector pier details 2

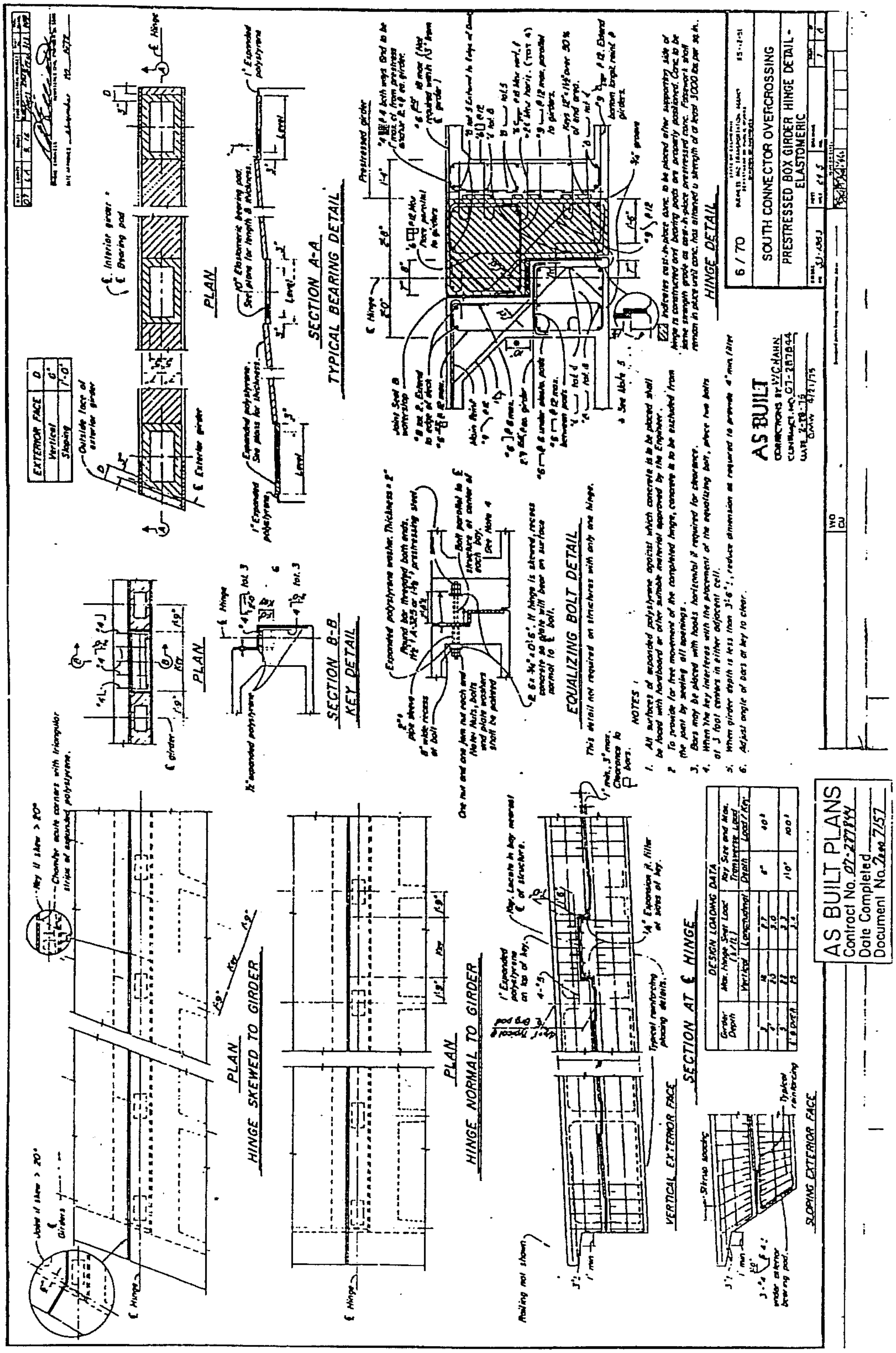
PLAN
HINGE SKEWED TO GIRDER
PLAN
HINGE NORMAL TO GIRDER
SECTION AT ℄ HINGE
VERTICAL EXTERIOR FACE
SLOPING EXTERIOR FACE
DESIGN LOADING DATA
PLAN
SECTION B-B
KEY DETAIL
EQUALIZING BOLT DETAIL
NOTES:
PLAN
SECTION A-A
TYPICAL BEARING DETAIL
HINGE DETAIL
EXTERIOR FACE
Vertical
Sloping
AS BUILT
6/70
SOUTH CONNECTOR OVERCROSSING
PRESTRESSED BOX GIRDER HINGE DETAIL - ELASTOMERIC
AS BUILT PLANS
Contract No. 07-287844
Date Completed
Document No.

Figure A.29 - South Connector prestressed box girder hinge detail - elastomeric

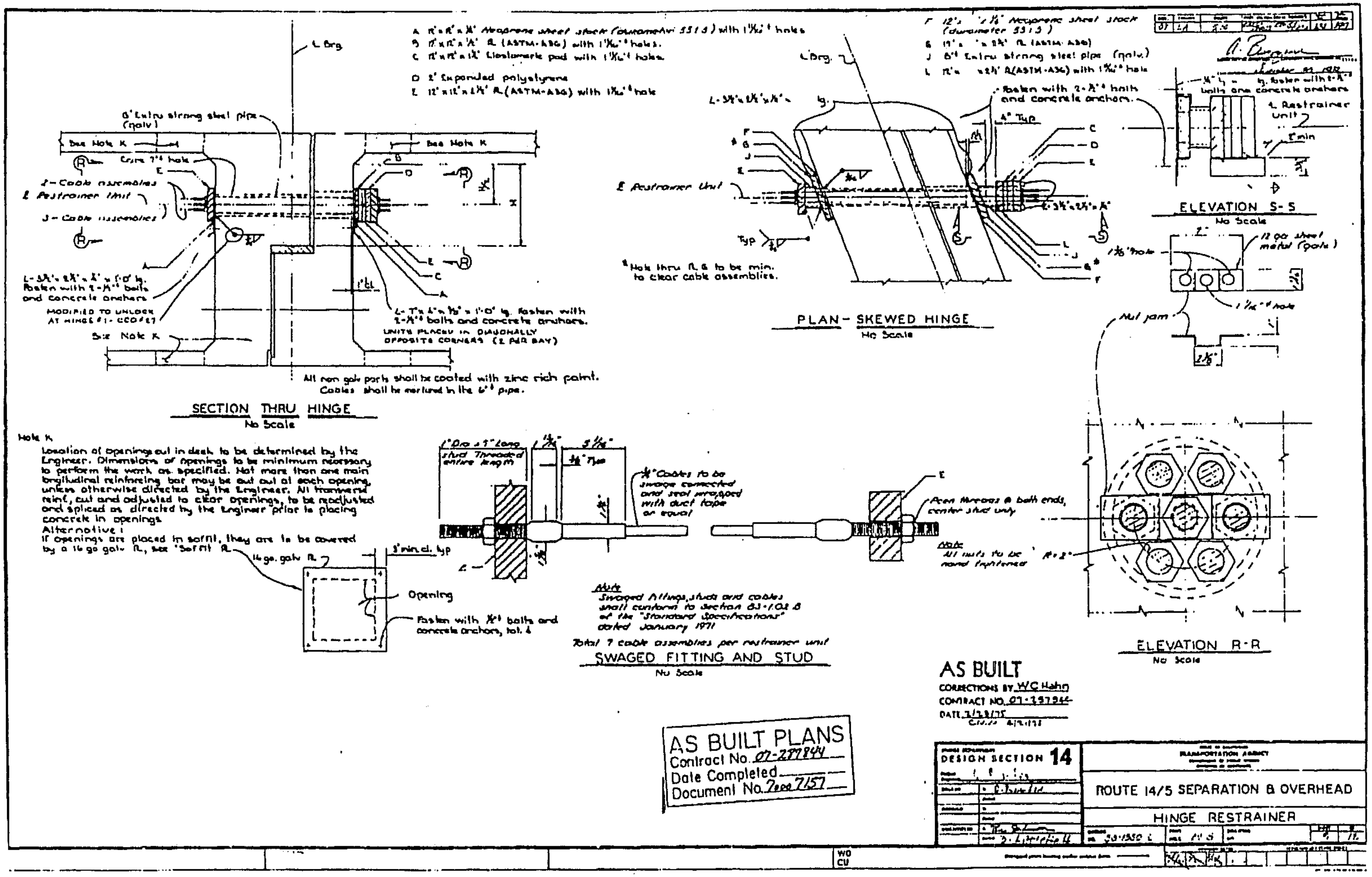

A 18"x18"x¾" Neoprene sheet stock (durometer 5513) with 1¹¹⁄₁₆" holes
B 18"x18"x¼" PL (ASTM-A36) with 1¹¹⁄₁₆" holes.
C 18"x18"x1½" Elastomeric pad with 1¹¹⁄₁₆" holes
D 2" Expanded polystyrene
E 12"x12"x1¼" PL (ASTM-A36) with 1¹¹⁄₁₆" hole
F 12"x ½" Neoprene sheet stock (durometer 5513)
G 11"x 1¼" PL (ASTM-A36)
J 6" Extra strong steel pipe (galv.)
L PL (ASTM-A36) with 1¹¹⁄₁₆" hole
℄ Brg.
6" Extra strong steel pipe (galv.)
See Note K
2 - Cable assemblies
℄ Restrainer Unit
3 - Cable assemblies
Modified to unlock at hinges
All non galv parts shall be coated with zinc rich paint. Cables shall be inserted in the 6" pipe.
SECTION THRU HINGE
No Scale
Note K
Location of openings cut in deck to be determined by the Engineer. Dimensions of openings to be minimum necessary to perform the work as specified. Not more than one main longitudinal reinforcing bar may be cut out at each opening, unless otherwise directed by the Engineer. All transverse reinf. cut and adjusted to clear openings, to be readjusted and spliced as directed by the Engineer prior to placing concrete in openings.
Alternative:
If openings are placed in soffit, they are to be covered by a 16 ga galv PL, see "Soffit PL"
16 ga. galv PL
Opening
Fasten with ⅜" bolts and concrete anchors, tot. 4
Hole thru PL G to be min. to clear cable assemblies.
Fasten with 2-⅜" bolts and concrete anchors.
4" Typ
Typ
PLAN - SKEWED HINGE
No Scale
℄ Restrainer Unit
ELEVATION S-S
No Scale
12 ga sheet metal (galv)
1⅛" hole
Nut jam
ELEVATION R-R
No Scale
Cables to be swage connected and seal wrapped with duct tape or equal
Peen threads @ both ends, center stud only
Note
All nuts to be hand tightened
Note
Swaged fittings, studs and cables shall conform to Section 83-1.02 B of the "Standard Specifications" dated January 1971
Total 7 cable assemblies per restrainer unit
SWAGED FITTING AND STUD
No Scale
AS BUILT
CORRECTIONS BY W.C. Hahn
CONTRACT NO. 07-237944
AS BUILT PLANS
Contract No. 07-237944
Date Completed
Document No. 7157
DESIGN SECTION 14
ROUTE 14/5 SEPARATION & OVERHEAD
HINGE RESTRAINER

Figure A.30 - South Connector hinge restrainer

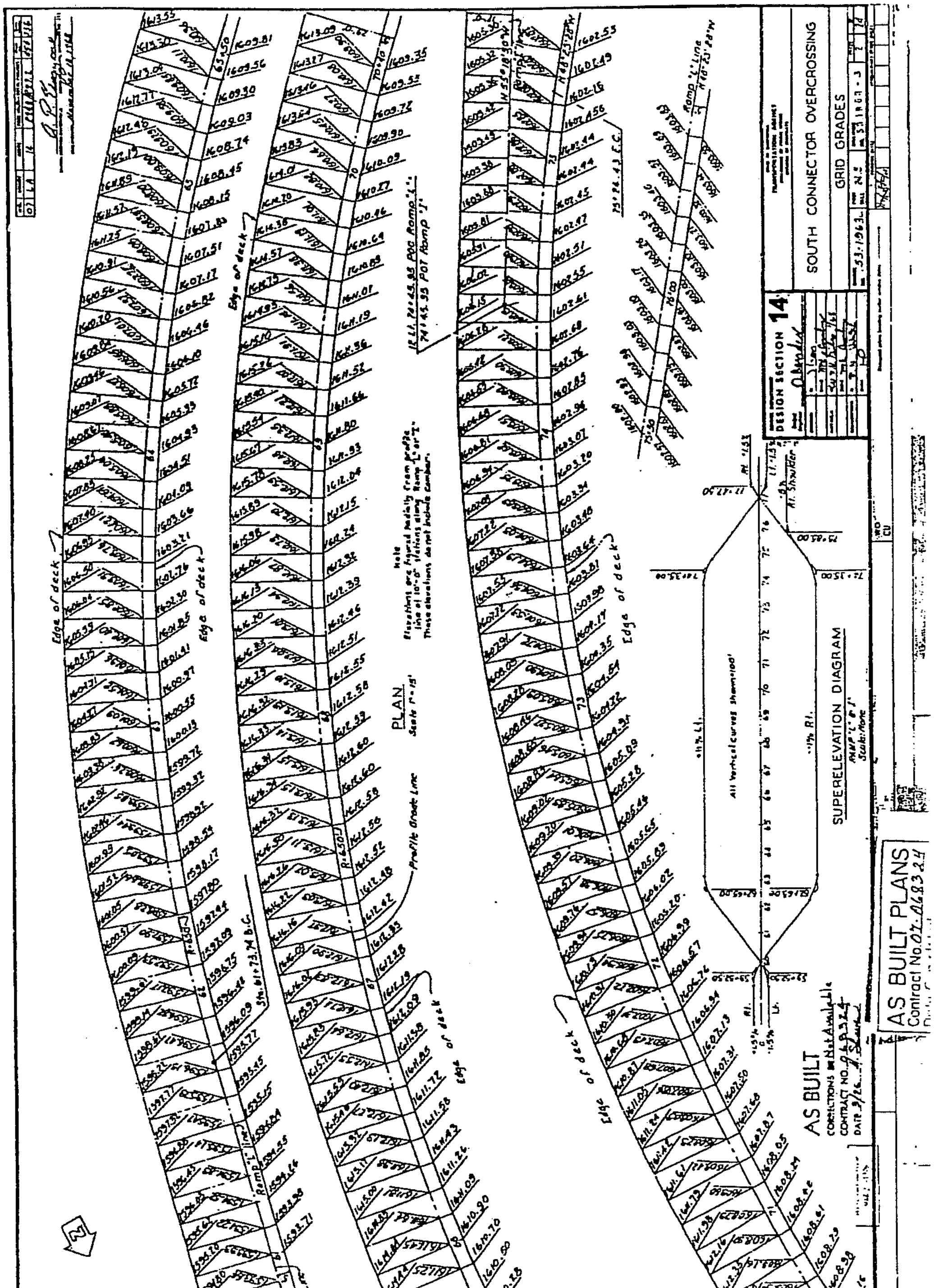
SOUTH CONNECTOR OVERCROSSING
GRID GRADES
DESIGN SECTION 14
PLAN
SUPERELEVATION DIAGRAM
Edge of deck
Profile Grade Line
AS BUILT
AS BUILT PLANS

Figure A.31 - South Connector grid grades

Appendix B

NCEER-Lamont-Doherty Observatory

Artificial Earthquake Records

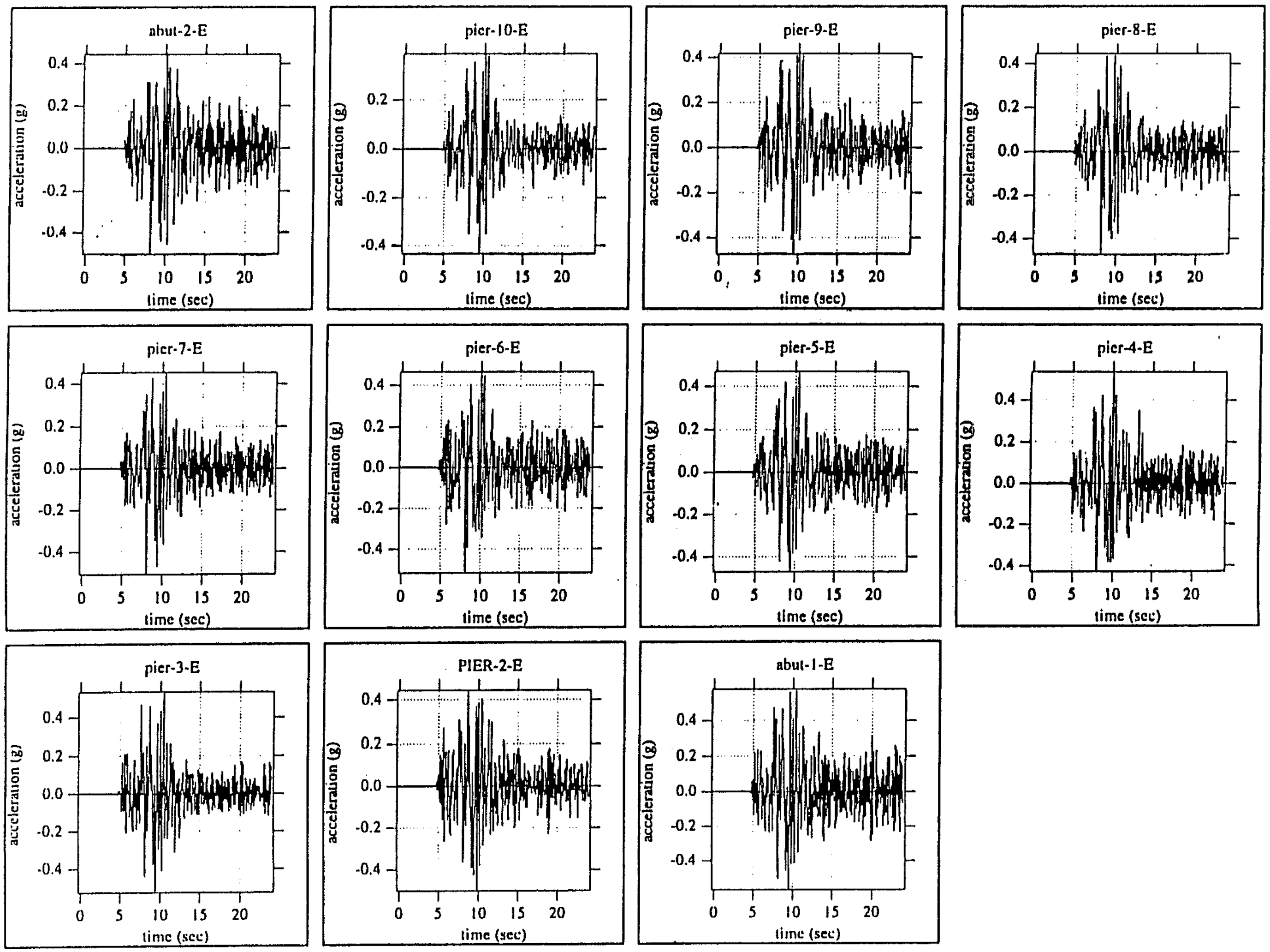

Figure B.1 - Artificial earthquake accelerations in E-W direction

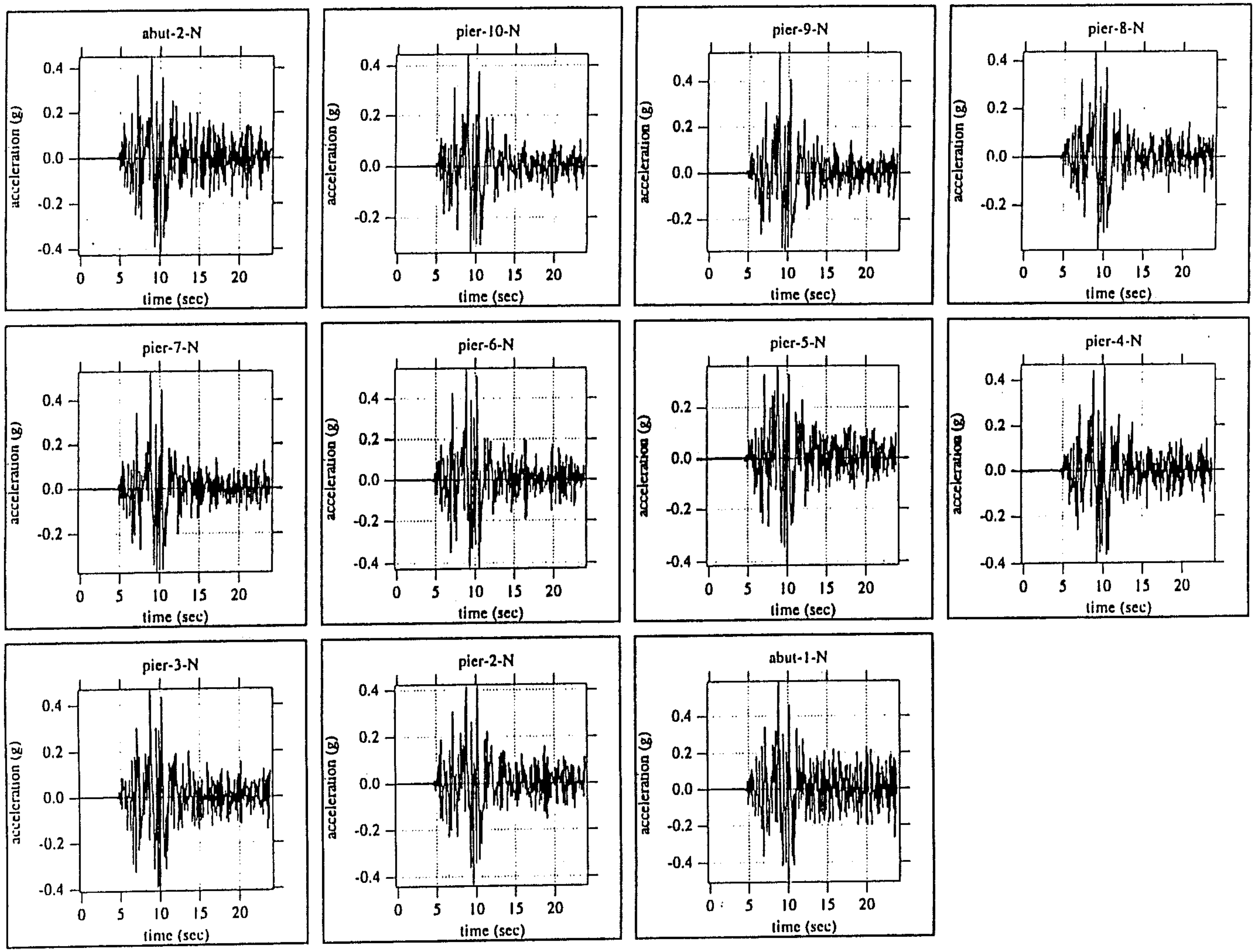

Figure B.2 - Artificial earthquake accelerations in N-S direction

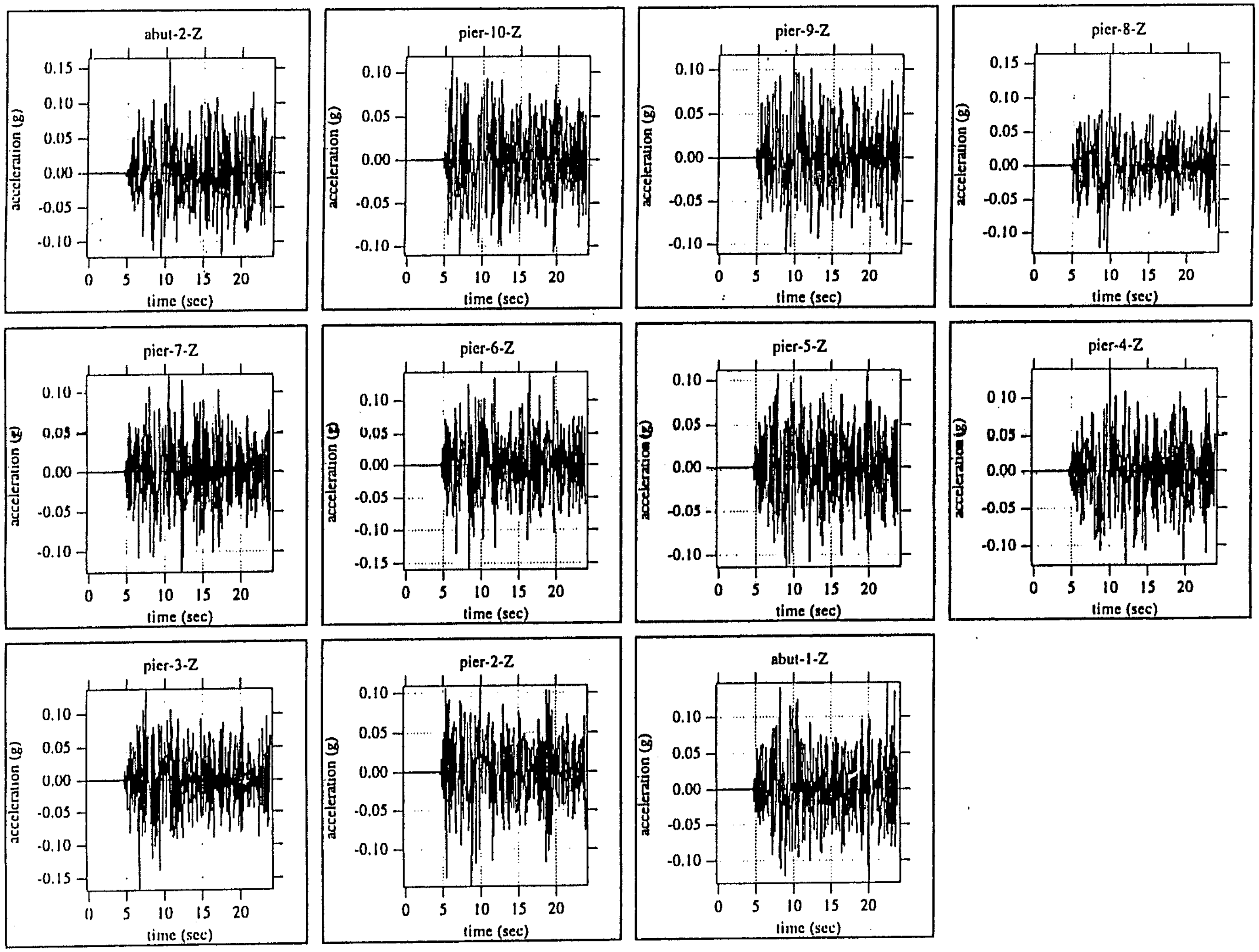

Figure B.3 - Artificial earthquake accelerations in vertical direction

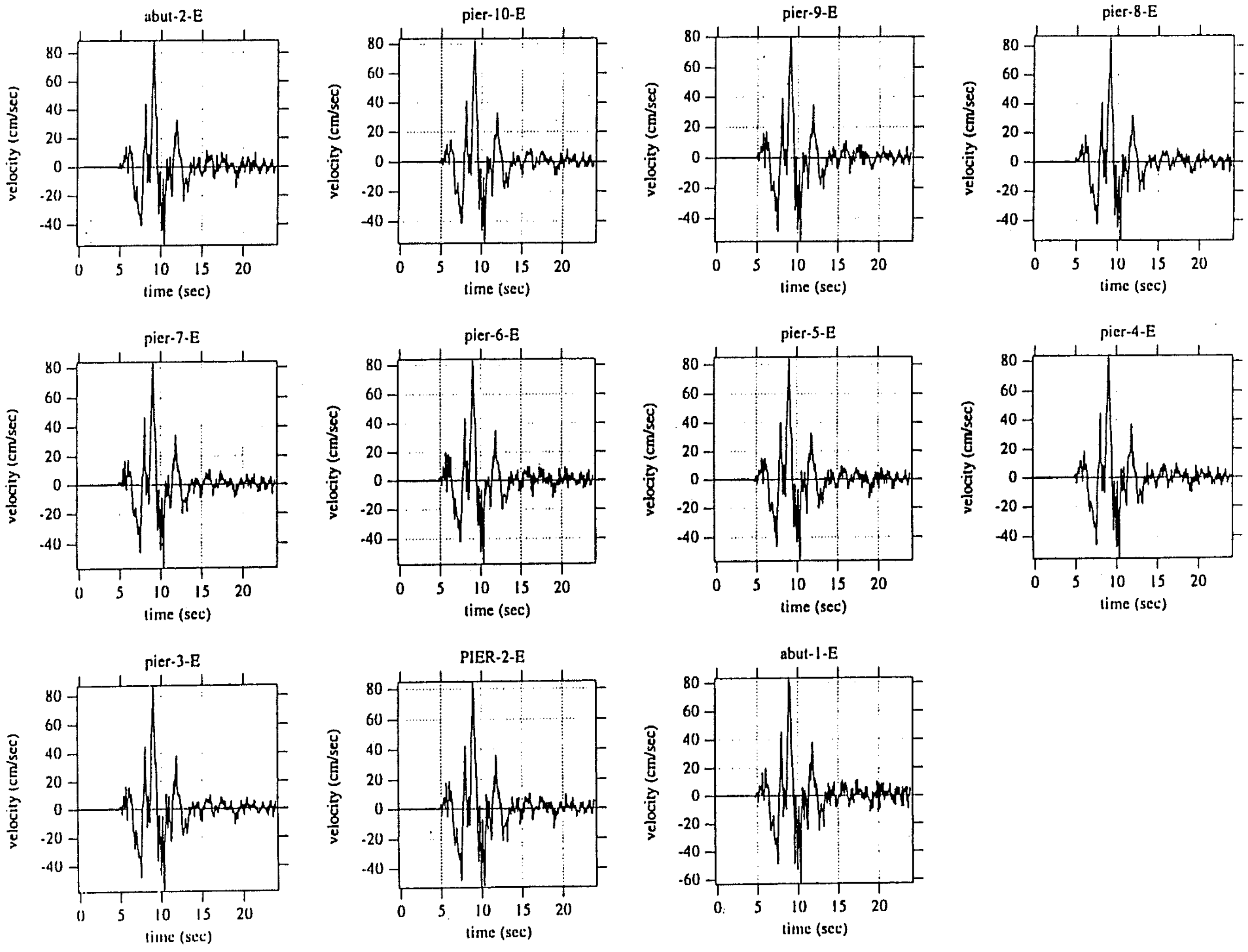

Figure B.4 - Artificial earthquake velocities in E-W direction

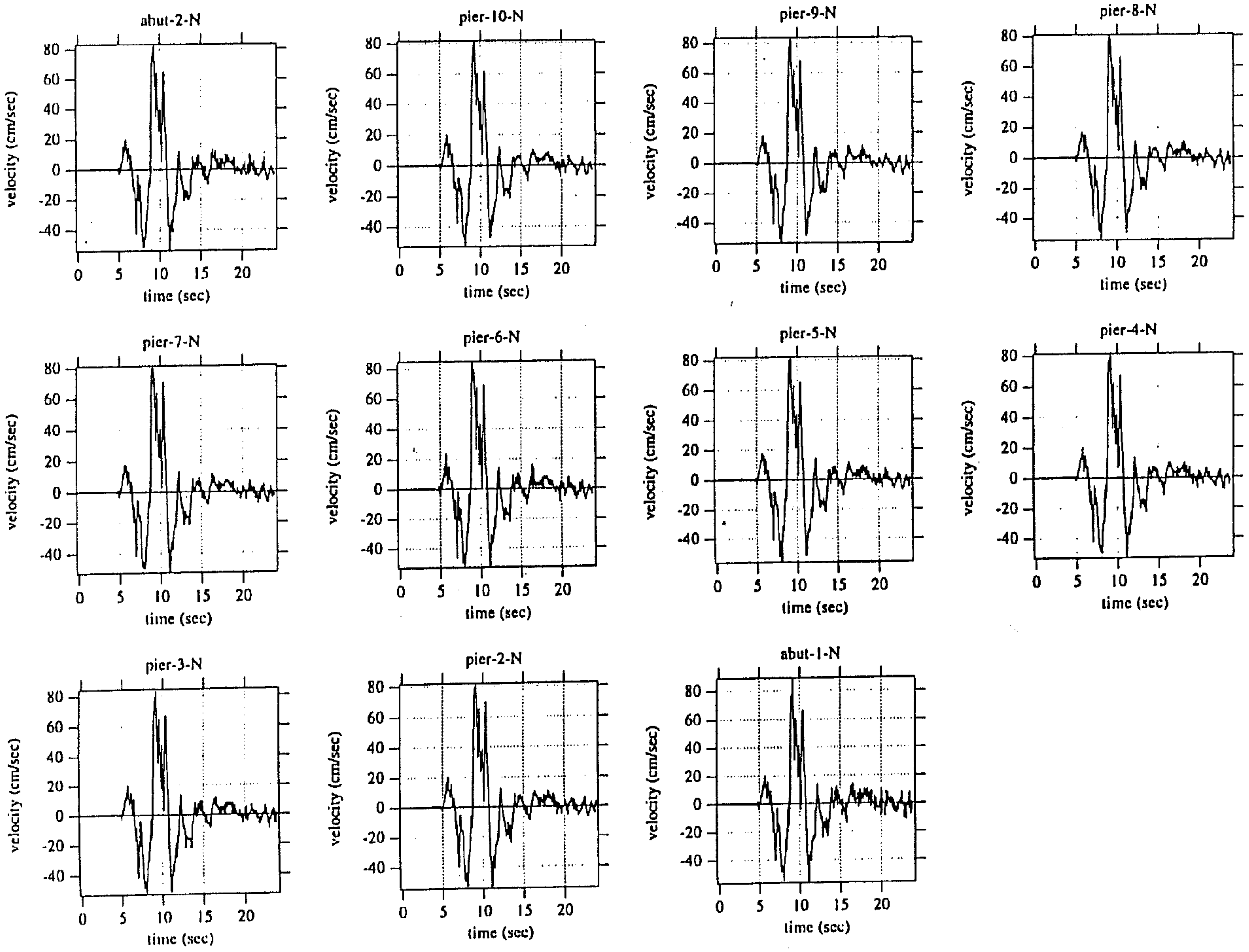

Figure B.5 - Artificial earthquake velocities in N-S direction

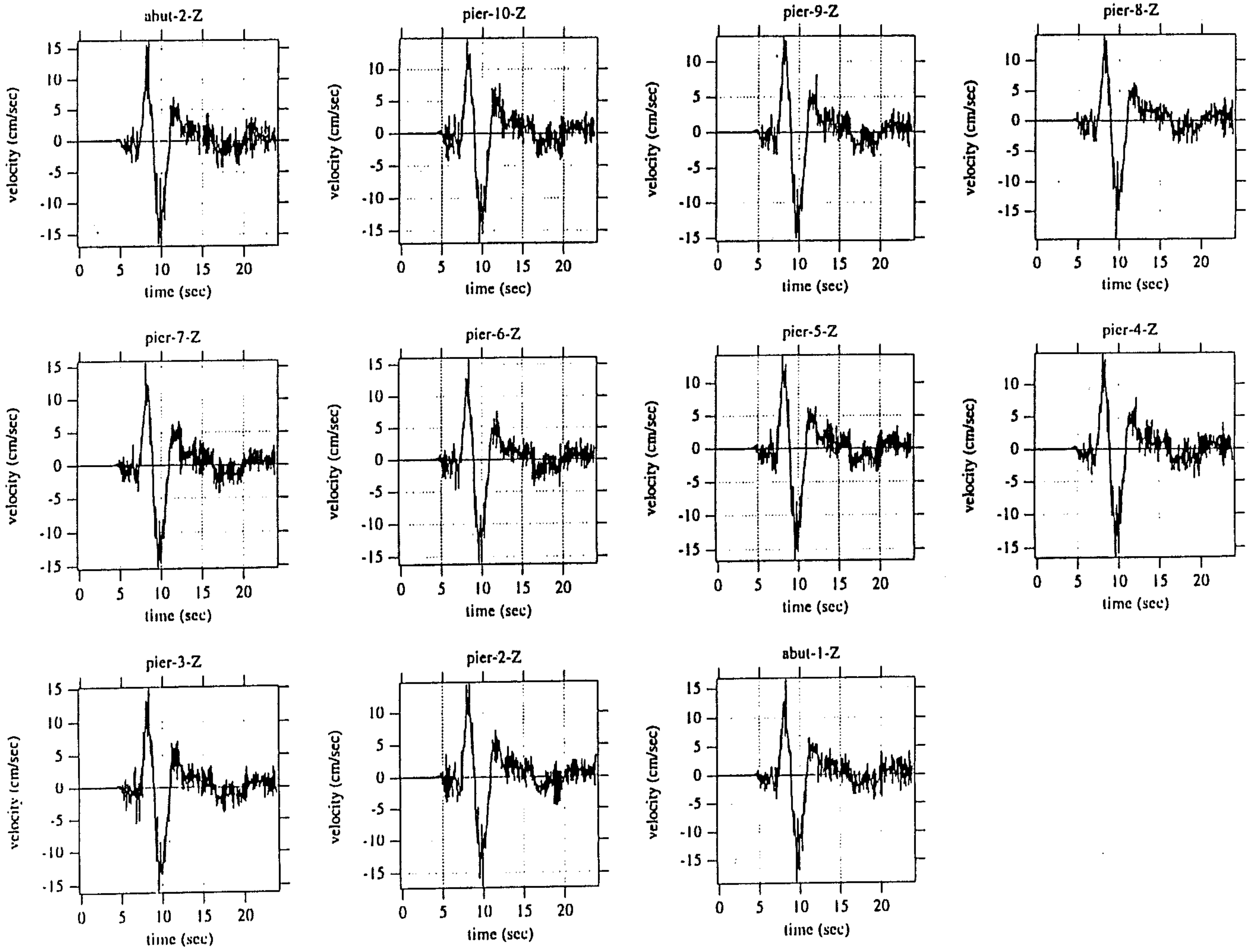

Figure B.6 - Artificial earthquake velocities in vertical direction

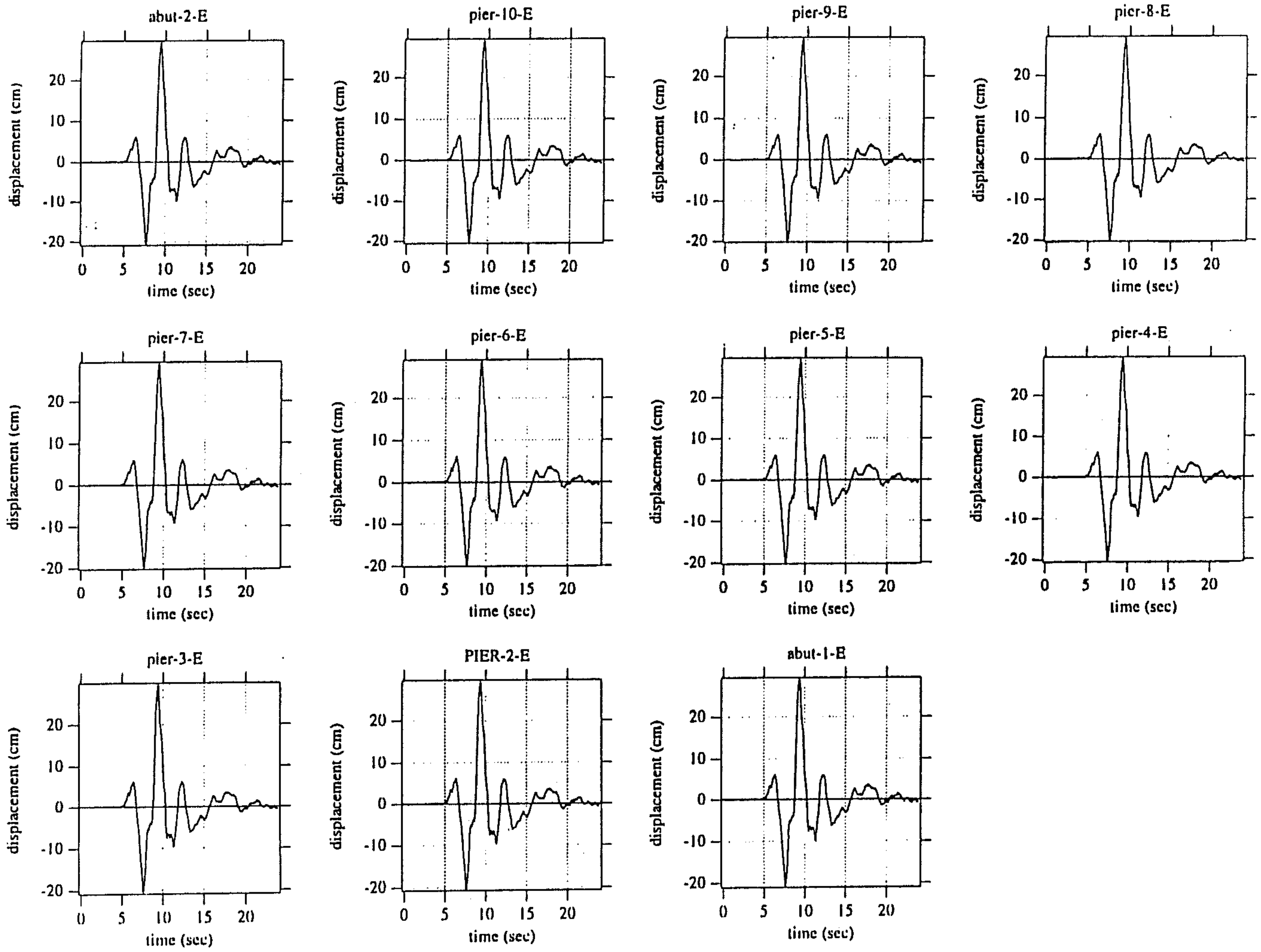

Figure B.7 - Artificial earthquake displacements in E-W direction

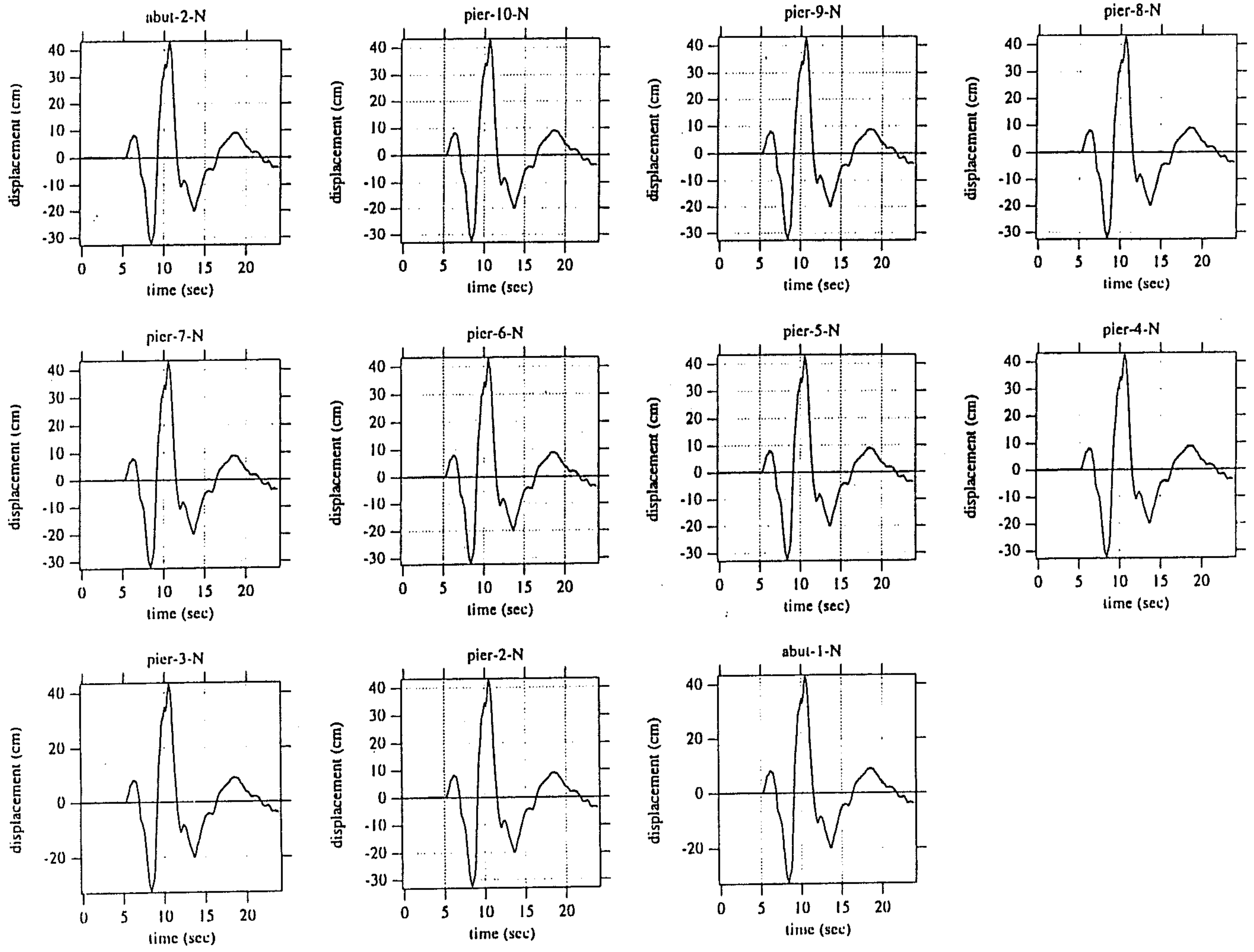

Figure B.8 - Artificial earthquake displacements in N-S direction

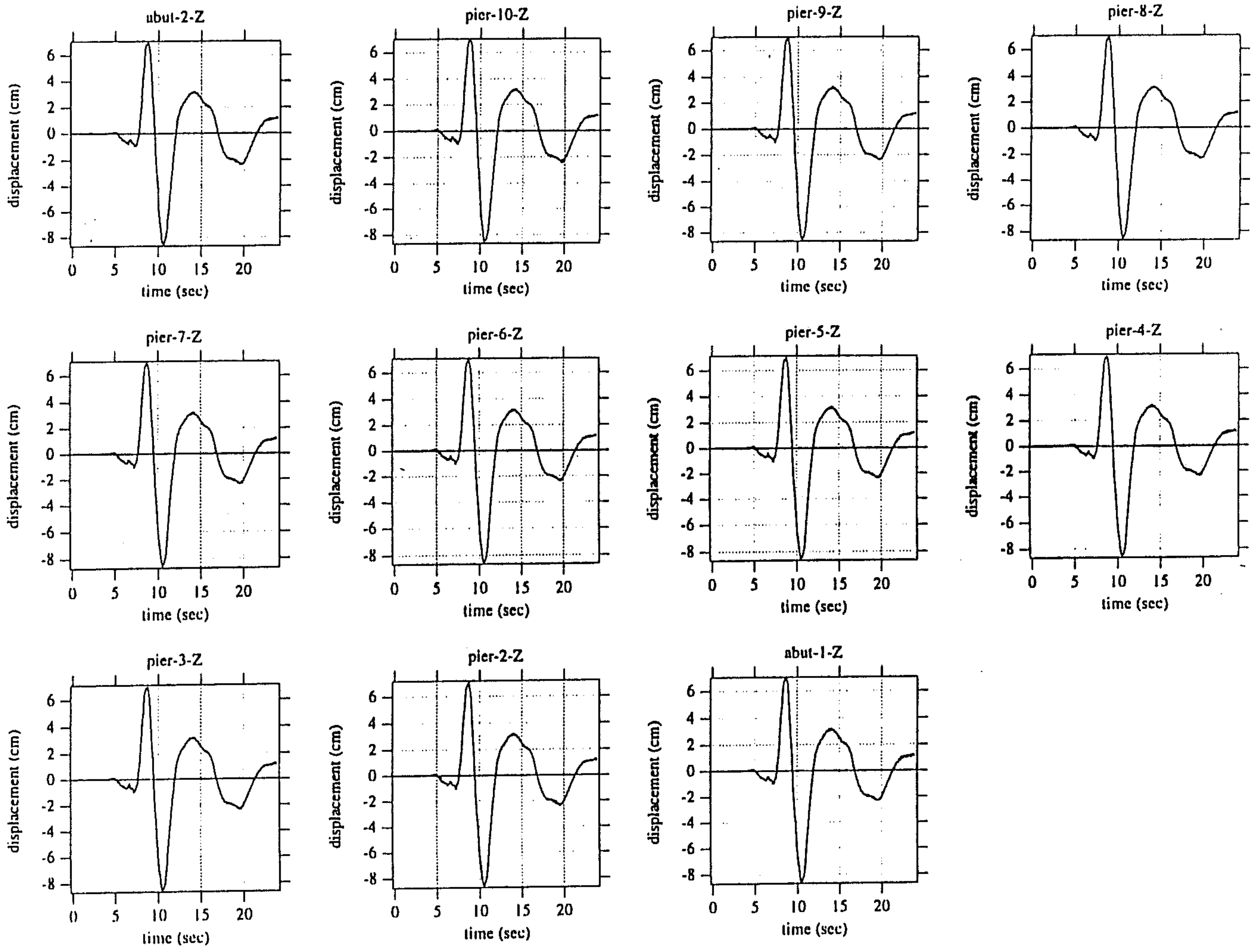

Figure B.9 - Artificial earthquake displacements in vertical direction

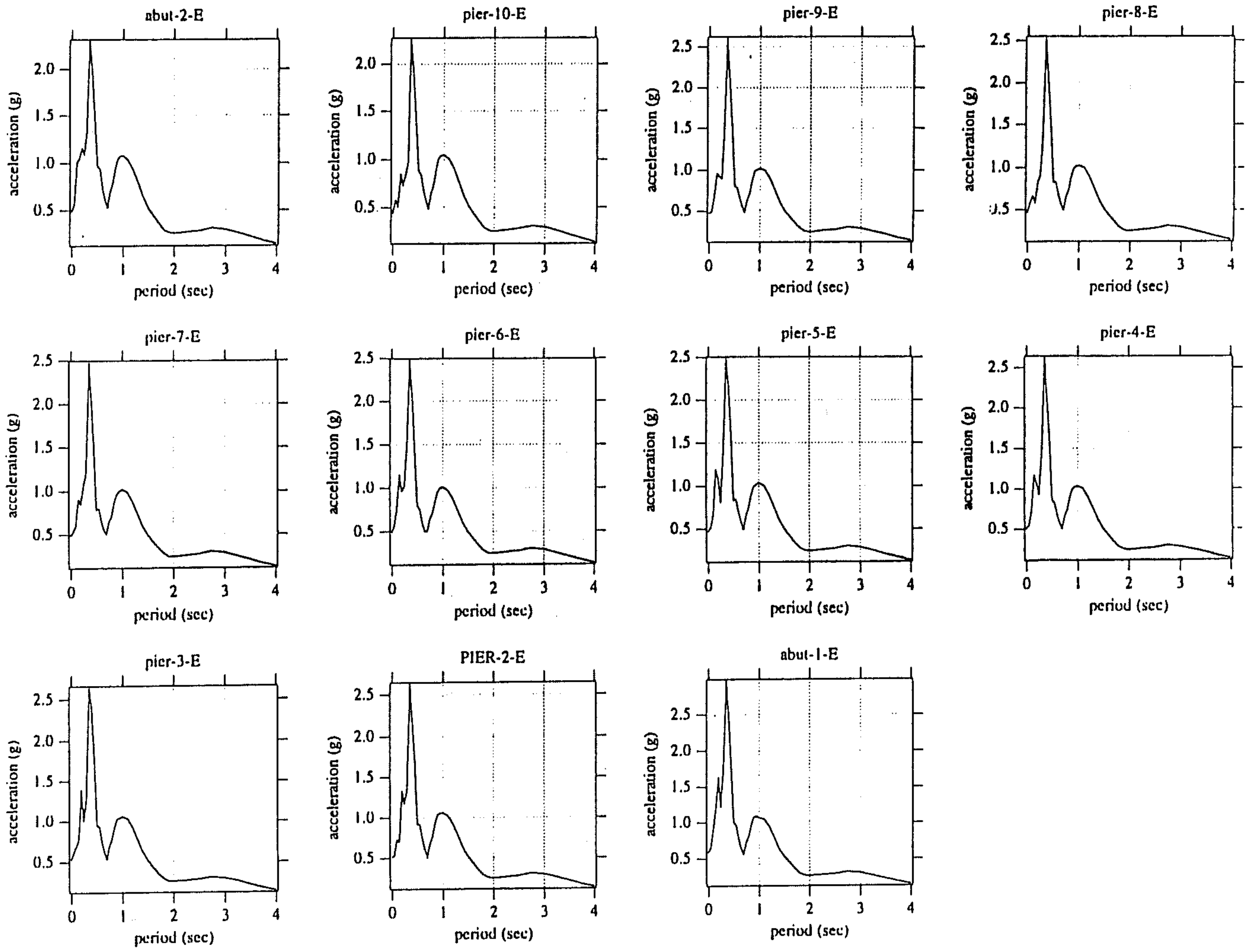

Figure B.10 - Artificial earthquake response spectrum accelerations in E-W direction

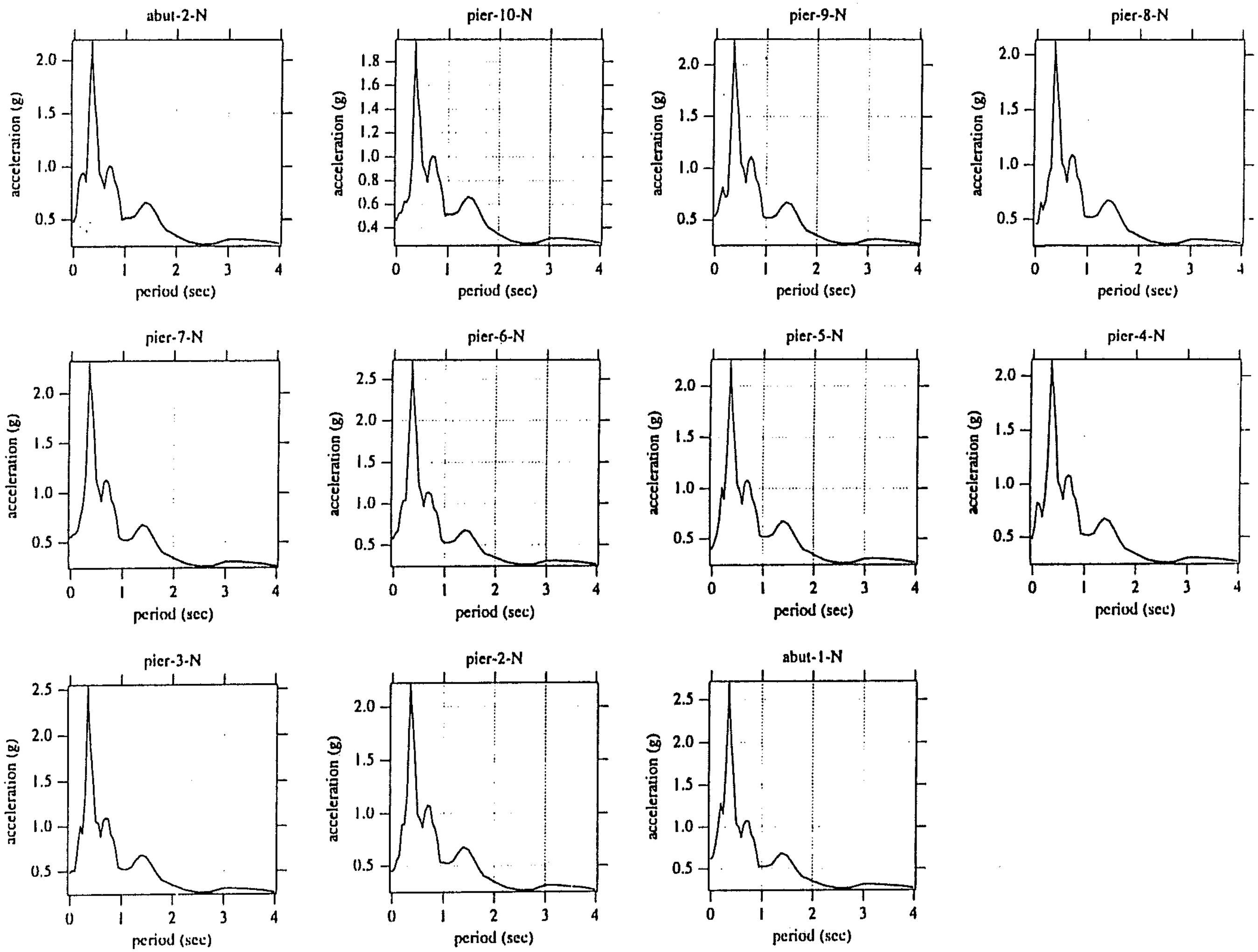

Figure B.11 - Artificial earthquake response spectrum accelerations in N-S direction

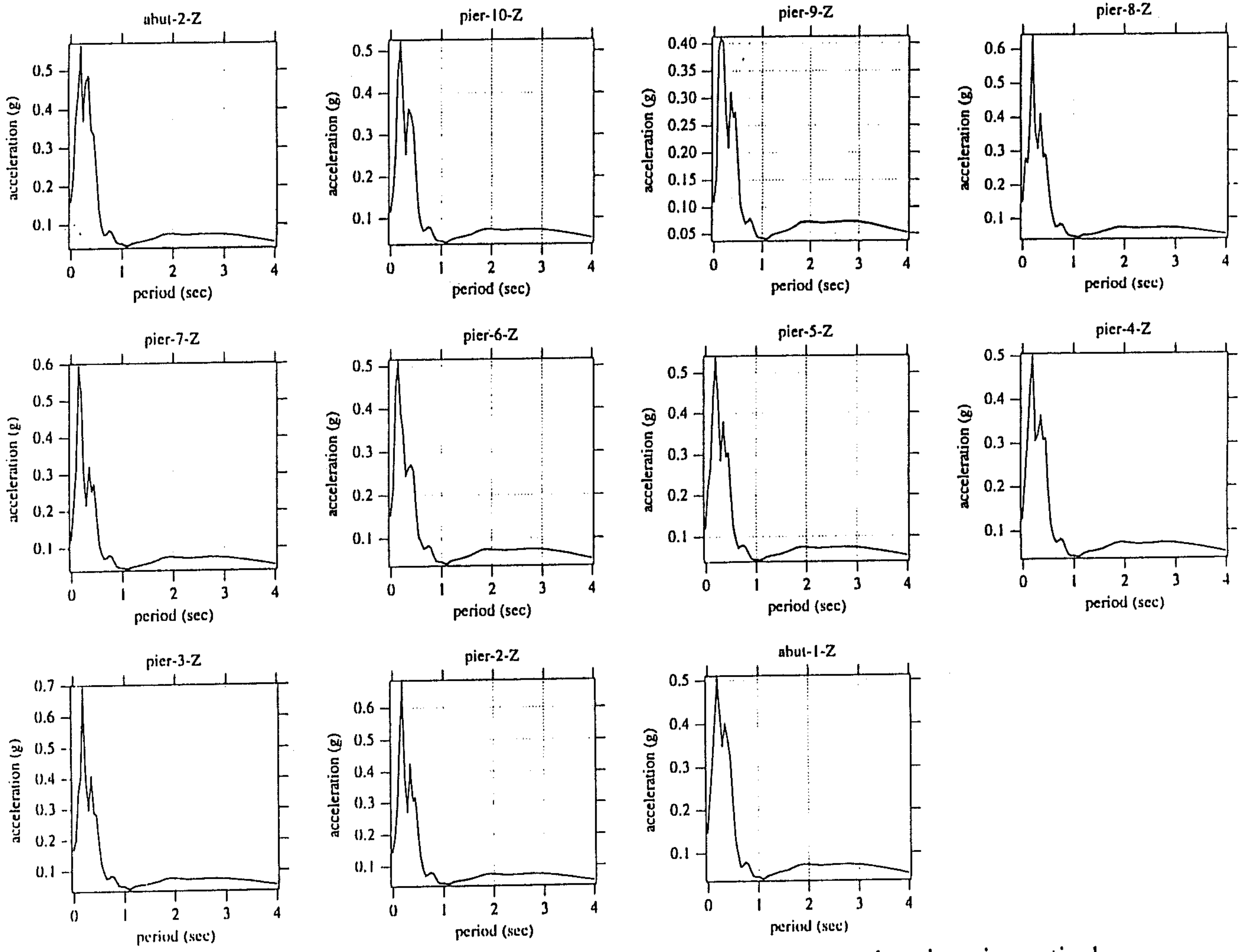

Figure B.12 - Artificial earthquake response spectrum accelerations in vertical direction

Appendix C

Calculation of Moment Capacity

Looking at Pier #5 in the North Connector

Dead Load Moment = 0 (assuming 1g upward acceleration in deck)

Dead Load Moment + Prestress Moment = 32,234 ft-K

Estimate that a ≈ 2" and that there is 2.5" cover to reinforcement.

$M_n = A_s * f_y * (d - a/2)$

$A_s = M_n / f_y / (d - a/2)$

$A_s = 32{,}234$ Ft-k / 60 ksi / (7.542 ft - .08')

$A_s = 72\ \text{in}^2$

According to the bridge plans, there are only approximately 40 - #5 bars placed in the top flange of the girder. While this steel prevent tension cracking, it is only 12.4 in^2, 17% of the amount calculated above. If the vertical acceleration acts is greater than 1g, the steel needed would be even greater.

Appendix D

Calculation of Prestress Moments and Stresses

Analysis of Spans 5 and 6 of the Separation and Overhead

Cross sectional properties for separation and overhead spans #5 and #6

	Midspan		At Pier
E (ksi) =	4031	E (ksi) =	4031
A (ft^2)=	94.5	A (ft^2)=	104.3
I (ft^4)=	677.8	I (ft^4)=	764.6
y top (ft.) =	3.21	y top (ft.) =	3.51
y bot (ft.) =	3.79	y bot (ft.) =	3.49

Prestress losses for separation and overhead spans #5 and #6

Friction losses mu =.25 K = 0.0002

Point	eccentricity (ft.)	segment	delta e (ft.)	length (ft.)	alpha	mu * alpha	KL + m*a	e^-(KL+m*a)	fraction of original stress at end of segment
A	0.000	AB	2.95	72.45	0.088	0.0219	0.0364	0.964	0.964
B	-2.948	BC	4.00	64.4	0.128	0.0319	0.0448	0.956	0.922
C	1.052	CD	1.33	24.15	0.111	0.0277	0.0326	0.968	0.892
D	2.385	DE	1.33	24.15	0.111	0.0277	0.0326	0.968	0.892
E	1.052	EF	4.00	64.4	0.128	0.0319	0.0448	0.956	0.922
F	-2.948	FG	2.95	72.45	0.088	0.0219	0.0364	0.964	0.964
G	0.000								

Anchor Set Losses

distance from support (ft.)	fraction of original prestress force loss
0	0.1260
16.1	0.1079
32.2	0.0897
48.3	0.0716
64.4	0.0535
80.5	0.0354
96.6	0.0172

Force Coefficients (symmetric for Spans #5 and #6 - calculation below for span #5)

Note: All losses are as a fraction of the original (1.0)

location	distance from support (ft.)	initial force coefficient (F.C.I.)	anchor set losses	long term losses	final force coefficient (F.C.F.)	F.C.I./F.C.F.
0L1	0	1.000	0.1260	0.0988	0.775	1.290
.1L1	16.1	0.992	0.1079	0.0988	0.785	1.263
.2L1	32.2	0.984	0.0897	0.0988	0.796	1.237
.3L1	48.3	0.976	0.0716	0.0988	0.806	1.212
.4L1	64.4	0.968	0.0535	0.0988	0.816	1.187
.5L1	80.5	0.959	0.0354	0.0988	0.825	1.163
.6L1	96.6	0.948	0.0172	0.0988	0.832	1.139
.7L1	112.7	0.938		0.0988	0.839	1.118
.8L1	128.8	0.927		0.0988	0.828	1.119
.9L1	144.9	0.917		0.0988	0.819	1.121
1.0L1	161	0.892		0.0988	0.794	1.124

Calculation of Ordinates of Curve for Moment Coefficients

location	eccentricity (ft.)	final force coefficient	P*e
0	0.000	0.775	0.000
0.1	-1.165	0.785	-0.915
0.2	-2.038	0.796	-1.621
0.3	-2.620	0.806	-2.111
0.4	-2.912	0.816	-2.375
0.5	-2.885	0.825	-2.380
0.6	-2.385	0.832	-1.985
0.7	-1.385	0.839	-1.162
0.8	0.115	0.828	0.095
0.9	1.793	0.819	1.468
1	2.385	0.794	1.893

Calculation of secondary moments for beam (see attached figure)

area #	area (PL/EI)	moment arm (L)	moment (PL^2/EI)
1	-0.0457	0.0667	-0.0030
2	-0.0915	0.1500	-0.0137
3	-0.0353	0.1667	-0.0059
4	-0.1621	0.2500	-0.0405
5	-0.0245	0.2667	-0.0065
6	-0.2111	0.3500	-0.0739
7	-0.0132	0.3667	-0.0048
8	-0.2375	0.4500	-0.1069
9	-0.0002	0.4667	-0.0001
10	-0.1985	0.5500	-0.1092
11	-0.0197	0.5333	-0.0105
12	-0.1162	0.6500	-0.0756
13	-0.0412	0.6333	-0.0261
14	-0.0537	0.7308	-0.0393
15	0.0004	0.7975	0.0003
16	0.0095	0.8500	0.0081
17	0.0686	0.8667	0.0595
18	0.1468	0.9500	0.1394
19	0.0213	0.9667	0.0206

total moment = -0.2882 PL^2/EI

reaction at support = -0.2882 PL/EI

By conjgate beam method, the reaction at the support also = secondary moment * L/3EI

secondary moment = 0.865 * the jacking force (labelled as P above)

Calculation of all Coefficients

Location	Force Coefficient	Primary Moment Coefficient	Secondary Moment Coefficient	Total Moment Coefficient
0.0L1	0.775	0.000	0.000	0.000
.1L1	0.785	-0.915	0.086	-0.828
.2L1	0.796	-1.621	0.173	-1.448
.3L1	0.806	-2.111	0.259	-1.852
.4L1	0.816	-2.375	0.346	-2.030
.5L1	0.825	-2.380	0.432	-1.947
.6L1	0.832	-1.985	0.519	-1.467
.7L1	0.839	-1.162	0.605	-0.557
.8L1	0.828	0.095	0.692	0.787
.9L1	0.819	1.468	0.778	2.246
1.0L1	0.794	1.893	0.865	2.758

Calculation of Stresses

P jack (kips) = 10800

Properties @ Midspan

Area (in^2) = 94.5
I (in^4) = 677.79
y top (ft.) = 3.21
y bot. (ft.) = 3.79

Properties @ Bent

Area (in^2) = 104.25
I (in^4) = 764.58
y top (ft.) = 3.51
y bot. (ft.) = 3.49

Location	Force Coefficient	Moment Coefficient	Prestress Force (kips)	Prestress Moment (ft-ips)	Stress due to prestress force (psi)	Stress due to prestress moment (top fiber - psi)	Stress due to prestress moment (bot. fiber - psi)	Dead load moment (ft-kips)	Stress due to dead load mmt. (top fiber - psi))	Stress due to dead load mmt. (bot. fiber - psi)	Percentage of dead load moment balanced
0.0L1	0.7752	0.0000	8372.16	0.00	615.24	0.00	0.00	0	0.00	0.00	100.00
.1L1	0.7854	-0.8282	8482.03	-8944.29	623.31	-294.17	347.32	12547	412.66	-487.22	71.29
.2L1	0.7955	-1.4484	8591.90	-15642.96	631.39	-514.48	607.44	21207	697.47	-823.49	73.76
.3L1	0.8057	-1.8519	8701.77	-20000.03	639.46	-657.78	776.63	25978	854.38	-1008.76	76.99
.4L1	0.8159	-2.0296	8811.64	-21919.55	647.53	-720.91	851.16	26861	883.42	-1043.05	81.60
.5L1	0.8248	-1.9474	8907.50	-21032.35	654.58	-691.73	816.71	23856	784.59	-926.36	88.16
.6L1	0.8323	-1.4667	8989.35	-15839.95	660.59	-520.96	615.09	16963	557.89	-658.69	93.38
.7L1	0.8390	-0.5571	9061.47	-6016.62	665.89	-197.88	233.63	6182	203.31	-240.05	97.33
.8L1	0.8285	0.7867	8947.53	8496.43	657.52	279.44	-329.93	-8487	-279.14	329.58	100.11
.9L1	0.8186	2.2459	8840.97	24255.39	649.69	797.73	-941.87	-27045	-889.48	1050.19	89.69
1.0L1	0.7936	2.7578	8570.88	29784.11	570.94	949.52	-944.11	-49685	-1583.97	1574.94	59.95

TOTAL STRESSES

location	top fiber prestress only (psi)	bot. fiber prestress only (psi)	top fiber with dead load and no live load (psi)	bot. fiber with dead load and no live load (psi)
0.0L1	615.24	615.24	615.24	615.24
.1L1	329.15	970.63	741.80	483.41
.2L1	116.91	1238.82	814.38	415.33
.3L1	-18.32	1416.09	836.07	407.33
.4L1	-73.37	1498.70	810.05	455.65
.5L1	-37.15	1471.29	747.44	544.93
.6L1	139.64	1275.68	697.53	616.98
.7L1	468.01	899.53	671.33	659.48
.8L1	936.96	327.59	657.82	657.17
.9L1	1447.42	-292.18	557.94	758.01
1.0L1	1520.46	-373.18	-63.51	1201.77

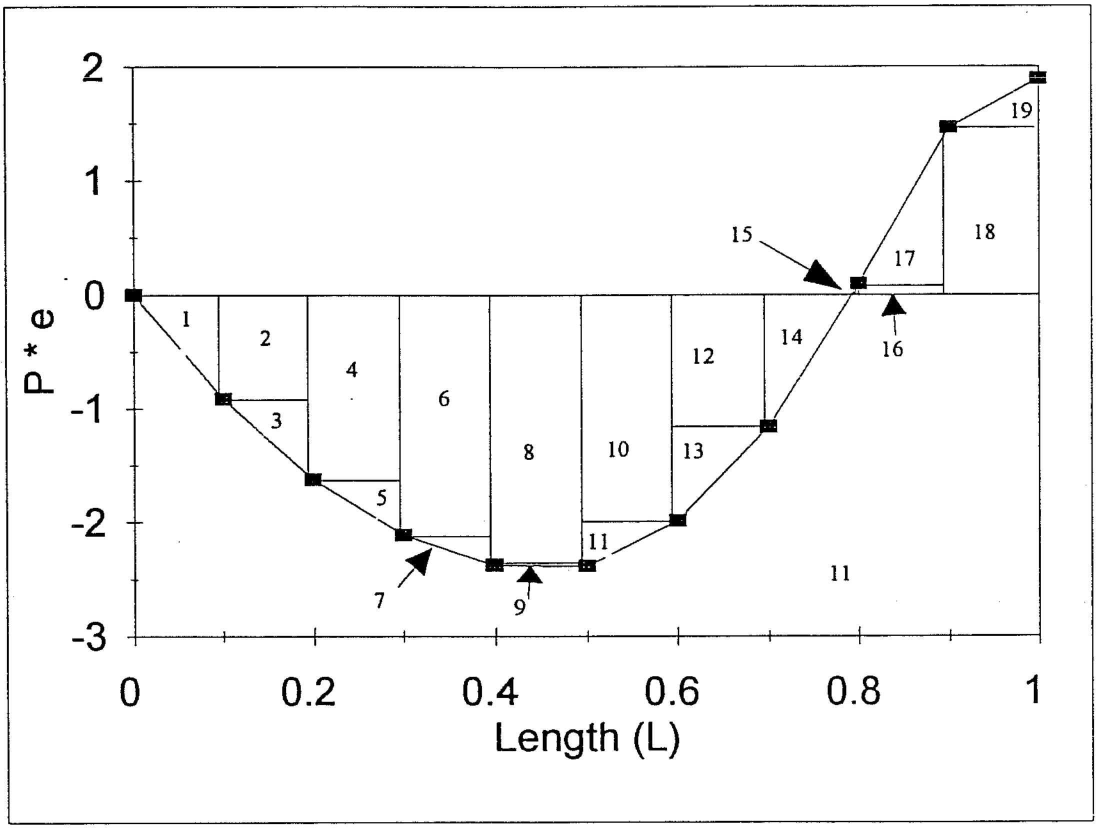

Figure D.1 - Areas used for calculation of secondary moment

Appendix E

Column Interaction Diagram Calculation

North Connector Moment Capacitites (Piers 3,4,6,9,10)

f'c = 5 ksi
fy = 66 ksi

Axial capacity (compression) **26316** kips

Longitudinal direction
Steel Strain = 0 c = 44.37 a = 35.496

Steel Layer	Dist. from top (in).	Number of Bars	Area of Bars (in^2)	Strain	Force (kips)	Moment arm (in.)	Moment (ft-kips)
1	3.63	9	36	0.002755	2223	20.37	3773.543
2	7.14	2	8	0.002517	494	16.86	694.07
3	12.24	4	16	0.002172	940	11.76	921.2
4	19.21	2	8	0.001701	360.6667	4.79	143.9661
5	28.79	2	8	0.001053	210.3922	-4.79	-83.9815
6	35.76	4	16	0.000582	270.1176	-11.76	-264.715
7	40.86	2	8	0.000237	55.05882	-16.86	-77.3576
8	44.37	9	36	0	0	-20.37	0
concrete 1					4879	16.60163	6749.944
concrete 2					8770.368	-0.748	-546.686
total					**18203**		**11310**

Longitudinal Yield Moment c = 25.23 a = 20.184

Steel Layer	Dist. from top (in).	Number of Bars	Area of Bars (in^2)	Strain	Force (kips)	Moment arm (in.)	Moment (ft-kips)
1	3.63	9	36	0.002568	2223	20.37	3773.543
2	7.14	2	8	0.002151	465.0345	16.86	653.3734
3	12.24	4	16	0.001545	648.6897	11.76	635.7159
4	19.21	2	8	0.000716	132.069	4.79	52.71753
5	28.79	2	8	-0.00042	-98.2069	-4.79	39.20092
6	35.76	4	16	-0.00125	-580.966	-11.76	569.3462
7	40.86	2	8	-0.00186	-431.172	-16.86	605.7972
8	44.37	9	36	-0.00228	-2376	-20.37	4033.26
concrete 1					4879	16.60163	6749.944
concrete 2					2523.072	6.908	1452.448
total					**7385**		**18565**

Steel Strain = 2.5 * ϵ_y c = 15.31821 a = 12.25457

Steel Layer	Dist. from top (in).	Number of Bars	Area of Bars (in^2)	Strain	Force (kips)	Moment arm (in.)	Moment (ft-kips)
1	3.63	9	36	0.002289	2223	20.37	3773.543
2	7.14	2	8	0.001602	337.5862	16.86	474.3086
3	12.24	4	16	0.000603	211.7241	11.76	207.4897
4	19.21	2	8	-0.00076	-176.828	4.79	-70.5837
5	28.79	2	8	-0.00264	-528	-4.79	210.76
6	35.76	4	16	-0.004	-1056	-11.76	1034.88
7	40.86	2	8	-0.005	-528	-16.86	741.84
8	44.37	9	36	-0.00569	-2376	-20.37	4033.26
concrete 1					4179.813	17.56084	6116.753
total					**2287**		**16522**

Longitudinal Plastic Moment c = 11.26 a = 9.008

Steel Layer	Dist. from top (in).	Number of Bars	Area of Bars (in^2)	Strain	Force (kips)	Moment arm (in.)	Moment (ft-kips)
1	3.63	9	36	0.002033	1969.306	20.37	3342.896
2	7.14	2	8	0.001098	220.6643	16.86	310.0333
3	12.24	4	16	-0.00026	-121.151	11.76	-118.728
4	19.21	2	8	-0.00212	-528	4.79	-210.76
5	28.79	2	8	-0.00467	-528	-4.79	210.76
6	35.76	4	16	-0.00653	-1056	-11.76	1034.88
7	40.86	2	8	-0.00789	-528	-16.86	741.84
8	44.37	9	36	-0.00882	-2376	-20.37	4033.26
concrete 1					2948.174	19.32038	4746.654
total					**0.9931**		**14090.84**

Steel Strain = 7.5 * ϵ_y c = 6.632629 a = 5.306103

Steel Layer	Dist. from top (in).	Number of Bars	Area of Bars (in^2)	Strain	Force (kips)	Moment arm (in.)	Moment (ft-kips)
1	3.63	9	36	0.001358	1264.874	20.37	2147.124
2	7.14	2	8	-0.00023	-53.2414	16.86	-74.8041
3	12.24	4	16	-0.00254	-1056	11.76	-1034.88
4	19.21	2	8	-0.00569	-528	4.79	-210.76
5	28.79	2	8	-0.01002	-528	-4.79	210.76
6	35.76	4	16	-0.01317	-1056	-11.76	1034.88
7	40.86	2	8	-0.01548	-528	-16.86	741.84
8	44.37	9	36	-0.01707	-2376	-20.37	4033.26
concrete 1					1653.121	21.28294	2931.94
total					**-3207**		**9779**

Steel Strain = 15 * ϵ_y c = 3.584206 a = 2.867365

Steel Layer	Dist. from top (in).	Number of Bars	Area of Bars (in^2)	Strain	Force (kips)	Moment arm (in.)	Moment (ft-kips)
1	3.63	9	36	-3.8E-05	-40.0162	20.37	-67.9275
2	7.14	2	8	-0.00298	-528	16.86	-741.84
3	12.24	4	16	-0.00724	-1056	11.76	-1034.88
4	19.21	2	8	-0.01308	-528	4.79	-210.76
5	28.79	2	8	-0.0211	-528	-4.79	210.76
6	35.76	4	16	-0.02693	-1056	-11.76	1034.88
7	40.86	2	8	-0.0312	-528	-16.86	741.84
8	44.37	9	36	-0.03414	-2376	-20.37	4033.26
concrete 1					863.611	22.54698	1622.652
total					**-5776**		**5588**

Axial capacity (tension) = **-8976** kips

Transverse direction

Steel Strain = 0 c = 91.36 a = 73.088

Steel Layer	Dist. from top (in).	Number of Bars	Area of Bars (in^2)	Strain	Force (kips)	Moment arm (in.)	Moment (ft-kips)
1	4.64	2	8	0.002848	494	43.36	1784.987
2	7.35	4	16	0.002759	988	40.65	3346.85
3	12.28	2	8	0.002597	494	35.72	1470.473
4	21	4	16	0.00231	988	27	2223
5	29.75	2	8	0.002023	435.3581	18.25	662.1072
6	38.5	2	8	0.001736	368.6988	9.5	291.8865
7	50.93	2	8	0.001328	274.0044	-2.93	-66.9027
8	57.5	2	8	0.001112	223.9527	-9.5	-177.296
9	66.25	2	8	0.000825	157.2933	-18.25	-239.217
10	75	4	16	0.000537	249.268	-27	-560.853
11	83.72	2	8	0.000251	58.20315	-35.72	-173.251
12	88.65	4	16	8.9E-05	41.29072	-40.65	-139.872
13	91.36	2	8	0	0	-43.36	0
concrete 1					2023	40.03922	6749.944
concrete 2					12053.95	4.456	4476.034
total					**18849.02**		**19647.89**

Transverse Yield Moment c = 51.9498 a = 41.55984

Steel Layer	Dist. from top (in).	Number of Bars	Area of Bars (in^2)	Strain	Force (kips)	Moment arm (in.)	Moment (ft-kips)
1	4.64	2	8	0.002732	494	43.36	1784.987
2	7.35	4	16	0.002576	988	40.65	3346.85
3	12.28	2	8	0.002291	494	35.72	1470.473
4	21	4	16	0.001787	761.303	27	1712.932
5	29.75	2	8	0.001282	263.4229	18.25	400.6224
6	38.5	2	8	0.000777	146.1944	9.5	115.7372
7	50.93	2	8	5.9E-05	13.66287	-2.93	-3.33602
8	57.5	2	8	-0.00032	-74.359	-9.5	58.86756
9	66.25	2	8	-0.00083	-191.588	-18.25	291.3728
10	75	4	16	-0.00133	-617.632	-27	1389.673
11	83.72	2	8	-0.00183	-425.643	-35.72	1266.997
12	88.65	4	16	-0.00212	-983.385	-40.65	3331.218
13	91.36	2	8	-0.00228	-528	-43.36	1907.84
concrete 1					2023	40.03922	6749.944
concrete 2					5622.208	20.22008	9473.457
total					**7985.184**		**33297.63**

Steel Strain = 2.5 * ϵ_y c = 31.54095 a = 25.23276

Steel Layer	Dist. from top (in).	Number of Bars	Area of Bars (in^2)	Strain	Force (kips)	Moment arm (in.)	Moment (ft-kips)
1	4.64	2	8	0.002559	494	43.36	1784.987
2	7.35	4	16	0.002301	988	40.65	3346.85
3	12.28	2	8	0.001832	391.0228	35.72	1163.944
4	21	4	16	0.001003	397.2049	27	893.711
5	29.75	2	8	0.00017	39.52014	18.25	60.10355
6	38.5	2	8	-0.00066	-153.562	9.5	-121.57
7	50.93	2	8	-0.00184	-427.849	-2.93	104.4666
8	57.5	2	8	-0.00247	-528	-9.5	418
9	66.25	2	8	-0.0033	-528	-18.25	803
10	75	4	16	-0.00413	-1056	-27	2376
11	83.72	2	8	-0.00496	-528	-35.72	1571.68
12	88.65	4	16	-0.00543	-1056	-40.65	3577.2
13	91.36	2	8	-0.00569	-528	-43.36	1907.84
concrete 1					2023	40.03922	6749.944
concrete 2					2291.483	28.38362	5420.049
total					**1818.82**		**30056.21**

Transverse Plastic Moment c = 25.195 a = 20.156

Steel Layer	Dist. from top (in).	Number of Bars	Area of Bars (in^2)	Strain	Force (kips)	Moment arm (in.)	Moment (ft-kips)
1	4.64	2	8	0.002448	494	43.36	1784.987
2	7.35	4	16	0.002125	917.9194	40.65	3109.452
3	12.28	2	8	0.001538	322.7708	35.72	960.781
4	21	4	16	0.0005	231.7698	27	521.482
5	29.75	2	8	-0.00054	-125.83	18.25	-191.366
6	38.5	2	8	-0.00158	-367.544	9.5	-290.973
7	50.93	2	8	-0.00306	-528	-2.93	128.92
8	57.5	2	8	-0.00385	-528	-9.5	418
9	66.25	2	8	-0.00489	-528	-18.25	803
10	75	4	16	-0.00593	-1056	-27	2376
11	83.72	2	8	-0.00697	-528	-35.72	1571.68
12	88.65	4	16	-0.00756	-1056	-40.65	3577.2
13	91.36	2	8	-0.00788	-528	-43.36	1907.84
concrete 1					2023	40.03922	6749.944
concrete 2					1255.824	30.922	3236.049
total					**-0.09007**		**26663**

Steel Strain = 6 * ϵ_y c = 16.45615 a = 13.16492

Steel Layer	Dist. from top (in).	Number of Bars	Area of Bars (in^2)	Strain	Force (kips)	Moment arm (in.)	Moment (ft-kips)
1	4.64	2	8	0.002154	465.7548	43.36	1682.927
2	7.35	4	16	0.00166	702.275	40.65	2378.956
3	12.28	2	8	0.000761	142.627	35.72	424.5529
4	21	4	16	-0.00083	-384.357	27	-864.804
5	29.75	2	8	-0.00242	-528	18.25	-803
6	38.5	2	8	-0.00402	-528	9.5	-418
7	50.93	2	8	-0.00628	-528	-2.93	128.92
8	57.5	2	8	-0.00748	-528	-9.5	418
9	66.25	2	8	-0.00908	-528	-18.25	803
10	75	4	16	-0.01067	-1056	-27	2376
11	83.72	2	8	-0.01226	-528	-35.72	1571.68
12	88.65	4	16	-0.01316	-1056	-40.65	3577.2
13	91.36	2	8	-0.01366	-528	-43.36	1907.84
concrete 1					1855.607	40.54656	6269.875
total					**-3026.09**		**19453.15**

Steel Strain = 12 * ϵ_y c = 9.042457 a = 7.233966

Steel Layer	Dist. from top (in).	Number of Bars	Area of Bars (in^2)	Strain	Force (kips)	Moment arm (in.)	Moment (ft-kips)
1	4.64	2	8	0.001461	304.8581	43.36	1101.554
2	7.35	4	16	0.000562	260.5377	40.65	882.5713
3	12.28	2	8	-0.00107	-249.194	35.72	-741.769
4	21	4	16	-0.00397	-1056	27	-2376
5	29.75	2	8	-0.00687	-528	18.25	-803
6	38.5	2	8	-0.00977	-528	9.5	-418
7	50.93	2	8	-0.0139	-528	-2.93	128.92
8	57.5	2	8	-0.01608	-528	-9.5	418
9	66.25	2	8	-0.01898	-528	-18.25	803
10	75	4	16	-0.02188	-1056	-27	2376
11	83.72	2	8	-0.02478	-528	-35.72	1571.68
12	88.65	4	16	-0.02641	-1056	-40.65	3577.2
13	91.36	2	8	-0.02731	-528	-43.36	1907.84
concrete 1					837.2907	44.06277	3074.445
total					**-5710.51**		**11502.44**

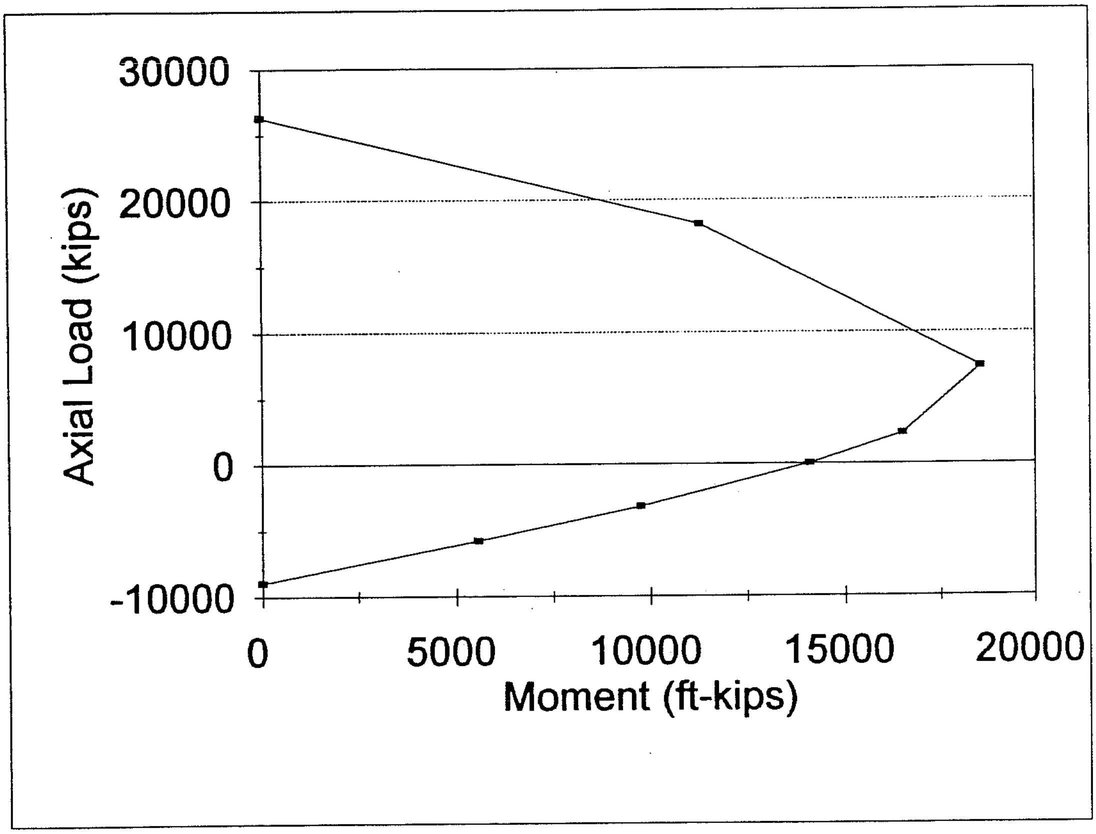

Figure E.1 - Moment interaction diagram for the longitudinals moments in piers #3,4,6,7, and 10 of the North Connector

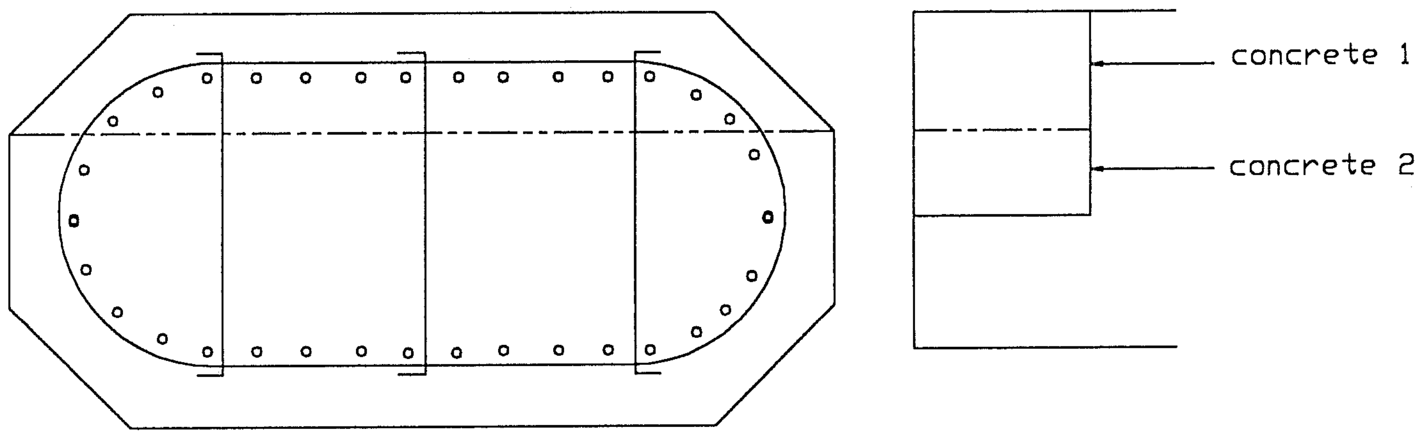
concrete 1
concrete 2

Figure E.2 - Force diagram used to calculate moment interaction diagram

Bibliography

1. *AASHTO LRFD Bridge Design Specifications*, 1st edition, American Association of State and Highway Transportation Officials, Washington, D.C., 1994.

2. *Bridge Design Aids Manual*, Section 14, California Department of Transportation (CALTRANS), Office of Structures, October 1989.

3. *Bridge Design Practice*, California Department of Transportation (CALTRANS), Office of Structures, March 1993 and June 1994.

4. *Bridge Design Specifications*, California Department of Transportation (CALTRANS), Office of Structures, August 1987.

5. *Building Code Requirements for Structural Concrete (ACI 318-95) and Commentary*, American Concrete Institute, Detroit, 1995.

6. Choek, G.S., and Stone, W.C., *Behavior of 1/6-Scale Model Bridge Columns Subjected to Cyclic Inelastic Loading*, Report NO. NBSIR 86-3494, National Bureau of Standards, Gaithersburg, MD, November 1986.

7. Darragh, R., Cao, T., et al., *Quick Reports on CSMIP Strong-Motion Data from the Northridge/San Fernando Valley Earthquake of January 17, 1994 (No. 1)*, Department of Mines and Geology, Sacramento, CA.

8. Fenves, G.L. and Desroches, R., *Response of the Northwest Connector in the Landers and Big Bear Earthquakes*, Report No. UCB/EERC-94/12, Earthquake Engineering Research Center, University of California, Berkeley, December 1994.

9. Imbsen, R.A., Nutt, R.V., and Penizen, J., *Seismic Response of Bridges - Case Studies*, Report No. UCB/EERC-78/14, Earthquake Engineering Research Center, University of California, Berkeley, June 1978.

10. *Memo to Designers*, Section 20-3, California Department of Transportation (CALTRANS), Office of Structures, May 1994.

11. *Memo to Designers*, Section 20-4, California Department of Transportation (CALTRANS), Office of Structures, March 1995.

Bibliography (con't)

12. Moehle, J.P., editor, *Preliminary Report on the Seismological and Engineering Aspects of the January 17, 1994, Northridge Earthquake*, Report No. UCB/EERC-94/01, Earthquake Engineering Research Center, University of California, Berkeley, January 1994.

13. Priestly, M.J.N., Seible, F., and Uang, C.M., *The Northridge Earthquake of January 17, 1994: Damage Analysis of Selected Freeway Bridges*, Report No. SSRP-94/06, Department of Applied Mechanics and Engineering Sciences, University of California at San Diego, February 1994.

14. Phone conversation, Mr. James Wright, Director, Engineering Science Center, California Department of Transportation, 14 March 1996.

15. Saadeghvarizi, M.A., and Foutch, D.A., "Dynamic Behaviour of R/C Highway Bridges Under the Combined Effect of Vertical And Horizontal Earthquake Motions", *Earthquake Engineering and Structural Dynamics*, Vol. 20,

16. Saadeghvarizi, M.A., and Foutch, D.A., *Inelastic Response of R/C Bridges Under Horizontal and Vertical Earthquake Motions*, Civil Engineering Studies, SRS No. 540, University of Illinois at Urbana-Champaign, June 1988.

17. Shephard, R.B., Wood, P.B, et al., "The Loma Prieta, California, Earthquake of October 17, 1989: Report of the New Zealand National Society for Earthquake Engineering Reconnaissance Team", *Bulletin of the New Zealand National Society for Earthquake Engineering*, Vol. 23, No.1, March 1990.

18. Stone, W.C., and Choek, G.S., *Inelastic Behavior of Full-Scale Bridge Columns Subjected to Cyclic Loading*, NIST Building Science Series 166, National Institute of Standards and Technology, Gaithersburg, MD, January 1989.

19. "Synthetic Data for the Northridge Earthquake for the Piers and Abutments of Ramp C", Lamont-Doherty Earth Observatory, Palisades, NY, 16 June 1995.

20. Todd, D., Carino, N., et al. *1994 Northridge Earthquake: Performance of Structures, Lifelines, and Fire Protection Systems*, NIST Special Publication 862, National Institute of Standards and Technology, Gaithersburg, MD, May 1994.

Bibliography (con't)

21. *Uniform Building Code*, 1994 edition, International Conference of Building Officials, Whittier, CA, 1994.

22. Werner, S.D., Levine, M.B., and Beck, J.L., *Seismic Response Characteristics of Meloland Road Overpass During 1979 Imperial Valley Earthquake*, Report No. R-8222-5603, Agbabian Associates, El Segundo, CA, March 1985.

23. Williams, D., and Godden, W.G., *Experimental Model Studies on Seismic Response of High Curved Overcrossings*, Report No. UCB/EERC-78/14, Earthquake Engineering Research Center, University of California, Berkeley, June 1978.

24. Yu, Chih-Peng, Dissertation in Progress, The University of Texas at Austin, November, 1995.

VITA

Daniel Scott Broekhuizen was born in Kalamazoo, Michigan, on January 25, 1972. He is the son of Gary Thomas Broekhuizen and Dorothy Jean Broekhuizen. After obtaining his diploma from Kalamazoo Christian High School in 1990, he entered Calvin College and Seminary in Grand Rapids, Michigan. While at Calvin College, he served as the secretary of the Calvin College Student Chapter of ASCE. He received the degree of Bachelor of Science in Engineering in May, 1994. The following fall (September, 1994), he entered the Graduate School at the University of Texas. He worked at McNamee, Porter, and Seeley in the summer of 1993 and StructureTec, Inc. during the summer of 1994.

Permanent Address: 1508 Southport Drive #107
Austin, Texas 78704

This thesis was typed by the author.